UNIVERSITY OF SOUTHAMPTON

FACULTY OF ENGINEERING AND THE ENVIRONMENT

Aerodynamics and Flight Mechanics

Dynamics of Non-spherical Particles in Turbulence.

by

Luis Blay Esteban

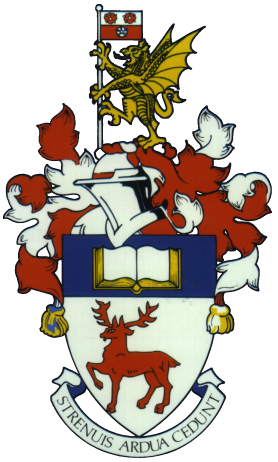

Thesis for the degree of Doctor of Philosophy

February 15, 2019

UNIVERSITY OF SOUTHAMPTON

ABSTRACT

DYNAMICS OF NON-SPHERICAL PARTICLES IN TURBULENCE.

by Luis Blay Esteban

Recent experimental and numerical investigations have enabled researchers to study directly the 3D time dependent motion of spherical and quasi-spherical particles in quiescent and turbulent flows. At the same time, fibre-like particles have been also extensively investigated during the last decades due to the high relevance of these geometries in the process industries. Although these studies have permitted the scientific community to understand several scenarios, the influence of turbulence on the settling dynamics of large, inertial, planar particles remains to be understood; and this represents not only an interesting research problem in itself but also a useful tool to optimize industrial processes, as for the case of Aquavitrum Ltd.

To tackle this problem we first extended the work carried for disks falling under the fluttering mode, but to other planar geometries. We found several modes of secondary motion for n-sided polygons falling in quiescent fluid that are associated with the particle dimensionless inertia and Reynolds number. We also measured the wake behind these particles and identified strong differences associated with their falling style. Other variations of disk-like particles with wavy-edge were investigated and drag correlations based on the particle geometry obtained. We also proposed a one-equation simple pendulum model to capture precisely the complete trajectory of the particle as long as the three dimensional state of the trajectory remains moderate.

Then, a random jet array facility to generate turbulence was built and two turbulence states were investigated. First, we focused on the homogeneity of the stationary state to later investigated the temporal decay of turbulent kinetic energy. We observed an overall enhancement of the decay rate as compare with previous studies and found that this was caused due to turbulent confinement.

Finally, the fall of inertial disks was investigated under the effect of background turbulence. We observed severe differences on the falling style of disks as compared with the quiescent case. We also found that the mean descent velocity of the particles was enhanced for the configurations tested and this was inversely correlated with the frequency of the oscillatory motion. Last, we measured particle dispersion and found the the radial position of the particles can be well captured with lognormal distributions.

Contents

List of Figures

List of Tables

Declaration of Authorship

I, Luis Blay Esteban, declare that the thesis entitled *Dynamics of Non-spherical Particles in Turbulence* and the work presented in the thesis are both my own, and have been generated by me as the result of my own original research. I confirm that:

- this work was done wholly or mainly while in candidature for a research degree at this University;
- where any part of this thesis has previously been submitted for a degree or any other qualification at this University or any other institution, this has been clearly stated;
- where I have consulted the published work of others, this is always clearly attributed;
- where I have quoted from the work of others, the source is always given. With the exception of such quotations, this thesis is entirely my own work;
- I have acknowledged all main sources of help;
- where the thesis is based on work done by myself jointly with others, I have made clear exactly what was done by others and what I have contributed myself;
- parts of this work have been published as:

1. **L.B. Esteban**, J. S. Shrimpton, P. Rogers and R. Ingram. Three Clean Products From Co-mingled Waste Using A Novel Hydrodynamic Separator. International Journal of Sustainable Development and Planning. Vol 11: 792-803 (2016)

2. **L.B. Esteban**, J. S. Shrimpton, B. Ganapathisubramani. Trajectory and wake differences between disks and square plates. Tenth International Symposium on Turbulence and Shear Flow Phenomena, Conference Proceedings. (2017)

3. **L.B. Esteban**, J. S. Shrimpton, B. Ganapathisubramani. Edge effects on the fluttering characteristics of freely falling planar particles. Physical Review Fluids 3, 064302 (2018)

4. **L.B. Esteban**, J. S. Shrimpton, B. Ganapathisubramani. Study of the circularity effect on drag of disk-like particles. International Journal of Multiphase Flow, 110: 189-197 (2019)

5. **L.B. Esteban**, J. S. Shrimpton, B. Ganapathisubramani. Laboratory experiments on the temporal decay of homogeneous anisotropic turbulence. Journal of Fluid Mechanics, 862: 99-127 (2019)

Signed:

Date: 16/04/2019

Acknowledgements

I came to the University of Southampton on September 2014 with the only purpose of doing a one year MSc program. After a few months of being here I met Prof. Bharath Ganapathisubramani in the *Turbulence* module that he was teaching. He was so passionate about this subject that I had the urge to learn more about it. He gave me the opportunity to do the MSc project in his research group and Eda Dogan and every other person in the group helped me to feel integrated.

I met Prof. John Shrimpton once this project was done and after a few meetings he accepted my application to undertake my PhD studies under his (and Bharath's) supervision. I only have nice words to explain how they treated me during these three years. They gave me very good guidance but always with the necessary freedom that allows you to fail, learn and improve. They supported my ideas and they were always there when I needed them. Thanks for all these moments, from the long discussions in the faculty to the always welcomed visits to the lab.

I would also like to thank all my colleagues and friends from the faculty, who have shared their time with me during these three years. Thanks for all these beers, meals, cakes, teas and coffees that we have shared. Thanks to all my old friends that have understood me and that keep spending time with me on every occasion that we have.

Thanks must also go to my parents for their unconditional support and faith on me. I would not be who I am without their love during all these years.

Words cannot describe how thankful I am to my partner, Adriana. All this would have been impossible without you.

Nomenclature

Roman Symbols

b	particle body force
d	particle diameter
d_{eq}	general particle equivalent diameter
$d_{V_{eq}}$	sphere diameter with equivalent volume
f	frequency
g	acceleration due to gravity
k	turbulent kinetic energy
ℓ	particle equivalent diameter (D_c/Q)
m	mass
t	particle thickness
t_L	eddy-turnover time
A_p	projected area
D	disk diameter with equivalent particle volume
D_c	diameter of circumscribed disk
E	energy spectrum
F_D	drag force
I	mass moment of inertia
L	integral length scale
P	particle perimeter
Q_{dis}	water discharge
R	distance from origin
S	skewness factor
T	energy transfer spectrum
T_i	torque
T_{v_z}	timescale of descent velocity fluctuations
U	velocity
U_t	terminal velocity

Non-dimensional Quantities

Ar	Archimedes number
C_D	Drag Coefficient
Fr	Froude number
G	Galileo number
Q	Isoperimetric quotient
Re	Reynolds number
St	Stokes number
St	Strouhal number
X	Best number

Greek

α_{v_z}	std. of descent velocity fluctuations
β	thickness to width ratio
ϵ	energy dissipation rate
η	Kolmogorov lengthscale
θ	particle nutation angle
θ_0	max. angle of pendulum model
κ	kurtosis
λ	Taylor length scale
μ	viscosity
ν	kinematic viscosity
ρ	density
σ	total stress tensor
τ	response time
τ_d	fluid time scale at scale d
$\tau_{p_{eff}}$	measured particle response time
τ_f	fluid response time
τ_v	viscous relaxation time
τ_w	wall shear stress
ϕ	fractional number of pumps in operation
ϕ_v	fractional volume of the dispersed phase
ψ	sphericity
ω	angular velocity
Λ	production rate of total kinetic energy

Subscripts

d	based on particle diameter scale
f	fluid magnitude
min	smallest value
med	intermediate value
max	maximum value
p	particle magnitude
q	magnitude in quiescent flow
r	relative to disk magnitude
z	vertical magnitude
L	based on integral scale
η	based on Kolmogorov scale
λ	based on Taylor scale
$\parallel$	parallel to the motion
$\perp$	perpendicular to the motion
1	along the horizontal direction
2	along the vertical direction

Superscripts

$.^*$	non-dimensional value
$.'$	root mean square

Abbreviations

BBO	Basset, Boussinesq and Ossen equation
CDF	Cumulative Density Function
CSF	Corey Shape Function
DNS	Direct Numerical Simulation
FOV	Field of View
HD	Homogeneity Deviation
HIT	Homogeneous Isotropic Turbulence
LES	Large Eddy Simulations
MFF	Mean Flow Factor
M-R	Maxey-Riley equation
MRF	Material Recovery Facility
MSRF	Mean Strain Rate Factor
OU	Ornstein Uhlenbeck process
PDF	Probability Density Function
PIV	Particle Image Velocimetry
PLA	Polylactide

SFT	Structure Funtion Fit
TKE	Turbulent Kinetic Energy

Operators

∇	divergence
$\langle \cdot \rangle$	spatial average
$\bar{\cdot}$	time average
$\mathbf{v}$	vector form of v

Chapter 1

Introduction

1.1 Aim of the Industrial Research Project

The industrial aim associated to this project is to improve the efficiency of a novel device that separates glass and plastic particles from a co-mingled waste product coming from Material Recovery Facilities (MRF). This waste product is mainly composed of glass, plastic, paper-based materials and metals. However, most of the metals are removed from the raw product before this enters the separator, whereas paper and other cellulose-based materials are suspended in water. Thus, the main task of this device is to separate plastics that are lighter and heavier than water from glass; and the later water treatment that permits to filter the pulp suspended in it.

The benefits of this project become evident when the environmental and social impact of indiscriminate land-filling and incineration are considered. The improper use of these disposal methods have been the source of severe pollution problems such as the increase in particulate matter carbon monoxide and hydrocarbons, as well as water pollution from landfill sites.

Policies and regulations to control these practices have tightened in most European countries during the last decades. The landfill tax in the UK has increased from £7 per ton of waste in 1996 to £82.6 in 2015, diminishing the economical attractiveness of this disposal method. Following on, the landfilling of any recyclables will be banned in the European Union by 2025.

Despite of the increase of waste separation at household level, municipal solid waste needs to be mechanically or optically sorted and cleaned to be able to carry out the recycling process. The use of MRFs at this stage favours material and energy recovery and reduces the economic cost of the total waste management chain. However, most of MRFs plants dealing with co-mingled recyclables and black bag waste generate a residual waste product that contains a very high proportion of glass, known as MRF

glass. This product has little or no commercial value as it is, since it is too contaminated to provide a viable feedstock for optical separation and hence recycling. Aquavitrum technology uses this product as the feedstock for their hydrodynamic separator, and therefore reduces enormously the volume of material to be landfilled.

Despite the great number of challenges that have to be tackled to achieve the industrial aim of this project; the research in here will be focused on understanding the motion of highly non-spherical particles in turbulent flows.

1.2 The Need for Fundamental Research

Dispersed multiphase flows are considered one of the most complicated topics in fluid mechanics, a full understanding perhaps an impossible challenge. These flows are encountered in many industrial and environmental environments. Some examples are the combustion processes inside automotive engines [Moffet and Prather, 2009]; and atmospheric phenomena such as seed dispersal [Sabban and van Hout, 2011] and the dispersion and deposition of pollutants in urban and natural environments [Janhall, 2015].

Frequently, dispersed multiphase flows are turbulent. The dispersed phase, i.e. particles, droplets or bubbles, is distributed within the carrier phase and interacts with the temporal and spatial scales of the turbulence. These interactions can lead to severe differences in the disperse phase motion over the laminar case. An example of such difference in particle behaviour is the phenomena of preferential concentration, reviewed in [Monchaux et al., 2012]. Particles under this effect interact with turbulence forming particle clusters in regions of low-vorticity. The increase in particle local concentration makes the hypothesis of disperse phase unrealistic, and particle-particle interaction must be considered.

Particle-turbulence interactions for the case of 'small' and 'heavy' -these attributes will be explained in detail further along this chapter- spherical particles have been extensively investigated. However, there is a gap in the literature concerning the motion of large, inertial, irregular particles and how these interact with turbulent flows. In here, the interaction between this type of particles and turbulence will be investigated through a detailed set of experiments with the aim of forming a fundamental understanding of particle-turbulence interactions for anyone to develop more robust models and strategies for predicting and controlling the behaviour of these particles. Furthermore, this work aims to clarify the separation process present in Aquavitrum technology by reproducing the scenarios that are present in Aquavitrum facility in the laboratory. The work presented in this thesis is limited in the sense that focus lies upon the following underlying research objectives;

1. Investigate the behaviour of planar particles in quiescent flow based on particle Reynolds number (Re) and dimensionless moment of inertia (I^*).

2. Design, build and test a facility to generate turbulence and investigate the free decay of turbulence in a confined domain.

3. Investigate the descent of single particles under the effect of turbulence.

1.3 Introduction to Multiphase Flows

Dispersed multiphase flows are found throughout the process industries at all scales and sectors; including the food, the pharmaceutical and the oil and gas industry among others.

In the oil and gas industry, the precipitation of paraffinic components forms solid-liquid multiphase flow that might block pipelines causing serious problems to the transportation systems, [Ashbaugh et al., 2005]. In order to solve this issue, hydrophobic solid particles are added to the raw material so that they act as emulsion stabilisers, [Binks and Tyowua, 2016], [Sullivan and Kilpatrick, 2002]. Another relevant application where multiphase flow is present is in the use of circulating fluidized beds. In these systems, upwards jets of air cause the solid fuels to be suspended, enhancing the gas-solid mixing for better heat transfer and chemical reactions, [Sinquin et al., 2004].

In the pharmaceutical sector, the understanding of these systems is required for the successful preparation of cosmetics and dermatological products, [Muller et al., 2002]; and the control of drug delivery [Muller et al., 2000].

Similarly, in combustion processes such as chemical looping combustion, [Derksen, 2009], [Hoef et al., 2008]; and coal combustion systems, [Bu et al., 2014], [Son and Kihm, 1998], multiphase flows also play a paramount role.

Last but not least, multiphase flows are also present in naturally and man made environmental processes. Being shore and river erosion, [Anping et al., 2016], [Barhtyar et al., 2009], [Dail et al., 2000], and the dispersion and deposition of industrial pollutants some of the most relevant, [Kolb and Worsnop, 2012].

The physics of dispersed multiphase flows are complex due to the range of scales present, ranging from the thickness of the boundary layer around a single particle to the largest scales in the flow. For non-spherical particles the shape of the boundary layer is a function of the particle orientation relative to the flow and this is often chaotic, even in a quiescent fluid. The unsteadiness of the boundary layer gives rise, in turn, to chaotic particle trajectories. Particle-particle interactions, i.e. wakes and collisions; and, for a turbulent continuum phase flow, an additional range of lengthscales complete the picture.

In view of this complexity, researchers have historically made the assumption of particle sphericity and immediately the problem becomes much more tractable, and amenable to theoretical treatment. A second assumption is needed to resolve the flow around the sphere, and it is that the disturbance flow produced by the motion of the sphere occurs at sufficiently low Reynolds number ($Re_p << 1$) that the fluid force perceived by the sphere can be obtained through results of unsteady Stokes flow. Because the '$Re_p << 1$ condition' is very much the exception rather than the norm in dispersed multiphase flow another key assumption is often made. The finite sized particle is assumed to be a point, and numerical models are used to account for the impact of boundary layer separation and wake formation on the particle acceleration. A final assumption is often invoked, in that the density ratio (ρ_p/ρ_f) is large, and the only acceleration term present that arises from the boundary layer interaction is that of drag. With these three key assumptions, 'sphericity, 'smallness' and 'heaviness' in place, dispersed multiphase flows become tractable and representative simulations of billions of particles in complex flow systems become possible. This segment of the subject is widely reported with general reviews, see [Balachandar and Eaton, 2010], and reviews covering several specific aspects, see [Monchaux et al., 2012] for particle preferential concentration and clustering in turbulence, [Gore and Crowe, 1989] for the effect of particle size on turbulence modulation, [Fox, 2012] for considerations on LES for multiphase flows or [Subramaniam, 2013], [Gouesbet and Berlemont, 1999] and [Toschi and Bodenschatz, 2009] for Lagrangian and Eulerian approaches for multiphase flows.

1.3.1 Scope of the Literature Review

An implicit concern, and the inspiration for this review on multiphase flows, is that the very well established conclusions for 'small' 'heavy' spheres made under these very restrictive conditions can easily be carried over to the motion of larger, lighter and non-spherical particles. Indeed, many correlations exist to 'correct' the average motion of non-spherical particles based on the 'fundamental' equations of motion for a 'small' 'heavy' sphere, as the shape factor corrections proposed by [Loth, 2008], [Holzer and Sommerfeld, 2008] and [Gabitto and Tsouris, 2008] among others. In this chapter, particles are classified into three characteristic types; i.e. 'spherical', 'quasi-spherical' and 'aspherical'. 'Quasi-spherical' and 'aspherical' particles are differentiated in terms of their secondary motions, i.e. deviations from the mean trajectory over many realizations. When these secondary motions are small, then the use of a shape factor (a one parameter correction factor) can make a reasonably accurate prediction of the particle drag coefficient for a single realization, [Loth, 2008]. The established convention of delimiting 'quasi-spherical' and 'aspherical' particles purely by geometric information can lead to unsafe predictions of particle motion. Therefore, 'sphericity' should be categorised in terms of the particle hydrodynamics, or more specifically, in terms of relevance of the secondary motion. As noted, this depends on Reynolds number and

particle shape, which can be captured by a more general parameter, the dimensionless moment of inertia (I^*). Thus, we believe that the use of traditional shape factors to estimate particle descent should be restricted to sub-critical Reynolds numbers where secondary motions can be neglected.

When a heavier than fluid 'aspherical' particle is released in a quiescent fluid, it takes some time to lose memory of its initial conditions and to follow a periodic or chaotic trajectory. If an 'aspherical' particle is in a turbulent flow, one can hypothesize that it will hop from one turbulent eddy to the next at a frequency defined by the level of turbulence present and that this motion will co-exist with the natural descent of the particle in quiescent flow. Therefore there should be a criteria, similar to Stokes number for 'small' 'heavy' spheres that could define the relative relevance of these two phenomena and predict whether an 'aspherical' particle exhibits secondary motion in turbulent flows or not.

Recent advances in optical diagnostics and also large scale fully resolved direct numerical simulations have enabled researchers to study directly the 3D time dependent motion of non-spherical particles in quiescent and in turbulent flows, [Fornari et al., 2016a], [Byron et al., 2015], [Klein et al., 2013], [Meyer et al., 2013], [Bellani et al., 2012], [Klein et al., 2013], [Zimmermann et al., 2011b], [Zimmermann et al., 2011a]. This data has permitted the scientific community to put the established empirical correlations that enable the prediction of the motion 'large' and/or 'light' and/or 'aspherical' particles through extension of the 'small' and 'heavy' equations to be put under scrutiny.

The primary focus of the literature review is the collation of recent fundamental research to understand the motion of non-spherical particles and how these interact with turbulent flows. To tackle this question we split the problem in two; first we focus on how spherical particles respond to turbulence and then on how aspherical particles behave in still fluid. The combination of these two problems will establish the basics for our research question: How do aspherical particles move in turbulence?

1.3.2 Plan of the Chapter

After the preliminary introduction to the industrial problem and to disperse multiphase flows in general, the next sections of this chapter are organized as follows. Section 1.4 presents the equations of motion of an arbitrary object and the assumptions that simplify them to the Basset-Boussinesq-Oseen (BBO) equation. In section 1.5 the physics of 'small' 'heavy' spheres in homogeneous turbulence is reviewed and the change in motion when they become 'large' 'light' spheres is studied in section 1.6. Then, non-spherical particles are introduced in section 1.7, and the motion of quasi-spherical objects and aspherical objects considered independently. Section 1.7.4 deals with the secondary motion of aspherical objects and the non-dimensional parameters that define the limits

between the descent regimes. Section 1.8 shows the scant research done on aspherical objects under turbulent conditions and propose several guidelines that might improve the current level of understanding of these flows. Finally, section 1.10 presents the specific problem of Aquavitrum Ltd. and shows an estimate of the turbulence characteristics within the hydrodynamic separator.

1.4 Equations of Motion for an Arbitrary Object in a Continuum Fluid

Independent of the particle shape, the motion of particles is derived by considering the conservation of linear and angular momentum. In integral form the equations can be defined as in [Taylor, 2005],

$$\frac{dX_i}{dt} = U_{p_i} \tag{1.1}$$

$$m_p \frac{dU_{p_i}}{dt} = \int_V b_i dv + \int_S \sigma_{ij} ds_j \tag{1.2}$$

$$\frac{dL_i}{dt} = I_{ij}\alpha_j \tag{1.3}$$

where

$$I_{ij} = \int_V \rho(r)(r^2\delta_{ij} - x_i x_j)dV \tag{1.4}$$

where U_p is the particle linear velocity, m_p is the particle mass, σ is the surface stress tensor, b are the body forces per unit volume, L is the angular momentum, I is the moment of inertia, α is the angular acceleration and r is the distance from the centre of mass. Equation 1.1 deals with the particle location, Eq. 1.2 with its linear velocity and Eq. 1.3 is responsible for the angular velocity of the particle.

The case exposed is for particles which centre of mass and centre of rotation are not the same; we will return back to these equations when aspherical particles are considered. However, first we briefly introduce the simplifications made for spheres.

1.4.1 Spherical Shape and Stokes Flow Simplification

Several assumptions are often found in the literature when particle motion is studied, a spherical particle shape and Stokes flow being the most frequent. When the spherical assumption is considered, Eq. 1.2 becomes the only necessary equation to define the particle motion. Furthermore, if Stokes flow is considered, $Re_p << 1$, the flow around the particle can be solved analytically. This, in turn, allows Eq. 1.2 to be solved, which gives the well known BBO equation, ([Basset, 1888], [Boussinesq, 1903] and [Oseen,

1927])

$$\frac{\pi}{6}\rho_p d_p^3 \frac{d\mathbf{U_p}}{dt} = 3\pi\mu d_p(\mathbf{U_f} - \mathbf{U_p}) - \frac{\pi}{6}d_p^3 \bigtriangledown \mathbf{p} + \frac{\pi}{12}\rho_f d_p^3 \frac{d}{dt}(\mathbf{U_f} - \mathbf{U_p}) + \frac{3}{2}d_p^2\sqrt{\rho_f \mu \pi}\left(\int_0^t \frac{(d/d\tau)(\mathbf{U_f} - \mathbf{U_p})}{(t-\tau)^{1/2}}d\tau + \frac{(\mathbf{U_f} - \mathbf{U_p})_0}{t^{1/2}}\right) + \sum_n \mathbf{f_n} \tag{1.5}$$

where the terms in bold stand for vector notation. The terms on the right hand side of Eq. 1.5 reveal the force distribution integrated over the particle surface, as previously shown in Eq. 1.2; and this can be decomposed into separate forces; which are, from left to right, the following:

- Drag force, usually the most important term; it includes friction and form drag.
- Local fluid pressure gradient along the fluid trajectory.
- Added mass, accounts for the form drag due to relative acceleration.
- Basset force with initial condition, addresses the temporal delay in boundary layer development as the relative velocity change.
- Body forces, such as gravitational and electrostatic forces.

If flow non-uniformity effects are included the Faxen force appears in the steady state drag term and an additional term appears in the Basset force. For simplicity, the terms due to flow field non-uniformity are not included in here.

The pressure term can be related to the fluid acceleration with the Navier-Stokes equation as follows

$$-\bigtriangledown \mathbf{p} = \rho_f \left(\frac{D\mathbf{U_f}}{Dt} - \mu \bigtriangledown^2 \mathbf{U_f}\right) \tag{1.6}$$

Then, the combination of the new pressure term with the virtual mass term gives the following form of the BBO eq,

$$\left(1 + \frac{1}{2}\frac{\rho_f}{\rho_p}\right)\frac{d\mathbf{U_p}}{dt} = \frac{18\mu}{\rho_p d_p^2}(\mathbf{U_f} - \mathbf{U_p}) + \frac{3\rho_f}{2\rho_p}\frac{D\mathbf{U_f}}{Dt} + 9\sqrt{\frac{\nu}{\pi}}\frac{\rho_f}{\rho_p}\frac{1}{d_p}\left(\int_0^t \frac{(d/d\tau)(\mathbf{U_f} - \mathbf{U_p})}{(t-\tau)^{1/2}}d\tau + \frac{(\mathbf{U_f} - \mathbf{U_p})_0}{t^{1/2}}\right) + \mathbf{g}\left(1 - \frac{\rho_f}{\rho_p}\right) \tag{1.7}$$

Several years after the introduction of the BBO equation, [Tchen, 1947] tackled the problem of generalising the equation to fluids with non-zero velocity. In order to do so he followed a two step procedure. First, he considered the case of a particle moving with

respect to the fluid $(U_p - U_f)$ being $U_f = 0$. Subsequently, the system is characterized with a time-dependent velocity $U_f(t)$, then the particle moves with velocity U_p in a fluid with velocity U_f. Following this approach, Tchen introduced an additional pressure gradient term due to the fluid acceleration; and from this new formulation an additional extra force appeared when the normal stresses on the surface of the sphere are integrated.

The procedure followed by Tchen gave rise to a long controversy that was resolved by [Maxey and Riley, 1983], who proposed a new equation of motion (M-R equation) that accounted for the influence of curvature in the velocity field.

1.4.2 'Heavy' Simplification

Now that the general equation of motion, Eq. 1.7, has been simplified for spherical particles, one can further simplify it by considering the particle density much greater than the fluid density ($\rho_p/\rho_f >> 1$). It is common in the literature to term particle-fluid systems where $\rho_p/\rho_f >> 1$ to be composed of 'heavy' particles. Thus, all forces acting on the particle can be neglected but the drag force and the gravity force. Then, Eq. 1.7 can be expressed, in extensive form, as:

$$m_p \frac{d\mathbf{U_p}}{dt} = \mathbf{F_D} + m_p \mathbf{g} \tag{1.8}$$

where g is the gravity acceleration and the surface force, F_D, is quantified by the drag coefficient through the following equation

$$\mathbf{F_D} = \frac{1}{2}\rho_f C_D A_p |\mathbf{U_f} - \mathbf{U_p}|(\mathbf{U_f} - \mathbf{U_p}) \tag{1.9}$$

where C_D is the drag coefficient and A_p is the projected area of the particle in the direction of motion.

On the other hand, the analytical solution of the flow field around the particle, via Stokes equation, gives a total drag force of

$$\mathbf{F_D} = 3\pi\mu d(\mathbf{U_f} - \mathbf{U_p}) \tag{1.10}$$

which is then used to solve the drag coefficient as

$$C_D = \frac{24}{Re_p} \tag{1.11}$$

only true for $Re_p << 1$, and being

$$Re_p = \frac{d_p|\mathbf{U_p} - \mathbf{U_f}|}{\nu} \tag{1.12}$$

Then, the equation of motion of a spherical particle under steady-state drag assumptions for $\rho_p/\rho_f >> 1$ and $Re_p << 1$ is expressed as

$$m_p \frac{d\mathbf{U_p}}{dt} = 3\pi\mu d(\mathbf{U_f} - \mathbf{U_p}) + m_p\mathbf{g} \tag{1.13}$$

or, in intensive form

$$\frac{d\mathbf{U_p}}{dt} = \frac{1}{\tau_v}(\mathbf{U_f} - \mathbf{U_p}) + \mathbf{g} \tag{1.14}$$

where τ_v is the viscous relaxation time of the particle.

$$\tau_v = \frac{\rho_p d_p^2}{18\mu} \tag{1.15}$$

This parameter represents a typical timescale of the reaction of the particle to changes in the carrier phase velocity.

When Eq. 1.14 is made non-dimensional to $U = U^* U_0$, $t = t^* t_0$, $d = d^* d_0$ and $g = g^* g_0$, one can obtain:

$$\frac{U_0^2}{d_0}\frac{d\mathbf{U}^*}{dt^*} = \frac{18\mu_{f_0}}{\rho_{p0} d_{p0}^2} U_0 \frac{\mathbf{U_f^*} - \mathbf{U_p^*}}{t_v} + g_0\mathbf{g}^* \tag{1.16}$$

$$\frac{d\mathbf{U}^*}{dt^*} = \frac{18\mu_{f_0}}{U_0\rho_{p0} d_{p0}} \frac{\mathbf{U_f^*} - \mathbf{U_p^*}}{t_v} + g_0\mathbf{g}^* \frac{d_0}{U_0^2} \tag{1.17}$$

which can be expressed in terms of non-dimensional numbers as

$$\frac{d\mathbf{U}^*}{dt^*} = \frac{18\rho_f}{\rho_{p_0}} \frac{1}{Re_p}(\mathbf{U_f^*} - \mathbf{U_p^*}) + \frac{1}{Fr^2} \tag{1.18}$$

Thus, the particle motion is a function of the density ratio ρ_f/ρ_p, Re_p and Fr. The Froude number (Fr), defined as the ratio of inertia to gravity forces, will play a relevant role in the particle motion when gravitational forces becomes dominant, whilst the Reynolds number (Re_p) will characterize the particle motion when the inertia term predominates. The Archimedes number, which is defined as the ratio of gravitational forces to viscous forces, ($Ar = Re_p/Fr$) is a useful estimation of the relative relevance of these two parameters.

A particle accelerating from stationary in a quiescent fluid ($U_f = 0$) will experience an increase in drag force up to a point in which the term balances the gravitational force, see Eq. 1.14. At that instant, the velocity derivative will be zero and the particle velocity will remain constant along its trajectory.

$$U_t = \tau_v g \tag{1.19}$$

Conversely, in many circumstances the particle Reynolds number is greater than unity, the flow field around the particle is no longer Stokesian, and the expression obtained for the drag coefficient, see Eq. 1.11, is no longer valid. Thus, the drag coefficient is

obtained by applying a Re_p correction to account for separation and wake formation. One of such Reynolds number corrections for $Re_p < 20$, from [Clift et al., 1978],

$$C_D = \frac{24}{Re_p}(1 + 0.1315 Re_p^n) \tag{1.20}$$

where the exponent n is defined as

$$n = 0.82 - 0.05 log_{10} Re_p \tag{1.21}$$

Thus, with the effect of finite Reynolds number introduced in the particle relaxation time as

$$\tau_p = \tau_v \frac{24}{Re_p C_D} = \frac{\tau_v}{1 + 0.1315 Re_p^n} \tag{1.22}$$

the Stokes flow considerations can be extended to particles covering a wider dynamic range. In summary, for spherical particles where $\rho_p/\rho_f >> 1$, the particle dynamics is characterised by Re_p and the relevance of gravitational effect by the Froude number (Fr), as seen in Eq. 1.18.

1.5 Validity of 'Small' 'Heavy' Spheres in Turbulent Flows

Before reviewing the motion of spheres in turbulent flows, it is of interest to provide a brief description of several turbulent flow quantities that will be used along the following sections. Turbulent motions range in size from the width of the flow itself to much smaller scales, becoming progressively smaller as fluid Reynolds number increases. The largest eddies in the flow are characterized by a lengthscale comparable to the flow scale, (L), and a velocity comparable with the root mean square of the velocity fluctuations,

$$u = \sqrt{(u_1')^2 + (u_2')^2 + (u_3')^2} \tag{1.23}$$

In contrast, the smallest scales have a universal form determined by ν and ϵ, as showed by [Kolmogorov, 1941]. Given these two parameters, there is just one possible length η, velocity u_η and time τ_η scale associated to the smallest turbulent structures:

$$\eta = \left(\frac{\nu^3}{\epsilon}\right)^{1/4} \tag{1.24}$$

$$u_\eta = (\epsilon\nu)^{1/4} \tag{1.25}$$

$$\tau_\eta = \left(\frac{\nu}{\epsilon}\right)^{1/2} \tag{1.26}$$

Additionally, in every turbulent flow at sufficiently high fluid Reynolds number, the range of scales can be divided into the inertial and dissipative sub-range; the Taylor microscale (λ) being the scale that roughly separates these two. The Reynolds number

based on this scale has been generally used to characterize turbulent flows that have no obvious large scale L

$$Re_\lambda = \frac{u\lambda}{\nu} \tag{1.27}$$

The particle motion defined as in the M-R equation, Eq. 1.7, or its simple form Eq. 1.14, does not include turbulent conditions. For this equation to be valid under turbulent conditions it is necessary that the time required for a significant change in the relative velocity is large compare to the timescale for viscous diffusion and that viscous diffusion remains the dominant mechanism for the transfer of vorticity away from the sphere. These conditions conflict with the space and time dependent character of turbulent flows (finite Reynolds number) in certain circumstances. However, if a Kolmogorov eddy is considered to be the smallest relevant domain in space, then one may expect that the M-R equation holds if the particle diameter is much smaller than the characteristic Kolmogorov length scale ($d_p/\eta << 1$), i.e. point particle approximation. As previously mentioned, it is usual to term particle-fluid systems where $d_p/\eta << 1$ and $\rho_p/\rho_f >> 1$ as to be composed of 'small', 'heavy' particles.

Then, since $d_p/\eta << 1$, the Stokes drag term becomes dominant and the Faxen correction term in the Stokes drag term can be dropped; the boundary layer develops much faster relative to the local fluid velocity.

[Elghobashi and Truesdell, 1992] summarized the requirements for the M-R equation to be used in a turbulent flow as follows:

- Re_p based on the fluctuating relative velocity (u), should be less than 0.5.
- The flow in the vicinity of the particle should be at most homogeneous shear
- The upper limit for 'small' particles should be $d_p/\eta \approx 1/6$.
- The flow must be 'dilute'. The particle spacing has to be much greater than the particle dimension, d_p. Then, there are no wake interactions.

1.5.1 Physics of 'Small' 'Heavy' Particles in Homogeneous Turbulence

The behaviour of heavy particles immersed in a turbulent flow has been investigated over the past few years. Here, the effect of the turbulence on the concentration field and on the settling speed of the particles are summarised.

When a particle heavier than the fluid interacts with a turbulent structure, the particle accelerates outwards from the center of the structure by centrifugal forces, as demonstrated by [Ruetsch and Meiburg, 1993], [Lasheras and Tio, 1994], and [Tio et al., 1993] among others. Direct numerical simulations of particle-laden flows were carried out along the same lines and confirmed that as particles interact with the velocity field they

tend to accumulate in low vorticity and high strain regions, leading to an inhomogeneous concentration field, see [Wang and Maxey, 1993], [Truesdell and Elghobashi, 1994] and [Yang and Lei, 1998].

It is noted that in the presence of gravity, the interaction between particles and vortices causes the particle to be preferentially swept to the downward side of the eddies, forcing the particle to settle faster than they would in still fluid, as defined by Eq. 1.19, [Wang and Maxey, 1993]. Nonetheless, this particle-turbulence interaction is Stokes number dependent (see equation 1.28) and the most significant interactions occur when the particle size is comparable to the smallest turbulent structures, i.e. the Kolmogorov scale. Thus, [Wang and Maxey, 1993] showed that the increase in terminal velocity (U_t) normalized by the fluid velocity fluctuations, $\Delta U_t/u$ reaches a maximum of 0.2 for $St = 1$ and $U_t/u_\eta \approx 2$.

[Wang and Maxey, 1993] were the first to state that the phenomena of particle accumulation and settling enhancement were dependent on two non-dimensional parameters, the Stokes number and the terminal velocity ratio. The Stokes number was defined as the ratio between the particle relaxation time, see Eq. 1.15, and the Kolmogorov time scale, Eq. 1.26, such that

$$St_\eta = \frac{\tau_p}{\tau_\eta} = \frac{1}{18}\left(\frac{\rho_p}{\rho_f}\right)\left(\frac{d_p}{\eta}\right)^2 \tag{1.28}$$

The other non-dimensional parameter, U_t/u_η, evaluates the importance of the terminal velocity of the particle to a characteristic velocity of the turbulence. However, [Aliseda et al., 2002] showed that this velocity ratio could be evaluated in terms of the Stokes number, being both phenomena characterized by a single non-dimensional parameter.

$$\frac{U_t}{v_\eta} = \frac{\tau_p}{\tau_\eta}\frac{g}{\left(\epsilon^3/\nu_f\right)^{1/4}} = St_\eta\frac{g}{\left(\epsilon^3/\nu_f\right)^{1/4}} \tag{1.29}$$

Following their reasoning, this velocity ratio can be also evaluated in terms of the Froude number (present in Eq. 1.18) based on the Kolmogorov scale as:

$$\frac{U_t}{v_\eta} = St_\eta\frac{g}{\left(\epsilon^3/\nu_f\right)^{1/4}} = St_\eta\frac{g\eta}{u_\eta^2} = \frac{St_\eta}{Fr_\eta^2} \tag{1.30}$$

Their results showed great agreement with the numerical simulations of [Wang and Maxey, 1993], being the preferential concentration maximized at $St_\eta \approx 1$ for $Re_\lambda \approx 230$.

In the experimental work carried out by [Wood et al., 2005] they analysed particles with $Re_p > 0.01$, so that a correction factor for the finite Reynolds number effect was applied. They considered the turbulence velocity fluctuations, u, as the characteristic velocity that the particle perceives and used it to calculate the Re_p. Although they considered the possibility of modifying the size of the Kolgomorov scale in the experiments according to the particle dimension, the experiments were performed for $d_p/\eta \approx 0.1$. Therefore, the

smallest turbulent scales present in the flow, i.e. Kolmogorov scale, were still affecting the particle behaviour.

The main findings regarding enhancement of settling velocity and clustering of 'small' and 'heavy' particles due to turbulence are as follows:

- The increase in settling velocity is due to the fast-tracking effect. Small inertial particles are expelled from the vortex cores spiralling outward and increasing their speed during the descent, Maxey and Corrsin [1986].
- The most significant increase in the mean settling speed ($40-50\%$) occurs when the particle response time and particle settling velocity are comparable to Kolmogorov scales. For $U_t/u_\eta = 1$ the settling rate increases and reaches a maximum when $0.5 < \tau_p/\tau_\eta < 1$ and approaches to zero with increasing τ_p/τ_η, [Wang and Maxey, 1993].
- The experimental investigation of [Yang and Shy, 2003] for $Re_p \approx 1$ is in good agreement with the DNS results from [Wang and Maxey, 1993] and [Yang and Lei, 1998]. However, due to experimental limitations they could not validate the results for $St_\eta > 0.2$. On the other hand, for $Re_p > 1$ the maximum settling velocity was always found for $St_\eta \approx 1$. They reported a 7% increase in the settling velocity for particles with $Re_p = 25$ and $U_t/u_\eta = 12$ and a 4% for the case of $Re_p = 39$ and $U_t/u_\eta = 15$.
- [Yang and Shy, 2003] found that for $St_\eta < 1$, the two particle characteristic timescales (τ_{c1},τ_{c2}) are both smaller than the turbulence integral timescale (τ_L) and Taylor timescale (τ_λ) respectively. However, for $St_\eta \approx 1$, $\tau_{c1} \approx \tau_L$ and $\tau_{c2} \approx \tau_\lambda$. They concluded that this might explain why the settling velocity is maximum at $St_\eta \approx 1$, because particle and fluid motions are in phase and therefore their velocities are nearly the same.
- Preferential accumulation is found to increase as Re_λ increases. More specifically, clustering is found to be Re_λ dependent in highly concentrated regions, whereas large depleted regions appear to be mostly independent of Reynolds number, [Obligado et al., 2014]. This can be interpreted as the fact that large depleted regions are mostly associated with large scale flow structures, which are not much affect as Re_λ increases.

Similarly, the following statements can be made for dilute one-way coupled systems:

- [Aliseda et al., 2002] reported that the settling velocity increases monotonically with the particle volume fraction, ϕ_v, in the flow. Since the low particle volume fraction in the experiments cannot significantly affect the turbulence in the flow, they suggested that the phenomenon of preferential accumulation could cause particles to interact with other particles' wakes, increasing their settling velocity.

- In poly-dispersed distributions of particles, the formation of clusters starts with particles with $St_\eta \approx 1$ which then entrain particles of all sizes. [Aliseda et al., 2002].
- The characteristic thickness of particle cluster is of the order of 10η, although they become denser and more numerous as the volume fraction of particles increases, [Aliseda et al., 2002].

In summary, preferential accumulation for 'small' 'heavy' particles in turbulent flows is controlled by a near unity Stokes number based on the Kolmogorov scale (St_η), although this phenomenon has been found to be Re_λ dependent. The reader should note the term 'small' is specific to turbulent flow, specifically $d_p/\eta << 1$, and if the fluid is not turbulent, then the terminal settling velocity is trivial to understand under the assumptions made.

1.6 'Large' 'Light' Spheres

Contrary to what was noted in section 1.4 for 'small' 'heavy' particles, [Balachandar and Eaton, 2010] discovered that the scale separation cannot be applied for particles larger than the Kolmogorov scales and the flow has to be fully resolved either through experiments or simulations. Thus, the motion of 'large' particles in turbulent flows has been recently investigated conducting experiments by [Xu and Bodenschatz, 2008], [Zimmermann et al., 2011b], [Zimmermann et al., 2011a] and [Byron et al., 2015] among others, and through simulations by [Bellani et al., 2012] and [Fornari et al., 2016a] among others. In this section, results from the literature will be analysed to explicitly highlight the differences observed for 'large', 'light' spheres.

[Xu and Bodenschatz, 2008] considered that for particles with larger size than the Kolmogorov length scale, the Stokes number base on the Kolmogorov time scale was no longer appropriate. They accounted for the size effect by substituting the Kolmogorov time scale by the turbulent time scale at the scale of the particle size,

$$\tau_d = \left(\frac{d_p^2}{\epsilon}\right)^{1/3} \tag{1.31}$$

Then the Stokes number is redefined as

$$St_d = \frac{\tau_p}{\tau_d} = \frac{1}{18}\left(\frac{\rho_p}{\rho_f}\right)\left(\frac{d_p}{\eta}\right)^{4/3} \tag{1.32}$$

Furthermore, the effect of having finite particle Reynolds number was considered and the relaxation time of the particles was not the viscous relaxation time from Stokes law

(τ_v), but the corrected version as in Eq. 1.20 leading the the following expression for the modified Stokes number,

$$St_d = \frac{\tau_p}{\tau_d} = \frac{1}{18}\left(\frac{\rho_p}{\rho_f}\right)\frac{(d_p\eta)^{4/3}}{1+0.1315Re_p^n} \tag{1.33}$$

where the particle Reynolds number was defined based on the fluctuation velocity of the turbulent flow

$$Re_d = \frac{ud_p}{\nu} \tag{1.34}$$

Here the main differences observed between 'small' and 'large' particles in the work done by [Xu and Bodenschatz, 2008] are listed;

- The probability density function (PDF) of the measured accelerations of 'large' particles depicts shorter tails than for 'small' 'heavy' particles. Thus, they conclude that 'large' particles might be filtering violent, fast events due to the modified response time. However, they do not obtain results that support that particles filter the turbulence at any specific scale.
- The acceleration variances for 'large' particles under Stokes number ranging from $0.45 > St_d > 0.22$ are nearly the same, being in good agreement with [Voth et al., 2002], who showed that the decrease in acceleration variance is noticeable only for particles with size ($d_p/\eta > 7$), i.e., particles in the inertial range.
- Although the phenomena of preferential concentration is not seen for 'large', 'light' particles, spatial inhomogeneity of the particles distribution was recorded, as previously reported by [Ott and Mann, 2000] and [Schmitt and Seuront, 2008]. The physical mechanism is unknown, but they considered the lubrication force between particles a possible explanation.

[Zimmermann et al., 2011a] and [Zimmermann et al., 2011b] focused their research on the dynamics of a single particle. They demonstrated that the translational and angular accelerations of a 'large', neutrally buoyant sphere in a Von Karman turbulent flow manifests intermittency. In their study, $d_p/\eta \approx 600$, they found that the particle acceleration statistics was described by the same PDF for all particles within the inertial range, as stated in [Qureshi et al., 2007].

[Bellani et al., 2012] investigated the effect of particle size and shape on particle-fluid interaction. Although two-way coupled systems are out of the scope of this review, they reported interesting findings in particle rotation statistics. The results exposed in here are for spheres of $d_p/\eta \approx 20$ and $\rho_p/\rho_f \approx 1$. They found that the PDF of these particles do not match the PDF of fluid enstrophy computed from the velocity field filtered at the particle scale. In fact, to match the curves they needed to filter the fluid velocity field with a much larger wavelength than the particle dimension. This suggests that

'large' particles ($d_p/\eta >> 1$) filter out the effect of small-scale high vorticity motion, being averaged out over the particle surface. In order to validate this hypothesis they estimated the particle rotational relaxation time as one third of the translation time and compared it with the time scale of vortices at the particle size, as considered by [Xu and Bodenschatz, 2008] in equation 1.31. Thus, they showed that the time scale of fluid motion at the particle size is very similar to the particle rotational relaxation time, which implies that particle rotation is affected by large spatial scales. Fluid motion at the particle scale do not persist long enough for the particle to come to equilibrium with them. If the same approach is applied for the translational motion, even larger spatial scales are filtered out. These finding suggest that the corrected Stokes number, St_p, introduced in [Xu and Bodenschatz, 2008] does not entirely capture the dynamics of the system since larger flow structures than the particle diameter appear to be filtered.

[Fornari et al., 2016a] investigated a suspension of 'large' ($d_p/\eta \approx 12-14$), near-neutrally buoyant spheres ($\rho_p/\rho_f \approx 1$) in turbulent conditions by means of numerical simulations and showed that the mean sedimentation velocity was reduced to 0.88 and 0.86 of the value seen in quiescent fluid for particle volume fraction of $\phi_v = 0.5\%$ and $\phi_v = 1\%$ respectively. They showed that the wake behind each particle was significantly reduced in the turbulent case and observed large-amplitude particle unsteady motions, being in accordance with [Bagchi and Balachandar, 2013] among others. The particle non-linear drag was estimated to be about 10-12 % of the total drag and they concluded that this term was the main responsible for the reduction of the settling velocity with respect to the quiescent flow; note that the effect of preferential concentration, as defined for 'small' 'heavy' particles is no longer present. It is interesting to note the contribution of the non-stationary effects to 'large', 'light' particles and how non-linear drag remains significant even though inertial effects are small. They introduced another two variations of the Stokes number, one based on the integral-scale St_L, and another on the Taylor microscale, St_λ. However, since the coupling between particle dynamics and the turbulent flow simulated occurred at the Taylor microscale, the later seems more appropriate for comparison purposes, being $St_\lambda = \tau_p/\tau_\lambda = 2.1$.

The results presented in [Fornari et al., 2016a] showed the strong influence of particle finite size and inertia on the particle settling behaviour. Whilst 'small' 'heavy' particles exhibit an increase in their settling velocity for $St_p = 2.1$ -based on the turbulent scale determined by the dimension of the particle-, 'large' 'light' particles depicts the opposite trend.

Despite of the findings reported in here, results on the mean settling velocity of 'large' particles, $d_p/\eta > 1$ are not conclusive. Therefore, it is necessary to investigate the effect of Re_λ on the trends observed and to determine precisely the smallest turbulent scales affecting the particle behaviour. Only after finding the appropriate time scale to define the Stokes number one could compare trends from particles of different sizes.

The differences seen in the motion of 'large' 'light' particles compared with 'small' 'heavy' particles can be explained by the existence of non-negligible terms in the M-R equation, i.e. Basset, Faxen and Saffman forces. Thus, liquid-solid flows for which densities are comparable need the use of the complete form of this equation. Unfortunately, the M-R equation only applies for $Re_p < 1$.

At this point, the behaviour of spheres -independently of their density and dimension- under isotropic and homogeneous turbulence has been reviewed. For 'small' 'heavy' particles, the Kolmogorov timescale (τ_η) is generally accepted to be the characteristic flow scale affecting the particle, whereas the flow scale affecting 'large' 'light' particles is not universal. Different approaches have been detailed and compared.

Next section deals with particle characterization and highlights the importance of inertia for highly aspherical particles, which in turn prevents the use of drag correlations based exclusively on geometric parameters.

1.7 Aspherical Objects

The motion of aspherical particles is much more complex than for the cases previously presented. The difference in location of the centre of pressure and mass do not coincide during the descent and this leads to a strong rotational force acting on the particle. The constant change in particle orientation during the descent develops a complex boundary layer and subsequent flow separation. Therefore, particle shape and inertia should be taken into account if one aims to predict the behaviour of these complex geometries. The regime map for freely falling disks based on the Reynolds number (Re) and dimensionless moment of inertia (I^*) identified in Willmarth et al. [1964] being a good example.

It is found that when inertial forces are small (small Re_p) the motion of aspherical particles is stable, and models based on the sphericity can be useful. This section first discusses shape, introduces the most general 'shape functions' and explores their performance in estimating drag coefficients for aspherical particle in various motion regimes.

1.7.1 Geometrical Classification of Shape

The work carried out in [Clift et al., 1978] and [Rhodes, 2008] provides extensive documentation on methods of particle size measurement; the most employed methods being sieving, microscopy, sedimentation, permeability, electrozone sensing and laser diffraction. Detailed description of devices and techniques for sampling are provided in [Allen, 1990]. In here we do not give detailed information of the methods stated, but we limit

ourselves to the definition of some basic parameters that are used to define the dependence of shape on motion.

One can create a particle group based on their quasi-spherical shape, i.e. particles ranging from spheroids with low aspect ratio to complex or porous surfaces but with quasi-spherical shape; and one can observe that these share similar falling characteristics. Quasi-spherical particles do not exhibit strong secondary motions, although they reorientate themselves towards a preferred falling orientation. Taking this into account, it is feasible to implement corrections on the drag coefficient based on their analogous sphere counterpart.

In contrast, strongly aspherical objects might exhibit induced lift that varies during the descent due to changes in particle orientation. Therefore, drag correlations depending exclusively on the particle shape are not able to capture accurately their complex motion along the descent, [Wadell, 1934]. [Christiansen and Barker, 1965] showed that secondary motions in the descent of cylinders affect the mean drag coefficient leading to the underprediction of drag (up to 20%).

A potential improvement to the drag average correlations could come from determining the time dependency particle orientation during its fall and then apply a shape correction factor based on this instantaneous local orientation, as conducted by [List and Schemenauer, 1971]. However, this approach requires the knowledge of the particle trajectory *a priori*, which for now remains unknown. In the following sections shape factors and their use in mean drag correlations are reviewed to later show the importance of particle inertia when secondary motions arise. Subsequently, particles with strong secondary motion are investigated with the aim of proposing a general model to predict their behaviour under quiescent and turbulent flows.

1.7.2 Shape Factors for Quasi-Spherical Objects

Considering the strong differences between the descent styles of irregular particles a new question arises: what parameter could define the limit between those particles that could be subjected to drag coefficient correlations and the ones that should not? Despite of the numerous parameters found in the literature, in here we consider the one proposed by [Christiansen and Barker, 1965] due to being the less ambiguous.

According to [Christiansen and Barker, 1965] and [Clift et al., 1978], particle shape can be defined by two dimensions, the longest (d_{max}) and shortest (d_{min}) particle dimension, later combined in the aspect ratio, $\beta = d_{max}/d_{min}$. They suggested that particles with $\beta \leq 1.7$ represent the extreme shape that could be still thought to be quasi-spherical. If $\beta > 1.7$ the particle should be classified under another generic shape, i.e. disk, ellipsoid, rod.

Providing a particle can be considered to be quasi-spherical, the particle equivalent diameter, d_{eq}, is the only parameter that remains to be defined. Again, many diameter definitions exist in the literature, and although they very similar values for $\beta \approx 1$, they greatly differ as the particle departs from the spherical geometry. Hence, the most accurate definition of the diameter to use depends upon particular characteristics of the particle, but there is not a specific diameter definition that show superior performance when used in drag coefficient corrections.

In case d_{eq} is the only particle information that remains after the classification, the information about the particle shape is obviously lost; therefore the use of additional shape factors is required. A wide variety of shape factors have been put forth for irregular particles, but the most common and successful is the Corey Shape Function (CSF). It is defined as the ratio of the smallest principal length axis of the particle d_{min} to the square root of the intermediate d_{med} and longest d_{max} principle length axis,

$$CSF = \frac{d_{min}}{(d_{med} d_{max})^{1/2}} \tag{1.35}$$

[Loth, 2008] argues that this shape characterization is much more convenient than the Sphericity (ψ) because the surface area of irregular particles is often impractical to measure, and the same applies for other measures like not-roundedness, anisometry and bulkiness ratio.

[Clift et al., 1978] compared the CSF with others shape factors such as the 'perimeter', 'circularity', 'shape entropy' or 'polygonal harmonics' but the CSF tend to be the strongest. In contrast, the multiple definitions for the sphericity, i.e lengthwise sphericity ($\psi_{\parallel}$), crosswise sphericity ($\psi_{\perp}$), permit to account for the pressure drag and friction drag terms independently using a single global definition. [Leith, 1987] suggested the following equation for C_D in the Stokes region, but the same can be done for a broader range of Re_p, [Holzer and Sommerfeld, 2008], where pressure drag will become the dominant term

$$C_D = \frac{8}{Re_p} \frac{1}{\sqrt{\psi_{\perp}}} + \frac{16}{Re_p} \frac{1}{\sqrt{\psi}} \tag{1.36}$$

The general term of sphericity is defined as the ratio of the surface of a sphere with the same volume as the particle and the surface area of the actual particle. Analogous to the sphericity, the crosswise sphericity is the ratio between the cross-sectional area of the volume equivalent sphere and the projected cross-sectional area of the considered particle perpendicular to the flow, while lengthwise sphericity is the ratio between the cross-sectional area of the volume equivalent sphere and the difference between half the surface area and the mean longitudinal (parallel to the direction of the relative flow) projected cross-sectional area of the considered particle.

Thus, the Corey Shape factor and the sphericity factor have been widely used to develop correlation formulae for the drag coefficient as a function of Reynolds number.

Nonetheless, correlations using crosswise sphericity and lengthwise sphericity are much more complicated to evaluate for particles falling in an unsteady manner, since these values depend upon the particle trajectory. Therefore, next section will regard drag correlations based either on the CSF or the sphericity exclusively.

1.7.3 Drag Correlations

There are many correlations that characterize the translational motion of quasi-spherical particles falling in quiescent fluid. Most of them employ the volume equivalent sphere diameter, $d_{V_{eq}}$, as the characteristic size and the sphericity ψ for their shape. Then, these correlations can be generally expressed as,

$$C_D = f(Re_{d_{V_{eq}}}, \psi) \tag{1.37}$$

The study of [Chhabra et al., 1999] compared five different correlations of the drag coefficient for non-spherical particles for $10^{-4} < Re_{d_{V_{eq}}} < 10^5$, [Haider and Levenspiel, 1989], [Ganser., 1993], [Chien, 1994], [Hartman et al., 1994] and [Swamee and Ohja, 1991]. All of them are based on the sphericity parameter but the work presented in [Swamee and Ohja, 1991] that uses the CSF.

They reported that the average error ranges from 16% to 43% although maximum deviations of more than 100% are found. The largest errors are found in hollow cylinders and agglomerates of spherical particles. Particles of such characteristics allow the flow within the objects, which cannot be considered by the sphericity parameter alone since their shape yields far from the quasi-spherical shape considered in here. Nonetheless, if such geometries are disregarded the maximum errors remain beyond 100% for certain shapes and flow characteristics. Therefore, general drag correlations for aspherical particles are only recommended to use under sphericity close to unity.

On the other hand, drag correlations for the mean translational motion of highly irregular planar crystals were investigated by [Heymsfield and Westbrook, 2010]. They evaluated the method proposed by [Mitchell, 1996] against laboratory data and measurements of ice crystals falling in air. This method assumed that a single relationship is sufficient to describe all natural ice particles falling at $Re_p < 1000$,

$$C_D = f(Re_p, X) \tag{1.38}$$

where the Best number (X) is defined as

$$X = \frac{\rho_f^3}{\nu^2} \frac{8 m_p g}{\pi A_r} \tag{1.39}$$

A_r being the ratio of the particle's projected area A_p to the area of a circumscribing circle, $A_r = A_p/[(\pi/4)d_p^2]$. The Best number can be related to already defined non

dimensional numbers as:

$$X \approx \frac{\rho_f^3}{\nu^2}\frac{32\pi d^3 g}{6\pi A_r} = \frac{\rho_f^3}{\nu^2}\frac{16 d^3 g \rho_p}{3A_r} = \frac{\rho_f^2 u^2 d^2}{\nu^2}\frac{gd}{u^2}\frac{16}{3A_r} = \frac{Re_p^2}{Fr^2}\frac{16}{3A_r} \tag{1.40}$$

Being the last term of the Best number another kind of 'sphericity' factor. Therefore, Eq. 1.38 can be rewritten as

$$C_D = f(Re_p, Fr, \psi) \tag{1.41}$$

In [Mitchell, 1996], the definition of two empirical constants C_0 and δ_0 accounts for the differences associated with particle shape, and the Reynolds number can be estimated as

$$Re_p = \frac{\delta_0^2}{4}\left[\left(1 + \frac{4\sqrt{X}}{\delta_0^2\sqrt{C_0}}\right)^{1/2} - 1\right]^2 \tag{1.42}$$

such that the drag coefficient is,

$$C_D = C_0\left(1 + \frac{\delta_0}{\sqrt{Re_p}}\right)^2 \tag{1.43}$$

Thus, circular discs ($A_r = 1$), hexagonal plates ($A_r = 0.83$) and broad branched crystals ($A_r = 0.74$) with aspect ratio of 0.02 are well approximated by the approach in [Mitchell, 1996], with error in computed fall speed of less than 20%. However, for the extreme case of the stellar crystal ($A_r = 0.185$) the terminal velocity is overestimated in more than 100%. Since the method in [Mitchell, 1996] is observed to be too sensitive to A_r, [Heymsfield and Westbrook, 2010] proposed a simple adjustment to the method shown that reduced the error to 25% for all the particles they tested. Nonetheless, there is a substantial scatter in the drag predictions that might come from the unstable motion of the crystal as they fall.

We consider that the reason why these correlations fail to estimate the drag coefficient accurately is because they all assume a unique falling regime across the whole range of particle Reynolds number and particle inertia. This assumption gives good results for very low Reynolds number; contrary, when $Re_p > Re_{cr}$ the falling motion becomes inertia dependent, making correlations of the form of equation 1.37 too simplistic. Drag correlations including rotational inertia effects might give much more accurate results within the regime of $Re_p > Re_{cr}$. The difficulty resides in finding a general method to obtain Re_{cr} as a function of particle shape. This would allow to define the boundaries between different regimes, as firstly identified in disks by [Stringham et al., 1969] but for any particle geometry.

The fall regime dependency with the dimensionless moment of inertia I^*, defined by [Stringham et al., 1969] as the ratio between the particle moment of inertia and a magnitude proportional to the moment of inertia of the body of revolution that the particle would form while tumbling ($I^* = I_p/\rho_f D^5$), shows that two particles with the same

Reynolds number might describe a completely different falling pattern, leading to strong differences in their mean drag coefficient.

In summary, drag correlation methods relying exclusively on geometrical shape factors are limited to the regime of sub-critical Reynolds number, for which secondary motions are quasi non-existent. Being a clear example the severe errors in drag prediction reported in [Chhabra et al., 1999] for particle Reynolds number in the critical regime. Methods such as the one in [Heymsfield and Westbrook, 2010], which includes a second parameter, i.e. the Froude number, reduce the errors for planar particles but are also limited to relatively small secondary motion. We believe that for the supercritical Reynold regime the inertia of the particle has to be accounted for on the estimation of the drag coefficient.

1.7.4 Secondary Motion

1.7.4.1 Disks and Other Planar Particles

[Willmarth et al., 1964] carried out a thorough investigation on the free-falling behaviour of disks in quiescent fluid. They suggested that the steadiness of the falling is dependent upon the stability of the pressure forces present in the wake of the particle. Depending on parameter values, they characterized the falling motion by three types of trajectories: 'Stable', 'Regular Pitching Oscillations' and 'Tumbling'. Although they did report disks falling in a chaotic manner, they considered this trajectory as the initial state of the tumbling motion. Five parameters of the particle and fluid were found to determine the particle falling behaviour: the diameter, thickness and density of the particle; and the fluid density and kinematic viscosity. The velocity of the planar particle is an outcome of the type of falling. From the physical variables here exposed, two dimensionless ratios are formed. The first is the dimensionless moment of inertia previously defined; for disks this quantity is defined as $I^* = I_{disk}/\rho f d^5$ whereas the second is the Reynolds number, see Eq. 1.12. The thickness to diameter ratio, t/d, does not play a significant role in the falling dynamics if $t/d < 0.01$.
They also painted disks with a water-soluble dye before releasing them into the water tank. Doing so, they observed the flow structures in the wake of the disks while settling. For small lateral translations, i.e small Re_p, a complete horseshoe-shape vortex ring was shed at the end of each swing, while for severe lateral motions additional vortex trails were formed on the edges of the disk perpendicular to the direction of motion, as occurs on aircraft wing-tips. Thus, direct flow visualization asserted the importance of vortex structures and its associated pressure distribution in particle orientation and path travel.

[Stringham et al., 1969] also investigated the effects of these non-dimensional parameters on the falling pattern of disks, obtaining results that agree well with [Willmarth et al., 1964]. [Field et al., 1977] extended the work on falling disks and mapped out four

trajectory types in the phase diagram: Steady, Oscillatory, Tumbling and Chaotic. They also suggested that the tumbling region could be separated in two: periodic tumbling motion, for very high values of I^*, and chaotic tumbling motion, for smaller values of I^*.

In line with the research carried out for disks, experimental and numerical studies have been done on the motion of freely falling rectangular plates. The study of freely falling plates started with [Maxwell, 1853], but the number of experiments on qualitative and/or average properties have greatly expanded during the last decades. Thus, [Dupleich, 1941] recorded the angle of descent and the tumbling frequency for different plate loading and aspect ratios. [Smith, 1971] measured a phase diagram for rectangular plates that was analogous to the one for falling disks. More specific research was done by [Belmonte et al., 1998], who quantified the transition from fluttering to tumbling for quasi two-dimensional particles. [Mahadevan et al., 1999] found a scaling for the dependence of the tumbling frequency on the width of a card.

More recent experimental and numerical studies have been done on the secondary motion of freely falling plates in quasi-2D flow. [Andersen et al., 2005b] investigated trajectories of four different plates experimentally in the periodic, chaotic and tumbling regime. Trajectories recorded were replicated by use of 2D CFD simulations, permitting the analysis of the forces acting on the plates over their trajectory. Thus, a quasi-steady model was developed to predict the dynamics of plates. Further research by [Andersen et al., 2005a] was done to analyse the transition between fluttering and tumbling regimes. The results from the direct numerical simulations (DNS) show a wide transition region with solutions that are mixtures of fluttering and tumbling. Further numerical studies have been focused on the descent of disks in quiescent flow at moderate particle Reynolds numbers ([Auguste et al., 2013] or [Churst et al., 2013]), showing a broad spectrum of particle descent styles as a function of dimensionless moment of inertia. Thus, from the results exposed in here, it seems evident that shape factors do not suffice to model even the mean descent motion of irregular particles, since these might describe different falling styles depending on other non-geometric parameters.

1.7.4.2 Non-Planar Aspherical Particles.

Research on the secondary motion of non-planar aspherical particles is scarce, however we summarized in here the few studies that investigated this type of particles.

[Stringham et al., 1969] also included cylinders; and oblate and prolate spheroids in the aforementioned study. Cylinders and spheroids were made of lead and aluminium, allowing them to investigate the falling pattern for a wide range of Reynolds numbers $10 < Re_p < 10^5$.

They observed that oblate spheroids maintained the steady fall up to $Re_p \approx 50000$. Beyond that point the unsteadiness did develop, leading to oscillations and tumbling. On the other hand, prolate spheroids and cylinders showed oscillations in a vertical plane about a horizontal axis followed by a horizontal oscillation about a vertical axis for much smaller Reynolds numbers. Cylinders showed instabilities first in both the vertical and horizontal plane at about $Re_p \approx 400$. They also point out that particles with circular cross sections show greater stability than particles with elliptical cross sections for the same CSF.

[Jayaweera and Mason, 1965] studied the free fall of cylinders in various viscosity liquids and made observations on the effects of Reynolds number on the falling patterns. At very low Reynolds numbers, $Re_p < 0.01$, the cylinders did not show preferential orientation, falling in the same attitude as they are released. However, for $0.01 < Re_p < 0.1$ the cylinders (of diameter d and length L) oriented themselves to offer maximum resistance to motion; therefore particles with $d/L < 1$ fall with their long axis horizontal, while particles with $d/L < 1$ fall like disks. The oscillations that occur before reaching the stable orientation are heavily damped once this orientation is reached. The flow visualization showed that when eddies break away from the edges as well as the sides, the cylinder flutters about a horizontal axis through the centre and normal to its length.

[Jayaweera and Mason, 1965] also studied the behaviour of cones under free fall conditions. They studied three set of conical particles; flat base cones, double cones and cones with spherical cap base. Each set of cones showed similar falling patterns but for different range of Re_p based on the base diameter. The non-dimensional moment of inertia was not studied and they did not propose any general model to describe the motion of these cone-shape particles.

The results exposed here agree well with results from recent numerical investigations by [Gustavsson et al., 2014] which highlight the importance of inertia effects on the tumbling rate of other large irregular particles such as rods and disks.

We believe the lack of an unambiguous measure of shape, size and orientation -particularly when secondary motions arise- during the settling of these particles represents the main obstacle to develop universally applicable correlations to predict their dynamic behaviour.

1.8 Aspherical Particles in Turbulence

The effect of turbulence on the motion of non-spherical particles is not fully understood, and most of the drag correlations noted in this chapter are only valid for quiescent flow or very narrow Reynolds numbers.

[Parsa et al., 2012] carried out the first 3D experimental measurements of the orientation dynamics of rod-like particles and disk-like particles in turbulent fluid flow. These results were in good agreement with their numerical simulations for tracer particles. They generated turbulence by using two oscillating grids at two Taylor Reynold numbers, $Re_\lambda = 160$ and $Re_\lambda = 214$; and the rods used had a length of 2.6η and 4.8η respectively. Disk-shape particles with $\beta < 1$ showed much larger rotation rate than spheres. However, the rotation rate of rods, with $\beta > 1$ was much smaller than spheres, although in both cases the rate-of-strain contributed to their rotation. The main reason why this occurs is that rod-like particles have a rotation rate strongly affected by their alignment with the vorticity vector, while the rotation rate of disk-like particles is less affected by their alignment. Thus, a significant difference of 80% in the mean square rotation was seen between particles with $\beta = 0.5$ and $\beta = 2$.

[Marcus et al., 2014] measured experimentally the rotation of crosses and rods in turbulence. The crosses were fabricated using a 3D printer with their largest dimension being 6η. The particle density was matched with the fluid density so that $\rho_p/\rho_f \approx 1$. The recorded motion of these particles in a turbulent flow with $Re_\lambda = 91$ was used to analyse their tumbling rate and preferential orientation. They showed that crosses tumble at a considerably smaller rate than randomly orientated axisymmetric ellipsoids, due to the effects of alignment by turbulence. Having defined the cross orientation vector as a vector perpendicular to their arms, they found that crosses preferentially align with their particle orientation vector perpendicular to the solid body rotation rate vector. Thus, crosses in turbulence preferentially rotate like a coin spun on its edge upon a table. They also reported that crosses are less strongly aligned than rods under turbulence effects. Similarly, recent DNS results from [Ni et al., 2014] show that rods approach almost perfect alignment with the strongest stretching direction in good agreement with the aforementioned experimental results. For more detailed information about fibre-like particles the reader is referred to the recent review of Voth and Soldati [2017], where most relevant numerical and experimental work on the orientation and preferential concentration of these particles is summarized. The experimental work on the following chapter is devoted to the motion of planar particles, and therefore the motion of fibre-like particles is not reviewed in more detail.

1.9 Summary of the Literature Review

The previous sections summarised the fundamental equations and the experimental and numerical results for solid particles settling through a viscous media. Concerning particles in turbulent flows, two features have been the focus of research in recent years: the effect of turbulence on particle, i.e. particle dispersion and settling velocity, and the effect of particle on the carrier phase turbulence, i.e. turbulence modulation. In here we have focused only in one-way coupled systems and therefore turbulence modulation

have not been considered. The main points that we want to emphasize from the previous sections are the following,

- The turbulent dispersion of small spherical particle is reasonably well understood for a range of flows, for which different models yield accurate results [Shirolkar et al., 1996].
- Particle-turbulence interactions are well captured with the Stokes number for the case of small spheres and the use of finite Reynolds number corrections allow to extend this approach to more realistic scenarios.
- For non-spherical particles there is not a clear understanding of the particle behaviour. The lack of an unambiguous measure of shape, size and orientation during the settling of irregular particles can be understood as the main obstacle to develop universally applicable correlations to predict the dynamics of irregular particles.
- For non-spherical particles the increased drag coefficient cannot be fully captured by a 'volume equivalent sphere' approximation, for both augmentation and attenuation of the descent velocity, [Sun et al., 2004].
- The dimensionless moment of inertia appears to be a control parameter for the particle descent style. Thus, it should be introduced into drag correlations to account for particle descent style and associated particle dynamics.
- Particle secondary motions make the definition of the particle relaxation time a non-trivial problem. At the same time, it suggests that turbulence effects might be more (or less) severe depending on the location of the particle along the trajectory.

1.10 Case Study of the Problem

The aim of this section is to present the specific problem of Aquavitrum Ltd. To do so several physical concepts are introduced to allow the reader to follow the assumptions made to estimate the turbulence characteristics of the Aquavitrum facility.

1.10.1 Aquavitrum Technology

The Aquavitrum project is to design a waste recycling technology to recycle 1.4 m tonnes of unrecovered packaging glass per year in the UK and divert it from waste streams such as landfill and incineration.

Their current technology has the capability of recovering most of the remaining glass cullet that is currently not recycled. It can take extremely dirty glass based feedstocks which are highly contaminated with other materials and process them to recover the

glass content. The feedstock is generally composed of small pieces of plastic, metal, paper, rubber and glass.

Aquavitrum Ltd. recognised that there are two main differences between the particles that have to be separated, which are shape and density. They found that glass and plastic are the most abundant materials present in the feedstock and these particles behave differently when immersed in a turbulent flow. Glass and plastic particles follow different trajectories in the turbulent flow created by a set of pressurised water jets in a water tank of variable bottom geometry. Consequently, glass travels along the bottom surface of the water tank until reaching the water tank outlet while plastic particles recirculate up to the surface of the water tank, where they travel until reaching a plastic gutter and are collected in inclined screen strainers. All this is a consequence of shape and density differences between particles.

1.10.2 Aquavitrum Water Tank

The separation process occurs in a water tank with three types of sections; the feed chute, the separation zone and the discharge chute. Co-mingled waste is fed into the separator by falling from a mobile trommel with a mesh size of 50 mm in a continuous and steady flow rate into the feed chute. The feed chute has a flat surface tilted downwards equipped with water jets. The design of the feed chute enables glass and plastic particles to gain inertia before reaching the separation zone, which is composed of two dimensional hill-like geometries located at the bottom of the tank. A set of five water jets per formation inject water at a chosen pressure to increase the water circulation at the valleys of each formation, ejecting low density particles away from the wall when they reach the top of the formation, see fig. 1.1.

Once plastic particles are ejected to the far wall region, the severe velocity fluctuations compared with the low settling velocity of the plastic delay its deposition, keeping them in recirculation near the water surface. The existence of an inherent reverse flow at the free surface of the water tank together with the presence of adjustable hydrofoils lead the plastic particles to the gutters installed at each separation zone. The gutters, located next to the last hydrofoil, collect water and plastics leading them to inclined screen strainers that separate plastics from water. At this point, plastics are carried by a moving belt to the plastics deposit, while the filtered water is sent to the water storage deposit. Water is then sent to the lamellas where the small particles suspended are removed. The lamellas are tested and show a suspended particle removal of approximately 80%, providing water with 8 ml of suspended solids per 1000 ml in the worst scenario. From this filtering process a third stream of sludge is obtained; all within a close loop that ensures minimum environmental contamination and maximum water reuse, as detailed in Esteban et al. [2016].

On the other hand, glass particles are carried by the mean flow and are led to the discharge chute. This last section is composed of a flat plate tilted upwards and another set of water jets. In this case, the jets force the glass to move upwards leaving the water tank and reaching the exit of the separator. At that point, glass particles are collected by a moving belt and sent to the glass deposit.

1.10.3 Working Principle

Solid-liquid interactions are the core of the hydrodynamic separator working principle. The water volume can be visualised as three sub-volumes, each with a different particle density. The estimation of the flow regime is generally made by comparing the particle viscous response (τ_p) with a characteristic timescale of the flow (τ_f), as in equation 1.28 for spherical particles.

The ratio of these two timescales is referred as the Stokes number (St), and it is used as a measure of how accurately a particle follows the flow. Thus, for $St > 1$ particles will detach from the flow when it accelerates abruptly, whereas for $St < 0.1$ the errors between particle and flow motion are below 1%, [Tropea et al., 2007].

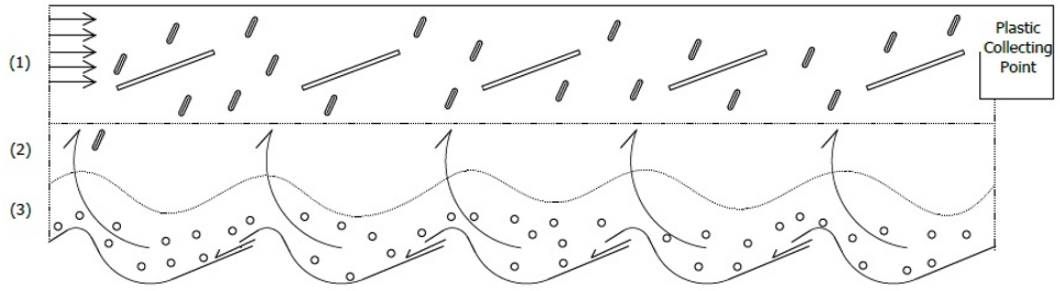

Figure 1.1: Separation section in the hydrodynamic separator. Water jets are distributed along the span-wise direction on top of the hill-like formations. The dotted lines separate the different sub-volumes of the tank according to the particle volume fraction, circles stand for glass particles and ovals for plastic contaminants.

At the upper and middle region of the separator the particle volume fraction is very low and flow is considered to be dilute (sub-volumes 1 and 2, respectively), and therefore we assume that turbulence characteristics do not change with the presence of particles. However, these two regions have strong differences. The hydrofoil region (upper region) is dominated by the surface reverse flow and the flow separation that occurs on the upper surface of the hydrofoils, whereas the middle region is clearly influenced by the turbulence structures generated in the bottom of the tank. The flow characteristics of this region are of paramount importance in the plastic separation. Contrary to the upper regions, the flow exhibits a dense regime at the bottom of the tank (sub-volume

3), where particles might modulate turbulence and particle-particle collisions dominate the solid dynamics.

The interest of this study resides in the effect of turbulence on highly aspherical particles, as it occurs in the dilute regime of the middle region. However, due to the difficulties associated with the reproduction of the system conditions in the laboratory and the high degree of specificity, quasi-isotropic homogeneous turbulence will be the focus of this study.

1.10.4 Particle Characterization

A series of drop tests with solid samples from co-mingled waste are performed to obtain the particle relaxation time. This parameter could be directly obtained from the particle characteristics in case of having a heavy spherical particle, as detailed in section 1.4.2. However, the strong influence of particle shape prevent the use of the general equation for spherical particles. In here, the particle relaxation time ($\tau_{p_{eff}}$) is obtained as

$$U_t = \tau_{p_{eff}}(1 - \frac{\rho_f}{\rho_p})g \tag{1.44}$$

where $\tau_{p_{eff}}$ captures the contributions due to particle shape and finite Reynolds number. Thus, settling velocities extracted from the drop test permit to get the approximate particle relaxation time, and these are shown in table 1.1.

	Settling Velocity [m/s]	Relaxation time [ms]	ρ [g/cm^3]
Plastic Particles	0.16	180	1.2
Glass Particles	0.29	50	2.5

Table 1.1: Glass and plastic parameters obtained from the drop tests.

The conclusions obtained from the particle characterization process are as follow:

- Glass particles have a terminal velocity that ranges from 0.26 to 0.32 m/s, whereas plastic particles have a terminal velocity magnitude that covers a wider range, from 0.12 to 0.28 m/s. This information combined with the density of the material show us how differently they interact with turbulence.
- The lateral dispersion of plastic and glass particles has the same basic characteristics in the sense that for every particle there is a characteristic timescale within which the trajectory of the particle is smooth, then an abrupt change occurs and another smooth period is followed. This fluttering motion has been extensively investigated for generic geometries such as rectangular plates or disks and has been shown to be defined by the particle Reynolds number and dimensionless inertia, [Willmarth et al., 1964]. These concepts will be further introduced in chapter 2.

1.10.5 Homogeneous Isotropic Turbulence

It is imperative for the understanding of this chapter to introduce the concepts of Homogeneous Isotropic Turbulence (HIT). It has to be kept in mind that HIT is an idealization never encountered neither in nature nor in laboratories. However, the challenge is to understand what are the aspects that can be applied to specific situations.

Statistically homogeneous turbulence implies that that all statistics of fluctuating quantities are invariant under translation of the coordinate system. On the other hand, a turbulent flow is said to be isotropic if all the statistics are invariant under translation, rotation and reflection of the coordinate system, then

$$\langle {u_i}^2 \rangle = 0 \tag{1.45}$$

where the brackets denote statistical average of the velocity fluctuations. The equation for the fluctuating kinetic energy for a constant density flow is an appropriate starting point to develop the ideas that will be further exposed. Nevertheless, for the sake of simplicity, the equation presented in here is already simplified by assuming the flow to have local homogeneity [Navier, 1822],

$$\left[\frac{\partial}{\partial t} + U_j \frac{\partial}{\partial x_j}\right] k = \frac{\partial}{\partial x_j}\left[\langle -u_j(u_i u_i + \frac{p}{\rho})\rangle + \nu \frac{\partial k}{\partial x_j} + \nu \frac{\partial}{\partial x_i}\langle u_j u_i \rangle\right] - \langle u_i u_j \rangle \frac{\partial U_i}{\partial x_j} - \epsilon \tag{1.46}$$

Each term of the former equation has a distinct role to play in the overall kinetic energy balance, being as follows

- Rate of change of kinetic energy per unit mass due to non-stationarity

$$\frac{\partial k}{\partial t} \tag{1.47}$$

- Rate of change of kinetic energy per unit mass due to convection by the mean flow through an inhomogeneous field

$$U_j \frac{\partial k}{\partial x_j} \tag{1.48}$$

- Transport of kinetic energy in an inhomogeneous field due to pressure fluctuations, turbulence and viscous stresses

$$\frac{\partial}{\partial x_j}\left[-u_j(u_i u_i + \frac{p}{\rho}) + \nu \frac{\delta k}{\delta x_j} + \nu \frac{\delta}{\delta x_i}(u_j u_i)\right] \tag{1.49}$$

- Rate of production of turbulence kinetic energy from the mean flow

$$-\langle u_i u_j \rangle \frac{\partial U_i}{\partial x_j} \tag{1.50}$$

- Rate of dissipation of turbulence kinetic energy per unit mass due to viscous stresses

$$\epsilon \equiv \nu \langle \frac{\partial u_i}{\partial x_j}^2 \rangle \tag{1.51}$$

Having defined the terms in the equation and considering homogeneous isotropic turbulence, the first three terms are neglected. This assumption forces the dissipation rate of turbulent kinetic energy to be equal to the production rate of total kinetic energy.

The strong assumption of HIT is the starting point to study the turbulence characteristics of the Aquavitrum water tank.

1.10.6 The Turbulent Box Assumption

Each separation section is an open tank of 3 m long, 1.2 m wide and 0.8 m deep, holding a volume of water of about 2.7m^3 when it is in operation. In here, we consider each section to be a closed box with the same volume of water. In each closed box, the dissipation rate of turbulent kinetic energy is balanced with the production rate of total kinetic energy (Λ), as $\Lambda = \epsilon$. At this point it is assumed that the kinetic energy that is injected in the tank by the nozzles becomes turbulent kinetic energy and it is dissipated in it, since there is no kinetic energy coming out from it. The rate of production of turbulence kinetic energy is estimated from the injection of water through the nozzles installed at the bottom of the tank. Thus,

$$\Lambda = N \frac{Q_{dis}}{V} k \tag{1.52}$$

where N is the number of nozzles, Q_{dis} is the water discharge, V is the volume of the tank and k represents the kinetic energy introduced in the system. However, it is not reasonable to assume that the mean flow along the box is zero since glass particles exhibit a clear steady motion from the inlet to the outlet of the system. Then, we consider that not all the kinetic energy from the jets, k, becomes turbulent kinetic energy but that 10% of it adds to the mean flow, (the induced mean flow being very low in the actual rig). Then, one assumes that the dissipation rate will match the 90% of the production rate,

$$\epsilon = N \frac{Q_{dis}}{V} k_{in-out} = N \frac{Q_{dis}}{V} 0.9k \tag{1.53}$$

Nonetheless, in the ideal case of having a 'Turbulent Box', the boundaries of the container would not be walls but imaginary planes that do not alter the flow field around them. Thus, wall viscous losses should be added to the system to obtain a better estimation of the dissipation rate. In this case, wall viscous losses are estimated from an average wall shear stress obtained from Ansys FLUENT, see appendix B.

Then, the dissipation rate of turbulent kinetic energy is given as,

$$\epsilon = N\frac{Q_{dis}}{V}k_{in-out} - \frac{\langle\tau_w\rangle A\langle u\rangle}{m} \tag{1.54}$$

where the first term represents the production rate of total kinetic energy and the second terms is the wall viscous losses. A is the total wall surface area, τ_w is the wall shear stress and m is the total mass of the 'Turbulent Box'. In here, the number of nozzles $N = 30$, the velocity at the nozzle outlet $u_0 = 20\,\mathrm{m/s}$, the radius of the nozzle $r = 4.5\,\mathrm{mm}$, the total wall surface area $A = 8.4\,\mathrm{m}^2$, the volume of water $V = 2.7\,\mathrm{m}^3$ and the mass of the system $m = 2700\,\mathrm{kg}$. The second term is representative of the mean wall viscous losses. In the actual rig, τ_w and u are position dependent, but in here we estimate the velocity fluctuations to be 7.5% of the velocity at the nozzle, $\langle u\rangle = 1.5\,\mathrm{m/s}$, and we take the average wall shear stress as a span-wise average of the central region of the bottom wall of the tank, $\langle\tau_w\rangle = 7.67\,\mathrm{Nm}^{-2}$. These assumptions lead to a dissipation rate $\epsilon = 6.09$ $\mathrm{m}^2\mathrm{s}^{-3}$.

η	$2.02 \times 10^{-5}\,\mathrm{m}$
τ_η	$4.0 \times 10^{-4}\,\mathrm{s}$

Table 1.2: Kolmogorov lenght and time scale obtained from the average energy dissipation rate

The Kolmogorov scales can be now obtained from the value of the energy dissipation rate (ϵ) and the kinematic viscosity of the fluid (ν), as discussed in section 1.5. The estimated magnitudes of η and τ_η are shown in Tab. 1.2.

Another important turbulence lengthscale is the Taylor microscale (λ), since this represents an approximate boundary between the dissipative scales ($\ell < \lambda$) and the inertial scales ($\ell > \lambda$). The magnitude of the Reynolds number based on the Taylor microscale (Re_λ) will be used in here to compare the assumptions taken with the results obtained from ANSYS Fluent. Following the reasoning in [Pope, 2000] and assuming the largest eddies in the flow to be of the same order of magnitude as the facility, the Taylor microscale can be obtained as

$$\lambda = \sqrt{10}Re_L^{-1/2}L \tag{1.55}$$

where $Re_L = k^2/\epsilon\nu$. Then, the Taylor microscale is found to be $\lambda = 1.4 \times 10^{-3}$ m.

Once this value is known, the turbulence Reynolds number based on the Taylor microscale is directly obtained as

$$Re_\lambda = \frac{u\lambda}{\nu} = 2034 \tag{1.56}$$

The scales that are considered to control the solid-liquid interaction are the Taylor microscale τ_λ and the integral lengthscale τ_L as suggested by [Yang and Shy, 2003] for

large enough solid particles. Again, following the approach detailed in [Pope, 2000], these parameters are $\tau_\lambda = 2.3 \times 10^{-3}\,\mathrm{s}$ and $\tau_L = 0.278\,\mathrm{s}$.

Conversely, we use an alternative method to obtain Re_λ that does not include the use of the integral lengthscale (L), also detailed in [Pope, 2000]. We estimate the Taylor lengthscale as

$$\lambda = \sqrt{15\frac{\nu}{\epsilon}u} \approx \sqrt{15\frac{\nu}{\epsilon}k^{1/2}} \tag{1.57}$$

where, k and ϵ are obtained from a geometric plane located at the middle depth region, and then obtain $Re_\lambda = 1575$. The severe difference between the Reynolds numbers obtained using slightly different approaches -see table 1.3- highlights the complexity of the flow and suggests that these results should be only taken as a first estimate of the scales in the actual facility. Despite the aforementioned difference between both

	Estimations	Simulations
Re_λ	2034	1575

Table 1.3: Turbulent Reynolds number based on the Taylor microscale.

approximations, the lowest estimation of the Reynolds number inside the facility remains too high to solve the industrial problem computationally or experimentally within the scope of this study.

With the estimation of the turbulence characteristics within the facility and the particle timescales obtained experimentally we can now define the Stokes number for the glass and plastic particles.

As discussed in [Wang and Maxey, 1993], for very small particles, i.e. $d_p/\eta < 1$, the Kolmogorov scale is the flow scale affecting the particle behaviour and therefore τ_η is the appropriate timescale of the flow to compute the Stokes number. However, large particles, i.e. $d_p/\eta > 1$, are believed to filter the turbulence at a lengthscale of the same order of magnitude than their dimension d_p, as considered by [Xu and Bodenschatz, 2008]. Thus, a new characteristic timescale of the flow should be used.

The Taylor microscale is considered an appropriate alternative for medium-size particles. However, in this case $\lambda \approx 1\,\mathrm{mm}$, so the difference between particle dimension ($d_p \approx 50\,\mathrm{mm}$) and this turbulent scale might be too large. Glass and plastic particles considered in here might be filtering turbulent structures even larger than the Taylor microscale. Therefore, the integral scale is used to formulate the Stokes number,

$$St_L = \frac{\tau_p}{\tau_L} \tag{1.58}$$

Thus, the Stokes numbers obtained for glass and plastics particles are $St_{L_g} = 0.18$ and $St_{L_p} = 0.66$ respectively.

The results exposed in here are promising since the different behaviour between plastic and glass particles in the separation process might be explained in terms of the Stokes number. However, further research have to be done to fully understand the physical mechanism that lies beneath the separation process.

1.11 Organisation of the Thesis

This thesis consists of four further chapters as follows:

1. Chapter 2 presents the dynamics of planar particles falling in quiescent fluid. This chapter is subdivided in three main sections. First, we discuss the effect of perimeter 'waviness' on the descent of disk-like particles. Second, we focus on the effect of number of edges and associated dimensionless inertia on the descent style of n-sided planar polygon particles. Last, we investigate the wake differences associated with the change in descent style for the case of n-sided planar polygons.

2. Chapter 3 introduces the facility built to generate homogeneous anisotropic turbulence and presents the experimental results on 'stationary' and 'free decaying' turbulence.

3. Chapter 4 presents the dynamics of disks falling under background turbulence with special attention to the change in particle descent velocity and dispersion.

4. Chapter 5 summarises the work done and gives advise on future research that could follow the research lines presented here.

Chapter 2

Planar Particles in Quiescent Fluid

The aim of this chapter is to investigate experimentally the effect of the frontal geometry on the settling dynamics of planar particles in quiescent flow. The question "What if the disc has a wavy edge?" formulated in Moffat [2013] is extended here not only to sinusoidal edge particles but to sharp edge polygons and three studies are combined to tackle this question. First, particle tracking experiments of disk-like particles with the perimeter described by sinusoidal functions are performed. We differentiate trajectories according to the degree of out of plane motion and obtain a drag correlation function that depends on the particle geometry. Second, trajectories of N-sided polygons with the same material properties and frontal area but different number of sides are also investigated by particle tracking experiments and a simple pendulum model is found to represent accurately the descent motion of these particles once the mean descent velocity is known. Finally, we perform measurements of the instantaneous three-dimensional velocity field on the wake of several of these polygons. We observe severe differences in the shedding mechanisms and these are related to the descent style of the particles. This chapter is structured as follows; in section 2.1 we introduce the topic and review the latest relevant contributions, in section 2.2 we present the experimental techniques used, section 2.3, 2.4 and 2.5 include the studies aforementioned and section 2.6 summarizes the results obtained.

2.1 Introduction

Aspherical particles, especially planar particles of different shapes and sizes, are ubiquitous in various environmental and industrial processes. Natural processes include pollen

and seed dispersion in the atmosphere, [Sabban and van Hout, 2011]; whereas industrial processes include pharmaceutical processing, [Erni et al., 2009], and the emission of contaminants from combustion processes as in Moffet and Prather [2009].

The descent motion of freely falling particles is complex, even for simple geometries such as thin disks and rectangular plates. These particles show a variety of falling regimes that go from steady fall to tumbling, going through fluttering and chaotic motion. In the limit of small thickness-to-width ratio, the falling regime of disks and rectangular plates can be predicted once the Reynolds number (Re) and the dimensionless moment of inertia (I^*) are known (see section 1.7.3 for Re and I^* definitions). The regime map for the descent style of disks was first defined in Willmarth et al. [1964] by experimental investigation considering only three falling regimes: steady, fluttering and tumbling. The same approach was followed by Smith [1971], constructing the corresponding phase diagram for falling plates.

A new falling regime was found in the transition between flutter and tumbling, the chaotic regime. This regime was firstly observed in disks, [Field et al., 1977], but it has been investigated in more detail for the quasi-two-dimensional case; [Andersen et al., 2005b], [Andersen et al., 2005a], [Belmonte et al., 1998], [Pesavento and Wang, 2004]. Different approaches have been followed to investigate this transition. [Belmonte et al., 1998] increased I^* in an experiment where the plate motion was constrained mechanically to two dimensions. Similarly, Andersen et al. [2005b] measured the instantaneous fluid forces from the two-dimensional plate accelerations. They also used direct numerical simulations of the two-dimensional Navier-Stokes equation and a fluid force model to investigate the transition between periodic fluttering and periodic tumbling, [Andersen et al., 2005a].

More recently, Lee et al. [2013] investigated experimentally the transition of a falling disk from zig-zag to spiral motion, both within the fluttering regime defined by Field et al. [1977]. They found that the transition from one sub-mode to another for thin disks is also determined by the dimensionless moments of inertia and the Reynolds number, independently of the disk initial conditions. Interestingly, Heisinger et al. [2014] showed a single disk ($Re \approx 1100$, $I^* \approx 3 \cdot 10^{-3}$) describing both types of motion; i.e. 'planar flutter' and 'hula hoop'. The disk geometry has been also modified, as in Vincent et al. [2016] where they investigated experimentally the stability of disks with a central hole, finding that the use of these could be used as a stabilization strategy for disk-shaped objects that are close to the transition between two falling modes.

In parallel, several investigations were carried out on the falling of planar crystals. List and Schemenauer [1971] investigated the steady fall of two sets of six snow crystals models each. The shapes chosen were a disk, an hexagonal plate, a broad-branched crystal, a stellar crystal with plates, a dendrite and a stellar crystal. All models were cut from a disk of 2 cm diameter, and therefore all had a different cross-sectional area.

They observed that the evolution of the drag coefficient (C_D) with Reynolds number for the snow crystal models was an almost parallel curve to the one for disks. As the cross-sectional area (A_p) of the models decreased the drag coefficient increased for $Re < 100$. This is not unexpected considering that the decrease in A_p coincides with an increase in the perimeter (for the particles investigated), leading to stronger viscous losses. They also observed that by $Re \approx 200$ small oscillations were present in disks, hexagonal plates and broad-branched models, with the biggest oscillations in disks. Jayaweera [1972] studied experimentally only the free fall behaviour of various planar particles within the same range of Reynolds number. All planar particles were manufactured with the same frontal area and thickness of a reference disk for the latter comparison. They showed that the terminal velocity of hexagonal plates was practically the same of the equivalent disk while for the case of star-shape particles the difference in the terminal velocity was up to 25% smaller.

Kajikawa [1992] studied the free-fall patterns and the variation in the vertical and horizontal velocities of unrimed plate-like snow crystals experimentally and showed that the stability of the particle descent velocity depends on the Best number -see section 1.7.3 for definition- and the dimensionless moment of inertia (I^*) of the crystals. The fall of these particles was very close to the stable regime, with very small oscillations during the descent. They also found that dendrite crystals with large internal ventilation fall with a stable motion over a larger Re range than the case of simple hexagonal plates. This fact suggested that the stability of the falling motion was influenced by the internal ventilation of the crystals, as confirmed later in Vincent et al. [2016] with perforated disks.

2.2 Experimental techniques

The experimental methods practised during this chapter are particle tracking and volumetric PIV. Details of each method and related experimental set up are introduced in this section.

2.2.1 Particle tracking

The experimental set up is composed of a water tank, two digital cameras and a diffuse light source, as shown in figure 2.1 a). The cameras can be mounted following different layouts as long as the 3-D components of the trajectory can be obtained. The square cross section water tank is 0.8 m high and 0.5 m side, and the drop position was centered to avoid wall effects during the particle fall. Particles are always released with zero initial velocity and zero tilted angle using a release mechanism that uses active suction. All particles were held in their initial position by a suction cup smaller than their internal

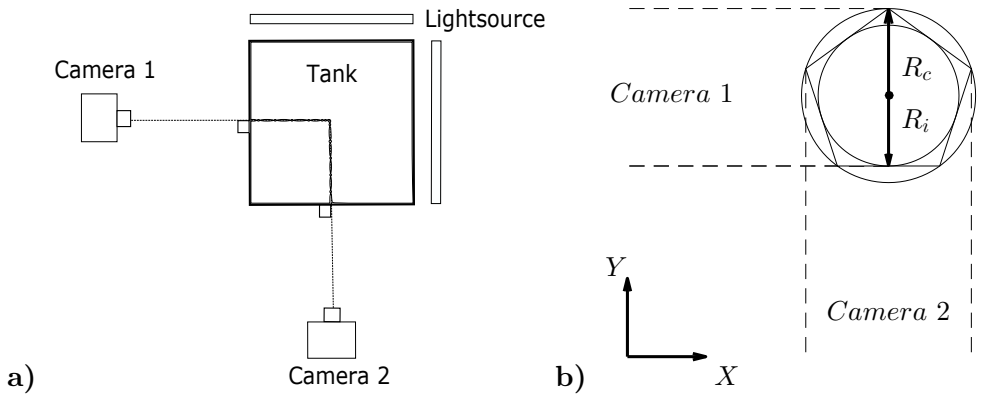

Figure 2.1: a) Schematics of the camera and illumination layout for the study in section 2.4; b) Top view of a pentagon positioned for maximum error in the determination of the center of gravity from the camera measuring the $Y-$coordinate.

diameter. The suction cup was part of a rigid frame attached to the water tank, ensuring that the particle initial conditions were the same in all realizations.

Two JAI GO-5000M USB cameras were used to capture two views of the falling particle. The cameras were both focused on the midpoint of the tank to minimize the image distortion due to lens curvature. Careful attention was paid to the camera alignment to make the two views orthogonal for the latter digital processing and trajectory reconstruction. The cameras were synchronized and triggered using an external 5 V signal sent from an Arduino. The trajectories were recorded at 60 frames per second and this frame-rate was sufficient to resolve the translation motion during all parts of the descent. In each frame the dark particle projection is recorded onto the white background and the position of the particle center of mass was obtained by locating the geometric center of each particle projection. The image processing was performed using an in-house script developed in MATLAB. The measured trajectories were smooth, but a polynomial filter of 3^{rd} order and frame length of 5 points was used to filter out high frequency noise. Both cameras were always positioned at a relative small distance from the tank, such that we had a minimum resolution of 200 px per particle diameter.

A set of releases of a polylactide (PLA) sphere falling in air was performed to establish limitations on the accuracy associated with the drop mechanism as well as the measurements taken by the cameras and account for image distortion from the lens. The variance in the landing position was interpreted as the uncertainty of the system, being two to three orders of magnitude smaller than the sphere diameter. This is in accordance with the uncertainty typically found in the literature, [Heisinger et al., 2014].

The process followed to obtain the particle center of mass did not add any uncertainty for the case of a thin disk or any planar particle with an even number of sides. However, the fact that the edges of the planar particles are not identified by the cameras could

add uncertainty to the determination of the center of gravity of particles with an odd number of sides, see figure 2.1 b). The maximum possible uncertainty in the center of gravity location associated with this issue is half of the difference between the radius of the circumscribed (R_c) and inscribed (R_i) circle, i.e. 0.6 mm for the heptagon and 1.3 mm for the pentagon.

The determination of the distance at which the particle motion is not influenced by the initial transient dynamics is non-trivial. In here, the term 'saturated path' stands for the section of the trajectory for which the statistics of the motion are independent of the vertical distance z. Churst et al. [2013] performed simulations of an infinitely thin disks with $I^* = 3.12 \times 10^{-3}$ and $G = 300$ (I^*, G both defined in sec. 2.3.1) and showed that it reached a saturated path at a vertical distance of $\approx 60\,D$ from the release point, whereas Heisinger et al. [2014] showed experimentally that for disks with $I^* \approx 3 \times 10^{-3}$ and $G \approx 4180$, the disk trajectory was saturated after a distance of $7\,D$. Here the reference disk lies closed to the parameter space in Heisinger et al. [2014], with $I^* = 3.4 \times 10^{-3}$ and $Re \approx 1800$ (or equivalent Galileo number $G = 9900$). We also found that the disk and other planar particles showed a saturated state at a distance of $7\,D$. Thus, a distance of $7\,D$ is given to the particle to accommodate to the fall before the trajectories are analysed.

As discussed in Heisinger et al. [2014], the bottom of the tank influences the landing position of the particle due to hydrodynamic interactions and the particle persistent motion once it is flat on top of the glass surface. To overcome these influences we do not process the particle trajectory once it reaches a distance of $2\,D$ from the bottom of the tank. Thus, we save trajectory sections that goes from $7\,D$ from the top (corresponding to a location were the particle trajectory is at a saturated state) to $2\,D$ from the bottom (unperturbed by the glass surface).

2.2.2 Volumetric PIV

Three-dimensional measurements of the instantaneous velocity field in the vicinity of the planar particles were taken with a V3V system from TSI. Three 2048 × 2048 pixels 12 bit frame-straddle CCD cameras were aligned in a coplanar triangle pattern to map a field of view (FOV) of 140 mm × 140 mm × 60 mm, as seen in figure 2.2. A synchroniser by TSI was used as an external trigger and connected to the laser and the camera system. A 200 mJ/pulse double-pulsed laser (Bernoulli-PIV Litron) was used to illuminate the FOV. Image pairs were acquired at 7.25 Hz and image triplets were analysed via Insight 4G software from TSI. The 3D imaging principle of this system is a multi-view photo-grammetry technique. The FOV of the three cameras intersect to form the camera system mapping region. Thus, any seeding particle inside the FOV is recorded from three different angles creating the basis for multi-view stereo vision. In the image plane, the three particle images form the coplanar camera arrangement form

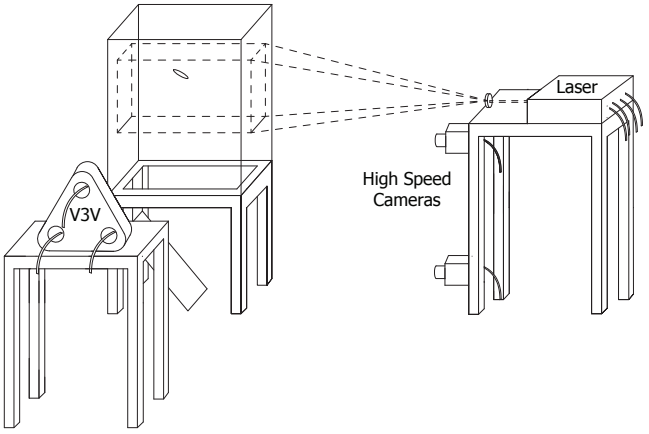

Figure 2.2: Sketch of the experimental setup for the combined measurement of the 3D particle trajectory and volumetric flow visualization.

a triangle, which size and center determines the depth (z) and planar (x-y) position of the particle respectively. The reader is referred to Pothos et al. [2009] for a more detailed explanation of the imaging and processing principles of this technique. Velocity accuracy depends on spatial accuracy of particle and timing accuracy. Lasers and electronics used have a negligible timing uncertainty compared with the spatial uncertainty during the particle identification. The maximum dewarping error found after the system calibration is smaller than 0.3 pixels. Typical particle displacements being $\approx$ 8 pixels, the spatial uncertainty is $< 4\%$. A node volume of $10mm^3$ was defined with a 75% of node volume overlap in the velocity interpolation process. The smoothing factor is set such as velocity information from neighbouring nodes do not contribute to the current node volume. The FOV of the V3V system was set after a vertical distance of 7 D from the release point to assure the saturated state of the particle. The water media was seeded with 55 μm polycrystalline particles.

2.3 Settling dynamics of disk-like particles

This section presents a study of the terminal fall velocity, drag coefficient and descent trajectory of 'wavy-edge' flat particles. Being highly non-spherical and with a size of up to a few centimetres, these particles show strong self-induced motions that lead to various falling styles that result in distinct drag coefficients. This study is based on experimental measurements of the instantaneous 3D velocity and particle trajectory settling in water.

2.3.1 Methods

A PLA circular disk of $D = 30\,\text{mm}$, $t = 1.5\,\text{mm}$ and $\rho = 1.38\,\text{g/cm}^3$ is manufactured as a reference particle. The disk was initially designed to lie within the Galileo number - dimensionless moment of inertia ($G - I^*$) domain corresponding to the fluttering regime. The Galileo number represents a true control parameter; unlike for the Re number, the measured descent velocity is not required to estimate this parameter,

$$G = \frac{\sqrt{|\rho_p/\rho - 1|gD^3}}{\nu} \tag{2.1}$$

where ρ_p and ρ stand for the particle and fluid density, respectively, g is the gravitational acceleration, D the disk diameter, and ν the kinematic viscosity. The dimensionless moment of inertia defined as in Willmarth et al. [1964],

$$I^* = \frac{I_p}{\rho D^5} \tag{2.2}$$

where I_p is the mass moment of inertia of the disk about the diameter. A total of 35 other particles with the same frontal area and material properties were manufactured. These are manufactured to have different amplitudes (a) of the sinusoidal wave on the edge and number of cycles (N) around the entire perimeter, as sketched in figure 2.3. Thus, 5 sets of particles are manufactured with different relative wave amplitudes; i.e. $a/D = 0.03, 0.05, 0.1, 0.15, 0.2$. Each set consisting of 7 particles from $N = 4$ to $N = 10$. The isoperimetric quotient (Q) is used as a measure of the particle circularity and is defined as

$$Q = \frac{4\pi A_p}{P^2} \tag{2.3}$$

where A_p and P stand for the frontal area of the particle and the perimeter respectively. All particles were laser cut within a precision of $\pm 0.5\,\text{mm}$. Table 2.1 shows the length of the perimeter of the particles manufactured, whereas table 2.2 summarizes the mass of the particles after the manufacture process was completed. Small differences in the mass of the particles were caused by the addition of black paint (to facilitate image processing).

In water, particles were released as described in the Particle Tracking technique in sec. 2.2. To build a baseline from which to compare the motion of the 'wavy-edge' particles a first set of 50 repeated drops of the disk in water was performed. Then, each particle is released 50 times in water at room temperature, $\rho_f = 0.998\,\text{g/cm}^3$ and $\nu = 1.004 \times 10^{-6}\,\text{m}^2/\text{s}$, the waiting time between drops being of 20 min, corresponding to more than 600 times the timescale of the oscillatory motion of the equivalent disk.

Two cameras were used to capture the falling particle. One camera captured a frontal view of the descent motion of the particle while the other captured the planar ($X - Y$) motion of the particle through a mirror at 45° underneath the tank.

	N						
a/D	4	5	6	7	8	9	10
0.03	96 (0.97)	96 (0.96)	97 (0.94)	98 (0.92)	100 (0.90)	101 (0.87)	102 (0.85)
0.05	98 (0.93)	100 (0.89)	102 (0.85)	105 (0.81)	108 (0.76)	111 (0.72)	115 (0.68)
0.1	108 (0.76)	115 (0.68)	122 (0.59)	131 (0.52)	139 (0.46)	149 (0.40)	158 (0.36)
0.15	122 (0.59)	135 (0.49)	149 (0.40)	163 (0.33)	178 (0.28)	194 (0.24)	210 (0.20)
0.2	139 (0.46)	158 (0.36)	178 (0.28)	199 (0.22)	220 (0.18)	242 (0.15)	264 (0.13)

Table 2.1: Particle perimeter (P) in millimeters for shapes with same area as a disk with $P = 94.2$ mm. Isoperimetric quotient Q is represented in brackets.

	N						
a/D	4	5	6	7	8	9	10
0.03	1.50	1.50	1.49	1.50	1.51	1.50	1.48
0.05	1.50	1.49	1.49	1.48	1.47	1.51	1.50
0.1	1.52	1.51	1.50	1.50	1.50	1.50	1.50
0.15	1.58	1.57	1.57	1.54	1.55	1.53	1.54
0.2	1.63	1.64	1.63	1.60	1.60	1.59	1.59

Table 2.2: Particle mass, units in grams.

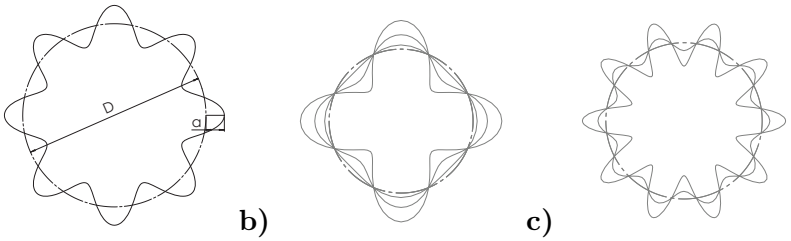

Figure 2.3: a) Sketch of a 'wavy-edge' particle about the disk perimeter (reference particle); b) 'Wavy-edge' particles with $N = 4$ and $a/D = 0.2$, 0.1, 0.03; c) 'Wavy-edge' particles with $N = 10$ and $a/D = 0.15$, 0.05.

2.3.2 Results

2.3.2.1 Planar dispersion, normal to the descent direction.

The measured radial dispersion of particles with $a/D = 0.2$ and variable N together with the radial dispersion of the reference disk is shown in figure 2.4 a). The radial distribution of the disk is the broadest of all particles tested, having its mean value at about 45 mm from the origin ($\approx 1.5\,D$). Then, as the isoperimetric quotient of the particle reduces, the radial dispersion of the particles becomes narrower, with particles of $N = 10$ having its mean value at about 17 mm from the origin ($\approx 0.5\,D$). Figure 2.4 b) shows a collapse of the statistics for the probability of finding a particle at a given radial distance from the origin once the perimeter of the particle (P) and the isoperimetric quotient (Q) are considered. The family of particles with $a/D = 0.2$ is chosen for

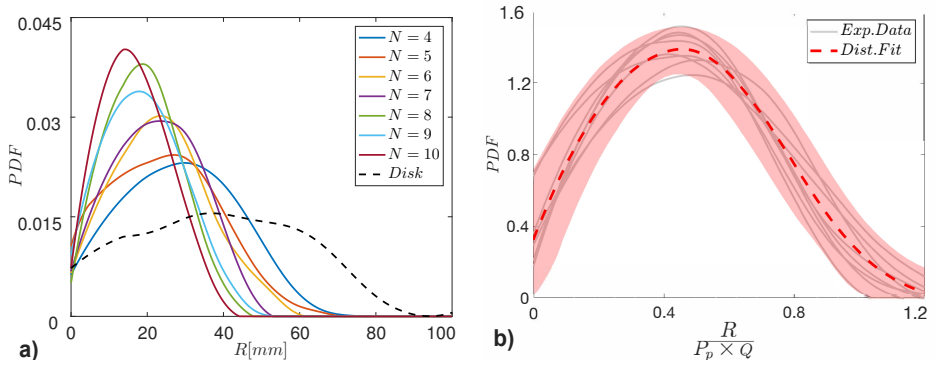

Figure 2.4: a) Probability density function (PDF) of finding a particle with $a/D = 0.2$ and variable N at a certain radial distance (R) from the release point. b) Probability density function (PDF) of finding a particle at a radial distance normalized with the particle diameter and the isoperimetric quotient. Data taken at $z > 7D$

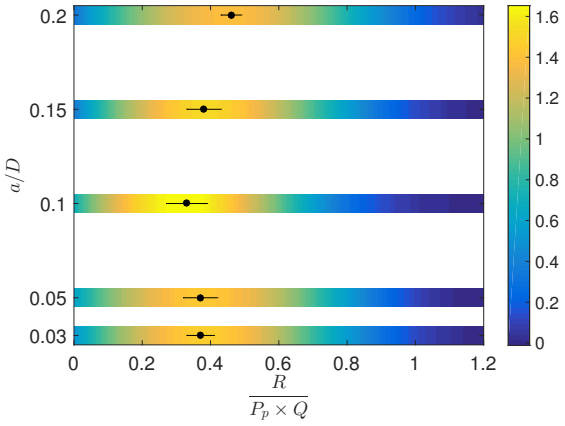

Figure 2.5: Contour plots of the probability density functions of finding a particle of a given family (a/D) at a radial distance normalized with the particle diameter and the isoperimetric quotient. The solid dot represents the peak of the contour plot and the horizontal line the dispersion of the peak location from particles with variable N.

representation since these are the particles characterized by the smaller circularity. This result suggests that the amplitude of the planar oscillations do not only depend on the particle perimeter but also on the frontal geometry (here defined by the isoperimetric quotient). Thus, Q is an appropriate parameter to make radial dispersion self similar with perimeter shape. The same approach is followed for all a/D families of particles and the contours of the probability density functions are shown in figure 2.5. The peaks of the distributions are represented with a solid dot, whereas the uncertainty on the peak location coming from the dispersion of the results for different particles within the same a/D family is represented with solid lines. The evolution of the peak location suggests that this normalization on the radial dispersion might overcompensate the results for the case of very irregular particles ($a/D > 0.2$), since it starts to deviate from the nearly constant value of 0.4 for $a/D \leq 0.15$.

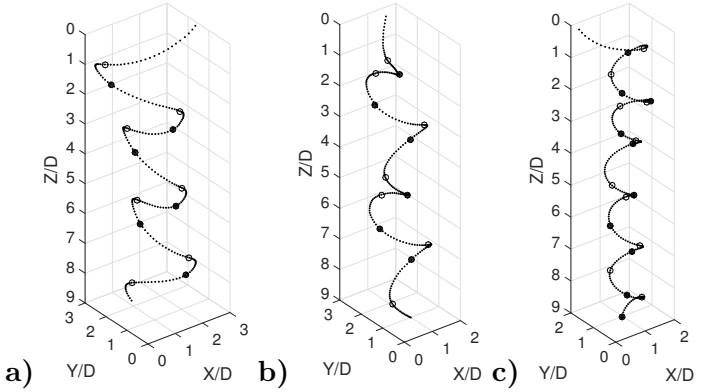

Figure 2.6: 3D trajectory reconstruction of sections of the particle descent: a) Disk, b) Planar particle with $a/D = 0.2$ and $N = 6$, c) Planar particle with $a/D = 0.2$ and $N = 10$. Solid and empty dots represent events of maximum and minimum descent velocity respectively.

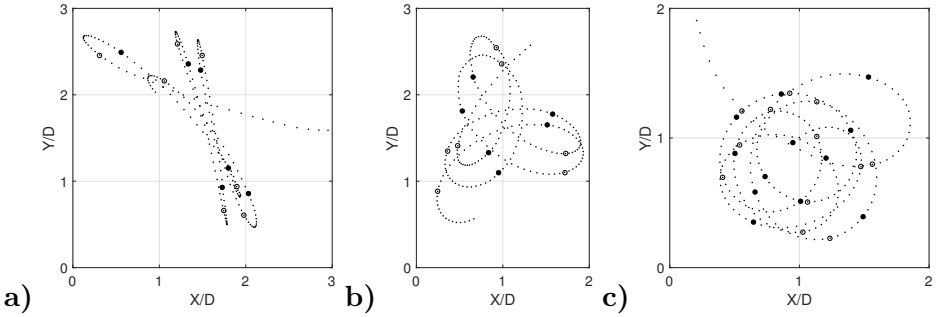

Figure 2.7: $X - Y$ trajectory reconstruction of the trajectory sections shown in figure 2.6. Solid and empty dots represent events of maximum and minimum descent velocity respectively.

2.3.2.2 Secondary motion

The differences observed in the particle planar dispersion suggest that these might exhibit different secondary motions depending on the characteristics of the particle perimeter. In this section, individual particle trajectories are plotted and compared to identify the main differences between geometries. Figure 2.6 shows trajectory samples of different particles, where maximum and minimum velocity events are shown with solid and empty dots respectively.

From the inspection of these trajectories one can observe that the disk, figure 2.6 a), describes a 'Planar zig-zag' motion that is approximately contained in a single plane of motion. We observe that as the number of waves around the perimeter increases the particle gains more out-of-plane motion, leading to a nearly spiral motion for the case seen in figure 2.6 c). There is another new type of trajectory in between these two clearly different styles of descent that remains stable for the length of the trajectories recorded. This type of descend is in fact a mixture of the 'Planar zig-zag' and 'Highly 3D'

motion, with the velocity in the $X-Y$ plane being a combination of angular and linear velocity (descent styles are explained in more detail in sec. 2.4.3.2). This leads to the characteristic descent footprint shown in figure 2.7 b), where the particle trajectory in the $X-Y$ plane resembles a rhodonea curve, as shown in Zhong et al. [2011] for disks with small dimensionless moment of inertia (I^*). Minimum and maximum descent velocity events appear at the same relative locations for the trajectory types of figure 2.6 a) and b), with the turning trajectory section being always bounded in between a minimum and maximum descent velocity event. In contrast, 'Highly 3D' trajectories do not show this clear distribution of fast and slow events in favour of a less organized arrangement of minimum and maximum descent velocity events. In the following sections we investigate if the various descent styles observed are associated with differences in descent velocity, particle orientation and drag coefficient.

2.3.2.3 Descent Velocity and Drag Coefficient

Results from the particle planar dispersion and particle secondary motion show strong differences in the settling characteristics of planar irregular particles. In this section, the descent velocity associated with the different falling styles observed is investigated. A mean descent velocity per trajectory is obtained from the trajectory section corresponding to $7\,D$ from the release point to $2\,D$ from the bottom ($\approx 15D$). Then, a unique descent velocity per particle geometry is obtained as the mean of 50 realizations. Figure 2.8 a) shows the variation of the measured mean terminal velocity (V_z) of all planar particles considered in this study. The mean terminal velocity is shown relative to that of the reference disk ($\tilde{V}_z = V_z/V_{z_{disk}}$). The mean terminal velocity is plotted as a function of the number of peaks (N) around the perimeter. The standard deviation from the 50 realizations is below 10% for all geometries investigated and it is not shown to help the figure visualization. The experimental data shows that particles with $N = 4$ and small a/D ratio; i.e. $a/D = 0.03$, $a/D = 0.05$ and $a/D = 0.1$, have a descent velocity that is slightly higher than the reference disk descent velocity. Also, there is a consistent increase in descent velocity for these families of particles as the number of peaks (N) around the perimeter increases. On the other hand, the decent velocity of the families with $a/D = 0.15$ and $a/D = 0.2$ lies below the disk descent velocity for $N = 4$ but rapidly increases, exceeding the descent velocity values of the particles with small a/D ratios for $N > 7$.

The drag coefficient (C_D) combines the mean descent velocity with the mass of the particle and the particle projected area to give a more robust comparison between perimeter shapes than the one presented in figure 2.8 a). The drag coefficient based on the projected area is of particular interest in this study because of the following reason: all particles share the same frontal area; however, when falling in quiescent flow they show strong differences in the descent style, as shown in the previous section. This leads to severe differences in the projected frontal area in the vertical direction, as can be

	N						
a/D	4	5	6	7	8	9	10
0.03	36	36	36	35	34	35	33
0.05	36	35	35	34	35	34	33
0.1	31	31	30	30	30	30	30
0.15	27	27	26	26	22	23	22
0.2	27	26	22	20	16	11	11

Table 2.3: Mean of the local maxima of the nutation angle, θ, of the particle during the fall. θ in degrees.

observed in table 2.3 from the change in particle nutation angle (θ). Thus, the drag coefficient based on the particle projected area can be understood as a measure of how efficient these geometries are to descend. Here, drag coefficient is obtained as

$$C_D = \frac{2m_{eff}g}{\rho_f A_p V_z^2} \tag{2.4}$$

where $m_{eff} = m_p - \rho_f V$ is the effective weight (buoyancy balanced) measured prior to the experiments, g is the gravity, V_z is the mean descent velocity for all particle realizations, A_p is the area of the particle projected to the descent direction and ρ_f is the fluid density. Figure 2.8 b) shows the variation in drag coefficient ($\widehat{C_D} = \frac{C_{D_p}}{C_{D_d}}$) as a function of the particle number of peaks (N) relative to the drag coefficient of the reference disk. The variation in drag coefficient across the entire range of particle geometries becomes more pronounced as the a/D ratio increases, maintaining the trends discussed in the particle descent velocity.

We believe that small a/D ratios are capable of changing the scale, and hence the lifetime, of the turbulent structures present in the wake of disks, reducing the suction effect over the top surface of the particle and therefore increasing the particle descent velocity. In contrast, particles with large a/D ratios and small number of peaks ($N = 4$) tend to move in the $X - Y$ plane with a given peak facing the planar motion, whereas a pair of peaks to each side are at almost 90^o with respect to the incoming flow. This configuration clearly favours lift production and therefore the particle descent velocity is reduced. As the number of peaks around the perimeter increases this particle-incoming flow configuration is gradually lost. We believe that the increase in the number of large peaks around the perimeter leads the formation and shedding of complex turbulent structures around the periphery of the particle with no preferential configuration. Thus, the particle falls following a more stable path with small inclination angles relative to the descent direction, an almost uniform descent velocity and a severe reduction of the $X - Y$ footprint. This tendency can be observed in the speed specific drag plotted in figure 2.8 b), where particles belonging to the $a/D = 0.2$ family exhibit a strong drag reduction as N increases, exceeding the reduction observed all other particles for $N > 8$.

Figure 2.9 a) depicts the evolution of the instantaneous descent velocity (v_z) of planar

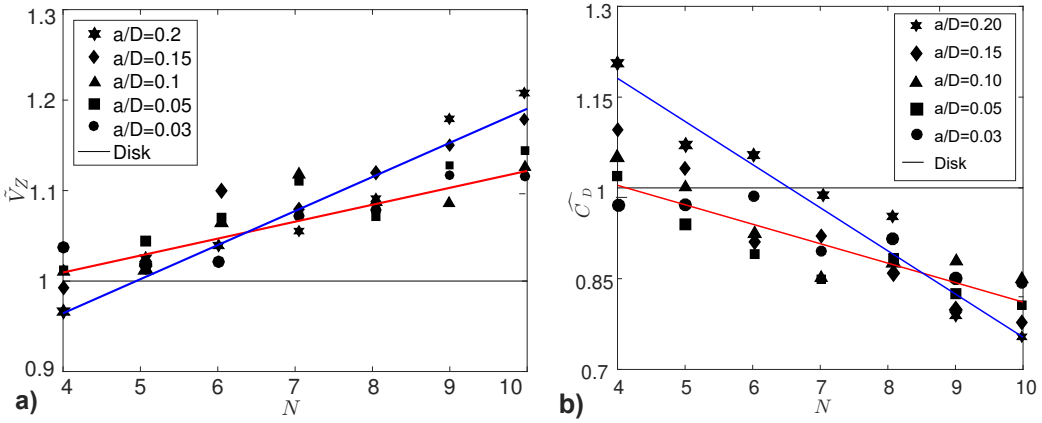

Figure 2.8: a) Particle mean descent velocity relative to the reference disk; b) Drag coefficient ($\widehat{C_D}$) based on the mean descent velocity (V_z) relative to that of the reference disk. Red and blue fitted lines show the trends for the particles belonging to the families of particles with $a/D = 0.03$ and $a/D = 0.2$ respectively.

particles with the same number of peaks ($N = 10$) but increasing the amplitude of the peaks from $a/D = 0.03$ to $a/D = 0.2$. The differences observed in the peak to peak velocity for individual trajectories in figure 2.9 a) are consistent for all realizations, and these can be seen in the standard deviation of the descent velocity for all individual trajectories detailed in figure 2.9 b). The standard deviation of the descent velocity of each trajectory is obtained and then, a unique value of the standard deviation per particle geometry is shown as the mean of the 50 realizations. The standard deviation of the descent velocity is shown relative to the disk ($\tilde{\sigma}_{V_z} = \sigma_{V_{z.p}}/\sigma_{V_{z.d}}$). The standard deviation of the descent velocity for particles with small a/D is marginally higher than the one found for disks and this corresponds to about 20% of the mean descent velocity. This is also consistent with the values shown for the mean descent velocity; both of these families show mostly 'Planar zig-zag' motion with slow and fast events (as in figure 2.6 a)) but with a higher mean descent velocity and therefore we also expect the oscillations about the mean to be stronger. In contrast, for $a/D > 0.1$ the descent style resembles more the rhodonea curve shown in figure 2.7 b) with a descent becoming more stable as a/D and N increases. Interestingly, we observe a change in the descent style of the particles with $N = 4$ and $a/D > 0.1$ when compared with other particles from the same a/D family. These particles describe a spiral-like paths but with greater $X - Y$ footprint than for the case of high N number. We believe these particles represent a special geometry case, for which the production of lift dominates the settling dynamics.

2.3.3 Drag correlation for planar irregular particles

As briefly reviewed in section 1.7, there are a large number of empirical correlations for predicting the drag coefficient of non-spherical particles associated with different ranges

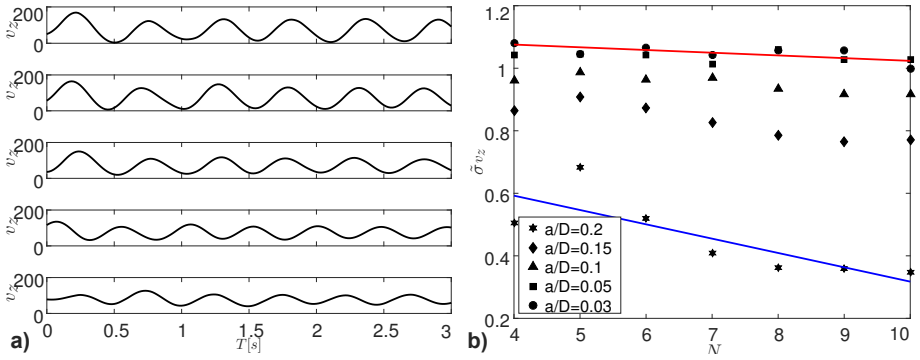

Figure 2.9: a) Time evolution of the descent velocity of different particles with $N = 10$ during specific realizations. From top to bottom: $a/D = 0.03$, $a/D = 0.05$, $a/D = 0.1$, $a/D = 0.15$ and $a/D = 0.2$. b) Standard deviation of the descent velocity along individual trajectories of all particles tested relative to the reference disk. Velocity units in mms^{-1}.

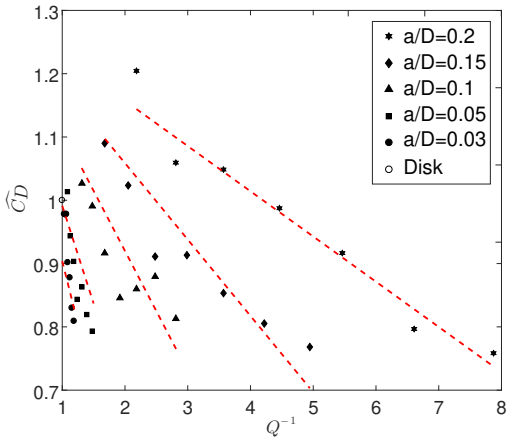

Figure 2.10: Drag coefficient relative to the reference particle based on the mean projected area during descent as a function of the isoperimetric quotient Q and relative peak amplitude a/D. Broken lines are fitted to the experimental data of particles belonging to each a/D family following equation 2.5.

of validity and accuracy in the literature, as in Bagheri and Bonadonna [2016], Mando and Rosendahl [2010], Holzer and Sommerfeld [2008], Loth [2008], Cong et al. [2004], Leith [1987] and Haider and Levenspiel [1983] among others. However, in most studies the shape descriptor used to characterize particles is the sphericity. Sphericity (ψ) is defined as the ratio of surface area of a sphere with equivalent volume as the particle to the true surface area of the particle, $\psi = \pi d_{eq}^2 / A_p$. As a result, particles with very different geometry can have the same value of sphericity, and this is in fact what occurs for all particles in this study, therefore the need of an alternative empirical correlation to characterize the settling dynamics of these particles. Although the isoperimetric quotient has a non-unique value for the particles in this study, particles with the same a/D ratio do not have the same isoperimetric magnitude. Therefore, Q is used for the

aforementioned purpose. As described in the previous sections, the geometry of the perimeter of planar irregular particles is directly linked to differences in the particle falling style and Drag Coefficient. In figure 2.10, the mean particle Drag Coefficient relative to the equivalent disk $\widehat{C_D}$ is shown as a function of the particle circularity (here defined by the isoperimetric quotient Q) and the relative amplitude of the peaks (a/D). Experimental data of particles belonging to different a/D families show distinctive linear trends as the isoperimetric quotient decreases. These trends are represented with straight lines on the $\widehat{C_D} - Q^{-1}$ domain, defined by equation 2.5, where the slope of the linear trends is defined as a function of the relative amplitude of the peaks (a/D).

$$\widehat{C_D} = m(a/D)Q^{-1} + 1.3 \tag{2.5}$$

where $m(a/D)$ is defined as

$$m(a/D) = 0.204 + 0.17\log(a/D) \tag{2.6}$$

Thus, the mean Drag Coefficient of a planar irregular particle relative to the equivalent disk can be approximated once the a/D ratio and the isoperimetric quotient Q are known.

Similarly, the fluctuations of the Drag Coefficient can be also captured by considering the complete range of values for the particle descent velocity along trajectories. Thus, one can estimate the complete particle descent using the mean descent velocity ($\tilde{V_z}$) and the standard deviation of the descent velocity ($\tilde{\sigma}_{vz}$) from figure 2.8 b) and 2.9 b) to construct quasi-periodic signals.

2.3.4 Summary

This experimental work investigated the effect of the particle edge waviness on the free falling motion of planar particles. The reference particle was chosen to be a circular disk in the $Re - I^*$ domain corresponding to 'planar zig-zag' motion. The Galileo number of the different planar particles was held a constant and the isoperimetric quotient (a measure of particle circularity) was varied by altering edge waviness of the particle to different wave amplitude (a/D) and number of oscillations (N) around the perimeter.

Disks and other disk-like families of particles with small a/D ratios were found to describe 'planar zig-zag' trajectories most of the time. This planar motion is characterised by a gliding phase followed by a turning phase. Particles belonging to families with large a/D ratios but only a few peaks ($N = 4$ and 5) also show a strong tendency to glide but with a given peak facing the horizontal motion. The pair of peaks to each side at nearly 90^o with respect to the incoming flow, clearly favouring lift production and reducing the particle descent velocity.

As the number of peaks around the perimeter increases the lift production configuration is gradually lost. We believe that the presence of large peaks around the perimeter leads the formation and shedding of complex turbulent structures around the periphery of the particle with no preferential configuration. Thus, the particle falls following a more stable path with small inclination angles relative to the descent direction, an almost uniform descent velocity and a severe reduction of the $X-Y$ footprint.

These falling styles are shown to be directly linked to the particle radial distribution, mean descent velocity and Drag Coefficient. The radial distribution of particles from the same a/D family collapse when the particle perimeter and isoperimetric quotient are used to make particle dispersion non-dimensional. On the other hand, Drag Coefficient of planar particles reduces with reducing the isoperimetric quotient for any given a/D family of particles, with the family $a/D = 0.2$ having more than 15% reduction for $N = 9$ and $N = 10$.

We propose an empirical correlation for the mean drag coefficient of these particles based on the isoperimetric quotient (Q) and the relative amplitude of the peaks around the perimeter (a/D), [Esteban et al., 2019b]; and show that the fluctuations of this parameter can be captured using the standard deviation of the descent velocity ($\tilde{\sigma}_{vz}$).

We believe that with information such as this, it is possible to simulate the vertical trajectory content of these particles using Monte Carlo type simulations with Lagrangian points and also that this same approach can be used to obtain a prediction of the Drag Coefficient of any planar irregular particle whose equivalent disk lies in the fluttering region. Similarly, data from the particle radial dispersion can also be used to predict the $X-Y$ particle behaviour during the descent.

2.4 Planar N-sided Particles in Quiescent Flow

In this section experiments are carried out to find whether the transition from 'Planar zig-zag' to 'Highly 3D' motion in the phase diagram defined by Lee et al. [2013] holds for planar particles with different frontal geometry than disks. To do so, we measure the 3D trajectories of planar regular polygons with similar mass (m), thickness (t) and frontal area (A_p) but different dimensionless moment of inertia (I^*). The reference particle is a disk that lies in the 'Planar zig-zag' region of the phase diagram defined by Lee et al. [2013]. Then we analyze the motion of planar polygons, i.e. heptagons, hexagons, pentagons and squares with smaller dimensionless moment of inertia.

2.4.1 Methods

In water, particles were released as described in section 2.2. To build a baseline from which to compare the motion of the planar particles a first set of 300 repeated drops of

	Disk	Heptagon	Hexagon	Pentagon	Square
Represented as	○	✳	✡	☆	□
$Side(mm)$	-	11	13	16	21
$A_p(cm^2)$	4.34	4.40	4.39	4.40	4.41
$R_c(mm)$	11.75	12.67	13	13.6	14.84
$A_c(cm^2)$	4.34	5.04	5.31	5.81	6.92
A_r	1	0.87	0.83	0.76	0.64
$Mass(g)$	1.07	1.02	1.01	1.02	1

Table 2.4: Particle dimensions. R_c refers to the radius of the circumscribed circle and the area ratio is defined as $A_r = A_p/A_c$.

the disk in water at room temperature ($\rho_f = 0.998\,\mathrm{g/cm^3}$ and $\nu = 1.004 \cdot 10^{-6}\ \mathrm{m^2/s}$) were performed. Then, a set of 300 drops for each planar polygon was performed under the same conditions.

All planar particles in this experiment are regular polygons and are manufactured to have the same frontal area within the precision of the laser cutter $\pm 0.5\,\mathrm{mm}$. Table 2.4 summarizes the dimensions of the particles manufactured. Triangles were also manufactured but the motion was dominated by very large gliding motions that made the facility inappropriate to take accurate measurements of the particle trajectory.

Two JAI GO-5000M USB cameras were used to record the particle descent. Each camera was positioned on one side of the water tank and a diffuse light used to illuminate homogeneously the opposite side of the tank, as shown in figure 2.1. The recording parameters and image processing method are the same as detailed in section 2.2.

2.4.2 Determination of Non-Dimensional Parameters and Phase Diagram

The motion of a freely falling disk, the reference particle, is characterized by five dimensional quantities, i.e. the diameter of the disk ($2R_c$), the thickness of the disk (t), the density of the disk (ρ_p), the density of the fluid (ρ_f) and the kinematic viscosity of the fluid (ν). From these five dimensional quantities one can form three non-dimensional numbers, i.e. the dimensionless moment of inertia (I^*), the Reynolds number (Re) and the thickness to diameter ratio (β). For all planar particles manufactured $\beta < 0.1$ and approximately the same, so that the dynamics of the fall is independent of this parameter, [Smith, 1971].

The dimensionless moment of inertia of all planar particle is estimated following the approach in Willmarth et al. [1964] for disks,

$$I^* = \frac{I_p}{\rho_f (2R_c)^5} \tag{2.7}$$

	Disk	Heptagon	Hexagon	Pentagon	Square
$I^* \cdot 10^3$	5.01	3.48	3.12	2.52	1.67
Re	1370	1450	1450	1540	1620

Table 2.5: Values of the dimensionless moment of inertia (I^*) and Reynolds number (Re) for the planar particles.

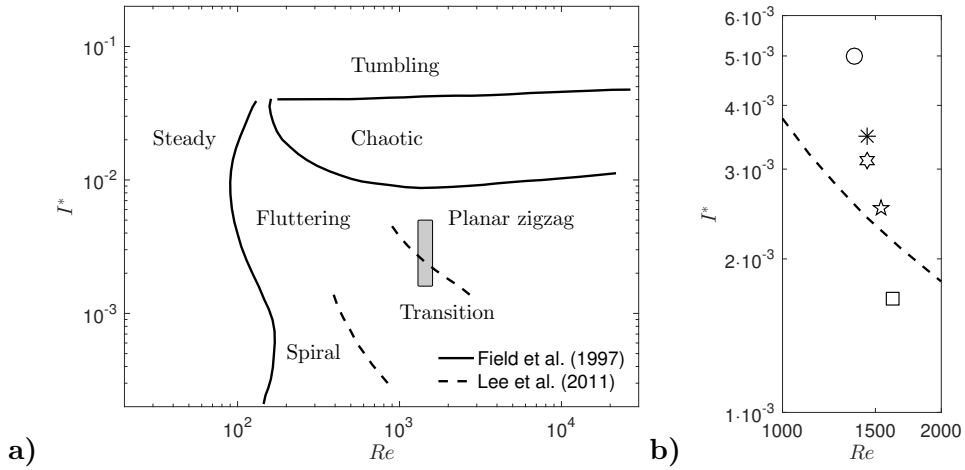

Figure 2.11: Phase diagram: a) Falling regimes of a disk, the parameter space is adapted from Field et al. [1977], spanned by the dimensionless moment of inertia (I^*) and Reynolds number (Re), b) Experimental region of the phase diagram studied.

where I_p is the mass moment of inertia of the particle about its diameter and the diameter of the circumscribed disk ($2R_c$) is used as a characteristic length scale. The Reynolds number is also estimated using the diameter of the circumscribed disk ($2R_c$) and the mean descent velocity (V_z), see table 2.6.

$$Re = \frac{2R_c V_z}{\nu} \tag{2.8}$$

The parameter space (Re, I^*) of all planar particles shows they lie within the fluttering region defined by Field et al. [1977].

In this study we also use the isoperimetric quotient (Q) introduced in sec. 2.3 to evaluate the particle circularity.

2.4.3 Results

2.4.3.1 Descent Velocity

The measured mean terminal velocity of all planar particles considered in this study is smaller than the disk terminal velocity and it reduces with the particle dimensionless

	Disk	Heptagon	Hexagon	Pentagon	Square
$\langle V_z \rangle (mms^{-1})$	58 ± 3	57 ± 3	55 ± 3	56 ± 3	55 ± 3
$\sigma_{v_z} (mms^{-1})$	32	30	28	27	23

Table 2.6: Values of mean ($\langle V_z \rangle$) and standard deviation (σ_{v_z}) of fall velocity for different shapes of planar particles over 300 realizations.

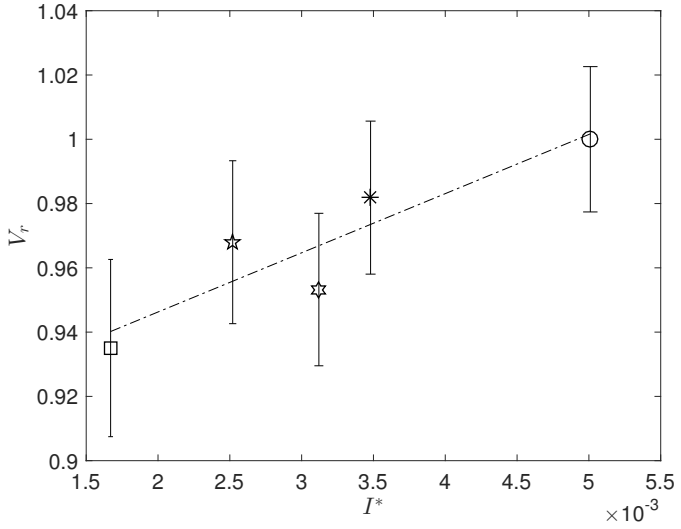

Figure 2.12: Particle velocity ratio V_r versus the dimensionless moment of inertia I^*. V_r is defined as the ratio of the particle descent velocity to the descent velocity of the equivalent disk. Symbols defined in table 2.4

moment of inertia.

The greatest difference in the mean descent velocity has been found in squares -the particles with the least numbers of symmetry planes and smaller inertia- being approximate 7.25% slower than disks. The magnitude of the velocity difference is in good agreement with the trend shown in Jayaweera [1972] for disks and hexagonal plates covering a Re range from 0.2 to 22. However, the particles in Jayaweera [1972] are in the steady regime and the secondary motion is absent.

On the other hand, the velocity standard deviation is maximum for disks, and it reduces together with the dimensionless moment of inertia, see table 2.6. Squares show a velocity standard deviation about 30% smaller than disks, so that the descent motion of these particle is much steadier than the observed in disks. These results are in good agreement with List and Schemenauer [1971], where at $Re \approx 200$ small oscillations were observed in disks, hexagonal plates and broad-branched models, with the biggest oscillations present in disks. The fluctuations of the descent velocity decrease as the particle dimensionless moment of inertia decreases and this is consistent with the sub-regimes proposed in Lee et al. [2013].

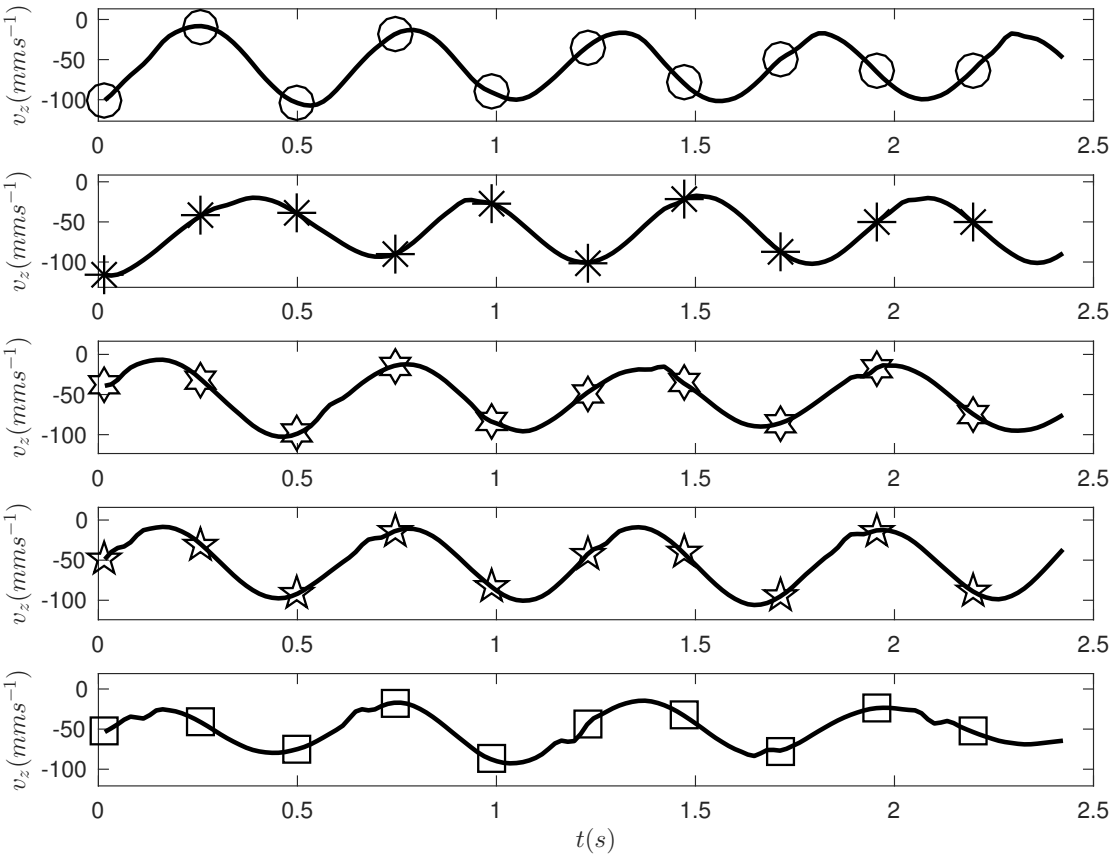

Figure 2.13: Time evolution of the measured vertical velocity for the geometries listed in table 2.6 falling in the 'Planar zig-zag' regime.

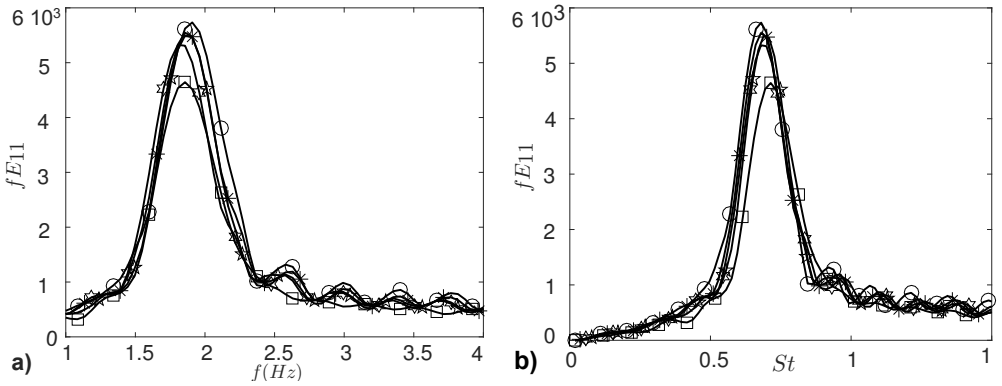

Figure 2.14: a) Mean pre-multiplied power spectral density as a function of frequency (f); b) Mean pre-multiplied power spectral density as a function of Strouhal number (St).

In figure 2.13, the time evolution of the descent velocity for the five planar particles is examined. The velocity data of all of them appear to be nearly periodic.

In order to obtain the frequency content of the descent velocity we apply Fast Fourier Transform to the descent velocity signal. Figure 2.14 a) shows the pre-multiplied power

spectral density function of all $n-$sided polygons. We observe that the dominant frequency of the descent velocity of all planar particles does not show dependency with the particle geometry and that this is $f \approx 1.8Hz$. The Strouhal number, defined as $St = f\sqrt{A_p}/\langle V_z \rangle$, is estimated to compare the oscillating flow mechanism along the particle descent, see figure 2.14 b). The dominant frequency (f) obtained from the Fourier transform of the descent velocity, the characteristic length ($\sqrt{A_p}$) and the mean descent velocity (V_z) are the characteristic parameters used. The value for the Strouhal number remains approximately constant ($St \approx 0.65$) as the number of symmetry planes and dimensionless moment of inertia of the particle decreases. This value is in good agreement with the Strouhal number found for disks in [Lee et al., 2013]. At the same time, it can be seen that the magnitude of the peak in the pre-multiplied power spectrum decreases with the particle dimensionless moment of inertia. This result shows that as the number of symmetry planes in a particle increases the descent trajectory gets locked into a single frequency.

The difference between the area under the curve of the pre-multiply power spectrum, figure 2.14 b) for square plates and disks is consistent with the magnitude of the velocity standard deviation along the trajectory, shown in table 2.6. This, together with the fact that the mean descent velocity of all the particles are very similar suggest that the non-fall velocity component of the particle from one planar particle to another may be different.

Therefore, we believe it is necessary to investigate the trajectories individually to group them if possible and extract more information about the particle falling characteristics.

2.4.3.2 Trajectories

Figure 2.15 shows two disk trajectories describing drastically different falling patterns. Figure 2.15 a) shows a 'Planar zig-zag" motion while 2.15 b) shows a trajectory with a much stronger out-of-plane motion along the particle descent, we term this 'Highly 3D' flutter. It is interesting to note that a disk with the same material properties falling in the same viscous medium can exhibit drastically different falling patterns along the descent, as observed in Heisinger et al. [2014] for disks of $Re \approx 1200$ and $I^* \approx 3 \cdot 10^{-3}$. In some instances the particle begins a 3D motion with much steadier descent velocity and then transitions to a 'Planar zig-zag' motion with strong oscillations in the descent velocity, as seen in figure 2.16, or in reverse order. This transition coincides with the dynamics of disks with Reynolds number in the range of $1000-2100$ observed in Lee et al. [2013]. The planar $(X-Y)$ projection added on the right hand side of the 3D trajectory shows the relevance of the angular velocity about the z-axis during the fall. Open and closed dots are added to the particle trajectory where the descent velocity is minimum and maximum respectively. As it can be seen, these points define two subsections along the particle path for the 'Planar zig-zag' motion, a 'gliding' section and a 'turning'

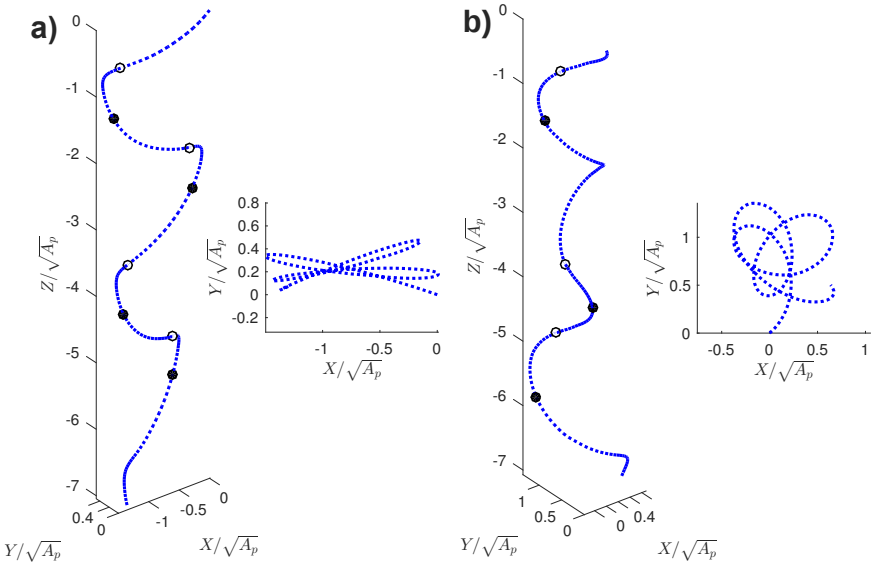

Figure 2.15: Reconstructed 3D trajectories and (X, Y) planar projections for a) 'Planar zig-zag' fluttering and b) 'Highly 3D' fluttering. Open and close dots stand for minimum and maximum descent velocity points respectively.

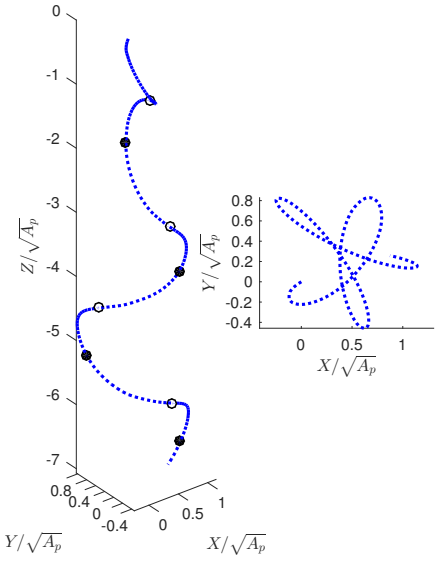

Figure 2.16: Reconstructed 3D trajectory and (X, Y) planar projection for a disk transitioning from 'Highly 3D' motion to 'Planar zig-zag' motion.

section. For 'Highly 3D' fluttering, figure 2.15 b), minimum and maximum velocity points seem randomly distributed. As the magnitude of the angular velocity about the $z-$axis increases and becomes more steady during the particle fall, the differences between sub-sections become negligible; as can be seen in figure 2.18 b).

The velocity components along the trajectory shown in figure 2.15 a) are plotted in figure 2.17 a) showing that the two components of the planar $(X - Y)$ velocity (v_x, v_y) form a nearly periodic and symmetric planar velocity. The descent velocity (v_z) also shows

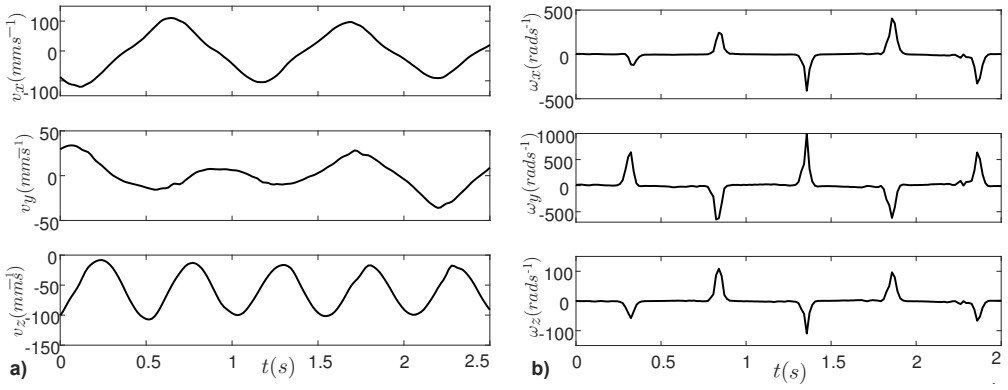

Figure 2.17: Time evolution of the measured velocities for a disk under 'Planar zig-zag' motion. *a*) Linear velocities; *b*) Angular velocities.

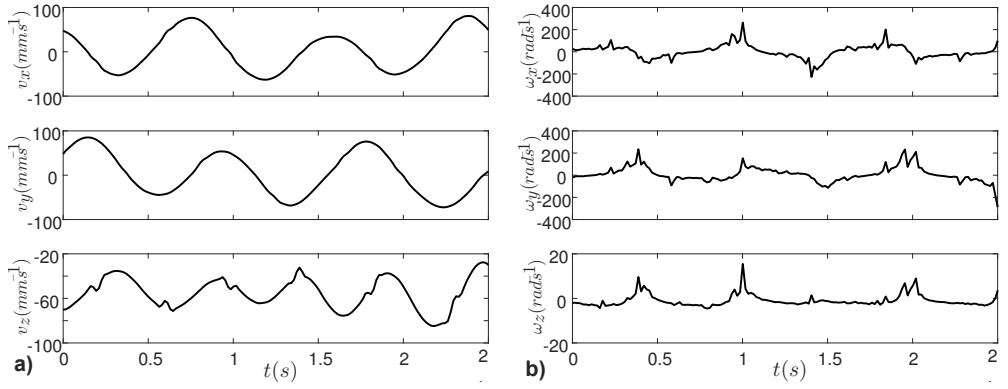

Figure 2.18: Time evolution of the measured velocities for a disk under 'Highly 3D' motion. *a*) Linear velocities; *b*) Angular velocities.

periodicity and symmetry about its mean value, with an oscillatory frequency twice the one seen for the planar $(X-Y)$ velocity. The three components of the angular velocity of the particle in figure 2.17 b), show that the turning sections are the only period of time when the angular motion is relevant. The angular velocity of the particle along the trajectory is obtained by fitting a circle every three points of the trajectory. Then, the radius of the circle and the particle linear velocity are used to compute angular velocity.

Figure 2.18 a) shows that for 'Highly 3D' motion, the three components of the linear velocity lose some degree of periodicity and symmetry; being the vertical component of the velocity the most affected. Equally, figure 2.18 b) shows that the angular velocity about the three axis is non-zero for the entire trajectory. These two modes of motion; i.e 'Planar zig-zag' and 'Highly 3D', have been observed in the literature for disks with different dimensionless moment of inertia, [Lee et al., 2013]. However, in this study we observe that the same disk can describe both types of motions, although they are not equally probable.

Due to the differences observed in the trajectories, a method to classify them according

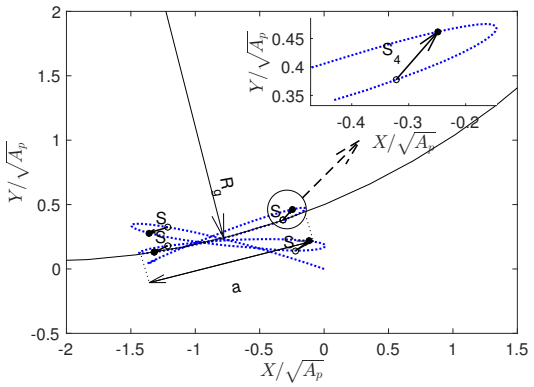

Figure 2.19: Schematics of the process to obtain the (a/R_g) ratio of each gliding section.

to the relevance of the planar $(X-Y)$ motion is proposed. To do so, each trajectory is split into blocks of gliding motion and blocks of turning motion. These trajectory blocks being defined by points of local minimum and maximum descent velocity, i.e. open and closed dots in figure 2.15.

From the observation of the planar $(X-Y)$ view of any trajectory describing 'Planar zig-zag' motion, it seems that the gliding blocks might be well approximated with a straight line in the $(X-Y)$ plane. Likewise, the turning blocks show a complete turn of approximately 180 deg in the $(X-Y)$ plane. In order to measure the curvature of the trajectory in the 2D $(X-Y)$ gliding section a circle is fitted to these trajectory points in the gliding section, as in figure 2.19, to compare the amplitude (a) of the planar motion with the radius (R_g) of the fitted circumference. If the particle describes a perfect 3D helicoidal motion, the planar $(X-Y)$ view will be represented as a circle, and therefore $a/R_g = 2$. However, if the particle describes a perfect planar motion the planar $(X-Y)$ view will be represented as a straight line, then the fitted circumference will have $R_g = \infty$, and therefore $a/R_g = 0$. The value of this ratio could be also zero if the particle falls with negligible planar $(X-Y)$ velocity since the amplitude of this motion would be also zero, but this would only occur for particles in the $Re - I^*$ parameter space of steady fall. This process is repeated for all gliding blocks of each particle and a mean value of a/R_g is obtained per trajectory. This new parameter is used for the trajectory classification.

In figure 2.20, the vertical axis represents the probability that a/R_g takes a value less than or equal to x. Although a/R_g could reach a maximum value of 2, figure 2.20 only shows the likeliness of having a trajectory of $a/R_g \leq 1$ since there is not a significant difference in the statistics after this value. It is interesting to highlight that the probability of having a trajectory with 'Planar zig-zag' motion is dependent on the particle dimensionless moment of inertia. Thus, planar particles show a less frequent 'Planar zig-zag' motion as Q decreases, with the exception of heptagons. The likeliness of having a particle falling with $a/R_g \leq x$ can be approximated by the following equation, as

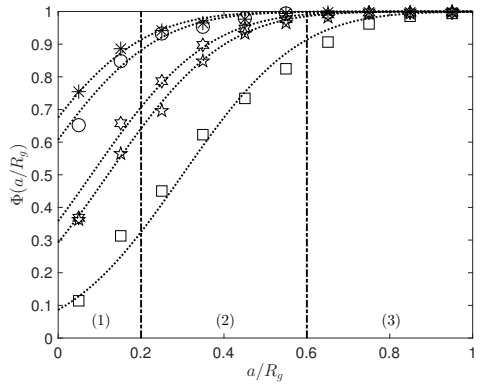

Figure 2.20: Cumulative distribution function (CDF) of the a/R_g ratio for each gliding trajectory with the sub-groups proposed; (1) 'Planar zig-zag' motion, (2) 'Transition' Motion and (3) 'Highly 3D' Motion.

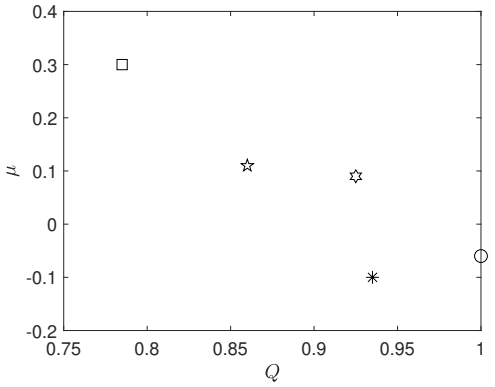

Figure 2.21: Dependency of the fitted constant μ with the particle isoperimetric quotient Q.

shown on figure 2.20,

$$\Phi(x) = \frac{1}{2}\left(1 + erf\left(\frac{x-\mu}{\sigma\sqrt{2}}\right)\right) \tag{2.9}$$

Where $\sigma = 0.22$ and μ changes with the particle characteristics. The change in μ with Q is illustrated in figure 2.21. The function $\Phi(x)$ defines the cumulative distribution of a Gaussian distribution with mean μ and standard deviation σ. For the measured data, the values of μ and σ that best fit the curves of each planar particle reasonably match the mean and standard deviation of the data, suggesting that the distribution of a/R_g is nearly Gaussian. The relationship μ with Q suggests that the particle isoperimetric quotient has a severe influence in the likeliness of having a 'Planar zig-zag' trajectory.

In this study we propose to separate the trajectories in three sub-groups; particles describing a trajectory with $a/R_g \leq 0.2$, particles describing a trajectory with $0.2 < a/R_g \leq 0.6$ and particles describing a trajectory with $a/R_g > 0.6$. Then, considering the characteristics of the trajectory, we propose three falling motions:

- 'Planar zig-zag' motion [$a/R_g \leq 0.2$]: The gliding blocks are well defined by a straight line within a $(X-Y)$ plane, while the turning blocks show small deviations from the idealized complete turn of 180 deg in the $(X-Y)$ plane.
- 'Transition' motion [$0.2 < a/R_g \leq 0.6$]: The particle descends following a oscillatory motion in a $(X-Y)$ plane, but with a superimposed constant angular velocity about the z-axis. The particle describes a (X-Y) motion as the bob in a Foucault pendulum seen from a co-rotating point of view.
- 'Highly 3D' motion [$a/R_g > 0.6$]: The gliding blocks are characterized by a severe angular velocity about the z-axis and the turning blocks do not show a relevant peak in the angular velocity. This fact results in an angular velocity about the z-axis that is almost constant along the entire trajectory and therefore the particle describes a nearly helicoidal descent.

The trajectories that are classified as 'Planar zig-zag' and 'Transition' will be investigated in more detail in section 2.4.5 and 2.4.5 respectively.

2.4.4 Revisiting the Phase Diagram

Disks and heptagons considered in this study show a strong tendency to fall following a 'Planar zig-zag' trajectory. However, as the isoperimetric quotient becomes smaller the out-of-plane motion of the particle gains relevance. This fact shows that the particle frontal geometry has a severe influence in the likeliness of the particle to describe one motion or another, this was already shown in section 2.3. In this case, it might be closely related to the likeliness of having a sharp corner aligned with the direction of the particle secondary motion and the resulting wake characteristics. When this occurs, the lift distribution on the particle surface is symmetric with respect to the plane of the secondary motion, and therefore the particle follows a nearly straight line during the gliding section of the trajectory (similar to the motion of a delta wing). We hypothesize that the deviation from the 'Planar zig-zag' motion is caused by flow disturbances that induce the particle rotation about the axis perpendicular to its surface, as discussed in Lee et al. [2013]. When the particle symmetry axis is not aligned with the secondary motion, the lift distribution on the particle surface lacks symmetry, thereby inducing the particle rotation and enhancing the transition to 'Highly 3D' motion. Thus, as the frontal geometry changes and the isoperimetric quotient becomes smaller, the out-of-plane motion of the particle gains relevance and the overall descent becomes similar to the one seen for disks with much smaller dimensionless moment of inertia ($I^* \approx O(10^{-4})$), as seen in Lee et al. [2013]. This suggests that the equivalent disks to these n-sided polygons will in fact be larger in diameter.

The differences observed between the trajectories of the particles investigated in here suggest that a characteristic length based on the frontal area of the particle does not

	Disk	Heptagon	Hexagon	Pentagon	Square
Represented as	○	✳	✡	☆	□
I^*_ℓ	5.01×10^{-3}	2.42×10^{-3}	1.95×10^{-3}	1.18×10^{-3}	5.13×10^{-4}
Re_ℓ	1370	1450	1450	1540	1620

Table 2.7: Values of the dimensionless moment of inertia (I^*_ℓ) and Reynolds number (Re_ℓ). ℓ refers to the new length scale proposed.

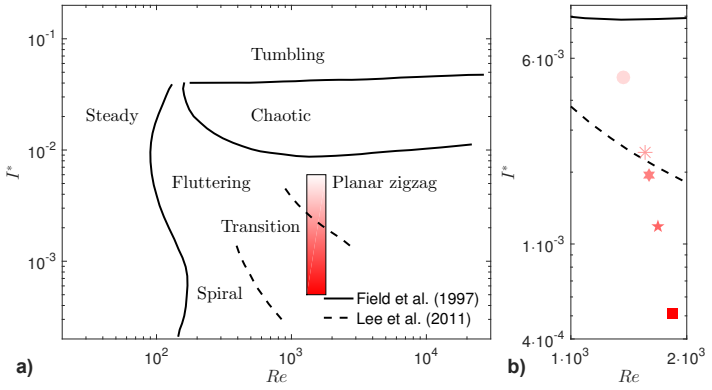

Figure 2.22: a) Phase diagram spanned by the dimensionless moment of inertia (I^*) and Reynolds number (Re). The rectangle corresponds to the region of the present work and the color represents the likeliness of the trajectory to be 'Planar zig-zag' (light red) or 'Highly 3D' (dark red). b) Zoom in the region of the present work.

estimate accurately the dynamics of the particle under free fall conditions. We hypothesise that there are two geometric factors affecting the particle motion: the longest distance between any two points along the perimeter of the planar particle and the presence of sharp corners. Both these physical parameters should be accounted for when determining the equivalent disk.

Based on our empirical data and the above-mentioned hypothesis, we propose a new length scale for the estimation of the dimensionless moment of inertia and Reynolds number. This length scale should be related to the diameter of the circumscribed circle around the particle (D_c). This will ensure that the equivalent disk encompasses the entire planar particle and account for the 'longest distance' in our hypothesis. However, this lengthscale is not sufficient as the edges add additional vorticity to the field. This edge effect can be accounted for through the isoperimetric quotient (Q). Therefore, a new length scale (ℓ) is proposed as the ratio between the diameter of the circumscribed circle and the isoperimetric quotient, [Esteban et al., 2018]. This new characteristic length scale, $\ell = D_c/Q$, will make the n-polygons have a much smaller dimensionless moment of inertia and a slightly different Reynolds number, which will alter the phase diagram. More importantly, this new definition reverts to the standard dimensionless

inertia and Reynolds number of the disk and is consistent with classical definition used in previous studies.

This length scale ($L\ell$) is used to estimate the equivalent dimensionless inertia and particle Reynolds number as seen in table 2.7. The $Re - I^*$ phase diagram based on this new lengthscale is computed and compared to the observations. First of all, it should be noted that the only change in this revised definition is that the different particles will have a different value of I^* depending on their shape (and the corresponding ℓ). The Reynolds number will also be slightly different (as it depends on ℓ and V_z). Since the values of I^* are dramatically different, the different particles now lie in different positions in the phase diagram of a circular disk. This is depicted in figure 2.22. It can be seen now that the squares lie well in to the 'Transition' sub-regime (from 'Planar zig-zag' to 'Highly 3D'). The other polygon particles, with higher values of Q are distributed more evenly in the 'Transition' sub-regime. Finally, disks are still located in the 'Planar zig-zag' sub-regime. These revised locations of the different particles in the phase diagram based on the new length scale agrees very well with the characteristics of the trajectories found in previous sections where we used a/R_g to classify the type of trajectory followed by the particles. Based on this new definition almost all particles are in the 'Transition' regime (except circular disks and heptagons) with particles with smaller number of edges having a tendency towards spiral motion.

2.4.5 Simple Pendulum Approach: Planar Flutter

A simple pendulum consist of a massive object, i.e. pendulum bob, hung by a string from a fixed point. If the pendulum bob is displaced from its equilibrium point and then released, it begins the back and forth swing about its equilibrium point. It is the restoring force what causes the bob to slow down as it moves away from the equilibrium point and to speed up as it gets closer to the equilibrium point. Ignoring air-resistance, there are two dominant forces responsible of this behaviour; the gravity and the tension force.

One can clearly see the similarities between the motion of an idealized simple pendulum and the motion described by a particle under 'Planar zig-zag' descent; as long as the mean descent velocity of the particles is ignored. Therefore, we propose to use the pendulum equation, eq. 2.10, to describe the particle oscillations about its mean descend motion.

$$\frac{d^2\theta}{dt^2} + K\sin(\theta) = 0 \tag{2.10}$$

where $K = g/L$ and L is the length of the pendulum. Since our imaginary pendulum is submerged in water, the acceleration of gravity should be corrected with the inclusion of the buoyancy term and therefore, $K = g(1 - \rho_w/\rho_p)C/L$. The constant C included in

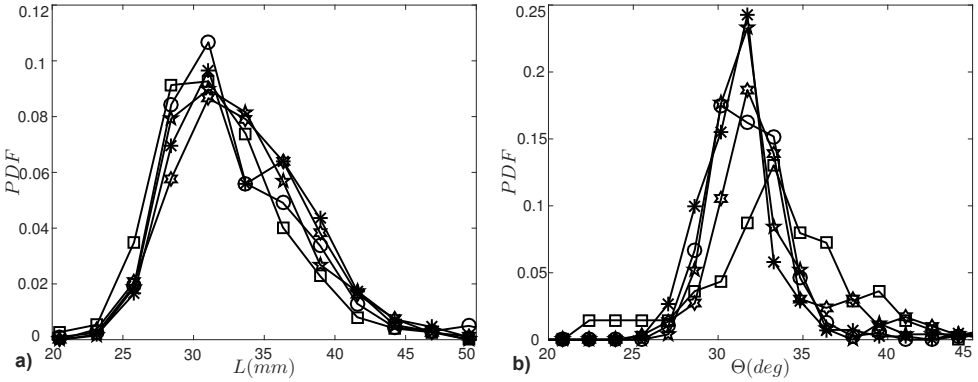

Figure 2.23: Probability density function (PDF) of the constants for the simple pendulum model from gliding sections only. a) Length of the imaginary pendulum L; b) maximum swing angle θ_0.

	Disk	Heptagon	Hexagon	Pentagon	Square
$L(mm)$	32.9	33.6	33.3	32.9	31.7
$\theta_{max}(deg.)$	32	32	35	32	36

Table 2.8: Mean value of the pendulum constants for all particles in planar motion.

the definition of K stands for all other accelerations acting on the particle throughout the fall.

Equation 2.10 can be used to extract the vertical and horizontal position of the bob relative to the origin of the pendulum as,

$$x(t) = L\sin(\theta(t)) \tag{2.11}$$

$$z(t) = -L\cos(\theta(t)) \tag{2.12}$$

If we now incorporate the measured mean descent velocity of the particle (V_z) as in equation 2.13, these pair of equations (eq. 2.11 and eq. 2.13) appear to represent accurately the motion of the free falling particle modelling it as a 'free falling pendulum' with the origin fixed in the $x-$ coordinates.

$$z(t) = -L\cos(\theta(t)) - V_z t \tag{2.13}$$

The angle $\theta(t)$ of the pendulum goes from θ_0 to $-\theta_0$, being θ_0 the angle when the bob is released. The magnitude of this angle will change slightly for every gliding section since the velocity components are not perfectly periodic. Similarly, the pendulum length (L) will also change at each gliding section. Thus, a single value for L and θ per swing is obtained by fitting the former equations to the measured trajectory; the mean value of these constants are listed in table 2.8.

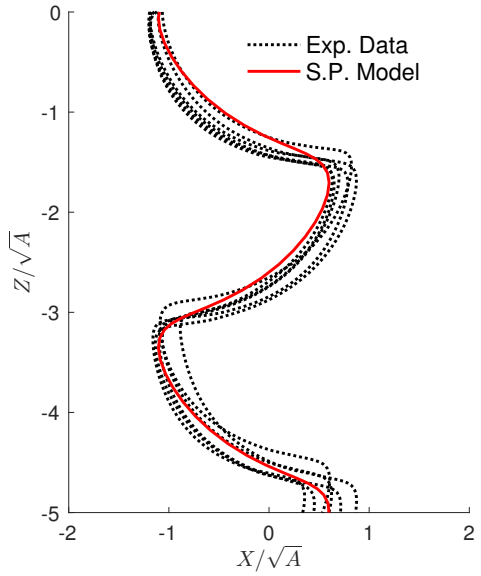

Figure 2.24: Comparison of the three dimensional reconstructed trajectories for the'Planar zig-zag' motion of a planar heptagon with the Simple Pendulum Model.

Figure 2.24 shows the comparison between the experimental data obtained for planar heptagons freely falling in water and the Simple Pendulum model proposed, (equations 2.11 - 2.12). The experimental trajectories are matched with the trajectory modelled at a point of maximum θ. It is observed that the gliding sections of the experimental trajectories are well defined and are the base of the Simple Pendulum Model, while turning blocks are more complex and show the biggest variation. The Simple Pendulum Model on its own is only defined by the gliding sections; once $|\theta(t)| = |\theta_0|$ the particle starts the next pendulum swing but V_z is still acting, allowing the transition from one gliding swing to the next and approximating the particle turning dynamics very well without any explicit model of the turning section used.

A sequence of swings defines the particle motion. Therefore, the pendulum constants could be modelled as stochastic variables with the same distribution as in figure 2.23, so that the simple pendulum model would become more realistic.

2.4.6 Simple Pendulum Approach: Transition Motion

The aim of this section is to extend the 2D pendulum equations so that particles under 'Transition' descent can also be modelled. In order to do so, the 2D pendulum equation is used as the starting point. Then, an extra equation (eq. 2.15) is added to account for the out-of-motion in the $(X-Y)$ plane occurring in the turning section. Also, a new variable $(\phi(t))$ is introduced to account for the angular frequency about the $z-$axis. Therefore, for trajectories describing a 'Transition' descent, $\phi(t)$ is defined as a step function that changes from 0 during the gliding section to a constant value during each turning section.

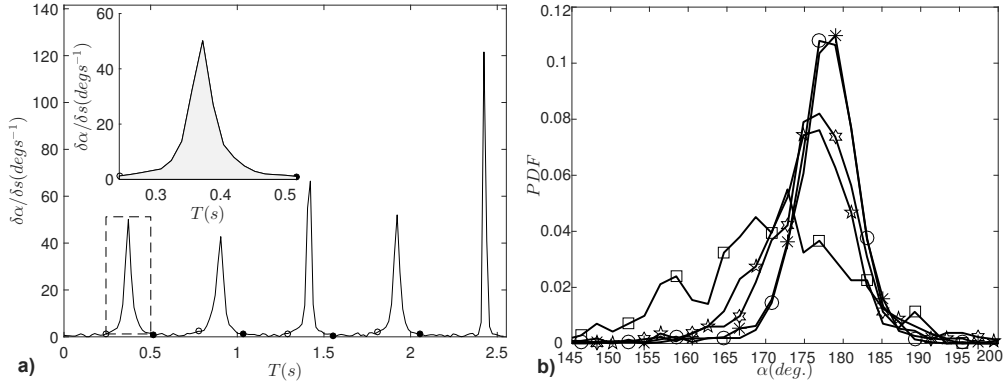

Figure 2.25: a) Measured variation of angle in the $(X-Y)$ plane for a 'Transition' trajectory; b) probability density function of the angle α during the turning points.

	Disk	Heptagon	Hexagon	Pentagon	Square
$\alpha(deg.)$	177	177	176	175	167
$T_{turn}(s)$	0.29	0.29	0.30	0.30	0.31
$\phi(deg/s)$	6.86	5.17	11.13	12.82	26.34

Table 2.9: Mean value of the angle turned during the turning sections (α) and the time T_{turn} associated with this motion.

The angular frequency of the turning section can be measured by obtaining the angle from one gliding plane to the next one and the time taken to perform this motion. The offset angle from one gliding plane to the next one is obtained as the angle between two vectors formed during each oscillation. The first vector connection the midpoint of the oscillation to the extreme of the oscillation and the second vector connecting the extreme with the midpoint of the next oscillation.

The new set of equations that is used to model the 'Transition' motion is as follows,

$$x(t) = L\sin(\theta(t))\cos(\phi(t)\cdot t) \tag{2.14}$$

$$y(t) = L\sin(\theta(t))\sin(\phi(t)\cdot t) \tag{2.15}$$

$$z(t) = -L\cos(\theta(t)) - V_z t \tag{2.16}$$

A limitation of this model is that it assumes that all gliding sections come back to the origin of the imaginary pendulum in the $X-Y$ plane. In here, we integrate the change in direction of the planar $(X-Y)$ velocity along the turning block, as shown in figure 2.25. If the integrated angle, α, is 180 deg the particle reverses its velocity direction to either the same or a parallel plane during the turning section, and this seems to be the case of most of the particles tested, with the squares showing the greatest deviations from the complete turn.

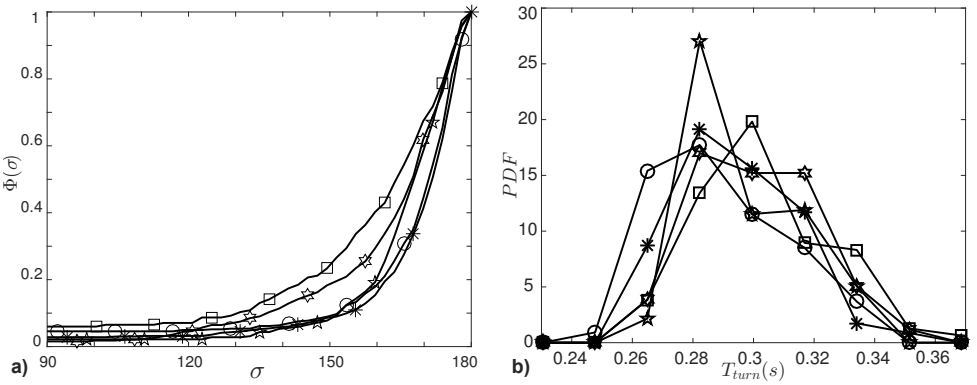

Figure 2.26: a) Cumulative distribution function (CDF) of the angle between two subsequent mean velocity vectors associated with turning sections; b) probability density function (PDF) of the time associated with the turning motion.

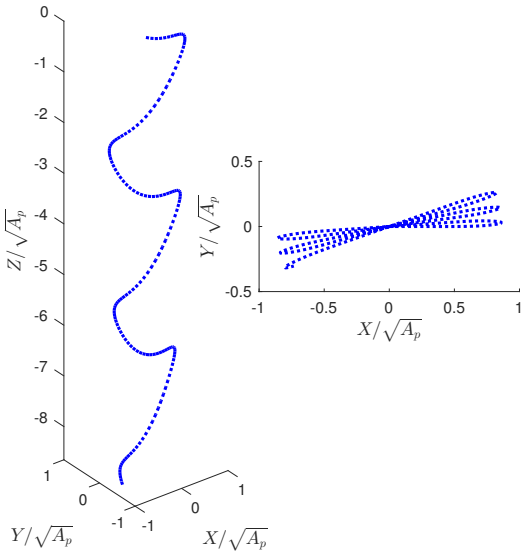

Figure 2.27: 3D trajectory model of a planar heptagon using the 3D Simple Pendulum approach.

It is also interesting to notice that the offset angle between subsequent gliding planes has a severe history effect, and we hypothesize that this is due to the wake dynamics. Thus, all planar particles describe a trajectory that turn either clockwise or anti-clockwise in the $X-Y$ plane during the fall. The cumulative probability in figure 2.26 shows the relevance of this effect, since the history effect would only be broken if the angle between subsequent S_i vectors, shown in figure 2.19 was smaller than 90 deg. This effect is also well captured by the 3D Simple Pendulum Model, as seen in figure 2.27.

2.4.7 Andersen Approach to Planar Flutter

The planar particles oscillate from side to side as they descend. The descent is similar to the descent of a 2D plate, alternating gliding sections that occur at low angle of attack

	Disk	Heptagon	Hexagon	Pentagon	Square
$V_1(mms^{-1})$	114	111	104	101	95
$V_2(mms^{-1})$	59	58	56	57	55
$V_3(mms^{-1})$	41	41	37	36	26
$\Omega(rads^{-1})$	12	12	12	11	11

Table 2.10: Fitted constants for the model in Andersen et al. [2005a].

with fast rotational motion at the turning points. [Andersen et al., 2005b] showed that the trajectory of a 2D plate is well described by a simple curve in the vertical (z) and horizontal (x) axis.

$$x(t) = \frac{V_1}{\Omega}\sin(\Omega t) \tag{2.17}$$

$$z(t) = -V_2 t - \frac{V_3}{2\Omega}\cos(2\Omega t) \tag{2.18}$$

where Ω, V_1, V_2 and V_3 are constants. The constant Ω is the angular frequency of the planar periodic motion, V_2 is the mean descent velocity, and V_1 and V_3 describe the amplitudes of the oscillations in v_x and v_z respectively.

The Simple Pendulum Model and the approach in Andersen et al. [2005b] look similar and the results would be almost identical when $2V_1 = V_3$. However, we strongly believe that the method proposed in this work provides a better insight into the physics of the particle fall, making an analogy between particle inertia and fluid resistance with the restoring force in the pendulum problem.

All measured fluttering planes within each trajectory are projected into the same virtual plane (as a 2D motion), and these trajectories are fitted to equations 2.17 and 2.18. Thus, we obtain the statistics of the variables V_1, V_2, V_3 and these are shown in 2.10. It is interesting to notice that the mean value of the fitted constant V_1 shows a decrease in the amplitude of the planar oscillations as the number of edges decrease. The mean descent velocity is well captured by the fitted constant V_2, showing very similar results to the measured values. Similarly to V_1, the fitted constant V_3 also depicts a reduction in the amplitude of the vertical oscillations with the decrease of the number of edges. All planar particles but squares share a similar probability density function. The wider spread seen in squares suggests a less repetitive secondary motion. This is consistent with the trend in the standard deviation for the descent velocity showed in table 2.6 and the results shown in the frequency domain.

The frequency of the planar ($X - Z$) motion, defined in this model by the motion in the $x-$coordinate, has been shown to be half the frequency of the vertical motion, the $z-$ coordinate. This effect occurs naturally in a simple pendulum where L and θ are independent but the equations of motion are coupled. However for the equations proposed in Andersen et al. [2005b] this issue is solved by changing the angular frequency accordingly (V_1/ω, whereas $V_3/2\omega$).

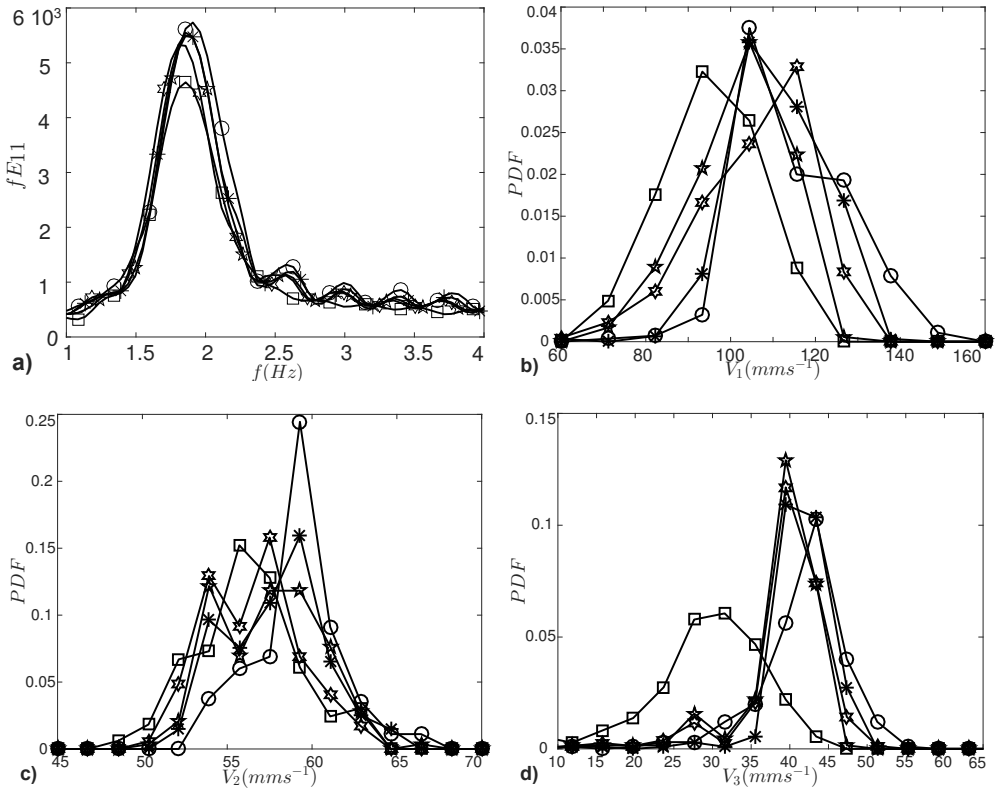

Figure 2.28: Probability density function (PDF) of the frequency content and fitted constants (V_1, V_2, V_3)n of the 'Planar zig-zag' trajectories. The dominant frequency is converted to angular frequency and used as the fourth fitted constant Ω.

2.4.8 Summary

Thin disks falling in a viscous medium have been extensively investigated during the last decade; as reviewed by Ern et al. [2012], and four falling regimes have been found to be sufficient to characterize the main falling styles: steady, fluttering, chaotic and tumbling. This work investigated the effect of decreasing the dimensionless moment of inertia by the change of the shape of the frontal area on the falling motion of a planar particle. According to the phase diagram developed by [Field et al., 1977], all planar particles manufactured are within the fluttering region of the disk, and as firstly assumed, all of them share some common falling dynamics. However, when the characteristics of the fall is investigated in more detail, one can see that the decrease in the dimensionless moment of inertia reduces the likeliness of having a 'Planar zig-zag' descent in favour to a more three-dimensional motion.

We found that the mean descent velocity of planar particles depends slightly on the particle circularity (Q), with this magnitude reducing as circularity does. We also found that all particles tested show a very similar dominant frequency on the descent velocity fluctuations, with the magnitude of these oscillations being dependent on the particle

inertia. Interestingly, we found that planar heptagons are more prone to describe 'Planar zig-zag' trajectories than any other particle even disks. Disks describe 'Planar zig-zag' trajectories almost as often as heptagons; while all other planar particles describe 'Planar zig-zag' trajectories less frequently as inertia reduces. The fact that heptagons show a greater number of these trajectories suggests that there might be a particle area ratio range for which this trend is consistent.

We separated all particle trajectories in three sub-groups according to the importance of the angular frequency about the $z-$axis; 'Planar zig-zag' motion, 'Transition' motion and 'Highly 3D' motion; and we developed a simple pendulum model that can reproduce 'Planar zig-zag' trajectories. This model is found to be consistent with the 2D equations developed by Andersen et al. [2005b] for quasi-two-dimensional plates freely falling in water. The main advantage of the Simple Pendulum model is that it can be easily adapted to approximate the motion of 3D particle motion.

The trajectories that are within the range of $0.2 < a/R_g < 0.6$ can be also modelled with the simple pendulum approach but with a constant value of the variable $\phi(t)$ along the entire trajectory.

Based on the trajectory analysis, a new characteristic length scale ($\ell = D_c/Q$) to determine an equivalent disk is proposed. This depends on the diameter of the circumscribed disk (D_c) and the isoperimetric quotient (Q). Comparison of the $Re - I^*$ phase diagram for circular disks in the literature with the location of planar particles using this new lengthscale shows that equivalent disks with diameter ℓ would undergo the same secondary motions as the planar polygons do. Although the overall tendency is well captured, one can observe that the differences in terms of out of plane motion between some geometries (hexagons and pentagons) in figure 2.20 is not accurately modelled by this approach leading to a large separation between particles in the regime map plotted in figure 2.22. More experiments along these lines would be necessary to establish the limitations of the lengthscale proposed. Despite these potential limitations, this work suggests that it might be possible to reconcile the effects of particle shape using an equivalent disk as long as the particle circularity is accounted for in determining the equivalent disk. An important future step would be to confirm the validity of this new length scale for particles of different sizes and complex shapes such as fractal edges. Similarly, it would be of great interest to extend the work to particles lying within other falling regimes such as the chaotic or tumbling regimes.

We also hypothesise that the wake characteristics goes hand by hand with the descent style of a particle along a given realization. The study of the turbulent wake behind these particles will allow us to show how the unstable particle descent is connected with the wake shedding. Thus, next section is fully devoted to the study of the wake behind n-sided polygons freely falling in water.

2.5 Wake characteristics behind N-sided polygons settling in quiescent flow

This section presents the wake characteristics of various thin particles with identical material properties but different frontal geometries (disks, hexagonal plates and square plates) introduced in 2.4. These are examined by means of three-dimensional measurements of the instantaneous velocity field (V3V 3D3C). This study is based on the combined data of the 3D trajectory reconstruction with instantaneous volumetric velocity fields.

2.5.1 Methods

In water, planar particles (see table 2.11) were released as described in the particle tracking technique section, (section 2.2). In this study, one camera captured a frontal view of the descent motion of the particle whereas the other captured the planar $(X-Y)$ motion of the particle through a mirror at 45 deg underneath the water tank, as in fig. 2.2. A set of 15 trajectories were recorded for the disk, hexagon and square plate and these were fully processed and reviewed to assure the robustness of the results. The waiting time between drops was 20 min, corresponding to more than 600 times the particle time-scale of the oscillatory motion. This waiting time was verified to be sufficient to have quiescent flow by visualising tracer particles with the V3V camera system.

	Disk	Hexagons	Square
A_p (cm^2)	4.34	4.39	4.41
D_c (cm)	2.35	2.6	2.97
P (cm)	7.4	7.8	8.4
Q	1	0.91	0.79
$Mass$ (g)	1.07	1.01	1
$\langle V_z \rangle$ (mm·s^{-1})	58 ± 2	56 ± 3	55 ± 3
σ_{V_z} (mm·s^{-1})	32	28	23

Table 2.11: Characteristics of the particles geometry; A_p refers to frontal area, D_c to diameter of circumscribed disk, P to perimeter of frontal geometry and Q to isoperimetric quotient. Mean descent velocity is $\langle V_z \rangle$ and velocity standard deviation is σ_{V_z}.

2.5.2 Results

In this section, results on the trajectory characteristics and flow visualization of the wake behind the planar particles are presented. First, an introduction to the trajectory

characteristics obtained from the high speed cameras is carried out and the differences between frontal geometries are compared. Second, vorticity iso-surfaces and contours in the wake of the particles are shown for trajectories that are representative of the motion of each geometry.

2.5.3 Trajectory Characteristics

Two views of the particle descent are acquired synchronously so that the 3D position of the particle can be obtained, as shown in figure 2.29. Trajectories are differentiated into three groups according to the degree of out-of-plane motion that they exhibit, as detailed in section 2.4. Thus, 'Planar zig-zag' motion refers to trajectories with two trajectory sections that repeat periodically; gliding sections where the particle oscillates within a $X-Y$ plane and turning sections where the particle shows small deviations from the idealised complete turn of 180 deg in planar velocity direction. Similarly, 'Transition' motion refers to trajectories with the same oscillatory pattern as in 'Planar zig-zag' motion but with a superimposed constant angular velocity about the $Z-$axis. The particle trajectory in the $X-Y$ plane resembles a rhodonea curve, as shown in Zhong et al. [2011] for disks with small dimensionless moment of inertia I^* and in Esteban et al. [2018] for n-sided polygons. Trajectories describing nearly helicoidal motion are named 'Highly 3D' and these have a $X-Y$ footprint composed of a sequence of circles with a finite offset between consecutive loops. These trajectories also show a much more steady descent velocity. This is captured in the descent velocity standard deviation shown in table 2.11.

The mean descent velocity of the particles is shown in figure 2.30 as a function of the

	Disk	Hexagon	Square
I^*_ℓ	$5.01 \cdot 10^{-3}$	$1.95 \cdot 10^{-3}$	$5.13 \cdot 10^{-4}$
Re_ℓ	1370	1450	1620

Table 2.12: Values of the particle Reynolds number (Re_ℓ) based on the mean fall velocity ($\langle V_z \rangle$) and the characteristic length-scale (ℓ); and dimensionless moment of inertia I^*_ℓ based on the length-scale (ℓ).

isoperimetric quotient Q -defined in section 2.3.1-; the magnitude of the mean descent velocity decreasing with the decrease in the axisymmetry of the particle frontal geometry. The vertical error bars show the standard deviation of the mean descent velocity from all realizations.

In Lee et al. [2013], they described how a non-uniform lift distribution over the disk surface can create a lift-induced torque, leading to the disruption of the original planar motion. Following the same reasoning they showed how the dimensionless moment of inertia of the particle (I^*) might either stabilise or destabilise the system depending on

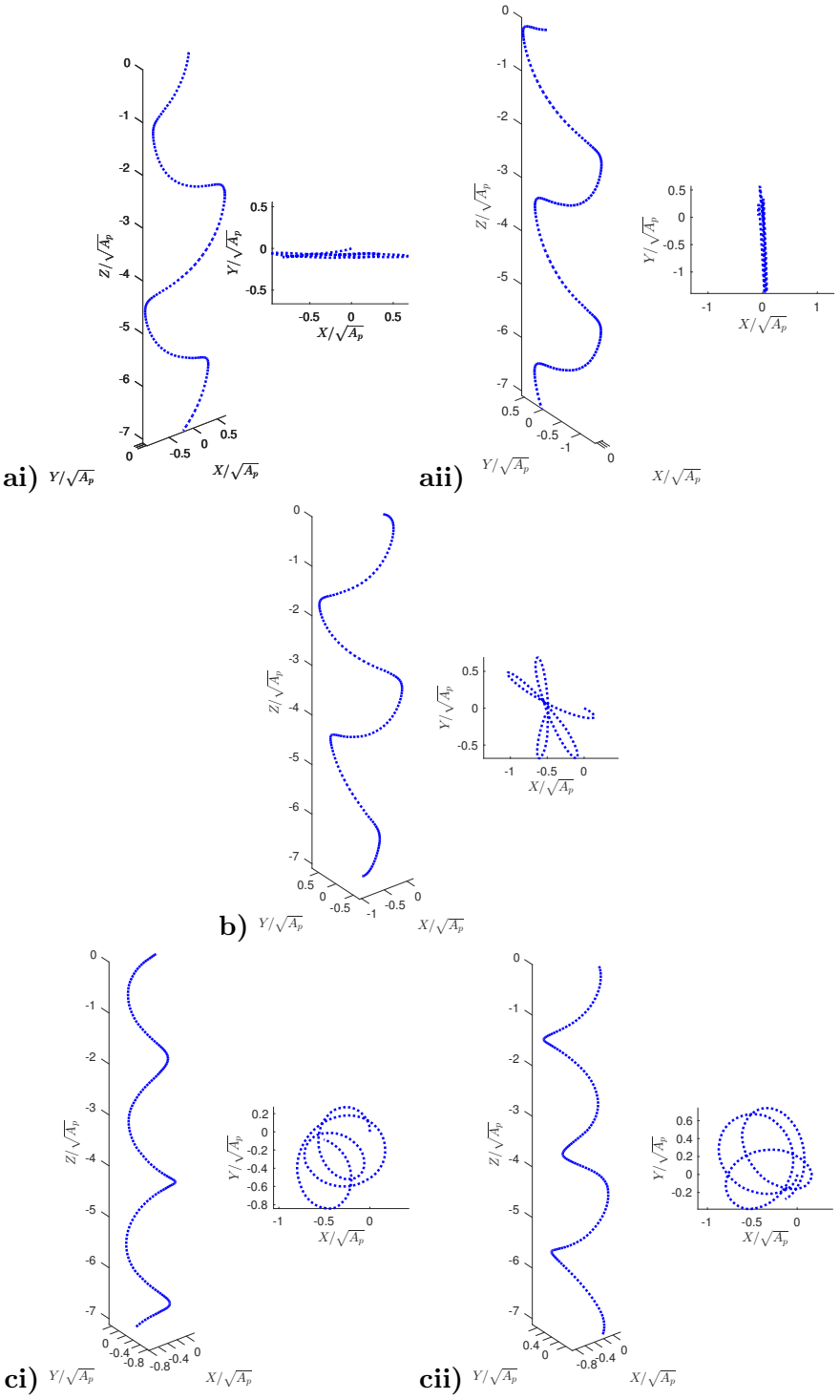

Figure 2.29: 3D Reconstructed trajectory sections of planar particles describing the three regimes proposed. ai) Disk under 'Planar zig-zag' motion; aii) Hexagon under 'Planar zig-zag' motion; b) Hexagon under 'Transition' motion; ci) Hexagon under 'Highly 3D' motion and cii) Square under 'Highly 3D' motion.

its relative magnitude. Therefore, if $I^* < I^*_{crit}$ the system instabilities grow at every turning point, while if $I^* > I^*_{crit}$ the system becomes more stable. The non-uniform

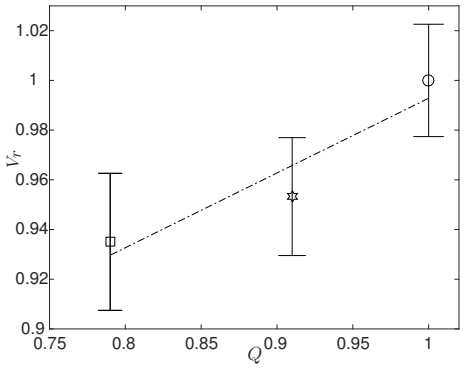

Figure 2.30: Mean descent velocity of planar particles as a function of the isoperimetric quotient (Q). V_r is defined as the ratio of the particle descent velocity to the descent velocity of the equivalent disk.

lift distribution explained in Lee et al. [2013] occurs naturally for particles with non-axisymmetric frontal geometries. We believe this mechanism is the reason why as the particle circularity reduces the likelihood of having a planar trajectory also reduces.

In the following section, the severe in the falling dynamics of particles with different frontal geometry is investigated by means of volumetric flow visualisation.

2.5.4 Wake characteristics

The effect of vorticity in the flow behind the particle is one of the key features to understand the path instability of planar particles. Disks freely falling in viscous media have been extensively investigated during the last 60 years, as in Willmarth et al. [1964], Field et al. [1977], Fernandes et al. [2005], Zhong et al. [2011] or Lee et al. [2013] among others. Fernandes et al. [2005] showed experimentally that the phase difference between the velocity and the inclination of the body axis greatly differs for the irrotational theory estimation, showing that vortical effects in the wake were crucial to understand body dynamics. A few years later, Zhong et al. [2011] showed that thin disks lying in the fluttering domain on the $Re - I^*$ regime map exhibit three different descent styles that are associated with a change in their dimensionless moment of inertia (I^*); i.e. 'Planar zig- zag', 'Transitional', and 'Highly 3D'. The vortex patterns corresponding to the 'Planar zig-zag' and 'Highly 3D' descent were visualized with fluorescence dye. These flow visualizations showed that for the 'Planar zig-zag' motion a pair of hairpin vortices were shed into the wake in each cycle, whereas for the 'Highly 3D' descent they observed a helicoidal vortex evolution. Similarly, Lee et al. [2013] performed flow visualizations with fluorescence dye and planar PIV measurements for disks describing a 'zigzag-spiral-zigzag' intermittency finding the characteristic turbulent structures in the wake of the particle go hand by hand with their descent mode. Thus, disks describing zigzag descent

create a vortex loop elongating in the direction of the body movement to form hairpin-like structures, but as the planar symmetry is broken, disks shed a vortex chain from the outer edge, forming a helicoidal vortex wrapping around the wake region.

To the best knowledge of the authors, this is the first experimental study showing three dimensional three component flow field in the wake of disks, hexagons and square plates under 'Planar zig-zag' and 'Highly 3D' motion. We found severe differences in the wake of a particle describing 'Planar zigzag' motion depending on its location relative to the turning point, whereas for particles describing a 'Highly 3D' descent the wake characteristics is almost unperturbed by the relative position of the particle along the trajectory. This is in accordance with previous experimental studies where the wakes were observed by flow visualization, as in Zhong et al. [2011], and planar PIV, as in Lee et al. [2013]; and also with results from numerical simulations of free falling thin disks for moderate Reynolds numbers, as in Churst et al. [2013].

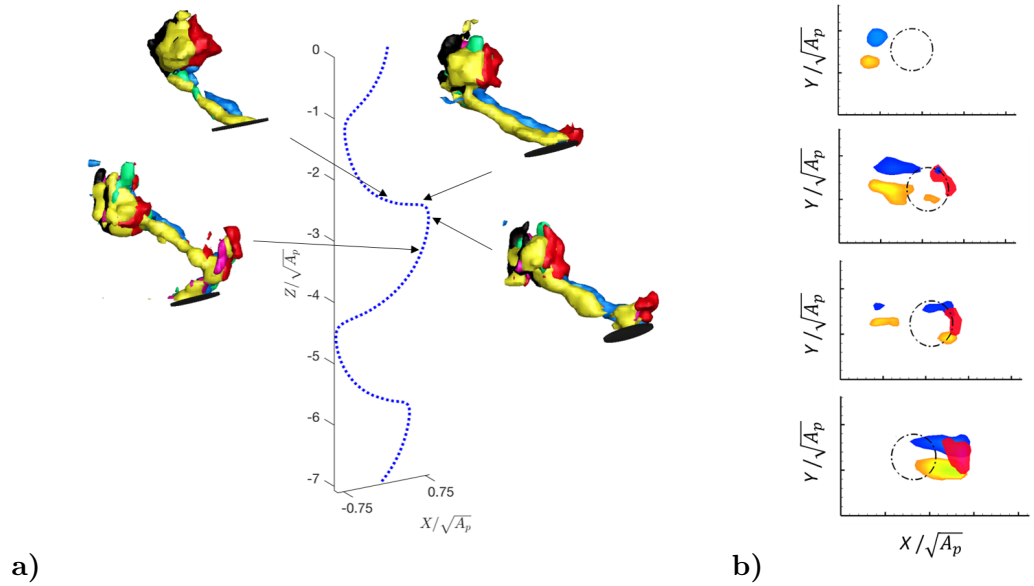

Figure 2.31: a) 3D Reconstructed trajectory section of a disk describing 'Planar zig-zag' motion with vorticity iso-surfaces of the wake behind the disk at different locations relative to the turning point. b) Contour plots of the vorticity magnitude in the $X-Y$ plane at a distance of $\sqrt{A_p}$ from the upper surface of the particle as the same locations. The iso-surfaces have a magnitude of 2.5×10^{-3} s and the contours are also saturated at 2.5×10^{-3} s. Yellow and blue contours represent positive and negative $X-$vorticity, black and red $Y-$vorticity, green and pink $Z-$ vorticity.

Disks

The wake behind a disk describing 'Planar zigzag' motion shows characteristic vortex structures that repeat periodically during the particle descent every gliding and turning

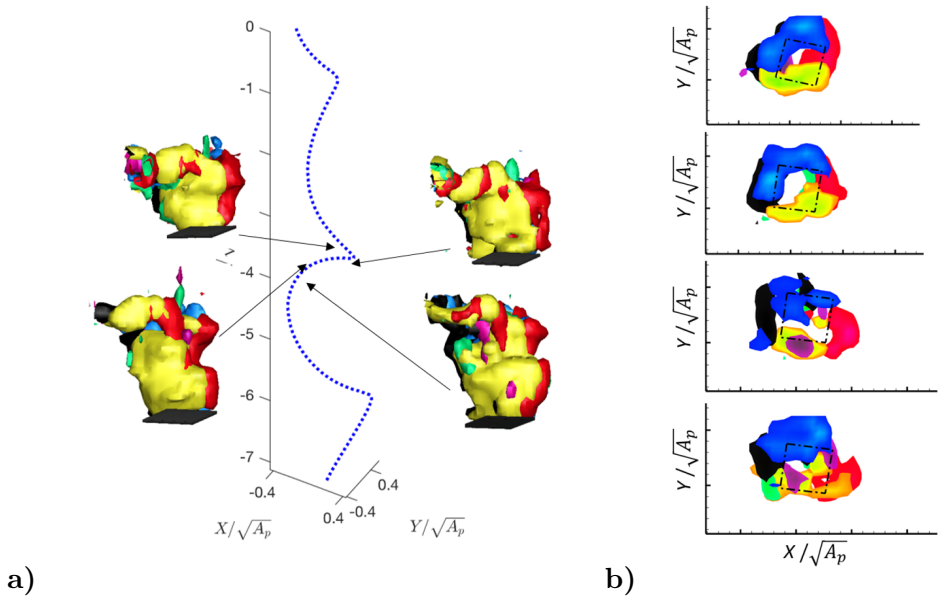

Figure 2.32: a) 3D Reconstructed trajectory section of a square describing 'Highly 3D' motion with vorticity iso-surfaces of the wake behind the hexagon at different locations. b) Contour plots of the vorticity magnitude in the $X-Y$ plane at a distance of $\sqrt{A_p}$ from the upper surface of the particle as the same locations. The iso-surfaces have a magnitude of 2.5×10^{-3} s and the contours are also saturated at 2.5×10^{-3} s. Yellow and blue contours represent positive and negative $X-$vorticity, black and red $Y-$vorticity, green and pink $Z-$vorticity.

section. As the disk describes a gliding section of the trajectory, a pair of counter-rotating vortices progressively forms in the downstream direction from both sides of the symmetry plane of the disk aligned with the gliding motion. These vortices remain primarily aligned with the motion of the disk, as shown in figure 2.31. As the disk approaches a turning event, it decelerates and increases angle of attack. When the angle of attack becomes too high the disk experiences stall (similarly to an aerofoil); and a recirculation zone, whose predominant vorticity is along the normal to the direction of motion, is formed at the leading edge of the disk. Then, the generation of lift reduces, drag increases due to the high angle of attack and the particle planar velocity becomes zero. At this point the disk motion reverses direction and the recirculation zone at the leading edge detaches forming a hairpin-like vortex. Lee et al. [2013] showed two recirculation zones forming, one on the lower surface and another on the upper surface at a similar relative location of the trajectory that eventually merge together and detach also forming a hairpin-like vortex. However, the limited time resolution of the system used in here (7.25 fps) is not sufficient to capture this wake dynamics.

Thus, the complete wake region of the disk includes two rows of hairpin-like vortices evenly space in the vertical direction that carry vorticity in opposite directions; and these are linked by a pair of counter rotating vortices. The vortical structures shed off at every extreme point of the oscillatory motion are responsible for the regions of

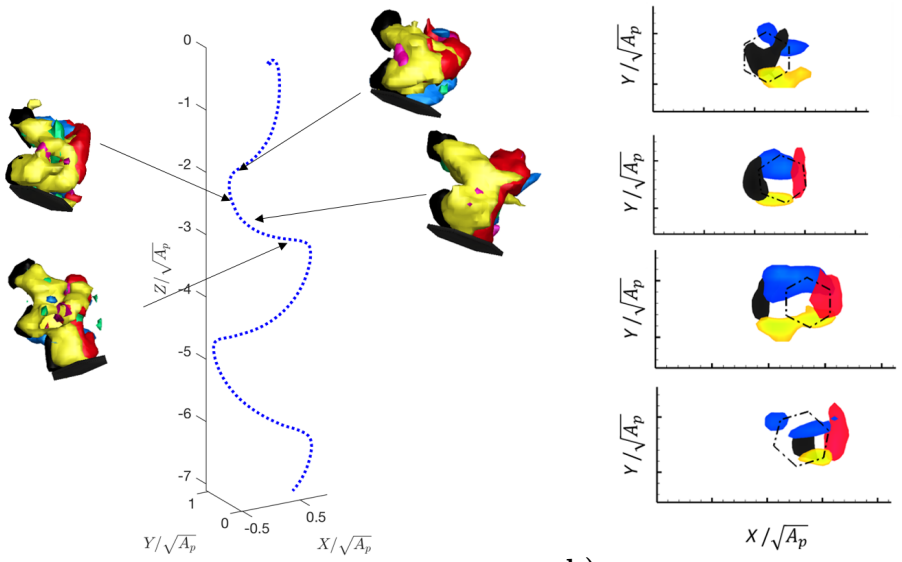

a) **b)**

Figure 2.33: a) 3D Reconstructed trajectory section of a hexagon describing 'Planar zig-zag' motion with vorticity iso-surfaces of the wake behind the hexagon at different locations relative to the turning point. b) Contour plots of the vorticity magnitude in the $X-Y$ plane at a distance of $\sqrt{A_p}$ from the upper surface of the particle as the same locations. The iso-surfaces have a magnitude of 2.5×10^{-3} s and the contours are also saturated at 2.5×10^{-3} s. Yellow and blue contours represent positive and negative $X-$vorticity, black and red $Y-$vorticity, green and pink $Z-$vorticity.

strong downwash in the wake of the disk. The magnitude of the velocity in the region dominated by the downwash is of the same order of magnitude of the descent velocity observed along the disk trajectory.

Square Plates

The wake behind a square plate falling under 'Highly 3D' motion is almost time independent, exhibiting shedding of vortical structures along the perimeter of the particle. The vortex structures are significantly different from those observed in the planar motion of a disk. Here, vortex structures with different dominant vorticity components are formed indistinctly during the descent of the particle, as in figure 2.32. This is primarily because the different edges of the square induce different components of vorticity. Taken together, these different vorticity components give rise to a large-scale vortex blob in the wake during the particle fall. This blob is best visualised by examining the contours in the wake (shown in separate contour plots on the right) taken at $\sqrt{A_p}$ behind the particle. These contours clearly show that there is nearly no difference in the strength of vorticity or a preference to which side of the particle this vorticity is present. It almost seems like the vorticity is axisymmetric, despite the fact that the particle itself is not axisymmetric. This axisymmetry in the vorticity strength is a reflection of the

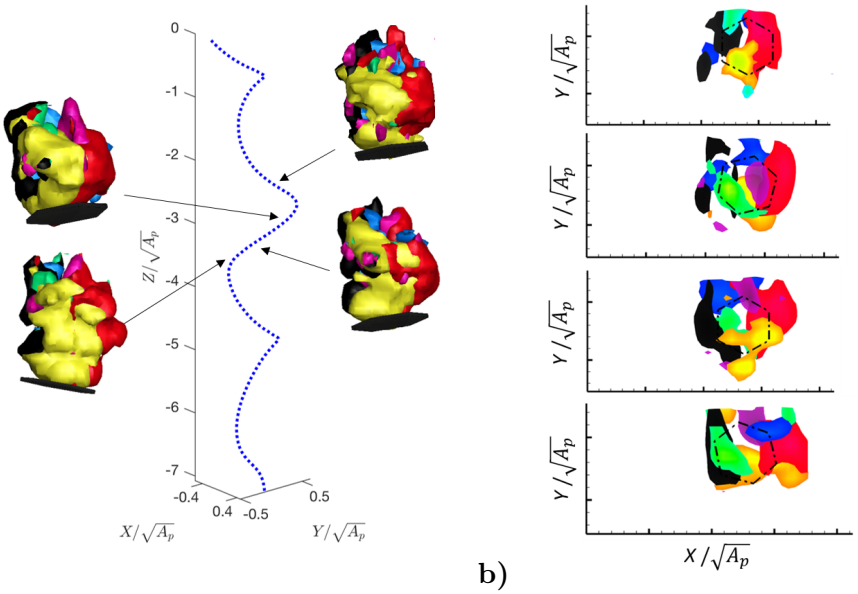

Figure 2.34: a) 3D Reconstructed trajectory section of a hexagon describing 'Highly 3D' motion with vorticity iso-surfaces of the wake behind the hexagon at different locations. b) Contour plots of the vorticity magnitude in the $X-Y$ plane at a distance of $\sqrt{A_p}$ from the upper surface of the particle as the same locations b). The iso-surfaces have a magnitude of 2.5×10^{-3} s and the contours are also saturated at 2.5×10^{-3} s. Yellow and blue contours represent positive and negative $X-$vorticity, black and red $Y-$vorticity, green and pink $Z-$vorticity.

type of motion followed by the square plates. When the square describes a section of the trajectory with any of its corners aligned with the direction of motion, a pair of counter-rotating vortices forms from both sides of the corner, propagating downstream. However, the strong instabilities present in the particle wake quickly realign the particle to a different orientation. In this new orientation, the same phenomenon is repeated. Therefore, the descent of a square particle becomes a series of reorientations all along its trajectory. This process results in the breaking down of individual vortical structures and gives rise to an 'axisymmetric' wake. Further time-resolved measurements are necessary to examine the finer details of this wake formation.

Hexagons

Freely falling hexagons describe both types of trajectories; i.e. 'Planar zig-zag' and 'Highly 3D' motion. When it describes 'Planar zig-zag', the wake behind the particle has some similarities to the wake behind disks previously shown in figure 2.31. The vortex structures shown for disks seem to be present in the wake of the hexagon but the strength of these structure for the hexagons is weaker and therefore not as clearly observed in the iso-surfaces. However, the contour plots taken downstream of the particle (2.33 b) show that the vorticity is preferentially distributed along the perimeter of the

particle just as in the case of the disks. As the hexagon describes a gliding section of the trajectory, two large counter-rotating vortices appear on both sides of the symmetry plane of the hexagon aligned with the motion, yet they are substantially altered by the vorticity generated on the other edges of the geometry. It is hypothesised that when the particle reaches a turning point, the non-uniform pressure distribution along the particle geometry is the reason why the particle rotates about an axis perpendicular to the particle surface and it is realigned towards a different plane of motion. Thus, the hexagon starts a new cycle, following a 'Planar zig-zag' motion but contained in a new oscillatory plane. However, when the hexagon describes 'Highly 3D' descent, see figure 2.34, the wake of the particle resembles the wake shown for square plates, with nearly axisymmetric distribution of vorticity along the particle descent. This is also clear in the contour plots obtained downstream of the particle and the similarities with the wake of a square are clear.

Thus, particles with different frontal geometry; i.e. disks and hexagons; and hexagons and squares, exhibit qualitatively similar wake structures when falling under the same mode. However, the modes of secondary motion for the same initial conditions are not equally probable for all particles, but depend on the particle geometry.

2.5.5 Summary

This work investigated the effect of the particle edge geometry on the free falling motion and associated wake of a planar particle in quiescent flow. The reference particle was a disk that lies within the 'Planar zig-zag' domain in the $Re - I^*$ regime map. The material properties and the frontal area of the particle were maintained constant and the isoperimetric quotient (a measure of the particle circularity) was varied by altering frontal geometry of the particle to different n-sided polygons; i.e. hexagons and squares.

High speed imaging and three-dimensional three component measurements of the instantaneous velocity field were used to characterise the particle trajectory and the associated wake behind the particle. Disks were found to describe 'Planar zig-zag' trajectories most of the time and these were characterised by a sequence of gliding - turning sections. The near wake of disks during the gliding phase is comprised by a pair of counter-rotating vortices that grow from the leading edge of the disk in the downstream direction. In contrast, the near wake during the turning section is characterised by leading edge flow separation whose predominant vorticity is along the normal direction of motion. Thus, when the motion of the disk is reversed the recirculation zone on the upper surface detaches forming a hairpin-like vortex structure that is shed into the wake.

In contrast, squares were found to describe 'Highly 3D' motion more often, with a wake dominated by a large-scale shedding of vorticity along the entire periphery of

the particle. The lack of a preferential vorticity component leads to the characteristic three-dimensional trajectory of these particles.

Hexagons exhibit 'Planar zig-zag', 'Transitional' and 'Highly 3D' motions. When these undergo a 'Planar zig-zag' motion their wake is qualitatively similar to the wake of a circular disk and for 'Highly 3D' motions the wake exhibit large-scale vortex shedding as seen for square particles.

Thus, one could expect to observe similar large vortical structures in the wake of planar irregular particles when describing the same oscillatory motion; i.e. disks and hexagons in 'planar zig-zag'. However, the presence of sharp corners in the perimeter of the particle will inevitably generate small turbulent structures that will differ from one geometry to another.

Further time-resolved measurements would be of great interest since this would provide the community with more detailed information on the wake evolution during the particle fall.

2.6 Conclusion

This chapter summarised the studies carried for planar particles freely falling in quiescent flow. Particle tracking allowed us to obtain general information regarding the trajectory characteristic of freely falling objects. Furthermore, its combination with volumetric flow measurements results in a powerful approach to obtain more detailed information regarding the dynamics of the vortex shedding and its dependence with particle geometry.

Results from 'wavy-edge' particles showed the dependence of the particle geometry on the descent velocity and trajectory style. An empirical drag correlation based on the particle geometry is proposed. We believe that the same approach can be used to obtain 3D statistics of the particle trajectory to integrate the motion of those particles into Monte Carlo type simulations with Lagrangian points.

On the other hand, results from the study of N-sided polygons allowed us to defined a new characteristic length scale (ℓ) for the estimation of an equivalent Reynolds number and dimensionless moment of inertia. This allowed us to used the phase diagram of freely falling disk originally defined by Willmarth et al. [1964] but for other planar particle, reconciling the effects of particle shape. Also, volumetric flow measurements carried on the wake of these particles showed the relevance of the vortex mechanism on the particle trajectory.

Chapter 3

Facility for Turbulence Generation

This chapter presents an experimental facility designed to generate and control turbulence in a laboratory. This consists of a modified version of the random jet array (RJA) proposed in Bellani and Variano [2013] that allows us to generate homogeneous and anisotropic turbulence. Moreover, this zero-mean flow facility can be used to investigate the temporal decay of turbulence without invoking Taylor's hypothesis. Thus, the aim of this chapter is twofold: first present the facility designed and second investigate the evolution of anisotropic turbulence over time and evaluate the spatial confinement effect. Once these two questions are answered we will have the tools to examine how different turbulent flows modify the descent style of large inertial particles; and this, at the same time will give us some insight into the particle behaviour inside Aquavitrum's tank. This chapter is structured as follows; in section 3.1 we introduce zero-mean flow facilities used to generate turbulence and we detail experimental and numerical results on the decay of turbulence with and without confinement effects, in section 3.2 we present the experimental setup and the measurement technique, section 3.3 and section 3.4 show the results for stationary and decay turbulence, respectively, and we conclude in section 3.5.

3.1 Introduction

Turbulent flows encountered in nature and in engineering problems are usually not isotropic; and in the absence of turbulence production, the energy contained in the flow decays over space and time. Therefore, the study of generation and decay of anisotropic turbulence is of paramount importance in furthering the understanding of the physics of these flows. Despite being a 'simple' flow, the generation of homogeneous turbulence in the laboratory has been a matter of investigation over the past several decades. Most studies have attempted to generate homogeneous isotropic turbulence (HIT). Mean

velocity gradients are generally needed for the production of turbulent kinetic energy (TKE) and they usually remain in the flow, introducing a certain degree of anisotropy. Various studies have attempted to reach the high Reynolds numbers that are desired so that the inertial and dissipation range of scales are sufficiently separated. At the same time, most of the experiments and simulations have been carried out for scenarios where confinements effects are mitigated (the largest scales of the flow are considerably smaller to the size of the facility or the Direct Numerical Simulation (DNS) box).

3.1.1 Turbulence in zero-mean flow facilities

The most common manner of generating turbulence in laboratories is by means of a steady flow passing through a grid or mesh. These flows can achieve relatively high Reynolds numbers when using active grids ([Makita, 1991], [Mydlarski and Warhaft, 1996], Mydlarski and Warhaft [1998], [Kang et al., 2003], [Larssen and Devenport, 2011]) or low viscosity fluids ([Kistler and Vrebalovich, 1966], [Bodenschatz et al. [2014]). In these scenarios, turbulence moves with the flow and is homogeneous and isotropic in planes parallel to the grid. However, turbulence generated with these methods exhibits anisotropy in the streamwise velocity component. To overcome this limitation, stationary turbulence has been widely investigated by using stirring devices during the last few decades. These methods use oscillating grids ([McDougall, 1979], [De Silva and Fernando, 1994], [McKenna and McGillis, 2004]) or counter-rotating disks separated by certain distance ([Marie and Daviaud., 2004], [Volk et al., 2006], [Blum et al., 2011]). Although these methods have been improved with optimal mesh sizes, strokes and frequencies of the grid oscillation, the turbulence generated still suffers from large mean flows with $\bar{U} \approx 0.25u'$ (where $\bar{U}$ stands for mean flow and u' for root mean square of the velocity fluctuations). Furthermore, a mechanical system driven by a motor is needed for the grid motion, fact that makes more difficult to build a large scale experimental setup where high Reynolds numbers are desired. Another interesting approach to generate HIT is the usage of loudspeakers symmetrically arranged in a three dimensional volume pointing towards the center of the chamber ([Hwang and Eaton, 2004], [Webster et al., 2004], [Warnaars et al., 2006], [Lu et al., 2008], [Goepfert et al., 2010], [Chang et al., 2012]). The activation of the loudspeakers generate synthetic jets and induce vortex rings that encounter each other in the center of the chamber. The quality of the turbulence reported using this approach is better than using oscillating grids, but the region of interest covers a small volume (for example, a 5 cm radius in Chang et al. [2012]). Similarly, loudspeakers can be substituted by propellers as in Zimmermann et al. [2010] and Dou et al. [2016], but the volume of interest remains a limitation for these systems.

A random jet array (RJA) is a relatively new approach to generate Quasi-HIT with zero mean flow ([Variano et al., 2004], [Lavertu et al., 2006], [Variano and Cowen, 2008],

[Delbos et al., 2009], [Khorsandi et al., 2013]). This device consist of a planar configuration of jets that are turned on and off, randomly and independently, to produce turbulence. The use of a single RJA creates a nearly homogeneous flow with turbulence decay in the direction normal to the plane of jets with negligible mean flow, $\bar{U} \approx 0.1u'$, [Variano and Cowen, 2008]. Additionally, the turbulence generated with this device is reported to have isotropy values of the same order of magnitude that in grid-generated wind tunnel turbulence ($u_1'/u_2' \approx 0.8 - 0.66$) and relatively high Reynolds numbers ($Re_\lambda \approx 314$) [Variano and Cowen, 2008]. Recently, in Bellani and Variano [2013] two RJA were separated by a distance of 162 cm, and faced each other. They used the same firing algorithm as proposed for the case of a single RJA [Variano and Cowen, 2008], resulting in a nearly HIT with a negligible mean flow at the middle region of the tank. At the same time, the isotropy was improved and was reported to be in the range of $0.95 - 0.99$. They also obtained high Reynolds numbers ($Re_\lambda \approx 334$) and a large region of HIT of approximately $0.4 \times 0.4 \times 0.2\,\mathrm{m}^3$. Following a similar approach as in Bellani and Variano [2013], Carter et al. [2016] presented a facility in air consisting of two planar arrays of quasi-synthetic jets (256 in total) creating the largest region of homogeneous turbulence to date. Contrary to what was found in [Bellani and Variano, 2013], they observed anisotropy at large scales for all configurations tested.

In here we aim to modify the design in Bellani and Variano [2013] to create a region of homogeneous but anisotropic (to a certain degree) turbulence; and this will allow us to explore how different turbulent scales decay over time and respond to confinement effects.

3.1.2 Decay of homogeneous turbulence

Together with the generation of turbulence, the study of its natural decay has been a matter of debate during the last century. The energy decay of incompressible turbulent flows is governed by the Navier-Stokes equations;

$$\frac{\partial u}{\partial t} + u\nabla u = -\nabla p + \nu\nabla^2 u \tag{3.1}$$

$$\nabla u = 0 \tag{3.2}$$

Where u is the turbulent velocity, p is the pressure and ν is the kinematic viscosity. Because of we consider homogeneous isotropic (and incompressible) turbulence, the two-point second-order moment tensors of velocity can be expressed in terms of a single scalar function $f(r,t)$, the longitudinal velocity correlation, defined as

$$f(r,t) = \overline{u(x,t)u(x+r,t)}/q(t)^2 \tag{3.3}$$

where r is the separation of the two points, t is the time, u is the velocity component in the r direction, and $3/2q^2$ is the turbulent energy. Similarly, $k(r,t)$, the triple velocity

correlation coefficient, is defined as

$$k(r,t) = \overline{u(x,t)^2 u(x+r,t)}/q(t)^3 \tag{3.4}$$

The dynamical equation connecting these two scalar functions derived by [Von Karman and Howarth, 1938] from the Navier-Stokes equations is given by

$$\frac{\partial(q^2 f)}{\partial t} = q^3(\frac{\partial k}{\partial r} + \frac{4}{r}k) + 2\nu q^2(\frac{\partial^2 f}{\partial r^2} + \frac{4}{r}\frac{\partial f}{\partial r}) \tag{3.5}$$

[Von Karman and Howarth, 1938] showed that completely self-similar solutions of the above equation, if they exist, must be of the form $f(r,t) = \tilde{f}[r/\lambda(t)]$ and $k(r,t) = \tilde{k}[r/\lambda(t)]$; and two constrains $q \times \lambda = const$ and $\lambda\frac{d\lambda}{dt} = const$ must be satisfied, where λ is the Taylor microscale. A power-law decay of the turbulent energy is consequently obtained with the decay exponent equal to one, that is,

$$\frac{3}{2}q^2 \sim t^{-1} \tag{3.6}$$

Although early experiments seemed consistent with this power-law decay, a subsequent study by Compte-Bellot and Corrsin [1966] showed even a better fit to their experimental data with decay exponents in the range 1.1 to 1.4 by adding a virtual time origin to the fit. A more general hypothesis of similarity may be formulated such that the decay exponent is nonequal to 1. George [1992], instead of assigning a self-similarity of the correlation coefficients, assumed a self-similar energy spectrum, $E(k,t)$ and energy transfer spectrum, $T(k,t)$, as follows:

$$E(k,t) = E_s(t)\tilde{E}(k\ell) \tag{3.7}$$

$$T(k,t) = T_s(t)\tilde{T}(k\ell) \tag{3.8}$$

Substituting into the spectral energy equation for isotropic turbulence

$$\frac{\partial E(k,t)}{\partial t} = T(k,t) - 2\nu k^2 E(k,t) \tag{3.9}$$

and enforcing consistency, he found

$$\ell = \lambda \tag{3.10}$$

$$E(k,t)/q^2\lambda = \tilde{E}(k\lambda) \tag{3.11}$$

$$T(k,t)/q^3 = Re_\lambda^{-1}\tilde{T}(k\lambda) \tag{3.12}$$

and an arbitrary decay exponent m, where $Re_\lambda = q\lambda/\nu$ is the Reynolds number based on turbulent velocity (q) and Taylor microscale. With the Re_λ^{-1} modification, any decay

exponent is now consistent. However, this modification implies stronger nonlinear interactions with decreasing Reynolds number, which is not physically reasonable. However, in George [1992] he hypothesized that such a similarity might exist at an early stage of the decay during which the turbulence is still in developing and the nonlinear terms are increasing. After that, possibly another self-similar state that includes the proper decay of nonlinear terms is entered. Thus, it is commonly accepted that a power law decay exists for the turbulent kinetic energy over time, which has the form:

$$q^2 \sim (t - t_0)^m \tag{3.13}$$

where $q^2 = u_1'^2 + u_2'^2 + u_3'^2$ is twice the turbulent kinetic energy, m is the power law exponent and t_0 the temporal virtual origin. Early values of m obtained experimentally in Compte-Bellot and Corrsin [1966] led to the present consensus that $m \leq -1$. From later experimental studies, as in Uberoi and Wallis [1967], Ling and Wang [1972] or el Hak and Corrsin [1974], other m values were obtained, ranging from -1 to -1.75.

Wind tunnels equipped with conventional passive grids, fractal passive grids and active grids have been extensively used to investigate the decay of quasi-homogeneous turbulence along stream-wise direction of the wind tunnel test section. However, in all these experiments, the temporal decay of turbulence is modelled as a function of downstream distance invoking Taylor's hypothesis [Taylor, 1938]. Lavoie et al. [2007] investigated whether the initial conditions can affect the decay exponent m of approximately homogeneous isotropic turbulence. They carried wind tunnel experiments with four different conventional passive grids and two test sections and did not find any significant effect of initial conditions on the decay exponent m. However, experimental results obtained from multi-scale grids in Krogstad and Davidson [2011] and further analysed in Valente and Vassilicos [2012] showed that the decay of approximately homogeneous turbulence remains dependent on the inflow conditions far downstream from its generation. Therefore, the decay exponent m changes when the turbulence-generating grid is modified $(1.15 - 1.25)$, [Valente and Vassilicos, 2012]. They believe that multi-scale wake interactions in the near-field of the turbulence-generating grid remain in the flow very far downstream and are responsible for the change in the decay exponent. Similarly, Hearst and Lavoie [2014] performed wind tunnel experiments with a square-fractal element grid at farther downstream locations than previous studies and showed that a classical power-law decay region exists with exponents $m = -1.37$ and $m = -1.39$ for Reynolds number based on the integral length scale $Re_L = 65000$ and $Re_L = 57000$, respectively. The decay in the near-field region $(x/L < 20)$ also followed a power-law evolution but with much higher decay exponents $m \approx -2.79$, being in accordance with results obtained in Valente and Vassilicos [2011] for multi-scale grids.

DNS of periodic three-dimensional box turbulence have been carried out to investigate the temporal decay of HIT. As in the experiments detailed above, DNS results also give a broad spread of m values for homogeneous isotropic turbulence, as in Huang and

Leonard [1994], de Bruyn Kops and Riley [1998], Wray [1998], Antonia and Orlandi [2004] or Burattini et al. [2006]. More recently, Goto and Vassilicos [2016] carried direct numerical simulations of decaying three-dimensional Navier-Stokes turbulence in a periodic box with values of Taylor length-based Reynolds number ($Re_\lambda = u'\lambda/\nu$, where λ is the Taylor micro scale) up to 300. They combined these results with grid-generated turbulence with $Re_\lambda \approx 350$ to reveal the 'Non-equilibrium dissipation law' for near-field regions. Among the features discovered, they found a critical time when the scaling of the turbulence dissipation changes from the one recently discovered in DNS' of forced unsteady turbulence and in wind tunnel experiments (for near-field) to the classical scaling proposed by Taylor [1935] and Kolmogorov [1941] (for far-field).

Similarly, Meldi [2016] performed numerical calculations based on the eddy damped quasinormal Markovian (EDQNM) model to investigate the signature of production mechanisms in isotropic turbulence. They showed that an exponential decay law can be observed if the intensity of the forcing is sufficiently strong to drive the turbulence dynamics and then the decay is followed by a classical power-law decay. These results are also in good agreement with Hurst and Vassilicos [2007], Mazellier and Vassilicos [2010] and Meldi et al. [2014] who also observed the near-exponential turbulence decay. As exposed in Meldi [2016], "while a power-law evolution of HIT statistical quantities is eventually reached for all the classes of turbulence decay investigated, exponential decay law can be initially observed" since this is governed by the forcing time evolution. An interesting point is also revealed by Meldi [2016] concerning the time-lasting effects of production mechanisms. They suggest that these effects can be significantly larger than the observation time in grid experiments. Therefore, other facilities for which Taylor's hypothesis is not invoked, and data can be taken at later decay times, are of interest to investigate these phenomena.

3.1.3 Confinement effects on decay of homogeneous turbulence

Although many numerical calculations (DNS, EDQNM) investigate the evolution of HIT decay over time, most studies do not continue simulations when the box-size becomes comparable to the integral length scale of the flow. This is because these studies want to avoid non-physical effects that result from meeting this condition in the presence of periodic boundary conditions. Thus, confinement effects due to wall interactions still represent a great challenge in the study of turbulence decay. This aspect is generally referred as turbulence saturation and is very relevant for the analysis of the test case of HIT. When the turbulent flow is unbounded, the exponent leading the evolution of the turbulent kinetic energy, the energy dissipation rate, the integral length scale and the Reynolds number is determined by the turbulence production mechanisms / initial

conditions. However, as the integral scale grows to the size of the box that contains the flow (simulation box-size or facility cross-section) an increase of the decay exponent for the TKE and dissipation rate (ϵ) is expected ($m = -2$ and $m_\epsilon = -3$), as introduced in Skrbek and Stalp [2000] and further discussed in Touil et al. [2002].

Works based on a spectral space approach connect the decay exponent with the energy distribution at very large scales; i.e. they express the decay exponent of the turbulent kinetic energy as a function of the slope (σ) of the energy spectrum at very small wavenumber (k) . The most studied values are $\sigma = 2$ and $\sigma = 4$, since they are related to the general conservation principles and historically used invariant quantities. The former is related to conservation of linear moment and the Birkhoff-Saffman invariant and is referred to as the Saffman turbulence. The latter is associated with the conservation of angular momentum and the Loitsyansky invariant and is referred to as Batchelor turbulence. In Touil et al. [2002], they compared results from DNS, Large Eddy Simulations (LES) and the EDQNM model on the decay of isotropic turbulence on a finite domain. In order to do so, they introduced a low-wavenumber cut-off into the energy spectrum. They used a pseudo-spectral technique with the low-wavenumber cut-off imposed at $k = 2\pi/d$ (d being the size of the box) but otherwise behaving as k^4 ($\sigma = 4$) at small k. An initial power-law decay was observed for all models tested with an exponent $m \approx -1.42$ in agreement with the analytical expression for the model spectrum introduced. Then, the decay exponent increased as the scales of the flow grew during the decay and once the flow was fully saturated a decay exponent $m = -2$ was observed.

On the other hand, most numerical investigations only explore the decay of HIT; yet the initial conditions in wind tunnel experiments are neither homogeneous nor isotropic, and they only become quasi-isotropic some distance downstream from the grid (i.e. far-field of the grid). In Biferale et al. [2003], they carried out a numerical investigation for the decay of three-dimensional anisotropic turbulence. They found that both large and small scales begin to 'isotropize' after roughly one eddy turnover time (t_L) and become fully isotropic (within statistical fluctuations) for $t > 100t_L$. However, small scales showed a much higher degree of isotropy than large scales.

To our best knowledge, the study of Hwang and Eaton [2004] is the only experimental study where a zero-mean flow facility has been used to investigate the effect of natural decaying turbulence. They generated stationary turbulence by using eight synthetic jet actuators on the corners of a cubic chamber. The integral length scale of the flow for forced turbulence was $L = 56\,\text{mm}$, which corresponded to $\approx 1/7$ of the size of the chamber. The relative size of the integral length scale in this setup is in fact considered 'too big' for unbounded flows in classical DNS with a periodic box domain. Unsurprisingly, they found a power-law decay for the TKE in time with an exponent of $m = -1.86$. They suggested a possible weak isotropy during the decay and the initial conditions to

be responsible for the high value of m. However, we believe the saturation effect might have played a crucial role during the decay.

3.2 Experimental setup and measurement technique

3.2.1 Facility Description and firing protocol

The experimental facility is an open glass (bottom and walls) and steel-framed tank of dimensions $200 \times 85 \times 100\,\mathrm{cm}^3$. The origin of the coordinate system is at the center of the tank, x_1 is oriented along the horizontal dimension of the tank (200 cm length), x_2 along the vertical dimension of the tank (85 cm length) and x_3 along the span-wise direction (100 cm length).
The structure holding the water tank is designed so that the center region of the tank ($100 \times 90\,\mathrm{cm}$) is optically accessible from the bottom. The instantaneous velocity vector $\tilde{U}(x_1, x_2)$ is defined to be aligned with the x_1 and x_2 axes at the center of the span-wise dimension. The tank is filled with tap water and is continuously filtered to 5 microns when experiments are not undertaken.
Turbulence is generated by two facing planes of randomly actuated jet arrays, in the same fashion as in Bellani and Variano [2013]. Each plane of jets contain 48 bilge pumps (Rule 24, 360 GPH) arranged in a 8×6 array as shown in figure 3.1. The pumps take in water radially at their base and discharge it axially via a cylindrical nozzle with 1.8 cm inner diameter. Each pump acts as a synthetic jet, in the sense that they only inject momentum to the system, since the pump intake and nozzle are contained within the same volume of fluid. The nozzle outlets are aligned so that they form a Cartesian grid with center-to-center distance (M, as the mesh length of a wind tunnel grid) of 10 cm in both horizontal and vertical directions. The temperature of water while the facility is in operation was monitored and found to change marginally during the experimental runs.
Each plane of bilge pumps (48 units) is connected to a solid state relay rack SSR-RACK48 equipped with quad-core relays SSR-4-ODC-05. Each relay closes a circuit that supplies 12 V and up to 3 A to any specific pump. The relays are triggered by transistor–transistor logic (TTL) signals from a Measurement Computing 96 channel digital output card (PCI-DIO96H) controlled by MATLAB. The firing algorithm we employ to force turbulence is the 'Sunbathing algorithm' originally proposed in Variano and Cowen [2008], and latter investigated in Bellani and Variano [2013] and Carter et al. [2016] among others. This forcing algorithm pertains to the family of stochastic forcing in both space and time. The time durations for each pump to be active or inactive are picked from Gaussian distributions with a characteristic mean and standard deviation for the 'on' and 'off' times. The normal distribution parameters are $(\mu_{on},\sigma_{on}) = (3, 1)$ s., and $(\mu_{off},\sigma_{off}) = (21, 7)$ s., which results in an average of $\phi = 12.5\%$ of the pumps

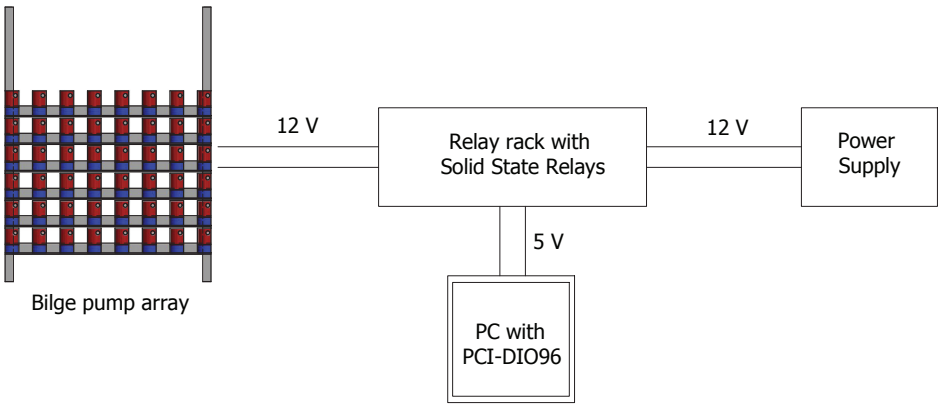

Figure 3.1: Sketch of a bilge pump array (RJA) connection to the SSR-RACK48, PCI-DIO96H and power supply.

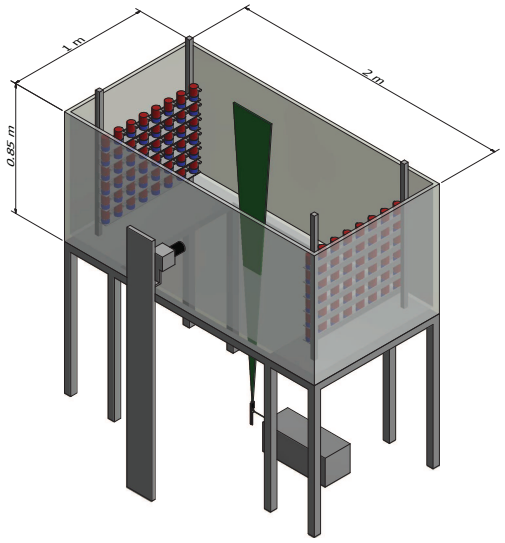

Figure 3.2: Sketch of the water tank equipped with a co-planar arrangement of RJA's and the PIV setup.

being 'on' at any given time. This algorithm was identified in the literature to provide the best turbulence quality in terms of homogeneity and isotropy. The average time for which the tank is operated under the same conditions ($\tau_f = \phi\mu_{on}$) is smaller than the elapse time between subsequent image samples (2 s) and therefore these are uncorrelated in time with the forcing scheme.

3.2.2 Particle Image Velocimetry (PIV) measurements

All measurements are performed along the $x_1 - x_2$ symmetry plane, whose origin is at the center of the water tank. The flow is seeded with $50\,\mu m$ polycrystalline particles. The seeding is mixed in the water tank prior to the experimental run while the jets are randomly actuated to assure an even mixture. The imaging system consist of a dual-pulse Nd:YAG laser (Bernouilli, 532 nm wavelength, 100 mJ/pulse) synchronized with a CCD camera (Imperx 6600×4400 px, $5.5\,\mu m$ px size). The laser beam is shaped into a $3-$mm light sheet (1.5 mm full width at half maximum) via a combination of two spherical and one cylindrical lenses and directed vertically through the glass bottom of the tank. We use a Sigma lens of 110 mm, leading to a magnification factor of ≈ 38 px/mm and a field of view of 110×160 mm on the $x_1 - x_2$ symmetry plane. An external synchronizer that allows variable pulse separation (dt) is used to trigger the laser and camera system. The pulse separation time is chosen such that the average particle displacement is limited to $4 - 6$ px. This low particle displacement is necessary to reduce out-of-plane loss of particles. The velocity fields are obtained using DaVis, with a sliding minimum intensity background subtracted from every image prior to the velocity processing. The image processing is done by using an iterative cross-correlation algorithm with one refinement and three passes (32×32 px first pass and 24×24 px second and third pass) with a 75% overlap. A Gaussian fitting function is used to determine sub-pixel displacement. The sampling frequency is 0.5 Hz, and we acquire 1250 pair of images for stationary forced turbulence.

Vector validation is based on signal-to-noise ratio and deviation from the median of the neighbouring vectors. Non-valid vectors are less than 4 % and are later interpolated from neighbouring vectors.
The random error on the statistics associated with the finite number of samples is smaller than 3% for the mean and for the root mean square velocity fluctuations, based on a 95% confidence level. We choose the sampling frequency of 0.5 Hz to guarantee full statistical independence of the realizations, given that the typical large eddy turnover time is $t_L \approx 1.5$ s. In the presentation of the results, the velocity measured $\tilde{U}_i$ is decomposed into the spatial averaged velocity U_i and velocity fluctuations u_i, such that $\tilde{U}_i = U_i + u_i$. The prime symbol stands for root mean square of the velocity fluctuations, defined as $u_i' = \sqrt{\langle \overline{u_i^2} \rangle}$; and the operators $\bar{\cdot}$ and $\langle \cdot \rangle$ indicate ensemble average and spatial average, respectively. The sub-index 1 and 2 stand for the velocity components along the horizontal and vertical direction, respectively.

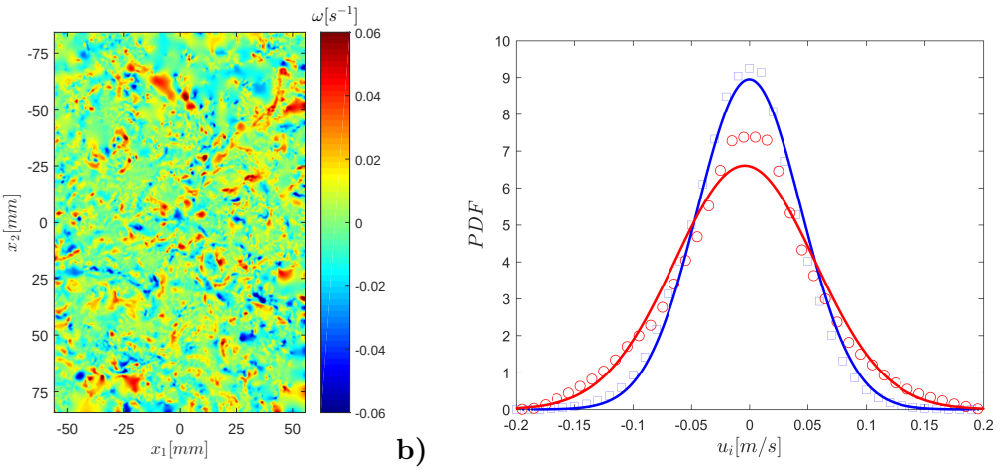

Figure 3.3: Instantaneous realization of out-of-plane vorticity a). Distribution of horizontal and vertical velocity fluctuations represented with circles and squares respectively. The solid lines represent the best fitted normal distribution b).

3.3 Results for Stationary Turbulence

3.3.1 Single-point statistics and flow quality

The statistics of the 'Sunbathing algorithm' for stationary turbulence are investigated using $2D$ PIV data, as aforementioned. Figure 3.3 a) shows a snapshot of the turbulent flow at the center of the water tank, visualized by means of out-of-plane vorticity. Besides, the probability density function of the horizontal and vertical velocity fluctuations (u_i) are shown in figure 3.3 b) (1250 pairs of images). The ensemble average of the in-plane mean velocity yields a value of $(\bar{U}_1, \bar{U}_2)$=(3.6, 1.5) mm/s. This is one order of magnitude smaller than the velocity fluctuations and consistent with other results in the literature; [Bellani and Variano, 2013], [Carter et al., 2016].

These two quantities, mean and velocity fluctuations, are characterized by having an homogeneous distribution that spans to all the region investigated in here.
The homogeneity deviation is used to evaluate the spatial variation of the rms velocity fluctuation as

$$HD = \frac{2\sigma_u}{u'} \tag{3.14}$$

where σ_u is the spatial standard deviation of the ensemble average of the velocity fluctuations ($\sqrt{\overline{u_i^2}}$), whereas the factor 2 warrants a 95 % confidence interval. HD is less than 0.1, showing good flow homogeneity in the domain investigated.
Similarly, the mean flow factor is used to show the strength of the mean flow in relation to the velocity fluctuations;

$$MFF = \frac{|\overline{U}|}{u'} \tag{3.15}$$

This flow factor is 0.012 showing the low relative strength of the mean flow in relation to the velocity fluctuations.

The strain-rate factor compares the strain within the ensemble average of the velocity fluctuations with the strain in the fluctuating velocity field as:

$$MSRF = \left\langle \frac{\frac{\partial \overline{u_1}}{\partial x_1}}{\sqrt{\overline{s_{11}^2}}} \right\rangle \tag{3.16}$$

where s_{11} is the longitudinal component of the fluctuating strain-rate tensor $s_{ij} = \frac{1}{2}\left(\frac{\partial u_i}{\partial x_j} + \frac{\partial u_j}{\partial x_i}\right)$. The velocity gradient $\partial\overline{u_1}/\partial x_1$ is verified to be the largest among the measured components of the ensemble average velocity gradient tensor. Therefore, the value of $MSRF = 0.043$ confirms the low level of mean flow strain compared with its fluctuating counterpart.

3.3.2 Multi-point statistics and flow scales

Two-point correlation functions are used to investigate turbulent integral length scales (L_{ij}) and Taylor microscale (λ_1,λ_2). The normalized correlation function is defined as:

$$\rho_{ii}(r) = \langle \overline{u_i(x+r)u_i(x)} \rangle / \langle \overline{u_i^2(x)} \rangle \tag{3.17}$$

being independent of the position vector x for homogeneous turbulence. The integral length scale that characterizes the velocity fluctuations u_i over separations aligned with the position vector x_j is obtained as:

$$L_{ij} = \int_0^{r_0} \rho_{ii}(r_j) dr \tag{3.18}$$

where r_j represents the separation in the direction x_j and r_0 is the first zero-crossing of the correlation function. The experimental data allows us the integration up to a distance of 16 cm. We extrapolate the tail of the correlation function using an exponential fit up to a value of $\rho_{ii}(r_j) = 0.005$ and found an integral length scale $L_{11} \approx 9.1$ cm for the horizontal velocity fluctuation along the longitudinal direction. This result show that the correlation function from the experimental data only resolves the flow to distances $r_1 < 2L_{11}$ and therefore, this magnitude should be taken as an estimate. Figure 3.4 shows the correlation function of the horizontal and vertical component of the velocity fluctuations along the longitudinal and transverse direction, with the vertical broken line marking the start of the extrapolation region.

Table 3.1 shows that large scales have significant anisotropy, with an integral scale ratio $L_{11}/L_{22} \approx 1.6$. There are several differences between the setup presented in here and the one in Bellani and Variano [2013] that introduce large scale anisotropy. The bilge pumps in Bellani and Variano [2013] are mounted horizontally with a 90^o elbow attached to the original cylindrical nozzle of the pump. This increases the size of the orifice from 18 to

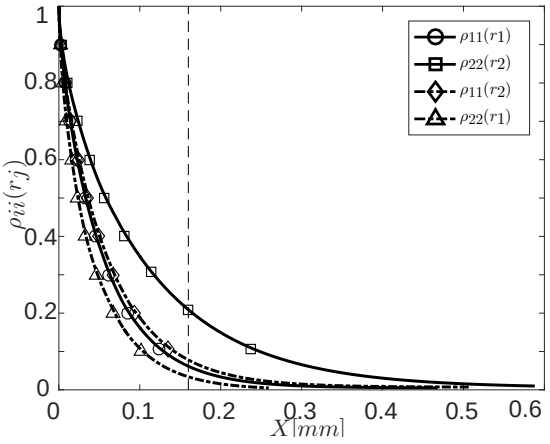

Figure 3.4: Longitudinal and transverse two-point correlation for the 'Sunbathing algorithm' firing scheme, where the vertical broken line shows the start of the extrapolation.

HD	MFF	MSRF	$u'_1[\times 10^{-2} ms^{-1}]$	$u'_2[\times 10^{-2} ms^{-1}]$	$L_{11}[cm]$	$L_{22}[cm]$	$\lambda_1[mm]$	$\lambda_2[mm]$	Re_{λ_1}
0.049	0.012	0.043	5.36	4.42	9.1 $\pm$0.1	5.6 $\pm$0.1	11	9.6	587

Table 3.1: Main turbulence statistics for the 'Sunbathing algorithm'.

21.9 mm and also modifies the components of the momentum introduced in the system, introducing strong secondary flows as detailed in Hellström et al. [2013]. The size of the water tank in Bellani and Variano [2013] is larger than the one presented in here, they use mesh grids in front of the RJA and the working distance between RJA is slightly larger. Similarly, we observed that the turbulence generated in their facility shows a relatively small mean velocity fluctuation and therefore Reynolds number compared with the one presented in here. It is also interesting to note that the water pump flow rate is proportional to the current supplied and therefore, small differences in power supplies can lead to differences in the flow generated. In here, the power supplied to the water pumps was verified to give the maximum flow rate.

On the other hand, in the thorough study of Carter et al. [2016], they observed similar values of large scale anisotropy as in here and suggested that an excess of stream-wise momentum was carried by their pressurized nozzles. They investigated the spacing between arrays of jets, the effect of passive grids and the spacing between working jets (M) and found that the large-scale anisotropy was almost unaffected. Therefore, we believe the excess of stream-wise momentum is also the cause of the large-scale imbalance in our facility.

The Taylor length scale is obtained by fitting a parabola to the three first uncorrelated points of the correlation function (excluding the origin). Then, the crossing point of the parabola with the $x-$axis defines the length of this turbulent scale, whereas the crossing of the parabola with the $y-$axis defines the 'true' rms velocity and also gives a measure

$\epsilon = C_\epsilon u'^3/L_{11}$	ϵ (Unfiltered)	ϵ (3η filter)	SFT
0.86	2.09	1.48	1.42-1.36

Table 3.2: Dissipation rate estimates. The direct estimate of ϵ from the unfiltered and filtered data comes from eq. 3.19; SFT stands for Structure Function Fit. Dissipation rate in $[m^2 s^{-3} \times 10^{-3}]$

of the random noise introduced during the PIV processing [Adrian and Westerweel, 2011], of $\approx 5\%$ in here.

To calculate the Kolmogorov scales of the flow, a reliable estimation of the turbulent kinetic energy dissipation rate is needed. To do so, first we evaluate the flow isotropy at small scales by comparing the velocity gradients of the 2D PIV data after applying a Gaussian smoothing of 3η as proposed in Ganapathisubramani et al. [2007]; i.e. $2\frac{\partial u_i}{\partial x_i} = \frac{\partial u_i}{\partial x_j}$ for isotropic turbulence. We observe that for forced stationary turbulence, the ratio of longitudinal to transverse velocity derivatives does not correspond to isotropic turbulence. In contrast, we observe an average ratio of $1.3\frac{\partial u_i}{\partial x_i} \approx \frac{\partial u_i}{\partial x_j}$ for both velocity components; i.e. $i \neq j$. Therefore, based on this result and the axisymmetric nature of the jet forcing around the x-axis reported in previous studies [Alvarado et al., 2016, Bellani and Variano, 2013, Carter et al., 2016, Variano and Cowen, 2008], we estimate the TKE dissipation rate following the equation derived in George and Hussein [1991] for local axisymmetric turbulence,

$$\epsilon = \nu \left[-\langle \overline{s_{11}^2} \rangle + 2\langle \overline{s_{12}^2} \rangle + 2\langle \overline{s_{21}^2} \rangle + 8\langle \overline{s_{22}^2} \rangle \right] \tag{3.19}$$

where s_{ij} is the fluctuating strain rate. The presence of noise in high-resolution PIV data rapidly increases the error in the dissipation rate leading to an overestimation of this parameter, as demonstrated by Saarenrinne and Piirto [2000]. The PIV data we use resolve all spatial scales of the flow, with a vector spacing $\Delta x \approx 0.9\eta$. However, the strong out-of-plane motion inherent of this facility increases the error associated with random experimental noise and consequently, dissipation rate for which the velocity gradients are calculated will be affected, as investigated in Tanaka and Eaton [2007] for sub-Kolmogorov PIV resolution and in de Jong et al. [2009] or Buxton et al. [2011] for $\Delta x > \eta$. To reduce the effect of noise in the direct estimation of the TKE dissipation rate, we apply a Gaussian filter to the velocity field with a kernel size 3η. This filter size in space -introduced in Ganapathisubramani et al. [2007]- is equivalent to a frequency filter of $1.75 f_\eta$ for point measurement techniques, identified in Antonia et al. [1982] as the optimum setting to capture velocity gradients accurately. The dissipation estimate can be also based on the scaling argument $\epsilon = C_\epsilon u'^3/L_{11}$, where C_ϵ is a constant of order unity [Sreenivasan, 1984]. Later results from DNS simulations of forced homogeneous isotropic turbulence in Sreenivasan [1998] and Burattini et al. [2005] found the value for C_ϵ (in their paper, it is represented as A) to be ≈ 0.5 for $Re_\lambda > 200$. Here, we

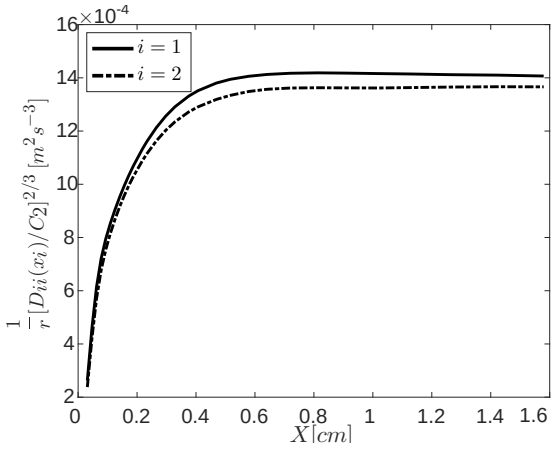

Figure 3.5: Longitudinal structure functions for both unfiltered velocity components, compensated as in eq. 3.21 to estimate TKE dissipation rate from the plateau value.

use $C_\epsilon = 0.5$ to estimate the dissipation rate in table 3.2, although this approach seems to underestimate TKE dissipation rate severely. The results obtained from the scaling argument and direct measure of the TKE dissipation rate are compared against the value obtained from the structure function fitting method. This is based on the relationship between the velocity structure functions and the dissipation rate invoking Kolmogorov's second similarity hypothesis [Kolmogorov, 1941] in the inertial sub-range. In here, we use compensated second-order structure functions. Second-order structure functions are defined as

$$D_{ii} = \langle \overline{[u_i(x+r) - u_i(x)]^2} \rangle \tag{3.20}$$

For homogeneous isotropic turbulence and separation values r_i within the inertial range and aligned with the velocity component u_i, Kolmogorov's theory states:

$$D_{ii}(r_i) = C_2(\epsilon r_i)^{2/3} \tag{3.21}$$

Thus, the compensated longitudinal second-order structure function in eq. 3.21 can be used to find the magnitude of the TKE dissipation rate. This is obtained by looking at the plateau value reached in the inertial range. The measure of dissipation rate with this method was considered in de Jong et al. [2009] as the most robust indirect method and has been extensively used in zero-mean flow facilities, [Bellani and Variano, 2013], [Carter et al., 2016]. The TKE dissipation rate estimates obtained from the longitudinal structure functions from both velocity components in figure 3.5 agree within a few percent, giving a TKE dissipation rate of $\epsilon \approx 1.4 \times 10^{-3}\,\mathrm{m^2 s^{-3}}$. Furthermore, this value is in good agreement with the dissipation estimate obtained from equation 3.19 after applying a Gaussian spatial filter to the velocity fields of $\approx 3\eta$ kernel size, which gives a value of $\epsilon = 1.48 \times 10^{-3}\,\mathrm{m^2 s^{-3}}$. As discussed in de Jong et al. [2009], the effect of the interrogation window size or the spatial filtering of the velocity field for the structure function fitting method is not as severe as in the direct methods. Velocity

ϵ (3η filter) $[m^2 s^{-3} \times 10^{-3}]$	η [mm]	τ_η [ms]	u_η [mms^{-1}]
1.48	0.1615	26	6.2

Table 3.3: Dissipation rate estimate and Kolmogorov scales, η refers to length scale, τ_η to time scale, and u_η to velocity scale.

differences in the structure function are calculated over much larger separation distances and therefore, the noise effect is attenuated. In view of the good agreement between the direct measure of turbulence and the structure function method, we favour the direct measure, from which Kolmogorov scales are obtained and included in table 3.3.

3.4 Results for decaying turbulence

The water tank was actively stirred using the 'Sunbathing algorithm' for both RJA's for a period of 5 minutes until the turbulence level reached a 'stationary' state. Then, all pumps were turned off simultaneously with the start of the $2D$ PIV system. This procedure was repeated so that seventy five data runs were ensemble averaged to obtain statistics for data sets of 40 image pairs each. The first data point is taken right after the actuators were turned off, corresponding to forced turbulence. The remaining data points were taken at intervals of 2 s for the first 20 image pairs (up to $t = 40$ s) and then at logarithmic spaced intervals from $t = 40$ s to $t = 400$ s. The pulse separation (dt) for the first pair of images was 2 ms and logarithmically increased up to 36 ms for the last image pair to maintain maximum displacements of $4 - 6$ px. as turbulence decayed.

Time evolution of turbulence statistics were investigated and time was made non-dimensional ($t^* = t/t_L$) with the characteristic eddy turnover time ($t_L = L_{11}/u'$) of the 'stationary' case. It is common to use a least-squares method to fit the experimental data of q^2 to equation 3.13. However, rather than treating t_0 as a free parameter, Hearst and Lavoie [2014] proposed to insert a range of values for the virtual origin t_0 into the power-law to latter determine m. There is also significant ambiguities associated with identifying the appropriate t_{min} that marks the beginning of the power-law decay range. It is generally accepted that in wind tunnel experiments, a distance of $30\,L_{11}$ downstream of the mesh is sufficient to be in the 'far-field' of the decay regime where turbulence has fully developed. However, in this turbulent flow it is not clear the time that must elapse before the turbulence fully develops. In here, we used the technique described in Hearst and Lavoie [2014] to overcome the ambiguity associated with this unknown, and it is as follows:

- A linear fit using a least-square regression algorithm is applied to equation 3.13 for virtual origins over a range of $-2 < t_0 < 2$ in increments of 0.5. At the same

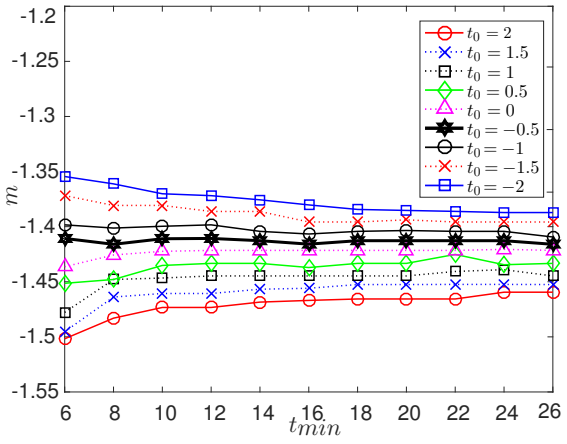

Figure 3.6: Variations of the exponent of the decay m with various t_{min} for a set of virtual origins t_0. These results correspond to the far-field data for q_v^2. The black thick line indicates the algorithm's chosen solution.

time, for each t_0, the power-law is estimated for various t_{min}. Doing so, a matrix of m values is generated where one dimension represents the dependence of m on t_0 and the other on t_{min}.

- The virtual origin t_0 is selected by choosing the value that gives the lowest standard deviation of m relative to its mean for all choices of t_{min}, indicating that the power-law is constant over the largest period of time.

- The root-mean-square deviation is then calculated between the data and the power-law fit for each possible choice of t_{min}. Then, t_{min} is chosen such that this parameter is minimized.

The above technique was applied to the experimental data of q^2, $q^2_{u_1'}$ and $q^2_{u_2'}$. Figure 3.6 shows the variation of m with t_{min} for different values of t_0 for $q^2_{u_2'}$. The uncertainties on the power-law parameters are $t_0 \pm 0.5$ and $m \pm 0.01$ and table 3.5 shows the results of the power-law fitting process. Fits are made to the near-field ($t^* < 10$) and far-field ($t^* > 8$) with a region of overlap of about two eddy turnover times. An additional fit is made for the decay on the saturation regime; $t^* > 40$ for $q^2_{u_1'}$. We also evaluate the uncertainty of the decay coefficients due to the statistical convergence of the 75 runs. We investigate the decay coefficient of ensemble averages of 45 and 60 randomly picked cases using a pseudo-random algorithm implemented in Matlab. We find that the deviation of the decay coefficient m for the ensemble averages of 45 cases is within 5% of the complete set and it reduces to 3% for ensemble averages of 60 cases. Thus, we propose to use the deviation in the ensemble average of 60 cases as the maximum uncertainty in the determination of m for the 75 cases.

First, we investigate the decay of q^2 under the assumption of axisymmetric turbulence; $q^2 = {u_1'}^2 + 2{u_2'}^2$. In figure 3.7 one can see that the near- and far-field fit clearly differ. The decay exponent found for the near-field ($m \approx -2.3$) is similar to the values obtained

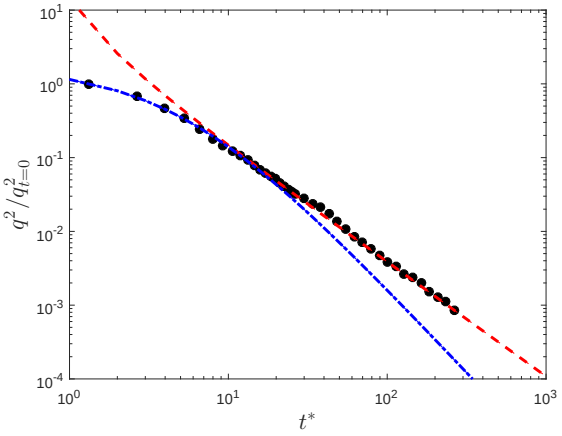

Figure 3.7: Time evolution of non-dimensional turbulent kinetic energy during the decay; $q^2/q^2_{t=0}$. The dashed-dotted line represents the near-field and the dashed line the far-field. Details about the fitting procedure are in included in this section and the fitted parameters are shown in table 3.4.

Quantity	Decay Range	Decay type	m	t_0
q^2	$t^* < 10$	Near-Field	-2.3	-5
q^2	$t^* > 8$	Far-Field	-1.55	0.5

Table 3.4: Fitted constants for the power-law decay of q^2. Near-field and far-field fits are made for data at $t^* < 10$ and $t^* > 8$, respectively.

in fractal-element grids for regions close to the grid where turbulence has not fully developed; $m \approx -2.5$ in [Valente and Vassilicos, 2011] or $m \approx -2.8$ in Hearst and Lavoie [2014] among others. In contrast, the far-field decay shows a decay exponent ($m = -1.55$) slightly higher that previous wind tunnel experiments ($m \approx -1.39$ in Hearst and Lavoie [2014] or $m = [-1.15, -1.25]$ in Valente and Vassilicos [2012]) and DNS studies ($m = [-1.19, -1.39]$ in Burattini et al. [2006]).

We hypothesise that the value of the decay exponent might be affected by the confinement of turbulence. Therefore, to investigate this phenomena we compare the evolution of each velocity component separately, i.e. $q^2_{u'_1} = {u'_1}^2$ and $q^2_{u'_2} = {u'_2}^2$. These magnitudes are made non-dimensional with $q^2_{t=0}$.

Figure 3.8 shows that both the near-field and far-field of the $q^2_{u'_2}$ decay can be well captured using their corresponding virtual origins and decay rates. We believe the near-field region is dominated by the turbulence production mechanism and therefore might be strongly facility-dependent. The decay exponent found for the near-field ($m \approx -2.3$) is consistent with the result from q^2 presented before. In contrast, the decay exponent found in the far-field regime ($m \approx -1.4$) is closer to the results previously exposed from wind tunnel experiments. This result also agrees with numerical calculation studies for which values of $m \approx -1.4$ have been obtained for Batchelor turbulence; [Meldi and Sagaut, 2017].

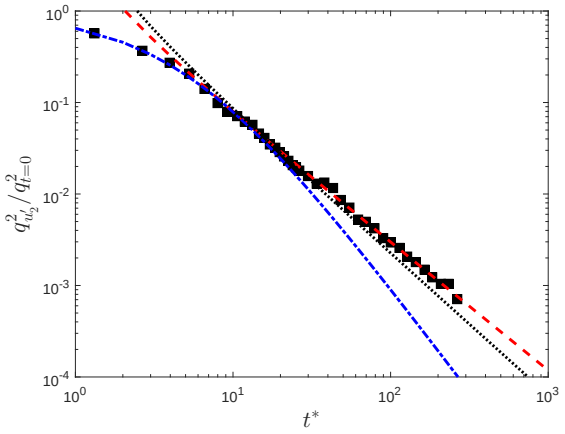

Figure 3.8: Time evolution of the non-dimensional turbulent kinetic energy from vertical velocity fluctuations ($q^2_{u_2'}/q^2_{t=0}$) during the natural decay. The dashed-dotted line represents the near-field, the dashed line the far-field and the dotted line the far-field fit of q^2 for comparison. Fitted parameters are shown in table 3.5.

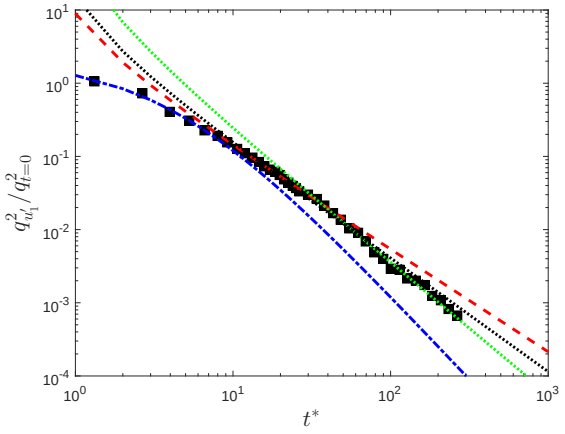

Figure 3.9: Time evolution of the non-dimensional turbulent kinetic energy from horizontal velocity fluctuations ($q^2_{u_1'}/q^2_{t=0}$) during the natural decay. The dashed-dotted line represents the near-field, the dashed line the 'first' far-field, the green dotted line the 'saturated' far-field and the black dotted line the far-field fit of q^2 for comparison. Fitted parameters are shown in table 3.5.

In figure 3.9, the evolution of $q^2_{u_1'}$ shows a near-field decay as in $q^2_{u_2'}$. Similarly, the start of the far-field decay is as the one observed for $q^2_{u_2'}$, but after $t^* \approx 40$ the decay is enhanced and this leads to a final period of decay corresponding to a decay exponent of $m = -1.8$. We hypothesise that the final period of the decay is dominated by turbulence saturation and this will be further discuss in the current section. In fact, the magnitude of the decay rate is very close to the results obtained in Hwang and Eaton [2004] for the decay of isotropic turbulence in a confined domain. Also, in Meldi and Sagaut [2017] they studied the sensitivity of the decay exponent to saturation effects and showed that for a intermediate configuration between the fully unbounded case and the completely saturated case, the decay exponent increased to $m \approx -1.7$, being in good agreement

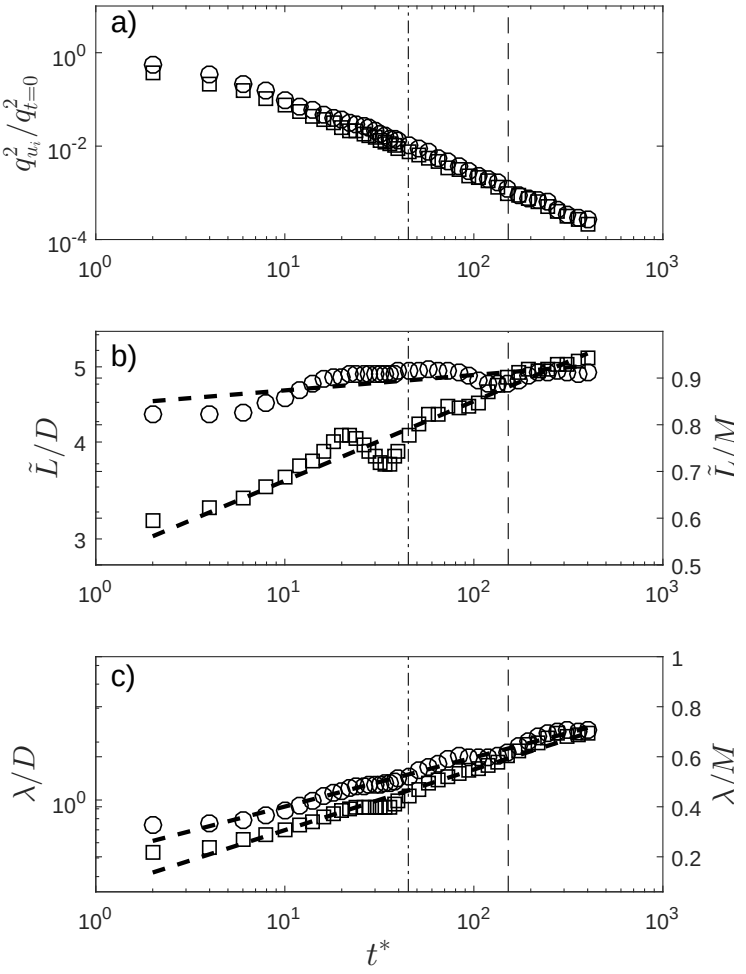

Figure 3.10: Time evolution of the turbulent quantities during the natural decay; $q^2_{u'_1}/q^2_{t=0}$ and $q^2_{u'_2}/q^2_{t=0}$ a), Taylor length scales (λ_i) b) and Integral length scales (L_{ii}) c).Circles and squares correspond to experimental data obtained from horizontal and vertical velocity fluctuations respectively. The dashed-dotted line represents the start of the saturation effects for the horizontal velocity fluctuations and the broken line the start of the large scale isotropy regime.

with the results found in here.

The aforementioned large-scale anisotropy can be clearly observed when both components are compared, as in figure 3.10 a). In fact, $q^2_{u'_1}$ appear to be about 60% stronger than the vertical counterpart ($q^2_{u'_2}$) for forced turbulence and small values of t^*. However, this difference becomes less prominent as turbulence decays, and after $t^* \approx 150$ both quantities collapse into a single curve, as observed in fig. 3.10 a).

As turbulence decays in time, the integral length scale grows in size and therefore the extrapolated region in the correlation function obtained from the PIV data also does so. We find that the results of the integral length scale are very sensitive to the shape of the

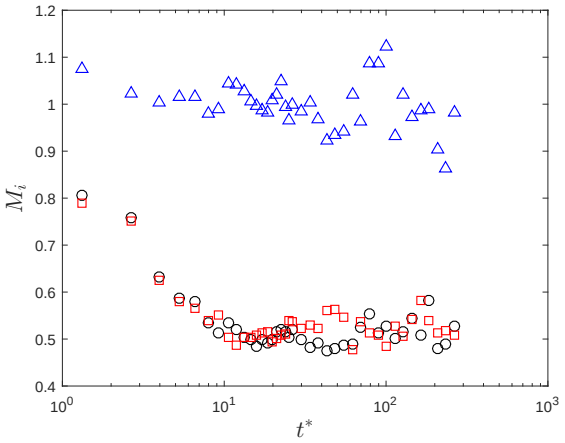

Figure 3.11: Time evolution of the ratio of velocity gradients during the natural decay. The triangles, circles, squares represent the gradient velocity ratios $M_1 = \langle \frac{\partial u_1}{\partial x_1} / \frac{\partial u_2}{\partial x_2} \rangle$, $M_2 = \langle \frac{\partial u_1}{\partial x_1} / \frac{\partial u_1}{\partial x_2} \rangle$ and $M_3 = \langle \frac{\partial u_2}{\partial x_2} / \frac{\partial u_2}{\partial x_1} \rangle$, respectively.

last region of the correlation function. To overcome this issue we propose to look at a magnitude proportional to the integral length scale ($\tilde{L_{ii}}$), that is the direct measure of the area under the correlation function without accounting for the region that should be extrapolated to obtain the true magnitude. We integrate the area under the correlation function for a square region of 4400 px to account for the original rectangular shape of the image sensor. In figure 3.10 b) we observe that $\tilde{L_{ii}}$ of the velocity fluctuations in the vertical direction grows logarithmically during all the decay region recorded. In contrast, its horizontal counterpart grows rapidly during the initial period of the decay and then reaches a plateau at about $t^* = 40$. This plateau corresponds to the approximate critical time when $q^2_{u'_1}$ experience a faster decay over time, as seen in figure 3.10 a). Therefore, we believe that the sudden change in the decay rate of $q^2_{u'_1}$ is dominated by turbulence saturation. This would also explain why the vertical counterpart $q^2_{u'_2}$, characterised by a smaller integral length scale, maintain the same decay rate during the experiments.

On the other hand, the evolution of the Taylor length scale (λ) is found to grow logarithmically in time along both directions; x_1 and x_2, as shown in figure 3.10 c). However, the rate of growth differs from one to another and at large decay times both quantities have a similar length. This trend suggests that while turbulence saturation restricts the growth of large scales, small scales keep growing in time and therefore the inertial range $L(t)/\eta(t)$ shrinks monotonically during the decay, as discussed in Biferale et al. [2003]. To evaluate the evolution of the small scale anisotropy during the decay we also compute the longitudinal and transverse velocity gradients, as in section 3.3. The small scale anisotropy is then evaluated by computing the following ratios; $M_1 = \langle \frac{\partial u_1}{\partial x_1} / \frac{\partial u_2}{\partial x_2} \rangle$, $M_2 = \langle \frac{\partial u_1}{\partial x_1} / \frac{\partial u_1}{\partial x_2} \rangle$ and $M_3 = \langle \frac{\partial u_2}{\partial x_2} / \frac{\partial u_2}{\partial x_1} \rangle$, and these are shown in figure 3.11. We observe that the longitudinal velocity ratio (M_1) fluctuates about unity whereas the longitudinal to transverse ratios (M_2, M_3) quickly approach the relation $2\langle \frac{\partial u_i}{\partial x_i} \rangle \approx \langle \frac{\partial u_i}{\partial u_j} \rangle$ as one would expect for homogeneous isotropic turbulence.

Similarly, the evolution in time of the TKE dissipation rate is also investigated. We first estimate it as detailed in sec. 3.3. However, as time elapses and turbulence decays, the turbulent scales of the flow grow in size and therefore the size of the Gaussian filter (3η) becomes time dependent. To find the appropriate filter size we follow an iterative process for each data set in time that is as follows: First we filter the PIV velocity field with a Gaussian filter corresponding to 3η (estimated from the 'stationary' forced turbulence), we use the filtered velocity field to estimate the TKE dissipation rate and make a first estimation of the Kolmogorov length scale η_t. This value of η_t is used to filter again the original PIV velocity field and to make a second estimation of the TKE dissipation rate and Kolmogorov length scale. This process is repeated until the estimation of the TKE dissipation rate obtained from the filtered data is within 1% of the previous iteration. The results obtained from this method are shown in figure 3.14 a).

In addition to this direct method, we also compute the TKE dissipation rate using the method introduced by Tanaka and Eaton [2007] for sub-Kolmogorov resolution. This method was introduced in Tanaka and Eaton [2007] as a direct method to estimate TKE dissipation rate from PIV data with sub-Kolmogorov resolution and it was formulated as

$$\epsilon \cong \frac{4\epsilon_D|_{2\Delta x} - \epsilon_D|_{\Delta x}}{3} \tag{3.22}$$

where the subscript, D denotes a quantity obtained from 2D PIV data. $\epsilon_D|_{\Delta x}$ is the TKE dissipation rate using second-order central difference approximation and $\epsilon_D|_{2\Delta x}$ is the dissipation rate at double grid spacing. This method was reported to give accurate results for a range of vector spacing (Δx) to Kolmogorov length scale (η) ratio of $0.7 > \Delta x/\eta > 0.2$.

According to our estimates this range only includes a small region of the decay (limited with dashed lines) in figure 3.12. For vector spacing ratios smaller than the working range, TKE dissipation rate is underestimated, whereas for larger vector spacing ratios it is overestimated, [Tanaka and Eaton, 2007]. This trend is consistent with the results presented in here, as observed in figure 3.12. In figure 3.12 the two direct estimates of dissipation are plotted together with the indirect estimate (from $D_{11}(r_1)$). Both longitudinal second order compensated structured functions ($D_{11}(r_1)$, $D_{22}(r_2)$) give dissipation estimates that are within 30% and therefore only $D_{11}(r_1)$ is plotted for clarity. Despite the difference between the two direct methods for small decay times, these become less pronounced as turbulence decays and then maintain a very similar decay rate. In contrast, the estimate from the structure function agrees very well with the direct estimate from the data with a Gaussian spatial filter of 3η kernel size for the initial period of the decay, whereas the direct estimate from the correction method seems to underestimate dissipation. For longer decay times, the decay rate from the structure functions gets more pronounced and therefore closer to the estimate from the correction method. Both direct estimates of the TKE dissipation rate for the last section of the decay appear to overestimate the dissipation rate. This result is in agreement with Tanaka and Eaton

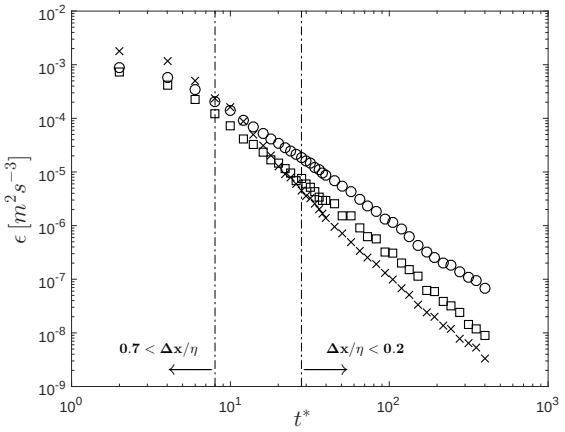

Figure 3.12: Time evolution of TKE dissipation rate during the natural decay. Squares represent values from compensated second order structure function $D_{11}(r_1)$, Circles from the correction method of Tanaka and Eaton [2007] and crosses after applying a Gaussian filter of size 3η as in proposed in Ganapathisubramani et al. [2007]. The dashed-dotted lines show the working range of the method proposed in Tanaka and Eaton [2007].

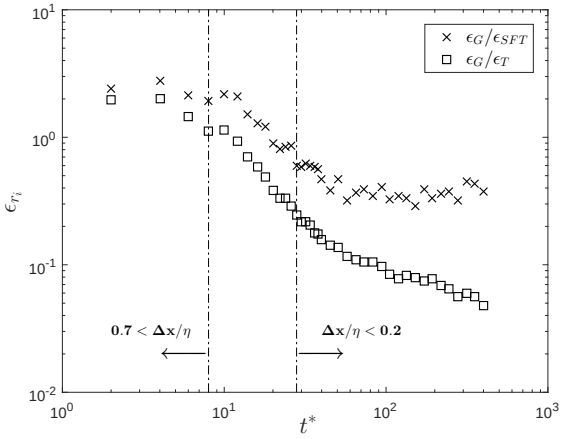

Figure 3.13: Time evolution of dissipation ratio ϵ_{ri} between the estimates of the TKE dissipation rate during the natural decay. The dashed-dotted lines show the working range of the method proposed in Tanaka and Eaton [2007]. The sub-indices T and G refers to the estimates based on the correction method proposed in Tanaka and Eaton [2007] and the estimates based on a velocity Gaussian smoothing of 3η as in Ganapathisubramani et al. [2007]

[2007], where they showed that their correction method underestimates dissipation for $\Delta x/\eta > 0.5$ and starts to overestimate dissipation for $0.2 < \Delta x/\eta$. Fig. 3.13 shows the time evolution of the dissipation ratios together with an estimate of the PIV spatial resolution in time as $\Delta x/\eta$.

The results obtained from the method proposed by Tanaka and Eaton [2007] appear to underestimate dissipation for $\Delta x/\eta > 0.5$ and starts to overestimate dissipation for $0.2 < \Delta x/\eta$. This agrees well with the results obtained from the iterative filtered data and give us confidence on the iterative filtering method. The results from this

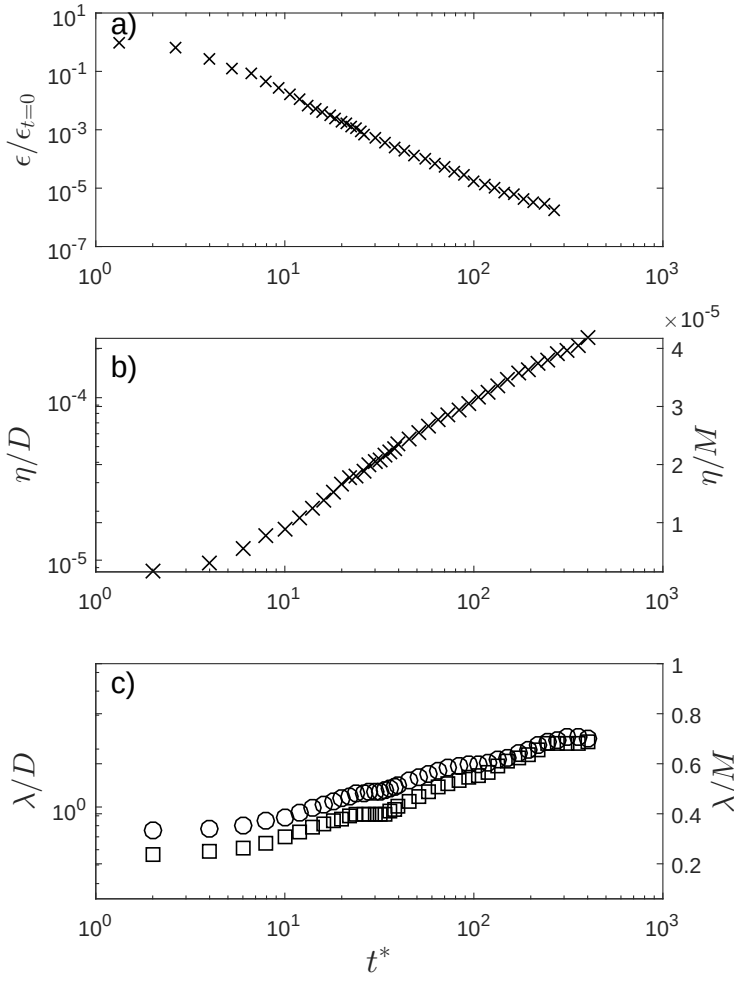

Figure 3.14: Time evolution of TKE dissipation rate (ϵ), Kolmogorov length scale (η) and Taylor length scale (λ) during the natural decay. M stands for the center-to-center nozzle distance and D for the nozzle internal diameter.

method are now used to calculate the evolution of the Kolmogorov length scale over time. As observed for the Taylor length scale, the evolution of the Kolmogorov length scale appears to be unaffected by the saturation of the large scales, as shown in fig. 3.14 b).

Also, the results of the TKE dissipation rate from the iterative filtering method are fitted to a power-law equation following the same technique as for q^2. Again, the evolution of the TKE dissipation rate over time can be divided in two regimes. The near-field regime can be fitted to a power-law function with $m = -4$ and $t_0 = -3$, whereas the fit for the far-field regime gives $m = -2.55$ and $t_0 = 2$. This result agrees well with the relation obtained from the energy budget for isotropic homogeneous turbulence naturally decaying in absence of production terms; i.e. $m_\epsilon = m - 1$, and give us confidence on the accuracy of the method used.

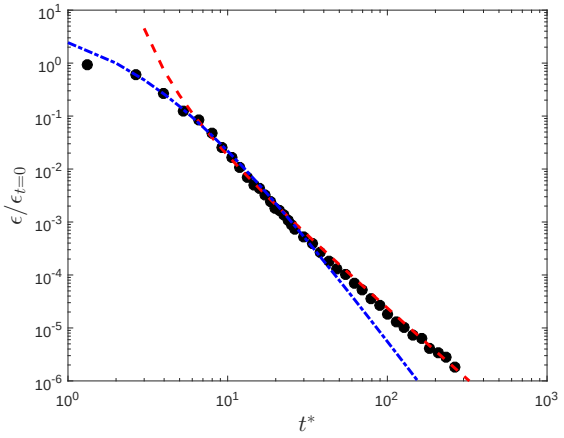

Figure 3.15: Time evolution of TKE dissipation rate estimate (ϵ_G) during the natural decay. The dashed-dotted line represents the near-field and the dashed line the far-field. Fitted parameters are shown in table 3.5.

Quantity	Decay Range	Decay type	m	t_0
$q^2_{u'_2}$	$t^* < 10$	Near-Field	-2.3	-5
$q^2_{u'_2}$	$t^* > 8$	Far-Field	-1.41	0.5
$q^2_{u'_1}$	$t^* < 10$	Near-Field	-2.3	-4
$q^2_{u'_1}$	$t^* > 8$	Far-Field	-1.41	0.5
$q^2_{u'_1}$	$t^* > 40$	Saturation	-1.8	0.5
ϵ_G	$t^* < 10$	Near-Field	-4	-3
ϵ_G	$t^* > 8$	Far-Field	-2.55	2

Table 3.5: Fitted constants for the power-law decay of turbulent quantities. Near-field and far-field fits are made for data at $t^* < 10$ and $t^* > 8$ respectively.

Finally, in figure 3.16, we investigate the evolution of the Reynolds number based on the Taylor length scale (Re_λ), the value of C_ϵ and the evolution of the integral length scale to Taylor length scale (L/λ) during the decay. We observe the Reynolds number (Re_λ) for $t^* = 0$ to be slightly higher than the value obtained for 'stationary' turbulence. However, this might be due to the finite number of runs computed (75 for the decay) and not a physical phenomena, as occurs in regions very close to the turbulence-generating grid in wind tunnel experiments, as reviewed in Vassilicos [2015]. Then, as turbulence decays the Reynolds number decreases logarithmically with time. The decay exponent of the Reynolds number ($m_{Re_\lambda} \approx -0.57$) agrees very well with previously reported values in Compte-Bellot and Corrsin [1966] and revisited by Meldi and Sagaut [2014], where $m_{Re_\lambda} = -0.5$ for complete saturation. In contrast, the value of C_ϵ fluctuates during the start of the decay and then transitions to reach a plateau at $C_\epsilon \approx 0.5$ for $t^* > 50$. We believe the forced 'stationary' state of the tank influences the value of C_ϵ during the near-field decay. However, C_ϵ becomes stable once the turbulence has fully developed and the influence of the forcing mechanism becomes negligible. It is interesting to note that C_ϵ remains nearly constant for $200 > Re_\lambda > 20$ where the flow

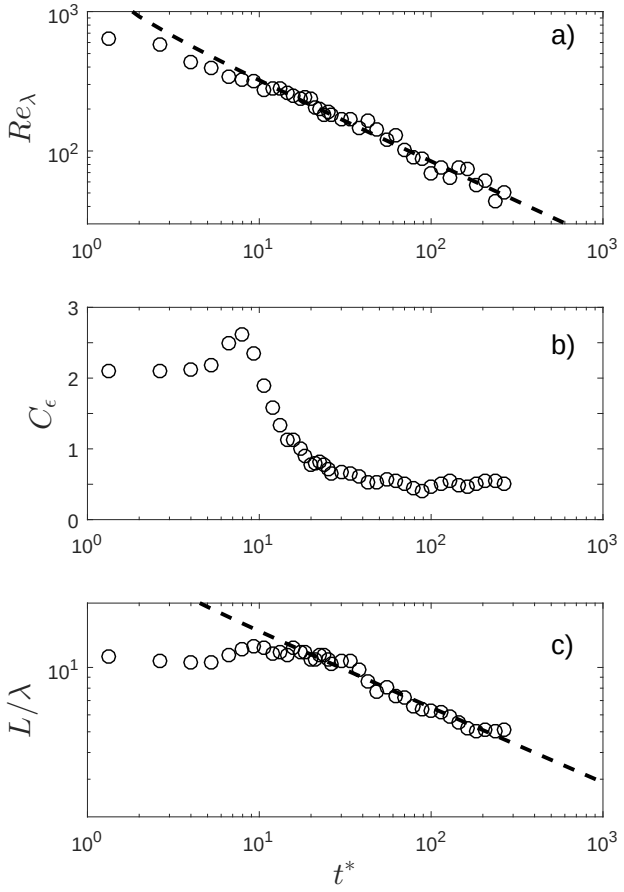

Figure 3.16: Time evolution of the Reynolds number based on the Taylor length scale (Re_λ) a), of $C_\epsilon = \epsilon L_{11}/u'^3$ b) and the integral length scale to Taylor length scale (L/λ) c) during the natural decay.

suffers from confinements effects. On the other hand, the ratio L/λ fluctuates about a value of ≈ 12 for the near-field decay, but for $t^* > 40$ it decreases logarithmically in time with a decay exponent $m_{L/\lambda} \approx -0.35$. Again, the decay region in the L/λ ratio corresponds to the saturated regime, where large scales are constrained by the facility but small and intermediate scales are still growing.

3.5 Summary

In this chapter, we investigated the evolution of anisotropic turbulence at large scales during natural decay in an experiment with initial Reynolds numbers (based on the Taylor microscale) of $Re_\lambda \approx 580$ over more than two decades in time. In contrast with wind tunnel experiments where Taylor's hypothesis is invoked to convert downstream distance x (generally made dimensionless as x/L_0) into time, we directly observed the evolution of turbulence over time and use the eddy turnover time (t_L) of the 'stationary'

forced turbulence to make time dimensionless. As turbulence decays and the large scales of the flow start to grow in size, the size of these become comparable to the facility that contains them, leading to turbulence saturation. Then, the sensitivity of free decaying anisotropic turbulence to saturation effect was investigated.

Ninety-six water-pump driven jets pointed towards the center of the rectangular water tank from opposite sides and were driven randomly following the 'Sunbathing algorithm' introduced in Variano and Cowen [2008] to produce anisotropic turbulence, instead of the HIT obtained in previous studies with a similar facility, [Bellani and Variano, 2013]. This forcing scheme for the facility presented produced a central volume of turbulence that had negligible shear, mean flow and was homogeneous. When the tank is in operation we observe a turbulent flow for which the ratio of horizontal to vertical velocity fluctuations are $u_1'/u_2' \approx 1.22$, with a ratio of integral length scales of $L_{11}/L_{22} \approx 1.6$.

The two RJA were turned off after 5 minutes of active forcing and 40 pairs of images were acquired with variable dt to limit the particle pixel displacement to $4-6$ px. and reduce out-of-plane motion. This process was repeated 75 times and results were ensemble averaged.

The natural decay of the flow was investigated for individual components of the velocity fluctuation. We observed that the large-scale anisotropy that exists at the start of the decay is progressively reduced and becomes statistically negligible for $t^* > 150$. We believe this process might have been enhanced by the saturation effect over the large scales of the flow. Power-law fits were obtained for q^2, $q^2_{u_1'}$ and $q^2_{u_2'}$ and ϵ following the method proposed in Hearst and Lavoie [2014]. We observed a very similar behaviour of $q^2_{u_1'}$ and $q^2_{u_2'}$ over time as compared with wind tunnel experiments equipped with multi-fractal passive and active grids ([Krogstad and Davidson, 2011], [Valente and Vassilicos, 2011], [Valente and Vassilicos, 2012], [Hearst and Lavoie, 2014]); and numerical simulations ([Perot, 2011], [Meldi et al., 2011]) for Batchelor turbulence. Two different regimes are observed for free decaying turbulence. First, we observe a fast decay of the TKE for $t^* < 10$. This region is present in wind tunnel experiments for a few integral length scales downstream of the grid and is referred as 'near-field' decay. This regime is believed to be strongly affected by the turbulence production mechanism as discussed in Meldi [2016] and therefore to be 'facility dependent'. Then, we observe a second region of logarithmically decaying TKE for $t^* > 8$. This region is also present in wind tunnel experiments after a distance of about $20\,L_{11}$ downstream of the grid and is referred as 'far-field' decay. The decay exponent of this region, either in time in numerical studies or in space domain in wind tunnel experiments, has been a matter of debate during the past decades. In here, we found the exponent of this region for the unsaturated case to be $m \approx -1.41$ and this is within the range of values observed for the 'far-field' decay on wind tunnel experiments and numerical results. Besides these two regimes, we found the turbulent kinetic energy to decay faster once large scales 'feel' the confinement effect, i.e. the integral length scale stops growing over time. The decay exponent during the

saturation regime becomes $m \approx -1.8$ and therefore approaches the value obtained from analytical results for complete saturation in Skrbek and Stalp [2000], that is $m = -2$. The decay exponent of the saturation regime is also in good agreement with the decay exponent observed in Hwang and Eaton [2004] where, we believe, confinement effects were present. The anisotropy evolution of the small scales is investigated by comparing velocity gradients; i.e. M_1, M_2 and M_3. We found that after $t^* = 10$ the relation between velocity gradients approaches the isotropic relation and this is consistent with the DNS study in Biferale et al. [2003] where they found small scales to 'isotropize' much quicker than large scales. Also, the dissipation rate of the TKE is estimated from direct measurements following an iterative filtering process. The goal of this process is to obtain the 'true' Kolmogorov length scale to filter the data using a Gaussian filter size of 3η as in Ganapathisubramani et al. [2007]. The results from this estimate agrees well with other direct and indirect methods, giving us confidence over the chosen approach. Also, the decay rate for the dissipation rate is found to be $m_\epsilon \approx -2.55$ and agrees well with the theoretical prediction of $m_\epsilon = m - 1$ for free decaying turbulence.

Chapter 4

Disks falling under background turbulence

Despite the ubiquity of turbulent flows with non-spherical particles, it has been only relatively recently that experiments have been developed to measure the motion and orientation of individual particles in a turbulent environment. Early experimental work was focused on particle motion in complex cases relevant to specific applications; Bernstein and Shapiro [1994] measured the orientation of glass fibre cylindrical particles suspended in a laminar and turbulent shear flow in a water tunnel and Noel and Sassen [2005] among others focused on ice crystals in clouds. Fibre-like particles have been extensively investigated during the last decades due to their direct application to several industrial sectors such as the papermaking industry, as reviewed in Voth and Soldati [2017]. However, most of the research done on these flows is focused on the orientation, preferential concentration and alignment of the fibres with the turbulent flow while these are suspended and not on the turbulence effect on the particle settling rate. Also, the severe differences in the dynamics of the fibres compared with the finite-size inertial disks investigated here represents a clear differentiator between these systems.

This chapter is structured as follows: section 4.1 reviews previous studies on the motion of spherical and quasi-spherical particles settling through a turbulent media to reveal different fluid-particle interactions and descent mechanisms; and then it comments on the motion of other irregular particles settling under turbulence. Section 4.2 is devoted to the details of the experimental set up. In section 4.3 we show the results obtained for disks falling in quiescent flow to later discuss the results of the same particles falling under turbulence. Finally, we conclude in section 4.4.

4.1 Introduction

Two-phase flows with a dispersed solid phase are present in many everyday phenomena, and these include not only natural situations, as in the oceanography or meteorology fields, but also in engineering environments such as in hydraulics or civil engineering. Two-phase flows represent an interesting topic of research since in most of these situations the carrier flow is characterized by having a turbulent behaviour, where chaotic changes occur in velocity and pressure at a broad range of scales. Furthermore, solids appear generally in a poly-dispersed phase where particles are far from being spherical, leading to complex interactions between phases. It is a well-known fact that stirring, and therefore turbulence, can keep particles suspended in fluids for a long time. Although this phenomena can be observed in many occasions during a day, (specks of dust in a room, solid particles in a cup of tea...) one should not conjecture that this applies to every two-phase flow with a turbulent carrier flow. In the following, we comment on the rigid particle settling phenomena influenced by turbulence.

4.1.1 Spherical particles settling under turbulence

The effect of turbulence on the settling velocity of solid particles has been a matter of debate during the past decades. Very different conclusions were drawn from the early experimental and numerical works in the 70's and 80's; some of them showing that turbulence does not affect the mean descent velocity of particles, whereas others showed an increased / reduced settling velocity. In the early work of Murray [1970], he examined the particle-settling velocity in grid-generated turbulence and found the velocity of quartz grains (inertial particles) to reduce with increasing the eddy shedding frequency of the grid (up to 30% of the velocity in laminar flow). Interestingly, he also found that the settling velocity of the tracers (nearly buoyant particles) was enhanced.

Reeks [1977] argued that in homogeneous turbulence there would be no net effect on the average settling velocity; and this is the case for a non-inertial particle since the average particle velocity would be just the sum of the terminal fall velocity in still fluid and the Eulerian mean flow velocity (zero by definition). Some years later, M. R. Maxey published his well-known paper [Maxey, 1987], where he proved that under random flow fields, the inertial particles (now simplified as small-heavy spheres) settle at a velocity higher than in still fluid. Subsequent publications showed this same effect, as in the numerical studies of Squires and Eaton [1991] and Wang and Maxey [1993]; and the experimental studies of Nielsen [1993], Aliseda et al. [2002] Yang and Shy [2003] and Yang and Shy [2005] among others.

From the work previously reported one can distinguish four specific mechanisms by which turbulence with zero mean flow can influence the settling speed of particles. The mechanisms that reduce the velocity descent of the particle are: non-linear drag due

to fluid acceleration first investigated in Ho [1964], trapping inside vortices as shown in Nielsen [1984], and in Nielsen [1992] and the loitering effect discuseed in Nielsen [1993], which in essence says that a particle settling through a non-uniform velocity field spends most of the descent with fluids moving in the opposite direction of its natural settling direction. On the other hand, the mechanism responsible for the enhancement of the descent velocity is the fast-tracking effect, [Maxey and Corrsin, 1986]. This effect becomes strongest for particles that couple best to the smallest turbulent structures. At the other limit, inertialess particles behave like tracers, whereas the coupling of more inertial particles to larger and slower structures is affected by smaller vortices. Thus, small inertial particles are the ones showing a stronger fast-tracking effect, since these tend to be expelled from vortex cores spiralling outward and therefore increasing their speed during the descent.

Later experimental and computational work in Good et al. [2014] proved that direct numerical simulations where a linear drag law is formulated cannot capture turbulence-reduced settling speeds and that it is necessary to introduce a non-linear drag law to observe this phenomenon (Wang and Maxey [1993]; Yang and Lei [1998]; Ireland and Collins [2012]. However, quantitative differences between these simulations and the experiments emphasized the need of studies using particle-resolved DNS. Their work also contained the first experimental observations of enhanced and reduced settling velocities for particles with a density ratio $\rho_p/\rho_f \approx 1000$, and the settling regimes of these appeared to be strongly dominated by particle inertia and the settling parameters ($S_{v_\eta} = \tau_p g/u_\eta$ and $S_{v_l} = \tau_p g/u'$).

Despite these studies on sub-Kolmorogov size particles, the literature on the settling of finite size particle under background turbulence is very scarce. Recent experiments by Byron et al. [2015] investigated the settling of Taylor-scale particles using refractive-index-matched hydrogel particles and particle image velocimetry and showed that particles with quiescent settling velocities of the same order of the turbulence root-mean-square velocity fall on average 40%–60% more slowly in turbulence (depending on their density and shape). Recently, Fornari et al. [2016a] compared the settling velocity of finite size spheres in quiescent and sustained HIT. The background HIT flow at a Reynolds number based on the Taylor microscale $Re_\lambda \approx 90$. Also, they controlled the sphere Galileo number through the density ratio, therefore also controlling the ratio between the settling velocity to turbulent velocity fluctuations. They showed a strong reduction of the settling velocity with reducing the Galileo number (from 10% to 55% when compared with a single sphere under free fall) and they attributed drag non-linearity as the dominant contribution.

The lateral motion of spherical particles influenced by turbulence has not received the same attention as the settling rate during the past years. Nevertheless, in the work of Fornari et al. [2016b] where they investigated numerically the settling of finite-size rigid spheres in sustained HIT they also found significant lateral relative velocities. They

investigated the contributions of the lateral motion of the spheres to the global drag and found that this was particularly relevant for particles with small Galileo number (about 30% of the overall drag for $Ga = 20$) and also found that this contribution was mitigated as Galileo number increased.

4.1.2 Quasi-spherical particles settling under turbulence

The understanding of the motion of non-spherical particles under turbulence is much more limited than for the case of spherical bodies. One of the first attempts to tackle this problem was carried out for the case of rigid spheroidal particles falling under gravity in a spatially periodic, cellular flow field, [Mallier and Maxey, 1991]. They investigated particles sufficiently small so that the surrounding fluid satisfies local Stokes flow conditions and found that the suspension of these particles is greatly reduced when compared with spherical particles. Besides, they found that individual particles undergo tumbling motions that can lead to a chaotic descent and also suggested that a fast-tracking effect, explained in the previous section, can also exist for non-spherical particles.

Some years later, Klett [1995] developed the first model to estimate the statistical distribution of particle orientation as a function of aspect ratio, Reynolds number, turbulence intensity and particle size for spheroids, disks, cylinders, hexagonal plates and columns. However, apart from these isolated studies, very little has been done on the settling velocity of particles under turbulent conditions. Recently, Siewert et al. [2014] investigated the motion of heavy and small ellipsoids using a DNS of isotropic turbulence. The density of the solid phase was about three orders of magnitude higher than the fluid phase, whereas the characteristic length scale was kept one order of magnitude smaller than the Kolmogorov length scale. Spheroids were released in a domain with the main component of the fluid velocity in opposite direction to gravity and turbulence was generated by adding synthetic turbulence at the inlet domain, resulting in a Reynolds number based on the Taylor microscale $Re_\lambda = 10$. They showed that spheroids under this conditions exhibit both preferential orientation and preferential sweeping. Interestingly, the first slows down the particles whereas the latter accelerates them; and this latter effect turns out to be dominant. As a result, they showed that oblate ellipsoids in decaying isotropic turbulence settle faster than spherical particles.

In this chapter we will comment on the effect of turbulence on the settling rate, dispersion and falling modes of disks. To the best of our knowledge, the effect of turbulence on the descent of planar particles has never been explored before.

4.2 Experimental setup

The technique of particle tracking described in chapter 2 will be used to reconstruct the 3D trajectories of disks falling under background turbulence. As in the previous sections, particles will be released always individually.

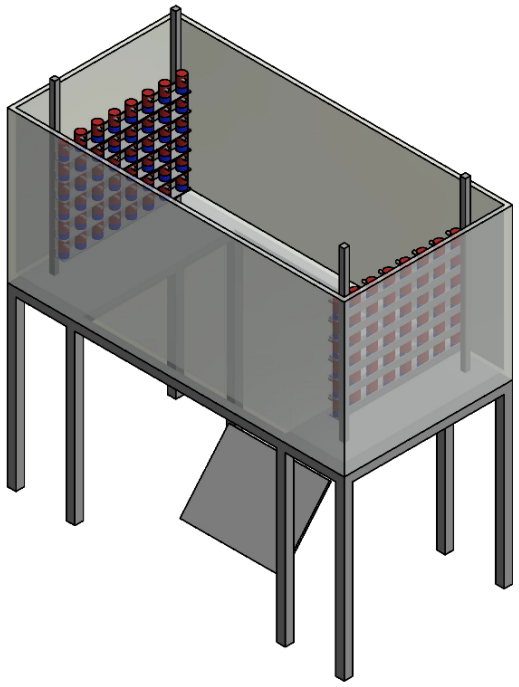

Figure 4.1: Sketch of the water tank equipped with a co-planar arrangement of RJA. The central region of the frame allows optical access from the bottom; in here through a 45^o mirror.

Turbulence is generated as in chapter 3; in an open glass (bottom and walls) and steel-framed tank of dimensions $200 \times 85 \times 100\,\mathrm{cm}^3$. In this facility, turbulence is generated by two facing planes of randomly actuated jet arrays (RJA), in the same fashion as in Esteban et al. [2019a]. Each plane of jets contains 48 bilge pumps (Rule 24, 360 GPH) arranged in a 8×6 array as shown in figure 4.1. The pumps take in water radially at their base and discharge it axially via a cylindrical nozzle (1.8 cm inner diameter). Each pump acts as a synthetic jet, in the sense that they only inject momentum to the system, since the pump intake and nozzle are contained within the same volume of fluid. Each plane of bilge pumps is connected to a solid state relay rack SSR-RACK48 equipped with quad-core relays SSR-4-ODC-05. The relays are triggered by TTL signals from a Measurement Computing 96 channel digital output card (PCI-DIO96H) controlled by MATLAB. The firing algorithm we employ to force turbulence is the 'Sunbathing' algorithm originally proposed in Variano and Cowen [2008], and latter investigated in Bellani and Variano [2013], Carter et al. [2016] and Esteban et al. [2019a] among others. The amount of pumps that are employed at a given time is in average $\phi = 12.5\%$.

The water tank was actively stirred using both RJA's for a period of 5 min until the turbulence level reached a statistically stationary state. Then, all pumps were turned off simultaneously and a disk was released after a given period of time (dt), being $dt = 2$, 10 and 20 s for the data presented here. This allows us to release the particles at different levels of background turbulence intensity and investigate how this parameter affects the descend mode of disks with different dimensionless numbers (Ga, I^*). The disk was recorded with two JAI GO-5000M USB 4 Mpx cameras at 60 frames-per-second and this was sufficient to capture the dynamics of the particle. One camera recorded the front-view of the descend while the other recorded the bottom-view of the descend through a mirror at 45^o. The release of the disk was synchronized with the start of the camera system using a 5 V signal from a National Instruments Data Acquisition Device (NI USB-6212). The videos were recorded with the JAI Camera Control Tool software and were initially saved in RGB but were frame-cropped and converted into grey-scale for memory save purposes using MATLAB. These videos were later used to obtain the particle position in the $Z-$coordinate (front view) and $X-Y$ coordinate (bottom view).

The method to obtain the particle position from the grey-scale image is a threshold based method. The raw images are converted into black and white images after applying a user defined intensity threshold. For the accuracy on the particle location we rely on a stable light intensity during all the trajectory. Commercial LED panels connected to a combination of two stable DC power supplies (IPS 303DD) connected in parallel, were used to back illuminate the field of view. Both LED panels are mounted to cover the complete field of view of both cameras; i.e. 60×60 cm for the bottom view and 60×80 cm for the front view. The panels were used at maximum light intensity. Thus, we were able to close the aperture of the camera diaphragm ($f.4$) and therefore increase the focal depth.

Disk	d [mm]	t [mm]	ρ[g/cm^3]	Ar	I^*
♯1	10	0.5	2.7	393	6.11×10^{-3}
♯2	12.5	0.5	2.7	492	5.44×10^{-3}
♯3	15	1	2.7	835	8.52×10^{-3}

Table 4.1: Main geometric and material parameters of the disks that define the Archimedes number (Ar) and the dimensionless moment of inertia (I^*), both defined in section 1.7.3.

In all experiments, the disk was released with the same initial conditions ($V_z = 0$, $\theta = 0$) using a release mechanism that employs active suction and is capable of accommodating all disks considered in here. When the suction circuit is opened the pressure difference maintaining the particle fixed vanishes and the particle begins its descent through the tank. The disks were dropped from a height sufficiently large (85 cm) to allow the falling regime to fully develop during the observation. This vertical path corresponds to

85, 68 and 56 disk diameters for the particles investigated. Each disk was released 50 times in quiescent flow to establish the dynamics of the motion without the influence of background turbulence. Then, each disk was released 200 times under each of the turbulence intensity levels; $dt = 2,\ 10,\ 20$ s.

The particles used in this study are manufactured to lie in the $(Re - I^*)$ domain corresponding to the 'Planar zig-zag' regime. Contrary to the particles manufactured in chapter 2, these will exhibit a highly planar oscillatory motion when released in quiescent flow. This will reduce the variability in the natural descent of the particle, revealing more clearly the effect of background turbulence. The size, material properties and dimensionless numbers of the disks used in this study are summarized in table 4.1.

4.3 Results

4.3.1 Disks in Quiescent Flow

In this section we summarize the main characteristics of the motion of the disks in table 4.1 falling in quiescent flow. The results correspond to the analysis of 50 independent trajectories per disk. The highly planar motion of the particles and the extended field of view compared with the trajectories in chapter 2 reduces the amount of trajectories needed to obtain good trajectory statistics.

4.3.1.1 Descent velocity

Table 4.2 shows the mean descent velocity of the disks during the fall and the statistic deviation from the 50 samples. The descent velocity is then used to compute the Reynolds number of the disks that confirm their location within the $Re - I^*$ domain (defined in Willmarth et al. [1964]) corresponding to 'Planar zig-zag' descent.

Disk	$\langle V_z \rangle$ [mms^{-1}]	Re	St
♯1	95 ± 4	947	0.52
♯2	92 ± 2	1140	0.63
♯3	158 ± 14	2360	0.30

Table 4.2: Values of the particle Reynolds number (Re) based on the mean fall velocity $\langle V_z \rangle$, and Strouhal number ($St = f \cdot D/\langle V_z \rangle$) based on the dominant frequency of the descent velocity.

Figure 4.2 shows a sample trajectory of each disk investigated released in quiescent flow. One can observe that these trajectories show very small deviations from an ideal

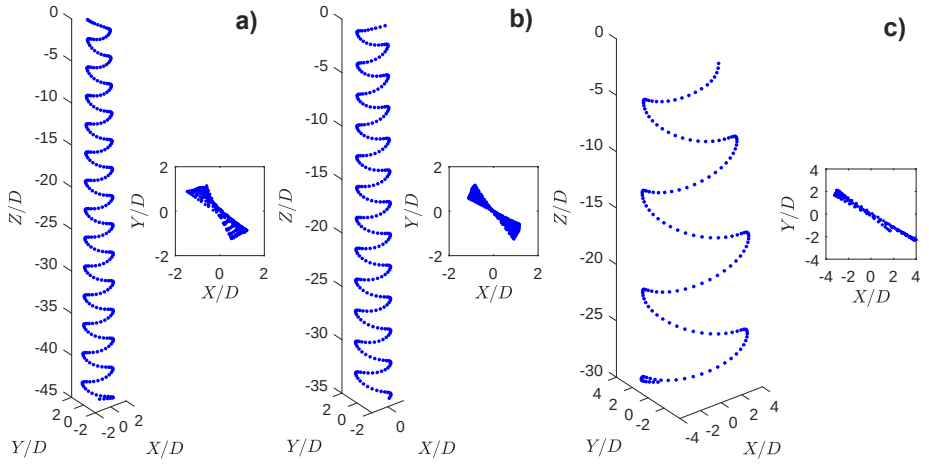

Figure 4.2: 3D trajectory reconstruction of sections of the disk descent. a) Disk ♯1, b) Disk ♯2 and c) Disk ♯3.

planar zig-zag motion. However, in some realizations we observe more pronounced deviations that are sustained along the complete descent, see figure 4.3. The rotation of the oscillatory plane in these instances is still very mild; with the particle descending more than $30\,D$ to complete a full rotation in the $X-Y$ plane. Despite the clear trajectory difference from the idealized planar zig-zag case we do not observe changes neither in the descent velocity nor in the radial dispersion of the disk. We do not have the experimental facilities to investigate which of these two descent styles correspond to the 'saturated' descent. However, we believe that the zig-zag motion with superimposed planar rotation might be actually the 'saturated' descent, as shown in the numerical simulations of Churst et al. [2013], but this can only be reached when wake instabilities develop (either naturally of induced by small flow perturbations in the domain). In contrast with the 'Transition' motion observed in chapter 2, the particle rotation is very mild and stable and the disk never returns to the 'Planar zig-zag' motion during the observation.

Figure 4.4 shows a representative evolution of the descent velocity (v_z) and the particle speed ($|v|$) as a function of time. One can observe that the velocity signals describe a nearly periodic evolution with a finite lag between the descent velocity component and the total velocity. It is also interesting to highlight that during the turning events the vertical component of the velocity reaches a positive value systematically (the disks elevate during a short period of time), as observed in Andersen et al. [2005b] for rectangular plates. On the other hand, the mean of the negative maxima of the descent velocity is obtained for each disk; i.e. $\overline{max(v_z)} \approx -186\text{mms}^{-1}$ for disk ♯1, $\overline{max(v_z)} \approx -179$ mms^{-1} for disk ♯2 and $\overline{max(v_z)} \approx -350$ mms^{-1} for disk ♯3, and these values will be later used as a threshold to capture single events during the descent.

The timescales of the velocity oscillations are measured by applying Fast Fourier Transform (FFT) to the descent velocity signal. We use a polynomial filter of 3^{rd} order and 5

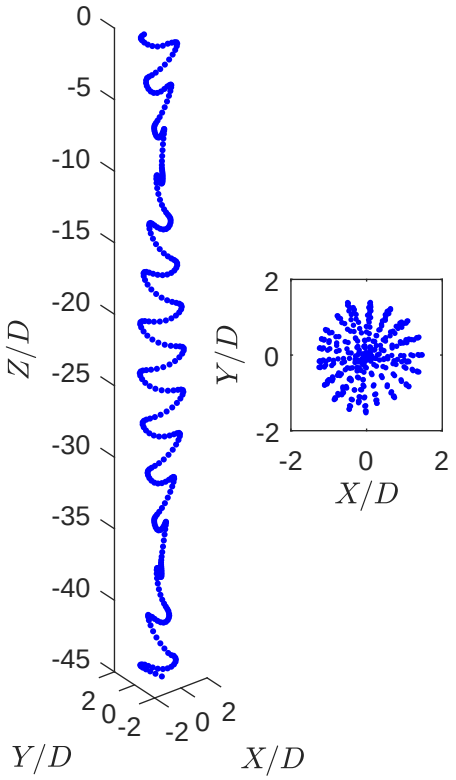

Figure 4.3: 3D trajectory reconstruction of sections of disk ♯1 during the descent. The top view shows the self-sustained particle rotation.

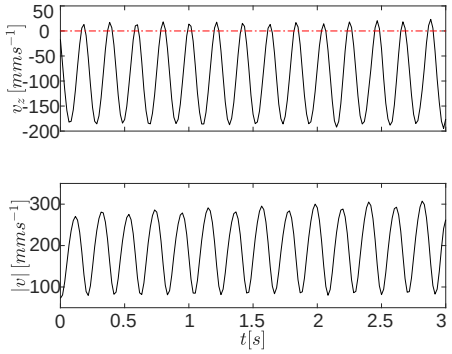

Figure 4.4: Time evolution of the velocity of disk ♯1 in quiescent flow. The top graph shows the evolution of the descent velocity (v_z), whereas the bottom graph shows the evolution of the total particle velocity ($|v|$). The red dash-dotted line showing the upward motion events in during the turns.

points of window size to remove high frequency noise prior to the FFT analysis. After the signal is filtered, we zero-pad it to the closest power of two length with the purpose of increasing the script efficiency.

As in Auguste et al. [2013], we also observe that the disk Strouhal number (St) increases with reducing the dimensionless moment of inertia (I^*). In figure 4.5 one can also notice the sharpness of the power spectrum in the frequency domain, showing that the descent is dominated almost entirely by one velocity frequency. We believe that the wider

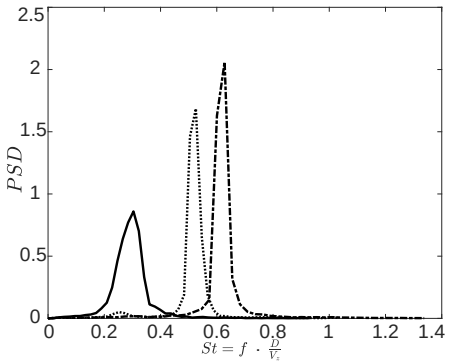

Figure 4.5: Normalized power density spectrum as a function of the Strouhal number. The peak on the spectrum is used to identify the characteristic particle Strouhal number. The dotted line represents disk ♯1, the dashed-dotted line disk ♯2 and the solid line disk ♯3.

spectrum of disk ♯3 might be caused by the relative shorter length of the signal, leading to stronger deviations in the frequency data per particle trajectory, and this agrees well with the more pronounced velocity deviation captured in table 4.2.

It is interesting to note that the power density spectrum of the particles in this chapter is considerably narrower than the one observed for the plastic particles in chapter 2. This emphasizes the effect of particle dimensionless inertia on the frequency content of the descent velocity fluctuations; and shows that for high dimensionless inertia the particle motion is much more stable. Thus, the trajectories in here does not contain a broad range of frequencies but are nearly periodic in all cases tested.

4.3.1.2 Planar $(X - Y)$ dispersion

The dispersion of the disks during the descent in quiescent flow is illustrated in figure 4.6. The scatter plots represent all the $X - Y$ particle locations during the descent of the 50 trajectories after the initial transient dynamics normalized with the diameter of the particle.

One can observe that the scatter plots for disks ♯1 and ♯2 are much denser than for disk ♯3 and this is caused by the smaller number of particle oscillations along a trajectory for disks with higher Reynolds number (Re) and dimensionless inertia (I^*). We also observe that the PDF's of the radial location of the disks -see figure **??**- are nearly unaffected with changing the $z-$ coordinate. In this chapter, the $z-$ locations will be represented with different colors; thus red, blue, green and yellow stand for 10, 20, 30 and 40 D from the start of the data analysis. Due to the finite size of the experimental set up, the data for disk ♯3 is limited to 30 D. The evolution of the PDF's shows that the transient dynamics are contained in the initial section of the trajectory (disregarded in this study), and that the results here correspond to 'saturated' trajectories where very small deviations from the idealized vertical fall with planar oscillations are observed.

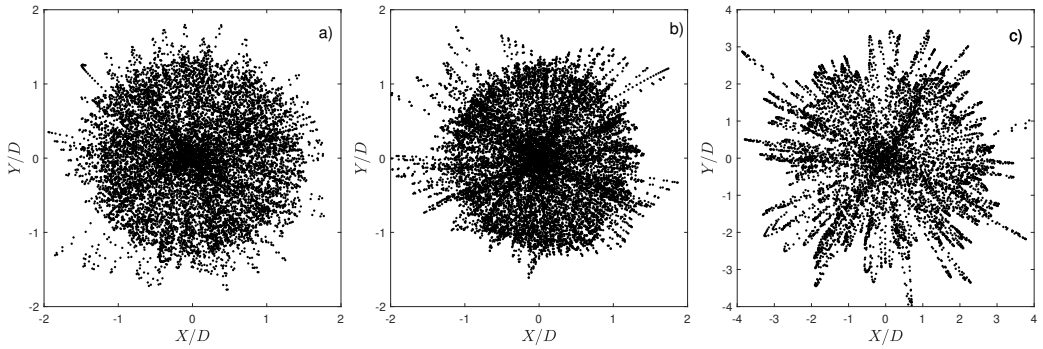

Figure 4.6: Scatter plot of the particle location in the $X-Y$ plane along the descent normalized with the particle diameter. The results show 50 trajectories per particle in quiescent flow. a) Disk ♯1, b) Disk ♯2 and c) Disk ♯3.

Here, the PDF's are normalized by the distance to the origin to compensate the increase in area as the particle departs from the origin. A gaussian function is fitted to the data in figure 4.7 and these are represented with broken lines of the same colour of the raw data. All three disks show a similar shape of the PDF, however we observe an increase in the relative dispersion as disk diameter increases. The dispersion of the fitted gaussian function for disk ♯1 is $\sigma_{\sharp 1} = 0.71\,D$, for disk ♯2 is $\sigma_{\sharp 2} = 0.78\,D$ and for disk ♯3 increases up to $\sigma_{\sharp 2} = 1.02\,D$.

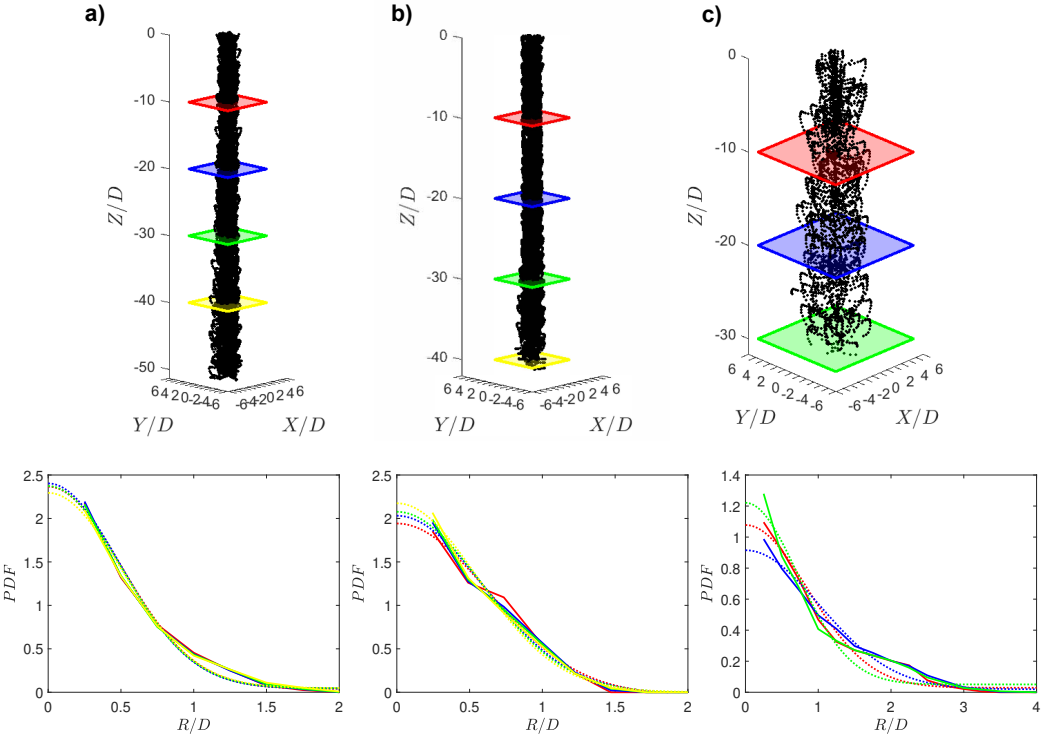

Figure 4.7: Vertically arranged ensemble trajectory reconstruction of disks freely falling in quiescent flow and associated probability density function of the particle at different $z-$locations. a) Disk ♯1, b) Disk ♯2 and c) Disk ♯3.

4.3.2 Disks in Turbulent Flow

In here we compare the characteristics of the motion of disks falling through background turbulence with the results of the previous section. We initially observed that the falling style of the disks vary severely during individual descents and also in different realizations. To capture the wide variability in the descent style we need a larger number of drops than for the case of quiescent flow. Therefore, the results in this section correspond to the analysis of 200 independent trajectories per disk and flow condition (dt). We consider three different turbulent conditions that correspond to different points in

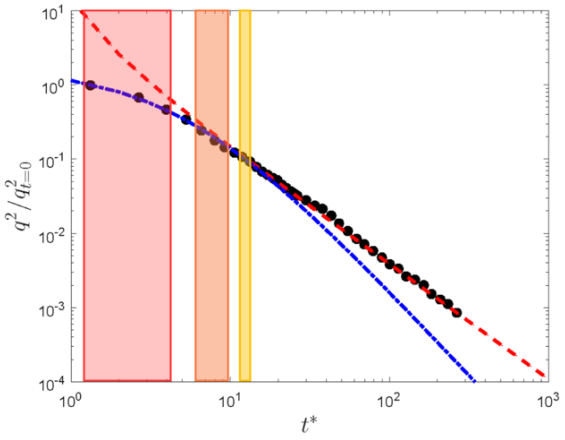

Figure 4.8: Time evolution of the turbulent kinetic energy during the decay; $q^2 = {u'_1}^2 + 2{u'_2}^2$. Time is made dimensionless with the eddy turnover time at the start of the decay (t_L) as $t^* = t/t_L$. The dashed-dotted line represents the near-field and the dashed line the far-field of the decay. The red, orange and yellow rectangles show the statistical turbulent kinetic energy that the disks will experience during the fall for $dt = 2$, 10, 20 s, respectively.

time during the free decay of the turbulence generated (see chapter 3). The turbulent kinetic energy (q^2) in the tank at these points during the decay is shown in figure 4.8. The ratio between the mean velociy fluctuations and the descent velocity of the particles in quiescent conditions (defined as $\tau_p g$ for spherical particles) has been extensively used to determine the change in settling speed of inertial particles (Nielsen [1993], Good et al. [2012], Good et al. [2014] and Byron [2015]). In here, the gravitational velocity ($\tau_p g$) is substituted by the descent velocity in quiescent flow (V_q) due to the difficulties associated with defining an appropriate particle relaxation time for particles with strong secondary motions. The ratio V_q/u', where $u' = \sqrt{q^2}$, is included in table 4.3 for each particle and flow condition. Also, table 4.3 includes the relative size of several characteristic turbulence length scales with respect to the disk diameter. For spherical particles, Good et al. [2014] found that turbulence enhances the settling of particles for particle gravitational velocities smaller than the turbulence velocity fluctuations ($\tau_p g/u' < 1$), whereas the settling is inhibited when the turbulence velocity fluctuations are smaller than the particle gravitational velocities ($\tau_p g/u' > 1$). However, the change in mean

		V_q/u'	L/D	λ/D	η/D
Disk ♯1	$dt = 2$	1.50	9.1	3.6	0.016
	$dt = 10$	3.17	9.42	4.2	0.093
	$dt = 20$	4.25	9.9	4.9	0.155
Disk ♯2	$dt = 2$	1.45	7.28	2.87	0.0128
	$dt = 10$	3.07	7.54	3.34	0.0744
	$dt = 20$	4.11	7.92	3.92	0.133
Disk ♯3	$dt = 2$	2.50	6.06	2.39	0.011
	$dt = 10$	5.27	6.28	2.78	0.062
	$dt = 20$	7.07	6.6	3.26	0.111

Table 4.3: Values of the particle-turbulence velocity ratio (V_q/u') and main turbulent structures to particle diameter ratios, where L stands for the integral lengthscale, λ for the Taylor lengthscale and η for the Kolmogorov lengthscale

velocity descent might not follow the same trend when aspherical particles with strong secondary motion are considered.

In here, the mean velocity fluctuations never exceeds the value of the particle descent velocity in quiescent flow and represents a velocity fluctuation of about $0.7V_q$ for the most turbulent case. Therefore, being in the $\tau_p g/u' > 1$ scenario, particles should always fall slower than in quiescent flow (if the trend for spherical particles is conserved). Sample

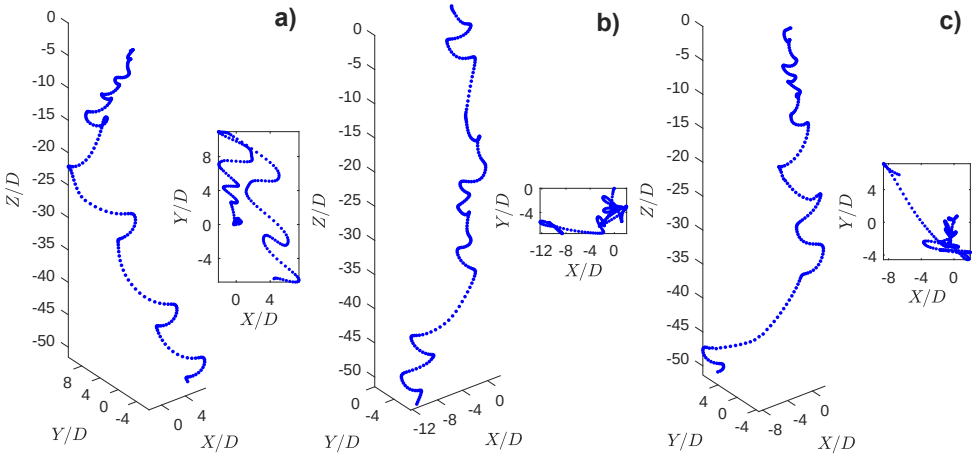

Figure 4.9: Reconstructed 3D trajectories and (X, Y) planar projection for disk ♯1 released after of waiting time $dt = 2$. The particle dispersion is normalized with the disk diameter.

particle trajectories falling under the effect of background turbulence are plotted in figure 4.9 to allow visual comparison with the trajectories of disks falling in quiescent flow (4.6). A few interesting events are observed for the cases presented; in figure 4.9 a) one can observe that the disk, strongly influenced by large turbulent structures in the flow can describe low frequency oscillations in the $X - Y$ plane, leading to very long gliding sections during the descent that increase severely the particle dispersion. At the same time, one can observe in all figures that the local slope of the gliding sections (and

therefore particle nutation angle θ) is considerably higher than in the case of quiescent flow. However, this does not occur after every turning section but depends on the local flow around the particle.

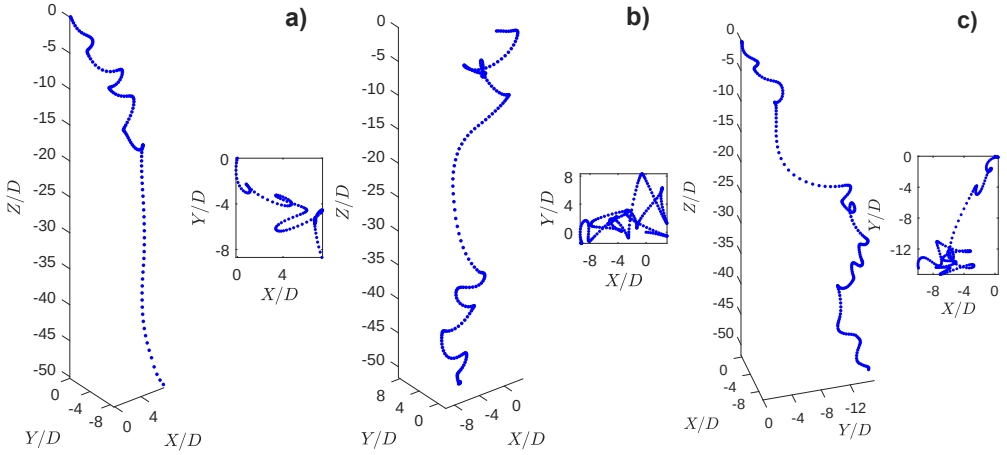

Figure 4.10: Reconstructed 3D trajectories and $X-Y$ planar view released after of waiting time $dt = 2$. The particle dispersion is normalized with the disk diameter. a) Disk ♯1, b-c) Disk ♯2

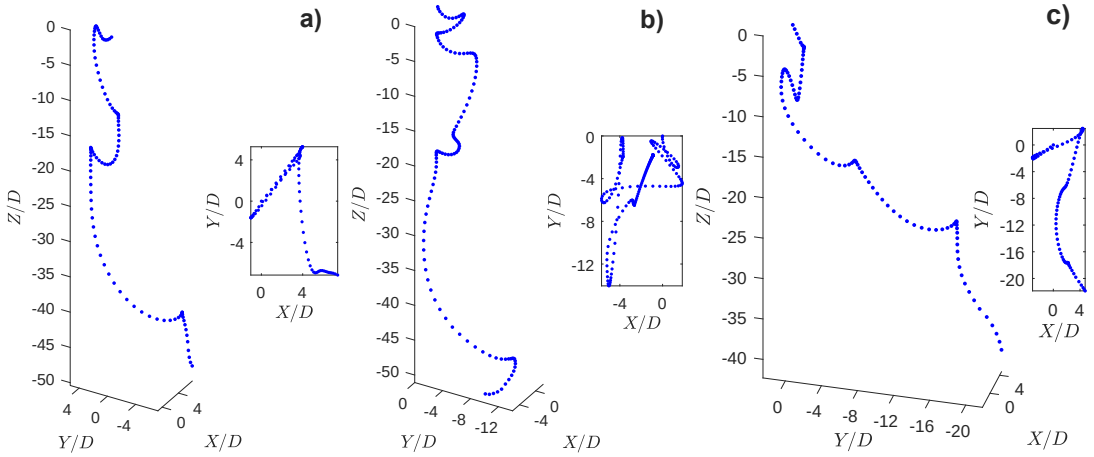

Figure 4.11: Reconstructed 3D trajectories and (X, Y) planar projection for disk ♯3 released after of waiting time $dt = 2$. The particle dispersion is normalized with the disk diameter.

We believe that the long gliding sections are caused by the flow to be moving locally in the same direction as the natural motion of the particle and therefore enhancing the particle flutter. However, these long gliding events can be attenuated during the descent and be substituted by 'standard' flutter, as in the mid descent of trajectory 4.9 b). On the other hand, we believe that trajectory sections of high nutation angle are governed by the particle-turbulence interaction during the previous turning event. Thus, if a turbulent structure destabilizes the particle at the turning point inducing a higher nutation angle, this can strongly modify the particle local descent (until the new turning

point is reached), as sketched in figure 4.12. In some rare instances we observe the

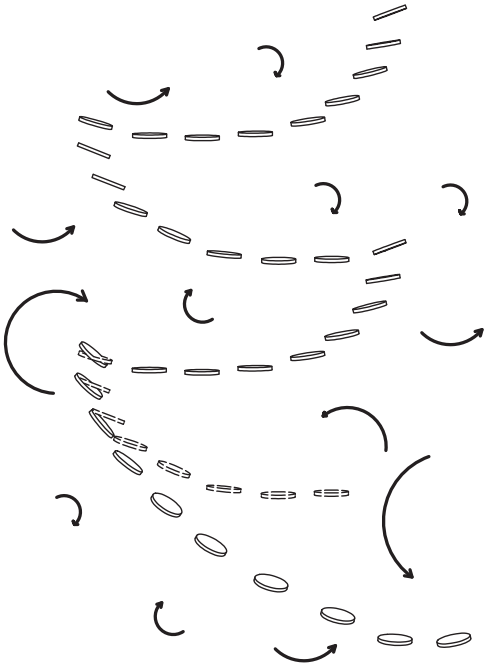

Figure 4.12: Sketch of a disk falling under the effect of turbulence to illustrate how turbulent structures destabilize the particle near the turning points. The particle with dashed contours represent the particle trajectory in quiescent flow.

particle to describe a complete 'tumbling event' in between successive gliding sections. This can be observed in figure 4.9 c) at about the vertical position of $Z/D \approx -35$. In these situations we believe that the particle inertia overcomes the fluid resistance during the turning point due to in increase in the relative velocity, leading to a complete particle revolution.

Similarly, figure 4.10 and figure 4.11 show other particle-fluid interactions leading to 'fast' descents. One can observe that in some cases the particle reaches a very high incidence angle right after the turning event, leading to a very fast descent with the disk leading edge aligned with descent motion, figure 4.10 a). Another interesting descent event observed is the slow tumble motion, as in figure 4.10 b). In this situation, the disk starts a standard gliding section but instead of the usual descent velocity attenuation before reaching the extreme of the planar oscillation, the descent velocity keeps increasing and the disk undergoes a complete rotation. We believe this might be caused by the particle interaction with a large turbulence structure that destabilize the particle steadily during the gliding section. We only observed this effect for disk ♯1 and disk ♯2 and we believe that these large turbulence structures might not be strong enough to overcome particle inertia for disk ♯3 (particle with higher I^*). In figure 4.11 one can observe some of the fast events described before; i.e. combination of high and low frequency oscillations in a-b) and tumbling events in c).

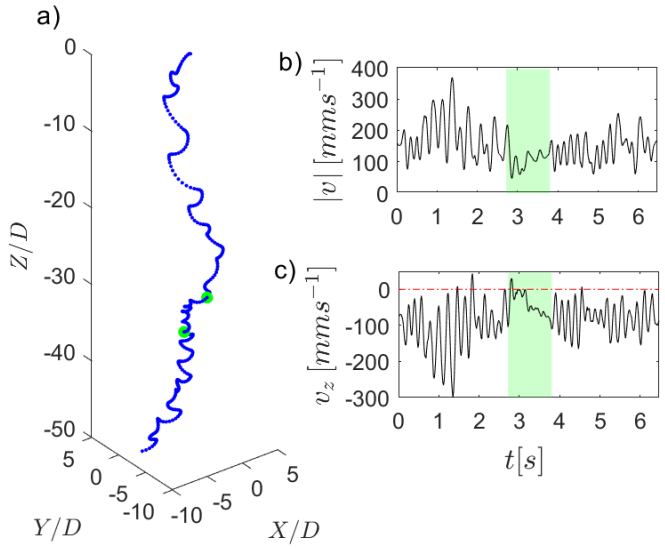

Figure 4.13: 'Slow' event during the descend of disk ♯1 under turbulence effects released after a waiting time $dt = 2$. a) Reconstructed 3D trajectory with the dispersion normalized with the disk diameter, green dots show the start and end of the 'slow' subsection. b-c) Time evolution of the particle speed and particle descent velocity, the green shaded region showing the 'slow' subsection.

Figure 4.13 shows a sample trajectory of disk ♯1 that contains a trajectory section with very low velocity magnitude that spans for two particle periods in quiescent flow. From the evolution of the speed and the descent velocity (figure 4.13 b) and c) respectively) one can observe that this event occurs in between two sections of 'standard' descend. This highlights the influence of turbulence in the local dynamics of the disk and shows that certain particle-turbulence configurations can lead to a severe reduction of the descent velocity and total speed for long durations. These trajectories, with 'slow' and 'fast' events contained within a single descent illustrate the complexity of the disk trajectories when background turbulence is introduced.

4.3.2.1 Descent velocity

The mean descent velocity of the disks, in table 4.4 and figure 4.14, show that the presence of background turbulence always enhances the particle descent for the nine cases tested. Furthermore, one can observe that as turbulent kinetic energy increases (reducing waiting time dt), all three disks fall faster. It is also important to highlight that as turbulent kinetic energy increases the spread of the data becomes more pronounced, suggesting that 'extreme' events occur more often.

Figure 4.15 shows the data corresponding to the 200 trajectories per disk (a) Disk ♯1, b) Disk ♯2, c) Disk ♯3) and waiting time ($dt = 2\,s$ in red, $dt = 10\,s$ in orange and $dt = 20\,s$ in yellow) in the form of probability density functions of the mean descent velocity per

Disk	$dt = 2\,[\mathrm{s}]$	$dt = 10\,[\mathrm{s}]$	$dt = 20\,[\mathrm{s}]$
♯1	111 ± 23	103 ± 16	98 ± 11
♯2	110 ± 29	103 ± 23	96 ± 13
♯3	193 ± 52	188 ± 48	177 ± 26

Table 4.4: Values of the particle mean descent velocity for the three points in time during the turbulence decay. Units in mms^{-1}.

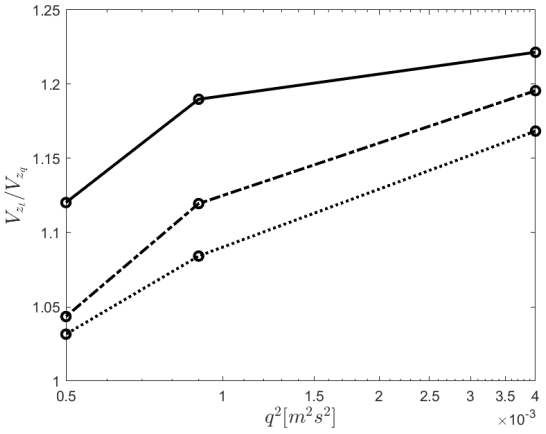

Figure 4.14: Evolution of the mean descent velocity of inertial disks as a function of the turbulence intensity. The descent velocity of the particles is normalized using the mean descent velocity of the particle in quiescent flow (V_{z_q}). Dotted line stands for disk ♯1, broken line for disks ♯2 and solid line for disk ♯3.

trajectory. These figures show that as the turbulent kinetic energy increases all three disks exhibit fast descents more often than in quiescent flow. In some extreme instances, the mean descent velocity along a single trajectory can double the descent velocity of the disk in quiescent flow; and this is observed for the three disks under strong background turbulence (red lines). However, one can also observe that the tails of the red lines in figure 4.15 also become wider towards the slower side of the velocity range.

The same results are shown as a cumulative density function (CDF) in figure 4.16 to emphasize the effect turbulence intensity on the mean descent of the particles. In these figures one can observe that independently of the particle characteristics and waiting time the descents that are slower than the mean descent in quiescent flow (left of the vertical broken line) correspond to about 20% of the total cases. Also, it is interesting to highlight that the region of overlap in the CDF's increases with increasing the particle Archimedes number (Ar). This suggests that as Ar increases the particle might be less sensitive to flow perturbations. However, we hypothesize that if these perturbations occur close to the turning point of the particle (when the particle inertia is at a minimum), the flow perturbations can significantly change the particle angle of attack; leading to steeper gliding sections with higher settling velocity.

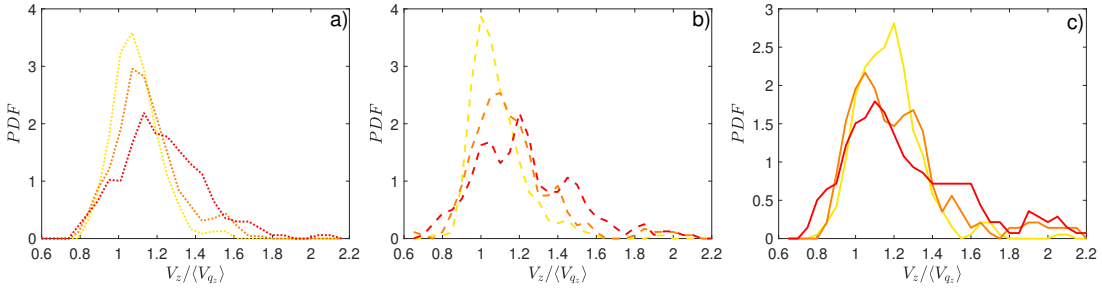

Figure 4.15: Probability density function (PDF) of the ratio of the measured mean descent velocity for disks falling in background turbulence to the measured mean descent velocity of the disks in quiescent flow. The colours of the PDF stand for different waiting times: yellow for $dt = 20$, orange for $dt = 10$ and red for $dt = 2$. a) Disk ♯1, b) Disk ♯2 and c) Disk ♯3.

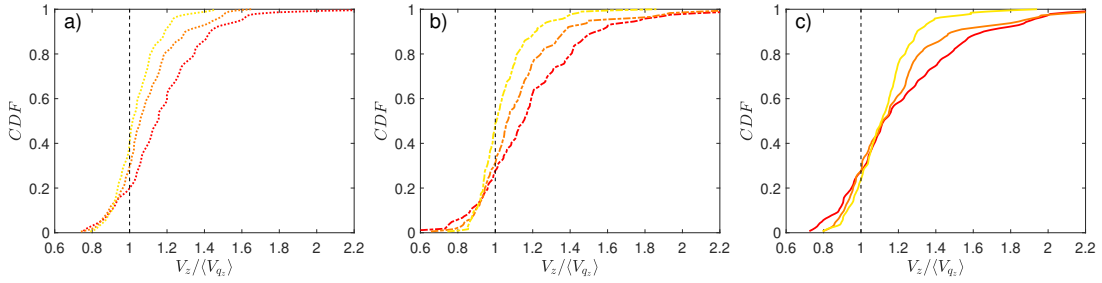

Figure 4.16: Cumulative density function (CDF) of the mean descent velocity normalized with the mean descent velocity of the disks in quiescent flow. The colours of the CDF stand for different waiting times: yellow for $dt = 20$, orange for $dt = 10$ and red for $dt = 2$. a) Disk ♯1, b) Disk ♯2 and c) Disk ♯3.

As aforementioned, we analyse the frequency content of the descent velocity signal by applying FFT using Matlab. In here, we plot the mean power spectral density (PSD) of all trajectories under the same turbulence conditions and compare it with the data obtained for the case of quiescent flow. Figure 4.17 shows the frequency content of the descent velocity signal for the three disks in the subfigures a), b) and c) respectively. One can observe that the oscillatory frequency of all three disks in quiescent flow (black line) is maintained independently of the strength of the background turbulence. However, as turbulence increases and interacts with the particle the relative strength of this frequency is reduced and the energy content is transferred to smaller frequencies. Interestingly, one can observe that the power spectral density of disk ♯3, that is the particle with higher dimensionless inertia, in figure 4.17 c) happens to be less affected as turbulent kinetic energy increases, whereas for disks ♯1 and ♯2 (figure 4.17 a) and b) respectively) a very similar trend is observed. Another important feature observed in the PSDs is that the frequency content does not only become wider, but also changes shape; and a high energetic frequency at about $f \approx 0.5\,\mathrm{Hz}$ is observed in all cases. This turbulence-induced frequency does not correspond to the characteristic frequency of any of the flow scales considered in table 4.5. In fact, we believe that for these particle-flow configurations the

Disk	$dt = 2$ [s]	$dt = 10$ [s]	$dt = 20$ [s]
t_L	1.76	7.75	18.15
t_λ	0.69	2.75	8.98
τ_η	0.024	0.080	0.255

Table 4.5: Values of the the integral timescale (t_L), Taylor lengthscale (t_λ) and Kolmogorov lengthscale (τ_η) for the three flow conditions. Units in seconds.

flow is not entirely responsible for the particle oscillation at $f \approx 0.5\,\mathrm{Hz}$ but that only destabilizes the particle acting as a trigger mechanisms that leads to the long gliding sections of the descent.

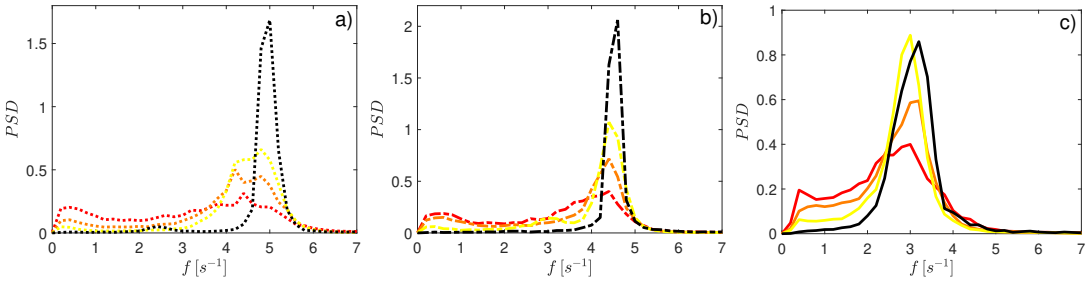

Figure 4.17: Normalized power spectral density (PSD) of the velocity fluctuations on the vertical direction. The colours of the PSDs stand for different waiting times: yellow for $dt = 20$, orange for $dt = 10$ and red for $dt = 2$. a) Disk ♯1, b) Disk ♯2 and c) Disk ♯3.

We believe that the severe changes in the mean descent velocity of the particle and the modulation of the descent velocity frequency content are associated with different types of turning events. Therefore, in the next section we will identify the 'fast' and 'slow' trajectories based on the mean descent velocity and see whether or not they share similar characteristics regarding falling style and frequency content.

To verify this hypothesis we first show the descent velocity of each trajectory as a function of the dominant frequency of the descent velocity fluctuations. In here, the dominant frequency and mean velocity are normalized with the values obtained from the quiescent case. Figure 4.18 shows the mean descent velocity of the particle along a trajectory versus the dominant frequency of the oscillations in the descent velocity for the three turbulence intensity cases and the quiescent baseline. The results of disk ♯1, disk ♯2 and disk ♯3 in figure 4.18 a), b) and c) respectively, show that trajectories with higher descent velocity than the quiescent case are more likely to describe small frequency oscillations. Contrary, trajectories with smaller mean descent velocity are shown to describe slightly higher velocity fluctuations than the natural frequency in quiescent flow. Interestingly, the frequency of the velocity fluctuations never exceeds $1.3 f_q$ independently of the flow condition, suggesting that particles might be filtering all

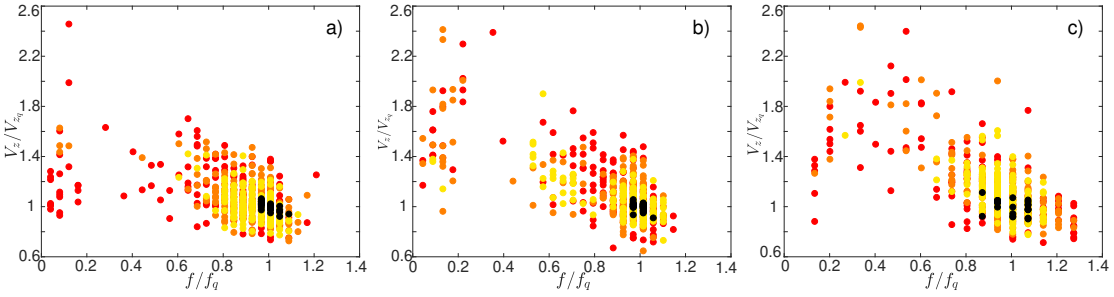

Figure 4.18: Mean descent velocity of disks in turbulent flow as a function of the dominant frequency observed in the fluctuations of the descent velocity. Velocity and frequency are normalized with the values of the quiescent cases. The colours in the scatter plot stand for flow configurations: black for quiescent flow, yellow for $dt = 20$, orange for $dt = 10$ and red for $dt = 2$. a) Disk ♯1, b) Disk ♯2 and c) Disk ♯3.

turbulence fluctuations with timescales smaller than $1/1.3f_q$; but more detailed experiments are needed to draw strong conclusions along these lines. Also, one can observe that as turbulence intensity increases the spread of the data also increases, leading to both very fast and considerably slow descents.

Now we can also group the trajectories according to the mean descent velocity of the particle. The velocity threshold that we use for 'slow' trajectories is the mean descent velocity of each disk in quiescent flow and this represents about 20% of the trajectories under turbulence effects. Then, to compare a similar amount of trajectories we group the 20% of the fastest descents for each particle. This represents a velocity threshold of about $V_z = 1.3, 1.4, 1.5\, V_{q_z}$ for disks ♯1, ♯2 and ♯3, respectively. These two groups of trajectories; i.e. 'slow' and 'fast' trajectories, are now investigated following the same procedure.

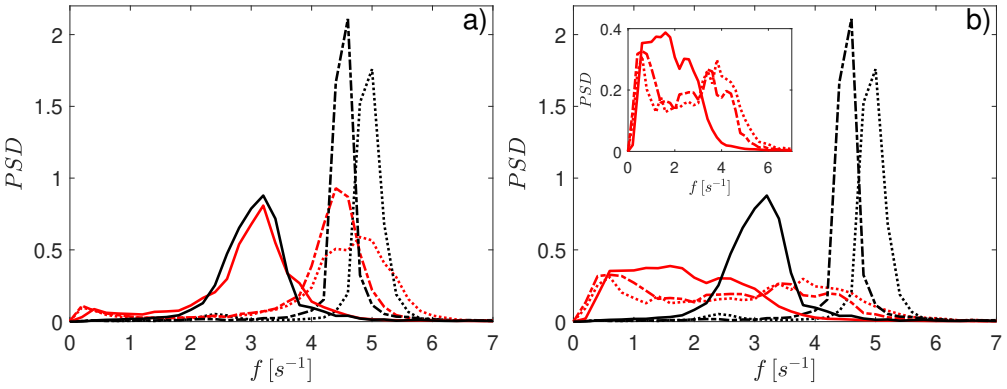

Figure 4.19: Normalized power spectral density (PSD) of the descent velocity fluctuations. The red lines stand for the conditional averaged trajectories 'Slow' trajectories in a), 'Fast' trajectories in b). The black lines correspond to the data for quiescent flow. The line styles represent the three different particles; dotted line for disk ♯1, broken line for disk ♯2 and solid line for disk ♯3.

Figure 4.19 shows the normalized power spectral density of the grouped trajectories. One can see that 'slow' trajectories (red lines in figure 4.19 a)) have a very similar energy distribution in the frequency domain as the trajectories for the disks in quiescent flow (black lines). Contrary, 'fast' trajectories (red lines in figure 4.19 b)) show a severe modulation of the energy distribution in the descent velocity signal, where low frequency motions appear to dominate the descent. It is also interesting to note the bimodal energy distribution observed for disk ♯1 and ♯2 in the inset of figure 4.19 b). The high frequency peak of these distributions is much more attenuated and is located at a lower frequency that in quiescent flow (3.8 and 3.4 Hz for disk ♯1 and ♯2 respectively), whereas the low frequency peak is in both cases at 0.6 Hz, as first estimated from figure 4.17 for all trajectories recorded. These results show that two different dominant frequencies can coexist in 'fast' trajectories; the natural frequency of oscillation of the disk and the 'turbulence induced frequency'. On the other hand, for the case of disk ♯3 the contribution of the two dominant frequencies are overlapped forming a wider unimodal energy distribution and therefore the two peaks are not as easy to identify as in the former cases.

Instead of identifying trajectories based on the mean descent velocity along the complete descent we can also identify them based on individual 'fast' or 'slow' events. We consider 'fast' events everything that occurs with a descent velocity higher than two times the mean of the maxima descent velocity in quiescent flow ($v_z(t) > 2 \cdot max(V_{q_z})$), with these values previously reported. On the other hand, slow events correspond to sections of the trajectory (at least of two periods of the particle in quiescent flow, $2/f_q$) for which the magnitude of the descent velocity does not reach half of the mean of the maxima descent velocity expected in quiescent flow ($v_z(t_i : t_{i+2/f_q}) < 0.5 \cdot max(V_{q_z})$). It is important to note that this distinction between 'fast' and 'slow' events is much more restrictive for slow events, since these have to be sustained for a relatively long period in time whereas fast events might correspond to a sharp peak on the velocity evolution.

Disk	$dt = 2$ [s]	$dt = 10$ [s]	$dt = 20$ [s]
♯1	$S = 10$, $F = 64$	$S = 3$, $F = 26$	$S = 1$, $F = 2$
♯2	$S = 8$, $F = 72$	$S = 2$, $F = 29$	$S = 1$, $F = 3$
♯3	$S = 3$, $F = 30$	$S = 1$, $F = 17$	$S = 1$, $F = 3$

Table 4.6: Number of trajectories with 'Slow' (S) and 'Fast' (F) events for the three flow conditions.

The probability of these events to occur along a trajectory is shown in table 4.6. One can observe that 'fast' events are dominant over 'slow' events for the particles and flow conditions investigated. For the cases of high and mid-level turbulence ($dt = 2\,s$ and $dt = 10\,s$), the probability of these events to occur is nearly the same for disk ♯1 and disk ♯2. Contrary, disk ♯3 shows a smaller number of extreme events, but we believe

this might be strongly influenced by the shorter relative length of the descent (about 30% shorter in terms of particle diameters). On the other hand, the statistics of all three disks for the case of low turbulence intensity are very similar.

4.3.2.2 Planar $X-Y$ dispersion

Figure 4.20 shows the scatter plots of disk ♯1 for the three flow conditions maintaining the reference color of the plane crossed.

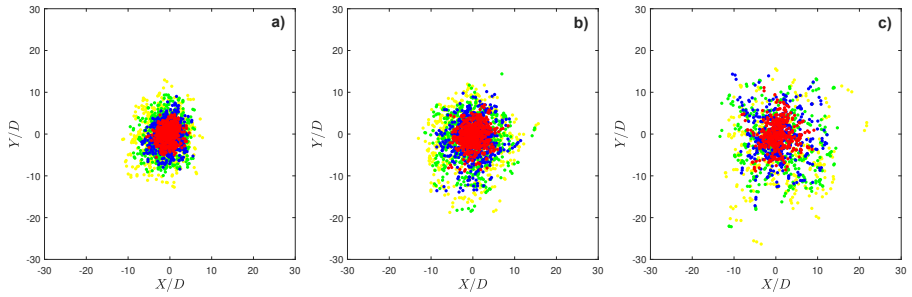

Figure 4.20: $X-Y$ scatter plot of disk ♯1 for the three flow conditions; a) $dt=20$, b) $dt=10$ and c) $dt=2$. The colours stand for the vertical particle location; red $Z/D=10$, blue $Z/D=20$, green $Z/D=30$ and yellow $Z/D=40$.

		$Z/D=10$	$Z/D=20$	$Z/D=30$	$Z/D=40$
Disk ♯1	$dt=2$	$\mu=1.41,\ \sigma=0.63$	$\mu=1.73,\ \sigma=0.62$	$\mu=2.15,\ \sigma=0.57$	$\mu=2.31,\ \sigma=0.55$
	$dt=10$	$\mu=1.22,\ \sigma=0.48$	$\mu=1.65,\ \sigma=0.65$	$\mu=1.89,\ \sigma=0.47$	$\mu=2.05,\ \sigma=0.55$
	$dt=20$	$\mu=0.98,\ \sigma=0.49$	$\mu=1.31,\ \sigma=0.58$	$\mu=1.55,\ \sigma=0.52$	$\mu=1.77,\ \sigma=0.49$
Disk ♯2	$dt=2$	$\mu=1.38,\ \sigma=0.65$	$\mu=1.90,\ \sigma=0.49$	$\mu=2.08,\ \sigma=0.64$	$\mu=2.18,\ \sigma=0.60$
	$dt=10$	$\mu=1.14,\ \sigma=0.55$	$\mu=1.56,\ \sigma=0.53$	$\mu=1.80,\ \sigma=0.65$	$\mu=1.89,\ \sigma=0.64$
	$dt=20$	$\mu=1.06,\ \sigma=0.50$	$\mu=1.34,\ \sigma=0.46$	$\mu=1.53,\ \sigma=0.69$	$\mu=1.61,\ \sigma=0.73$
Disk ♯3	$dt=2$	$\mu=1.34,\ \sigma=0.42$	$\mu=1.74,\ \sigma=0.57$	$\mu=2.09,\ \sigma=0.56$	–
	$dt=10$	$\mu=1.18,\ \sigma=0.46$	$\mu=1.51,\ \sigma=0.42$	$\mu=1.59,\ \sigma=0.53$	–
	$dt=20$	$\mu=1.04,\ \sigma=0.46$	$\mu=1.29,\ \sigma=0.44$	$\mu=1.50,\ \sigma=0.57$	–

Table 4.7: Mean (μ) and standard deviation (σ) of the lognormal distribution fitted to the dispersion data.

We observe that the scatter plots of the data are nearly radially symmetric and therefore, in the following analysis, we simplify the particle dispersion as a function of a unique scalar value ($R=\sqrt{(X-X_0)^2+(Y-Y_0)^2}$), where the particle absolute position at the start of the analysis (X_0-Y_0) is subtracted. We also observe a severe increase in particle dispersion at a vertical location $Z/D=40$ (yellow markers on figure 4.20), being for the three cases one order of magnitude larger than for the quiescent case (figure 4.6 a)).

Figure 4.21 shows the ensemble particle trajectories for disk ♯1, disk ♯2 and disk ♯3 at the different flow conditions. In this figure one can observe that disks increase significantly lateral dispersion in all turbulence cases compared with the quiescent case. To better illustrate the particle dispersion during the fall, the particle $X-Y$ position is obtained

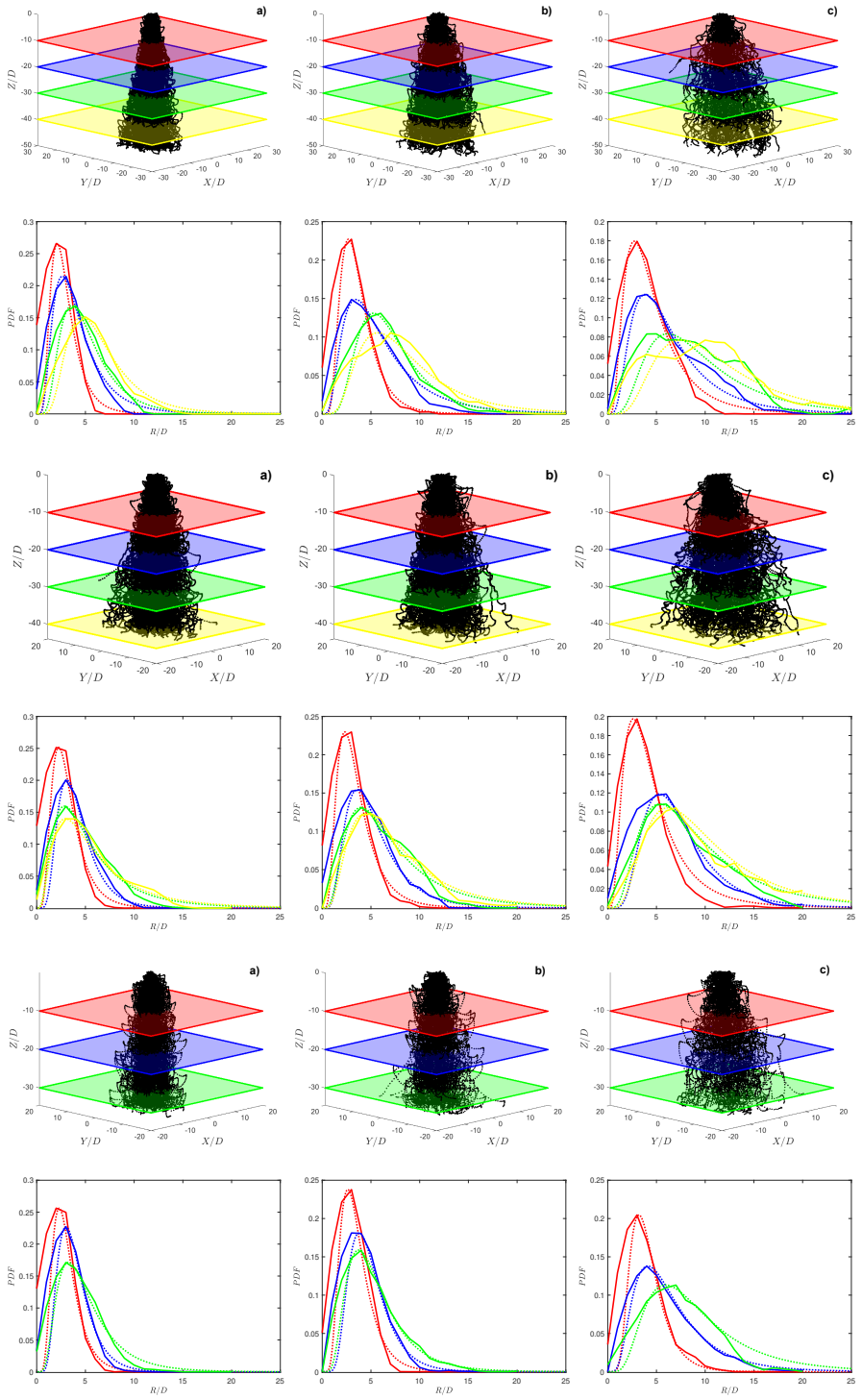

Figure 4.21: Reconstructed 3D trajectories for disk ♯1 (top row), disk ♯2 (middle row) and disk ♯3 (bottom row). The horizontal planes are located at 10, 20, 30 and 40 D from the start of the measurements. Each vertically arranged pair of figures corresponds to a different turbulence intensity background; a) $dt = 20$, b) $dt = 10$ and c) $dt = 2$. The PDFs show the associated measured data (solid line) and log-normal fits (dotted line) at the vertical locations aforementioned.

at vertical intervals of $10\,D$ from the start of the data analysis. These locations are depicted in figure 4.21 with coloured horizontal planes.

The radial dispersion of the disks at the aforementioned vertical locations are shown below in the ensemble 3D trajectory reconstruction of the particle for the three flow conditions, see figure 4.21. We found that the dispersion of the particle can be well predicted by log-normal distributions, also shown with dotted lines. The fits show a clear deviation from the measured data in the region close to the origin but capture accurately the peak and outer region of the particle dispersion. The same approach is used for all radial distributions and the parameters of the fitted functions are included in table 4.7. To directly compare the particle dispersion from one disk to another we plot

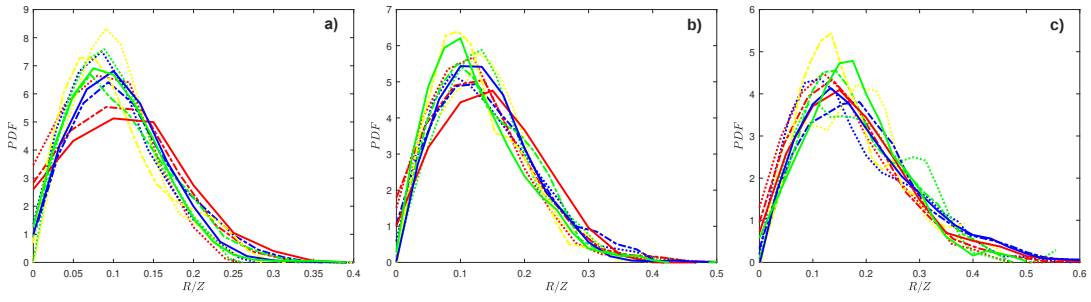

Figure 4.22: Measured probability density function of the particle radial location for disks ♯1 (dotted lines), ♯2 (broken lines), ♯3 (solid lines) falling at the three flow conditions; a) $dt = 20$, b) $dt = 10$ and c) $dt = 2$. The colours stand for the particle location in the $z-$ coordinate; red for $Z/D = 10$, blue for $Z/D = 20$, green for $Z/D = 30$ and yellow for $Z/D = 40$.

the probability density function of the three disks for each flow condition separately (not shown here). We observe the tails of the PDFs to increase with the particle descent and therefore we propose to use the $z-$ location associated with each measurement plane to collapse the radial dispersion of the particle, as in figure 4.22. A constant virtual origin is used to make the data collapse as, $R/(Z_{v.o}+Z)$, where $Z_{v.o} = 150\,mm$ for all cases shown here. The collapse of the data for disks with different dimensionless number under the same flow conditions proves that the relative dispersion of the particle is non-universal and it depends on the particle design parameters and flow conditions.

4.3.2.3 Ornstein–Uhlenbeck (OU) process to model descent velocity fluctuations

In this section, the OU process is used to model the fluctuations of the particle descent velocity falling under the effect of turbulence. The probability density function of the instantaneous descent velocity fluctuations for the cases $dt = 10\,s$ and $dt = 20\,s$ departs noticeable from the Gaussian distribution and therefore only the high turbulence intensity case ($dt = 2\,$s) will be used in this section.

A fundamental question for predicting particle dispersion is how turbulence and particle shape interact, leading to a broad range of particle velocity fluctuations. As we have seen in the previous sections, the particle velocity fluctuations for inertial particles describing secondary motions is not entirely determined by turbulence itself. We believe that particle motion is controlled by a combination of the particle preferential motion / alignment with the local turbulent flow. This represents a very challenging problem that cannot be analytically solved and empirical correlations that can capture the particle dynamics are an important input when modelling particle motion.

The stochastic description of particle velocity fluctuations can have multiple forms, but in here we explore the use of a diffusion process, the Ornstein–Uhlenbeck (OU) process, to model the turbulence effect on the particle velocity fluctuations. The OU process is a temporary homogeneous Gaussian and Markov model that has been traditionally used to describe diffusion of massive brownian particles under the influence of friction. As reported in Pope [2000], OU processes together with their corresponding Langevin equation can be used to predict fluid-particle turbulent dispersion. Being the OU process a Markov chain model implies that the next state of the particle only depends on the current state and we believe that this might be a good approximation for the motions observed in here.

An OU process is completely characterized by a Gaussian distribution and an exponentially decaying autocorrelation, both of which are statistically stationary, as described in Doob [1942]. The autocorrelation of a time series -in this case descent velocity $v_z(t)$- is defined as $\rho(\tau) = \langle v_z(t)v_z(t+\tau)\rangle$; being t time, τ a time lag, and the angle brackets standing for expectation values. For an OU process, the autocorrelation $\rho(\tau)$ is a negative exponential of the form $\rho(\tau) = \alpha^2 e^{-\tau/T}$, where α^2 is the variance of the distribution of $v_z(t)$ (which is Gaussian), and the timescale T is known as the integral timescale of the process.

Pope [2000] showed the viability of using the OU process to describe accurately the Lagrangian velocity of fluid-particles in turbulent flow. Thus, by means of assuming that the particle motion is described by OU processes one can obtain the time-dependent eddy diffusivity that characterize the particle turbulent diffusion. This approach has been recently used to describe the rotational diffusion of neutrally buoyant large solid particles under turbulence effects, [Meyer et al., 2013].

As explained in Meyer et al. [2013] for particle rotation, the OU process can be also used to determine the translation time-dependent eddy diffusivity of large particles in turbulence flow as

$$K_{v_z} = \int_0^t \rho(\tau)d\tau = \alpha_{v_z}^2 T_{v_z}(1 - e^{-t/T_{v_z}}) \tag{4.1}$$

where α_{v_z} represents the standard deviation of the descent velocity fluctuations and T_{v_z} the integral time scale of the descent velocity fluctuations.

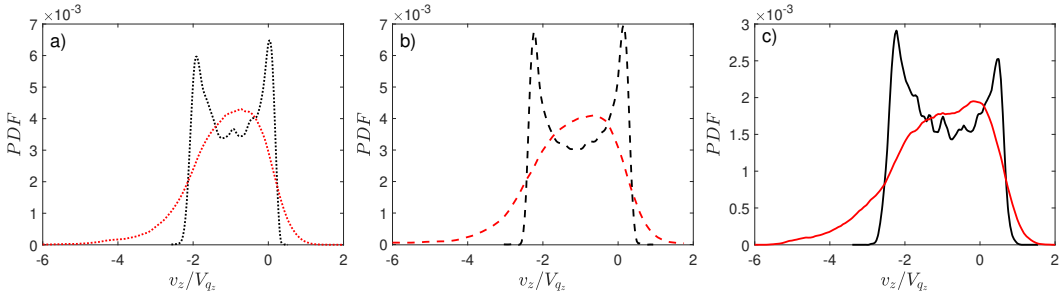

Figure 4.23: Measured probability density function (PDF) of the instantaneous particle descent velocity falling under high turbulence intensity background ($dt = 2$) in red. The quiescent data is plotted in black for comparison. a) disks ♯1 (dotted lines), b) disk ♯2 (broken lines) and c) disk ♯3 (solid lines).

First, it is of interest to verify that the specific process of particle sedimentation in here meets the three conditions to be a OU model. The gaussian assumption is investigated by measuring the kurtosis (κ) of the distribution of the instantaneous descent velocity fluctuations (shown in figure 4.23). The magnitude of the kurtosis is shown in table 4.8 and these are reasonably close to the characteristic value $\kappa = 3$ for Gaussian distributions. The PDF's of the instantaneous descent velocity of the disks in quiescent flow is also shown in figure 4.23 to show the reader the severe change in the dynamics of the particle. The two peaks in the PDFs of the quiescent trajectories (characteristic of the sinusoidal and nearly periodic descent) vanish in favour of a more uniform distribution of the descent velocity fluctuations. Similarly, figure 4.24 shows the descent velocity au-

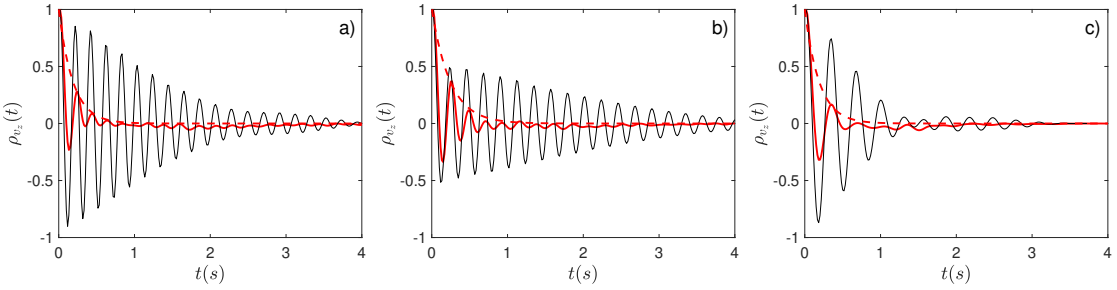

Figure 4.24: Autocorrelation function normalized with the root mean square of the velocity fluctuations of the particle descent velocity falling under high turbulence intensity background ($dt = 2$) in red. The quiescent data is plotted in black for comparison. The broken line corresponds to the fitted exponential decay to the peaks of the autocorrelation function. a) Disks ♯1 , b) Disk ♯2 and c) Disk ♯3.

tocorrelation (ensemble average of 200 trajectories) for the three particles investigated. This figure shows that the autocorrelation does not describe a simple negative exponential decay but that it describes oscillations with amplitudes exponentially decreasing. This is a remaining footprint of the natural oscillation of the particle; and shows that despite the severe influence of turbulence, all three disks tend to oscillate as in free fall.

In here, the peaks of the autocorrelation function are used to create an adapted negative exponential evolution of the autocorrelation and therefore the OU process will only capture the dynamics of the descent fully governed by turbulence and not the natural oscillation of the particle. The parameters of the exponential functions fitted to the experimental data are shown in table 4.8.

Statistics	Disk ♯1	Disk ♯2	Disk ♯3
α_{v_z}	1.55 (1.51, 1.60)	1.64 (1.55, 1.72)	2.56 (2.46, 2.65)
T_{v_z}	0.188 (0.164, 0.220)	0.243 (0.200, 0.312)	0.190 (0.153, 0.25)
κ_{v_z}	3.4 (-)	3.9 (-)	2.9 (-)

Table 4.8: Moments of descent velocity probability density functions (PDFs) with 95% confidence intervals (CIs). Here κ if the kurtosis of the PDF of v_z; and α_{v_z} and T_{v_z} are the noise-free standard deviation and integral time scale obtained from the exponential fit.

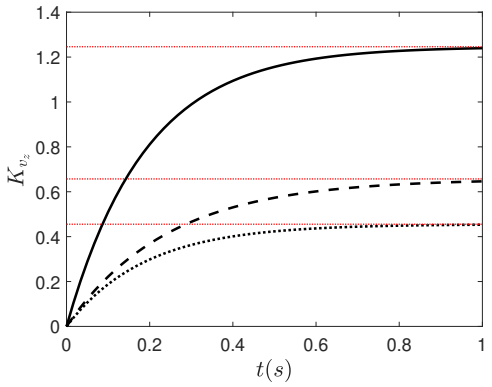

Figure 4.25: Time-dependent descent velocity diffusivity model for the disk ♯1 (dotted line), disk ♯2 (broken line) and disk ♯3 (solid line). Red dotted lines stand for the Fickian asymptote $\hat{K} = \alpha_{v_z}^2 T_{v_z}$.

Figure 4.25 shows the time-varying diffusivity predicted by using the OU process, as described by equation 4.1. When the exponential term diminishes, the diffusivity tends to a constant value, known as the Fickian asymptote $\hat{K} = \alpha_{v_z}^2 T_{v_z}$. The Lagrangian integral timescale of the descent velocity fluctuations is different for each of the particles considered but the results are non-conclusive regarding the effect of particle dimensionless inertia (I^*) or particle Archimedes number (Ar). Similarly, the variance of the descent velocity fluctuations, also shown in table 4.8, is very similar for disk ♯1 and ♯2 but increases severely for disk ♯3.

We have shown that the descent velocity fluctuations of inertial particles settling under the effect of background turbulence (homegeneous and nearly isotropic) can be modelled as an OU process. However, the nearly periodic motions that arise due to particle secondary motion have to be disregarded (as shown in figure 4.24). It is only after doing so that the correlation of the velocity fluctuations follow a negative exponential evolution over time and therefore become suitable for an OU process. We observed that

particle dimensionless inertia does not suffice to account for the change in diffusivity and therefore a more detailed analysis ought to be done.

4.4 Summary

Contrary to what was found for spherical particles, finite-size inertial disks show an increase in the descent velocity for turbulence velocity fluctuations smaller than the particle gravitational velocity ($V_q/u' \approx [1.45 - 7]$). However, we found that this velocity ratio is not the only parameter responsible for the velocity enhancement since different disks show a different relative velocity increase for similar velocity ratios. We believe that the physical mechanisms responsible of the change in the descent velocity of aspherical planar particles are different from the ones observed for spheres. In the case of finize-size inertial disks, as turbulence intensity increases the likeliness of the particle to reach a higher angle of attack also increases. When this occurs, the particle strong inertia and relative small drag acting on the particle at this configuration leads to a severe enhancement of the local descent velocity.

We found that disks under strong turbulence effects may describe features that are characteristic of other descent styles associated with different particle dimensionless number in still fluid, as the tumbling motions. We also found that the motion of disks seems to be unaffected by turbulence structures with characteristic timescales approximately smaller than the inverse of the natural frequency of the particle in quiescent flow ($1/1.3f_q$), since the footprint of these are not captured in the frequency content of the particle descent velocity. Besides, we observe that the mean descent velocity and the magnitude of dominant frequency of the oscillatory motion are inversely correlated for individual trajectories.

We observed a strong turbulence footprint on the particle dispersion for all cases tested. Small mean velocity fluctuations (corresponding to less than 25% of the particle descent velocity in quiescent flow) increase significantly the particle dispersion compared with the quiescent case. The PDF of the particle radial position can be well captured with lognormal distributions and we observed a linear increase in the peak of the distribution with vertical position.

Last, we explored the use of the Ornstein–Uhlenbeck process to model the particle descent velocity fluctuations for the high turbulence intensity cases. From the inspection of the PDF's of the instantaneous descent velocity fluctuations, these appear to be the most suitable cases for this approach. We observed that we can model the velocity fluctuations along the descent with this approach only if a modified version of the autocorrelation function is employed. Despite the promising results regarding the time dependent eddy diffusivity, a more detailed analysis is needed to assure the robustness of the approach

for the experimental data taken and to extract conclusive results regarding the effect of particle dimensionless numbers and turbulence characteristics.

Chapter 5

Conclusions

In this study, the descent motion of planar particles in quiescent flow and under turbulence effects has been investigated. Experiments were conducted to explore the motion of irregular planar particles in quiescent flow always with a equivalent disk (same frontal area) as a baseline. Then, a zero-mean flow turbulence facility was designed and built; and the flow in the central region of the facility was characterized non only for the statistically stationary case but for free decaying turbulence. Last, the descent of inertial disks under zero-mean flow turbulence was investigated. The study was conducted as an experimental work using particle tracking, volumetric velocimetry (V3V) and planar PIV. The outcomes of the study will be summarised below.

For the quiescent flow scenario, the frontal geometry of a disk was modified following two main approaches; first a sinusoidal wave around the original perimeter allowed us to modified the particle circularity by changing the amplitude and wavelength sinusoidal perimeter, second the particle number of symmetry planes was reduced by creating $n-$ sided polygons with the same frontal area as the reference disk. We observed that as the particle circularity decreases, either by an increase in the amplitude of the peaks (a) or the number of peaks (N), a transition from planar motion to a more three dimensional descent takes places. We developed an empirical correlation function to capture the change in the drag coefficient associated with this change in particle descent. The model is based on the drag coefficient of the equivalent disk and the particle design parameters, that are the amplitude over diameter ratio (a/D) and the number of peaks around the perimeter (N). We observed a severe increase in the mean descent velocity for highly irregular particles (low isoperimetric quotient) and this appears to be well captured with the correlation proposed.

Similarly, we modified the frontal geometry of the disk to include sharp edges ($n-$ sided polygon particles). We observed that polygons describe a similar descent as wavy edge disks (regarding the out-of-plane motion) as the number of symmetry planes reduces. However, the mean descent velocity appears to be almost unaffected by the change in

frontal geometry. We proposed a new length scale ($\ell = D_c/Q$) to characterize irregular particles that does not affect the $Re - I^*$ regime map of a the disk and that reconciles the change in descent style for planar irregular particles with the well established regime map proposed in Willmarth et al. [1964] for thin disks.

Also, we investigated the wake characteristics of three different particles (disks, hexagonal plates and squares) by mean of volumetric velocimetry. We observed similar three dimensional flow structures for different particles falling under the same descent style. Thus, disks and hexagonal plates describing 'Planar zig-zag' motion show two counter rotating vortices that develop during the gliding section of the trajectory followed by a detached hairpin vortex at every turning point. However, we observed changes in the location of the elongated counter rotating vortices for the hexagonal plates that appear to be linked to the relative location of the particle edges with respect to the velocity direction. On the other hand, when the hexagon plate describes a more three dimensional descent the wake is very similar to the one observed for square plates, with complex flow structures shed continuously and nearly uniformly from the particle perimeter.

In parallel to this experiments we built a random jet array (RJA) facility to generate zero-mean flow turbulence in the laboratory. We performed planar PIV in the central region of the facility and verified that the turbulence generated is homogeneous and anisotropic to a certain extent ($u_1'/u_2' \approx 1.2$), as observed by Carter et al. [2016] in a similar facility but in air. We performed experiments not only for the statistical stationary case but for free decaying turbulence and observed a rapid 'isotropization' of the small scales, whereas large scale anisotropy persists in the flow for much longer decay times. We also observed confinement effects on the largest scales of the flow and measure the associated turbulent kinetic energy decay rate. We developed an iterative approach to measure dissipation that agrees well with the results from compensated second order structure functions and the sub-kolmogorov resolution method introduced in Tanaka and Eaton [2007] but that can be extended to higher sub-kolmogorov resolutions.

The characterization of the turbulence decay in the facility allowed us to investigate the descent motion of inertial disks falling through different levels of turbulence intensity, but always under zero-mean flow conditions. The turbulence effect at three different instants in time during the decay was investigated for a set of three inertial disks, with the quiescent case as a baseline. We observed that the mean descent velocity of all three particles in turbulence increases with increasing turbulence intensity up to 20% higher than in quiescent flow. The change in mean descent velocity is associated with long and steep gliding motions and we believe that these are induced by large turbulent structures that destabilizes the particle (most of the time during the turning section of the descent). The frequency content of the descent velocity signal shows that the three particles appear to be unaffected by turbulence structures with timescales smaller than $1/1.3f_q$. We quantified the particle dispersion in turbulence and show that radial

probability density functions can be well predicted with lognormal distributions, which tails increase with increasing turbulence intensity.

We also explored the use of a Ornstein–Uhlenbeck (OU) process to model the particle descent velocity fluctuations for the high turbulence intensity cases. We observed that we can model the velocity fluctuations along the descent with this approach only if the measured autocorrelation function is adapted and the secondary motion of the particle are not included. However, a more detailed analysis is needed to assure the robustness of the approach used. This, at the same time, should provide more conclusive results regarding the effect of particle dimensionless numbers and turbulence characteristics.

5.0.1 Future work

This study provided high quality data of a zero-mean flow turbulence facility, particularly interesting in the free decay region and under confinement effects, which was missing in the existing literature. In light of the outcomes of this study, we are currently exploring the evolution of the invariants of the reduced Reynolds stress tensor for free decaying turbulence. We hope to observe changes in these as turbulence becomes isotropic at larger scales and relate this with the evolution of the energy transfer across scales.

This study focused on the evolution of the turbulent kinetic energy for a unique (statistically speaking) initial flow condition. It could be interesting to look into the extent in time of the signature of the forcing scheme for different initial conditions, and also to explore if the initial period of the decay is the same for other turbulence intensities. To tackle this question the facility could be adapted to control the current drawn by the water pumps, leading to a variable power input and therefore initial flow conditions. Similar experiments could be performed to investigate if the geometry of the water pump nozzles has a direct effect on the nature of the large scales in the flow as in fractal jets investigated in Breda and Buxton [2017].

The data regarding inertial disks falling into turbulence has been used to extract the general trends observed; i.e, mean descent velocity and mean particle dispersion. However, we believe this dataset is very unique and will be used to further analyse the effect of turbulence intensity on the particle motion. The simple pendulum model developed for particles falling in quiescent conditions will be adapted with the aim of capturing the particle velocity fluctuations induced by background turbulence.

Appendix A

Equations of motion

This appendix provides equations of motion which are relevant to the topic of this thesis. Although these equations are not directly used along the thesis, they give insight on the motion of particles under different fluid conditions.

The evaluation of the forces acting on a spherical particle arise the BBO equation, which can be expressed as,

$$\begin{aligned}\rho_p V_p \frac{dU_p}{dt} = 6\pi a\mu(U_f - U_p) + V_p(\rho_p - \rho_f)g + \rho_f V_p \frac{dU_f}{dt} + \frac{1}{2}\rho_f V_p \frac{d}{dt}(U_f - U_p) \\ - 6\pi a^2 \mu \int_0^t \left(\frac{(d/d\tau)(U_f - U_p)}{(\pi\mu(t-\tau)/\rho_f)^{1/2}} \right) d\tau\end{aligned} \tag{A.1}$$

The right hand side terms of the former equation correspond to the drag force, gravity force, pressure gradient force, virtual mass force and Basset history force.

The Tchen equation is defined as:

$$\begin{aligned}\frac{dU_p}{dt} + aU_p + c\int_{-\infty}^{t} \frac{dU_p}{dt}(t-\tau)^{-1/2} d\tau = aU_f + b\frac{dU_f}{dt} \\ + c\int_{-\infty}^{t} \frac{dU_p}{dt}(t-\tau)^{-1/2} d\tau - \frac{2(s-1)}{2s+1} g\end{aligned} \tag{A.2}$$

in which:

$$a = \frac{18\nu}{(s+1/2)d^2} \tag{A.3}$$

$$b = \frac{3}{2(s+1/2)} \tag{A.4}$$

$$c = \frac{9(\nu/\pi)^{1/2}}{(s+1/2)d} \tag{A.5}$$

$$s = \frac{\rho_p}{\rho_f} \tag{A.6}$$

and

$$\frac{d}{dt} = \frac{\delta}{\delta t} + U_j \frac{\delta}{\delta x_j} \tag{A.7}$$

Then, the temporal derivative is evaluated along the discrete particle trajectory. The diameter of the particle is d, while ρ_p and ρ_f are the density of the particle and the fluid respectively, U_p and U_f are the velocity of the particle and of the fluid respectively and g is the gravity.
The extra force term that comes from the integration of the normal stress on the sphere surface reads as:

$$F_{press} = \frac{\pi d^3}{6} \rho_f \frac{dU_f}{dt} \tag{A.8}$$

and is incorporated in the term bdU_f/dt of Eq A.3

On the other hand, the modified Riley equation is given as:

$$\begin{aligned} \rho_p \frac{\pi d^3}{6} \frac{dU_p}{dt} = & -\frac{\pi d^2}{8} \rho_f C_D (U_f - U_p)|U_f - U_p| - \rho_f \frac{\pi d^3}{6} C_A \frac{d(U_p - U_f)}{dt} + \frac{\pi d^3}{6}(\rho_p - \rho_f) g \\ & + \rho_f \frac{\pi d^3}{6} \frac{DU_f}{Dt} - \frac{\pi d^2}{4} C_H \frac{\sqrt{\rho_f \mu}}{\pi} \int_{-\infty}^{t} \frac{d(U_p - U_f)}{dt} (t - \tau)^{-1/2} d\tau \end{aligned} \tag{A.9}$$

in which the following terms are corrected by means of empirical correlations to extent the applicability of the equation to larger particulate Reynolds numbers:

$$C_D = \frac{24}{Re_p}(1 + 0.15 Re_p^{0.687}) Re_p \leq 200 \tag{A.10}$$

$$C_A = 1.05 - 0.0066 / \left(A_C^2 + 0.12\right) \tag{A.11}$$

$$C_H = 2.86 - 3.12 / \left(A_C^2 + 1\right)^3 \tag{A.12}$$

$$A_C = \frac{|U_p - U_f|^2}{d|\frac{d(U_p - U_f)}{dt}|} A_C \leq 60 \tag{A.13}$$

with the particulate Reynolds number is

$$Re_p = \frac{|U_p - U_f| d}{\nu} \tag{A.14}$$

and

$$\frac{D}{Dt} = \frac{\delta}{\delta t} + U_j \frac{\delta}{\delta x_j} \tag{A.15}$$

meaning that the extra pressure gradient term is evaluated along the fluid motion instead of along the particle trajectory.

Appendix B

Ansys FLUENT: 2D Backward-facing step

In this appendix a numerical investigation of 2D Backward-facing step flow is presented. Although numerous investigations have been carried out on this test case, it is still interesting to perform this numerical simulation with the aim of understanding the physical characteristics of the flow separation and vortex formation in this region as well as the validation of the turbulent model for the further investigation of the Aquavitrum Separator geometry.

The parameter that will be primarily considered to identify the accuracy of the model used is the reattachment length. The normalized value of this parameter is seen to increase sharply with Reynolds number for the laminar flow regime, then it decreases irregularly with Reynolds number during the transient regime until reaching a steady value within the turbulent region. The effect of Reynolds stresses are believed to be the main cause of the decrease of the recirculation length beyond the laminar regime.

B.1 Introduction to the problem

The characteristics of separated flow has been a matter of study for decades to understand the physics of the separated shear layers and their instability mechanisms. Studies by Ross and Kegelman [1986] demonstrated that by actively controlling the flow at separation, characteristics of the coherent structure can be modified and consequently alter the flow dynamics to meet certain specifications.

Due to the complexity of separated flows, different simplified geometries are studied to understand the core of separated flows. This is the case of the backward-facing step, geometry that contains a single fixed separation point and the wake dynamics present is not perturbed by the downstream disturbances.

This particular geometry has two main regions: the free shear layer and the re-circulating bubble. It is generally believed that due to instabilities, the vortices in the shear layer roll up and pair with adjacent vortices to create larger coherent structures.

Although there have been many experiments conducted over this type of geometry, the discrepancy on some flow and geometric parameters is still a problem when comparing them. These parameters include, the expansion ratio, aspect ratio, free stream turbulence intensity, Reynolds number (based on $2H$) and the boundary layer state and thickness at separation. However, there are several characteristics that remain present or that evolve with a clear trend with the parameter modification.

B.1.1 Common Features of the Backward-Facing Step Flow.

Based on the important flow features studied by previous researchers in a backward-Facing Step geometry, the flow wake can be distinguished into three main regions: the shear layer, re-circulation zone and the reattachment zone. The general characteristics of this flow starts with a boundary layer separating at the step edge due to the adverse pressure gradient that develops into a thin shear layer. Further downstream, the shear layer grows in size with the gathering of the turbulent structures present on it. These turbulent structures entrain fluid from the non-turbulent region outside the shear layer, causing the formation of a low velocity recirculation region. As the shear layer progresses, the favourable pressure gradient originated by the fluid entrained makes it curve down towards the wall. With the latter impingement at a location known the reattachment point. However, the reattachment point has an oscillatory motion due to the inherent motion of the shear layer. In this particular test case the reattachment length is the primary parameter of interest, since its accurate prediction will give us valuable information regarding the turbulence model that better fits for our geometry. Nevertheless, the understanding of the flow at every region will be of great importance for the later analysis of the particle-fluid interaction.

B.1.1.1 Shear Layer Region

It is defined as the layer of fluid with a velocity gradient subjected to viscous shearing. The free shear present in this model is created due to the fast moving fluid on the top and the low momentum fluid in the back of the step.

Vortex Rolling and Pairing Mechanism.
Winant and Browand [1974] were the first to observe the presence of a periodic train of vertical structures in a mixing layer using flow visualization. These vortices are formed by the rolling and pairing of the adjacent turbulent structures. To describe this phenomenon, they considered the inviscid instability of a constant-vorticity layer between

two parallel streams. The presence of a small amplitude wave can trigger a vertical velocity fluctuation that make the instability to grow between the two streams until they eventually break into discrete vorticity lumps. After this point, adjacent vortices start to merge due to the slight imperfections in the vortex spacing and strength. Then, due to viscous diffusion their identities are smeared out leaving a single large vortex. The resulting large scale turbulent structure which is phase correlated over its spatial extent is commonly termed coherent structure. This instability mechanism involving vortex rolling and pairing observed in the mixing layer is related to the Kelvin-Helmholtz Instability.

Coherent Structures.
As it has been previously introduced, coherent structures can be understood as a connected turbulent fluid mass with instantaneously phase-correlated vorticity over its spatial extent. They are spatially non-overlapping and have their own boundaries. Thus, a turbulent shear layer can be decomposed into coherent and incoherent turbulence. Even though small scale turbulence –Kolmogorov scale- is the most coherent, the large-scale structures are generally the ones referred as coherent structures because of their dynamical significance.

B.1.1.2 Reattachment Zone.

The reattachment point of a shear layer is rarely fixed at a single point. Instead, the unsteadiness of the shear layer associated with the low frequency oscillations lead to a moving reattachment point. The source of the flapping behaviour is not clearly understood yet, although there are several hypothesis based on experimental and numerical research.

B.1.1.3 Recirculation Zone.

This region is dominated primarily by a large two-dimensional vortex that possesses a low circulation velocity. However, there is another significant secondary vortex located at the corner of the step that influence the overall flow behaviour. Scarano and Reithmuller [1999] suggested that the main vortex extends from the step edge to the reattachment point while the secondary vortex remains in the corner of the step wall. Nevertheless, the existence of this secondary vortex is only present in the 3D case.

B.1.2 Important Flow Parameters

Apart from the flow complexity due to the inner instabilities of this flow configuration, there are several flow and geometric parameters that are shown to modify the flow

characteristics behind the step. Aspect ratio, expansion ratio, free stream turbulence intensity, Reynolds numbers and the boundary layer state and thickness at separation are among them. The effect of each individual parameter on the reattachment length is reviewed in this section, since this parameter is the primary one of comparison.

B.1.2.1 Effect of Expansion Ratio

It is defined as the ratio of downstream to upstream height of the channel at the step. Eaton and Johnston [1995], compared expansion ratios ranging from 1.1 to 1.67 keeping other parameters such as Reynolds number or boundary layer thickness under small variations. They observed that the reattachment length increased together with the expansion ratio. The same trend was also observed by Kuehn [1990], who attribute this behaviour to the change in adverse pressure gradient. On the other hand, Otugen [1991] results from expansion ratios ranging from 1.5 to 3.13 suggested the reverse trend. However, they attributed this reduction to the gradual increase in turbulence levels in the separation shear layer.

B.1.2.2 Effect of Aspect Ratio. 3D Effects.

If three dimension flow is considered, the originally considered two-dimensional flow is affected by vortices developing from the corners of the step. Brederode and Bradshaw [1972] traced oil-film patterns on the floor of the downstream region for different aspect ratios. They observed that the flow remained almost two-dimensional for aspect ratios greater than 10.

B.1.2.3 Effect of the Free Stream Turbulence Intensity.

Free stream turbulence intensity is defined as the ratio of the turbulent fluctuation to the free stream velocity

$$I = \frac{\sqrt{u'^2 + v'^2 + w'^2}}{U_\infty} \tag{B.1}$$

Isomoto and Honami [1989] investigated the effects of this parameter to the reattachment length in a systematic study. Their results show the reattachment length to decrease monotonically with the increase in FST.

B.1.2.4 Effect of Boundary Layer Separation.

The effect of boundary layer state is difficult to isolate from Reynolds number and boundary layer thickness at separation. However, the research carried by Eaton and Johnston [1995] show the sharp increase of the reattachment length from laminar to

transitional boundary layer, followed by a decrease to a steady length for fully turbulent boundary layer.

B.1.2.5 Effect of Boundary Layer Thickness at Separation.

As previously mentioned, the effect of this parameter is difficult to isolate; however, it appears to have a limited effect on the reattachment length. The application of boundary layer suction very close upstream of the step has been the procedure used to investigate this effects. Unfortunately, it changes the boundary layer properties, making this procedure not reliable. Thus, further experimentation is required to verify its effect on the reattachment point

B.2 Test Case Developed.

Although different trends regarding the recirculation length are observed for each flow regime, the turbulent regime is the one that will be primarily analysed along this study. This is due to the fact that laminar and transient regimes are not present in the experimental rig. However, an initial study of the laminar case using the fine mesh is interesting to make a first validation of the mesh. In order to compute the flow over the backward-facing step, a CFD package, FLUENT, is used. For turbulent flows, the Spalart-Allmaras, $k-\epsilon$ models, $k-\omega$ models, Reynolds stress model and large eddy simulation model are available. The turbulence models used in this study are the $k-\epsilon$. Although there are many possible variations to use this set of models, the one that is considered here is the realizable $k-\epsilon$. The near-wall treatment methods used in this study are enhancement wall treatment and non-equilibrium wall functions. While the enhancement wall treatment method is exclusively used for very fine mesh, which automatically disconnect the wall functions, the non-equilibrium wall functions are used with a coarse mesh. The usage of non-equilibrium wall functions is recommended for use in complex flows with separation, reattachment and impingement where the mean flow is subjected to strong pressure gradients. Thus, because of its capability to account for pressure gradient effects, the prediction of the wall shear can be potentially improved. A pressure based solver is employed since the flow is assumed to be incompressible. This model is used as a first approach since Kim et al. [2005] demonstrated its acceptable performance for backward-facing step flow for high Reynolds number, i.e. Re=38000. The method used for solving pressure is the pressure correction technique. By applying this method, the momentum equations are solved using a guessed pressure field to obtain a predicted velocity field. The continuity equation is then solved providing corrections to the velocities and pressure which yield mass conservation. The technique followed is the semi-implicit pressure linked equations (SIMPLE). A convergence criterion of $1e-06$ is used for continuity, $x-$velocity, $y-$velocity, k and ϵ. All solutions converged with Second

Table B.1: Mesh characteristics for the backward-facing step case.

	Non-Eq. wall function	Enhancement wall treatment
Number of cells	4800	39000
y+	> 25	< 1

Order Spatial Discretization. The computations domain starts from an inlet located at $15h$ upstream from the step. The outlet boundary is placed at $25h$ downstream from the step and the height of upstream channel is $2h$. The inlet boundary conditions are specified as a constant inlet velocity with 5% turbulent intensity and turbulent viscosity ratio of 10. At the outlet, zero-diffusion condition was applied. The wall boundaries are defined with no-slip condition and smooth wall. The flow is assumed to be incompressible since Mach number is much below 0.3 Several quadrilateral meshes of varying resolution were considered to establish the mesh-independency of the solutions. The characteristic meshes of each near-wall treatment method are shown in Fig. B.1. The

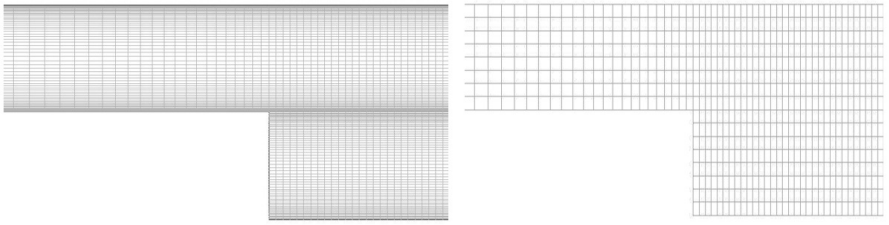

Figure B.1: Meshes for the backward-facing step. Mesh for enhanced wall treatment (left) and mesh for wall functions (right)

characteristics of the ultimate meshes used for each near-wall treatment are shown in Tab. B.1. Most studies on backward-facing step flows were carried out for a wide variety of relevant parameters such as Reynolds number, expansion ratio and aspect ratio. Here, the case is simply used to validate the accuracy of different turbulence models when shear layers, recirculation zones and reattachment points are present.
Although slight differences in geometry and flow characteristics have been proved to greatly modify the results obtained, the main goal of this study is to study throughout this simple geometry some flow characteristics that will be present in our real model.

B.3 Results

B.3.1 Laminar Range

The plot in Fig. B.2 compares the present results with the experimental results from Armaly et al. [1983] Good agreement is found with the experimental results. It is

important to notice that the Reynolds limit of $Re < 400$ is considered in order to minimize the discrepancies between the 3D effects present in their study and the current results from the 2D simulations. When a second order polynomial curve is fitted to the

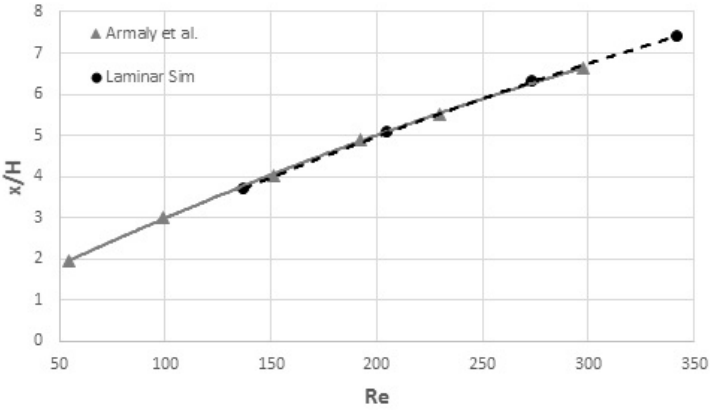

Figure B.2: Normalized reattachment length as a function of Reynolds number

experimental results obtained by Armaly et al. [1983] and the current numeric results, both curves show a significant superposition, Fig B.2. This results show that the mesh employed in this study is sufficiently fine to give accurate solutions.

B.3.2 Turbulent Range

The predicted reattachment lengths are shown in Fig. B.3 according to the near-wall treatment and the Reynolds number with measured values by Armaly et al. [1983]. In order to obtain the reattachment length from numerical simulations the Skin friction evolution is analysed. The point for which its value reaches zero is recorded as the reattachment point. The interest in this geometry and the characteristic flow around

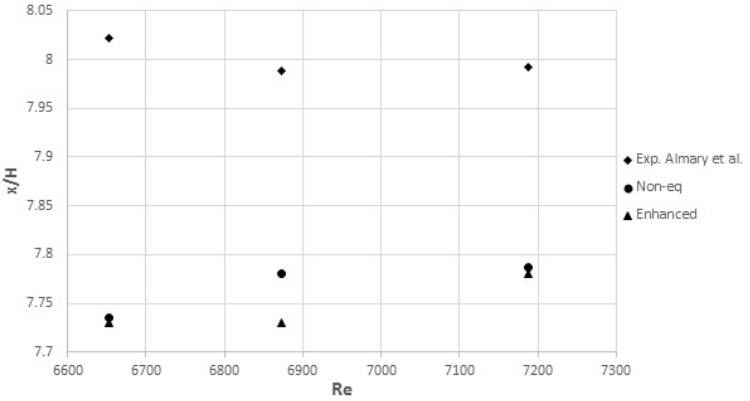

Figure B.3: Normalized reattachment length as a function of Reynolds number for different wall treatments

it was intensified with the work of Armaly et al. [1983]. They presented a detailed

investigation for an expansion ratio of $E.R = 1.9423$, an aspect ratio of $W/h = 36$ and Reynolds numbers up to $Re_D = 8000$. However, above $Re_D = 400$, the three-dimensional effect appeared to create slight discrepancies in the recirculation length between the experimental and the numerical predictions.

B.4 Conclusion

FLUENT software was used to simulate experiments of Armaly et al. [1983]. Reynolds number was varied for matching the existent data. The following conclusions were drawn from this study:

- The re-attachment lengths are predicted well by the Realizable $k-\epsilon$ model for this range of Reynolds numbers
- Using Non-equilibrium wall treatment yields results as accurate as resolving the flow down to the wall in terms of re-attachment length. This greatly reduces the computational cost of the simulation, although the velocity vector field has a considerably lower resolution.
- Fluent is able to capture the physics of the re-circulation region to a better extent at higher turbulent Reynolds numbers. Thus, the Realizable $k-\epsilon$ model with any of the wall treatments considered could give valuable information of the flow in the Aquavitrium Separator due to the higher Reynold number that it is expected to have.
- The high dependency of the flow characteristics with the flow and geometry parameters mentioned along this study prevents the direct comparison between backward-facing step flow and the one originated around the shape formations at the bottom of the Separator tank.

B.5 Ansys FLUENT; Aquavitrum Plant

The first approach to solve the fluid domain of a single separation section is to perform a 2D simulation in Ansys Fluent. However, several strong geometry assumptions have to be done when the 3D volume is simplify to a 2D plane. A $X-Y$ plane at a spanwise location where the jets of the formations are placed is considered to be the most representative $X-Y$ plane. However, doing this 2D transformation jets are not punctual sources of mass and momentum but sources that are assumed to be present along the span-wise component. This facts implies that the outlet of the $X-Y$ plane has to deal with an enormous amount of fluid coming from these sources. This fact leads to a high velocity region close to it that clearly distorts the flow field. Although reducing the mass

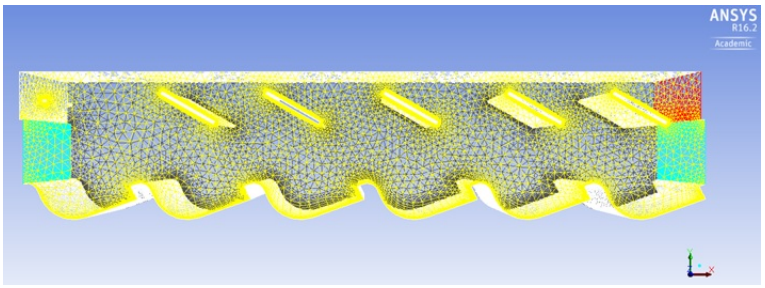

Figure B.4: 3D mesh developed for the analysis of the Aquavitrum separator

injected by the jets could be a solution for the outlet to cope with the mass flow rate, this would modify the flow characteristics at the formations, leading to an inaccurate flow field.

In order to obtain a representative flow field, the whole 3D geometry is analysed in Ansys Fluent. The model used is the Realizable $k-\epsilon$ model with Non-equilibrium wall functions. The mesh with highlighted surfaces is shown in Fig. B.4. The surfaces in

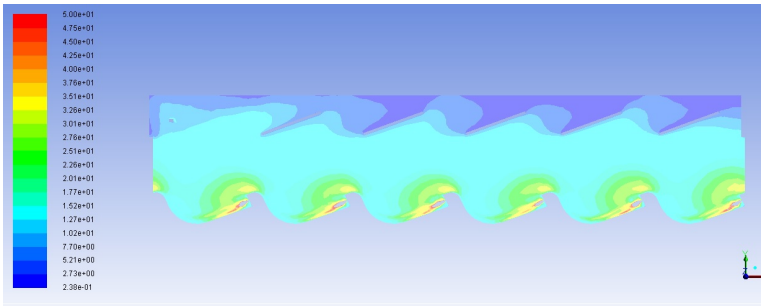

Figure B.5: Turbulent intensity contour plot for the symmetry plane of the 3D simulation

yellow are defined as fixed walls, the ones in light blue are periodic regions, the one in red is the outlet -which represents the gutter that collects contaminants- and the one in grey is a $X-Y$ symmetry plane.

Fig. B.5 shows how the turbulent intensity is enhanced at the ski jump of each forma-

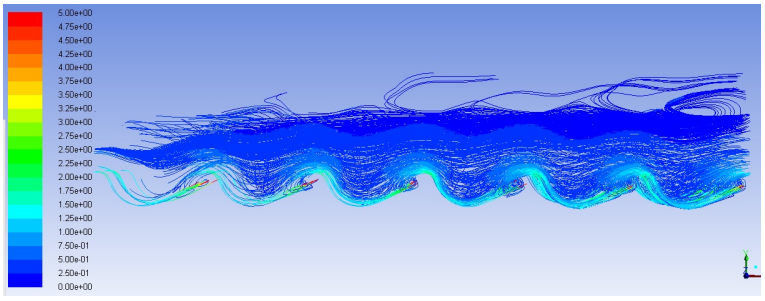

Figure B.6: Velocity streamlines of the 3D simulation

tion due to the flow separation. The eddies that are formed at these locations enables the particle separation due to differences in inertia and relaxation times. The hydrofoils

at the upper part of the separation increase the steadiness of the reverse flow, preventing the settling of plastic particles above them.

Similarly, streamlines in Fig. B.6 show the presence of a reverse flow on the upper part of the tank and the existence of high velocity regions along the formation of the bottom, previously reported.

References

Adrian, R. J. and Westerweel, J. (2011). *Particle Image Velocimetry*. Cambridge University Press.

Aliseda, A., Cartellier, A., Hainaux, F., and Lasheras, J. C. (2002). Effect of preferential concentration on the settling velocity of heavy particles in homogeneous isotropic turbulence. *J. Fluid Mech.*, 468:77–105.

Allen, T. (1990). Particle size measurements. *Chapman and hall, London 4th ed. 1990*, 20.

Alvarado, A. P., Mydlarski, L., and Gaskin, S. (2016). Effect of the driving algorithm on the turbulence generated by a random jet array. *Exp. Fluids*, 57:20–32.

Andersen, A., Pesavento, U., and Wang, Z. J. (2005a). Analysis of transitions between fluttering, tumbling and steady descent of falling cards. *J. Fluid Mech*, 541:91–104.

Andersen, A., Pesavento, U., and Wang, Z. J. (2005b). Unsteady aerodynamics of fluttering and tumbling plates. *J. Fluid Mech*, 541:65–90.

Anping, S., Fanghua, L., Guosheng, L. H. D., and Xing, Z. (2016). Characteristics of particle size distributions for the collapsed riverbank along the desert reach of the upper yellow river. *International Journal of Sediment Research*.

Antonia, R. A. and Orlandi, P. (2004). Similarity of decaying isotropic turbulence with a passive scalar. *J. Fluid Mech*, 505:123–151.

Antonia, R. A., Satyaprakash, B. R., and Hussain, A. K. M. F. (1982). Statistics of fine-scale velocity in turbulent plane and circular jets. *J. Fluid Mech*, 119:55—-89.

Armaly, B. F., Durst, F., Pereira, J. C. F., and Schonung, C. (1983). Experimental and theoretical investigation of backward-facing step flow. *J. Fluid Mech.*, 127.

Ashbaugh, H. S., Guo, X., Schwahn, D., Prudhomme, R. K., Richter, D., and Fetters, L. J. (2005). Interaction of paraffin wax gels with ethylene/vinyl acetate co-polymers. *Energy and Fuels*, 19:138–144.

Auguste, F., Magnaudet, J., and Fabre, D. (2013). Falling styles of disks. *J. Fluid Mech.*, 719:388–405.

Bagchi, P. and Balachandar, S. (2013). Effect of turbulence on the drag and lift of a particle. *Phys. Fluids*, 11(15):3496–3513.

Bagheri, G. H. and Bonadonna, C. (2016). On the drag of freely falling non-spherical particles. *Powder Technology*, 301:526–544.

Balachandar, S. and Eaton, J. K. (2010). Turbulent dispersed multiphase flow. *Annu. Rev. Fluid Mech.*, 42:113–133.

Barhtyar, R., Barry, D., Li, L., Jeng, D., and Yeganeh, B. (2009). Modeling sediment transport in the swash zone: A review. *Ocean Engineering*, 36:767–783.

Basset, A. B. (1888). A treatise on hydrodynamics. *Cambridge: Deighton Bell*, 2.

Bellani, G., Margaret, L. B., Collignon, A. G., Colin, R. M., and Variano, E. A. (2012). Shape effects on turbulent modulation by large nearly neutrally bouyant particles. *J. Fluid Mech.*, 712:41–60.

Bellani, G. and Variano, E. A. (2013). Homogeneity and isotropy in a laboratory turbulent flow. *Exp. Fluids*, 55:1646–1666.

Belmonte, A., Eisenberg, H., and Moses, E. (1998). From flutter to tumble: intertial drag and froude similarity in falling paper. *Phys. Rev. Lett.*, 81:345–348.

Bernstein, O. and Shapiro, M. (1994). Direct determination of the orientation distribution function of cylindrical particles immersed in laminar and turbulent shear flows. *J. Aerosol. Sci.*, 25:113–136.

Biferale, L., Boffetta, G., Celani, A., Lanotte, A., Toschi, F., and Vergassola, M. (2003). The decay of homonegeous anisotropic turbulence. *Phys. Fluids*, 15:2105–2112.

Binks, B. P. and Tyowua, A. T. (2016). Oil-in-oil emulsions stabilised solely by solid particles. *Soft Matter*, pages 876–888.

Blum, D. B., Bewley, G. P., Bodenschatz, E., Gibert, M., Gylfason, A., Mydlarski, L., Voth, G. A., Xu, H., and Yeung, P. K. (2011). Signatures of non-universal large scales in conditional structure functions from various turbulent flows. *New J. Phys.*, 13(113020).

Bodenschatz, E., Bewley, G. P., Nobach, H., Sinhuber, M., and Xu, H. (2014). Variable density turbulence tunnel facility. *Rev. Sci. Instrum.*, 85(093908):331–368.

Boussinesq, J. (1903). Theorie analitique de la chaleur. *Paris: Gauthier-Villars.*, 2.

Breda, M. and Buxton, O. R. H. (2017). Near and far-field analysis of an axisymmetric fractal-forced turbulent jet. *Progress in Turbulence VII*, pages 211–217.

Brederode, V. and Bradshaw, P. (1972). Three-dimensional flow in nominally two-dimensional separation bubbles part 1: Flow behind a rearward-facing step. *Tech Rep. Imperial College. Report*, 10.

Bu, C., Liu, D., Chen, X., Pallares, D., and Gomez, A. (2014). Ignition behavior of single coal particle in fluidized bed under o_2 co_2 and o_2 n_2 atmospheres: A combination of visual image and particle temperature. *Applied Energy*, 115:301–308.

Burattini, P., Lavoie, P., Agrawal, A., Djenidi, L., and Antonia, R. A. (2006). On the power law of decaying homogeneous isotropic turbulence at low reynolds number. *Phys. Rev. E*, 73:066304.

Burattini, P., Lavoie, P., and Antonia, R. A. (2005). On the normalized turbulent energy dissipation rate. *Phys Fluids*, 17:098103.

Buxton, O. R. H., Laizet, S., and Ganapathisubramani, B. (2011). Dissipation rate estimation from piv in zero-mean isotropic turbulence. *Exp. in Fluids*, 51:1417—-1437.

Byron, M. (2015). The rotation and translation of non-spherical particles in homogeneous isotropic turbulence. *PhD Thesis*.

Byron, M., Einarsson, J., Gustavsson, K., Voth, G., Mehlig, B., and Variano, E. (2015). Shape-dependence of particle rotation in isotropic turbulence. *Phys. Fluids*, 27:035101.

Carter, D., Petersen, A., Amili, O., and Coletti, F. (2016). Generating and controlling homogeneous air turbulence using random jet arrays. *Experiments in Fluids*, 57:189.

Chang, K., Bewley, G. P., and Bodenschatz, E. (2012). Experimental study of the influence of anisotropy on the inertial scales of turbulence. *J. Fluid Mech*, 692:464–481.

Chhabra, R. P., Agarwal, L., and Sinha, N. K. (1999). Drag on non-spherical particles: an evaluation of available methods. *Powder technology*, 101:288–295.

Chien, S. F. (1994). Settling velocity of irregularly shaped particles. *SPE Drilling and Completion*, 9:281–289.

Christiansen, E. B. and Barker, D. H. (1965). The effect of shape and density on the free settling of particle at high reynolds number. *AIChE journal*, 50(11):145–151.

Churst, M., Bouchet, G., and Dusek, J. (2013). Numerical simulation of the dynamics of freely falling discs. *Physics of Fluids*, 25:044102.

Clift, R., Grace, J. R., and Weber, M. E. (1978). Bubbles, drops, and particles. *Academic Press, New York*.

Compte-Bellot, G. and Corrsin, S. (1966). The use of a contraction to improve the isotropy of grid-generated turbulence. *J. Fluid Mech.*, 62:115–143.

Cong, S. T., Gay, M., and Michaelides, E. E. (2004). Drag coefficients of irregular shaped particles. *Powder Technology*, 139:21–32.

Dail, H. J., Merrifield, M. A., and Bevis, M. (2000). Steep beach morphology changes due to energetic wave forcing. *Marine Geology*, 162:443–458.

de Bruyn Kops, S. M. and Riley, J. J. (1998). Direct numerical simulation of laboratory experiments in isotropic turbulence. *Phys. Fluids*, 10:2125–2127.

de Jong, J., Cao, L., Woodward, S. H., Salazar, J. P. L. C., Collins, L. R., and Meng, H. (2009). Dissipation rate estimation from piv in zero-mean isotropic turbulence. *Exp. in Fluids*, 46:499–515.

De Silva, I. and Fernando, H. (1994). Oscillating grids as a source of nearly isotropic turbulence. *Phys. Fluids*, 6:2455–2464.

Delbos, S., Weitbrecht, V., Bleninger, T., Grand, P. P., Chassaing, E., Lincot, D., Kerrec, O., and Jirka, G. H. (2009). Homogeneous turbulence at an electrodeposition surface induced by randomly firing jet arrays. *Exp. Fluids*, 46:1105–1115.

Derksen, J. J. (2009). Scalar mixing with fixed and fluidized particles in micro-reactors. *Chemical Engineering Research and Design*, 87:550–556.

Doob, J. L. (1942). The brownian movement and stochastic equations. *Ann. Math.*, 43:351—-369.

Dou, Z., Pecenak, Z. K., Cao, L., Woodward, S. H., Liang, Z., and Meng, H. (2016). Piv measurement of high-reynolds-number homogeneous and isotropic turbulence in an enclosed flow apparatus with fan agitation. *Measurement Science and Technology*, 27:3, 035305.

Dupleich, P. (1941). Rotation in free fall of rectangular wings of elongated shape. *NACA Tech. Memo.*, 1201:1–99.

Eaton, J. K. and Johnston, J. P. (1995). A review and control of a turbulent reattaching flow. *J. Fluid Mech*, 298.

el Hak, M. G. and Corrsin, S. (1974). Measurements of the nearly isotropic turbulence behind a uniform jet grid. *J. Fluid Mech*, 62:115–143.

Elghobashi, S. and Truesdell, G. C. (1992). Direct simulation of particle dispersion in a decaying isotropic turbulence. *J. Fluid Mech.*, 242:655–700.

Ern, P., Risso, F., Favre, D., and Magnaudet, J. (2012). Wake-induced oscillatory paths of bodies freely rising or falling in fluids. *Annu. Rev. Fluid Mech.*, 44:97–121.

Erni, P., Cramer, C., Marti, I., Windhad, E. J., and Fisher, P. (2009). Continuous flow structuring of anisotropic biopolymer particles. *Adv. Colloid Interface Sci.*, 150:16–26.

Esteban, L. B., Shrimpton, J., and Ganapathisubramani, B. (2019a). Laboratory experiments on the temporal decay of homogeneous anisotropic turbulence. *J. Fluid. Mech.*, page (In Press).

Esteban, L. B., Shrimpton, J. S., Rogers, P., and Ingram, R. (2016). Three clean products from co-mingled waste using a novel hydrodynamic separator. *Int. J. Sust. Dev. Plan.*, 11:792–803.

Esteban, L. B., Shrimpton, J. S., Rogers, P., and Ingram, R. (2018). Edge effects on the fluttering characteristics of freely falling planar particles. *Physical Review Fluids*, 3:064302.

Esteban, L. B., Shrimpton, J. S., Rogers, P., and Ingram, R. (2019b). Study of the circularity effect on drag of disk-like particles. *International Journal Multiphase Flows*, 110:189–197.

Fernandes, P. C., Ern, P., Risso, F., and Maugnadet, J. (2005). On the zigzag dynamics of freely moving axisymmetric bodies. *Phys. Fluids*, 17:098107.

Field, S. B., Klaus, M., Moore, M. G., and Nori, F. (1977). Chaotic dynamics of falling disks. *Nature*, 388:252–254.

Fornari, W., Picano, F., and Brandt, L. (2016a). Sedimentation of finite-size spheres in quiescent and turbulent environments. *J. Fluid Mech.*, 788:640–669.

Fornari, W., Picano, F., Sardina, G., and Brandt, L. (2016b). Reduced particle settling speed in turbulence. *J. Fluid Mech.*, 808:153—-167.

Fox, R. O. (2012). Large-eddy-simulation tools for multiphase flows. *Annu. Rev. Fluid Mech.*, 44:47–76.

Gabitto, J. and Tsouris, C. (2008). Drag coefficient and settling velocity for particles of cylindrical shape. *Powder Technol.*, 183:314–322.

Ganapathisubramani, B., LakshminarasimhanN, K., and Clemens, T. (2007). Determination of complete velocity gradient tensor by using cinematographic stereoscopic piv in a turbulent jet. *Exp. in Fluids*, 42:923–939.

Ganser., G. H. (1993). A rational approach to drag prediction of spherical and non-spherical particles. *Powder technology*, 77:143–152.

George, W. K. (1992). Locally axisymmetric turbulence. *Physics of Fluids A*, 4:1492.

George, W. K. and Hussein, H. J. (1991). Locally axisymmetric turbulence. *J. Fluid Mech.*, 223:1–23.

Goepfert, C., Marie, J. L., Chareyron, D., and Lance, M. (2010). Characterization fo a system generating a homogeneous isotropic turbulence field by free synthetic jets. *Exp Fluids*, 48:809–822.

Good, G. H., Gerashchenko, S., and Warhaft, Z. (2012). Intermittency and inertial particle entrainment at a turbulent interface: the effect of the large-scale eddies. *J. Fluid Mech.*, 694:371—398.

Good, G. H., Ireland, P. J., Bewley, G. P., Bodenschatz, E., Collins, L. R., and Warhaft, Z. (2014). Settling regimes of inertial particles in isotropic turbulence. *J. Fluid Mech.*, 759(R3):1–12.

Gore, R. A. and Crowe, C. T. (1989). Effect of particle size on modulating turbulent intensity. *Int. J. Multiphase Flow*, 15(2):279–285.

Goto, S. and Vassilicos, J. C. (2016). Unsteady turbulence cascades. *Phys. Review E*, 94:053108.

Gouesbet, G. and Berlemont, A. (1999). Eulerian and lagrangian approaches for predicting the behaviour of discrete particles in turbulent flows. *Progress in Energy and Combustion Science.*, 25:133–159.

Gustavsson, K., Einarsson, J., and Mehlig, B. (2014). Tumbling of small axisymmetric particles in random and turbulent flows. *Physical Review Letters*, 112.

Haider, A. and Levenspiel, O. (1983). Drag coefficient and terminal velocity of spherical of non-spherical solid particles. *Powder Technology*, 58:63–70.

Haider, A. M. and Levenspiel, O. (1989). Drag on non-spherical particles: an evaluation of available methods. *Powder technology*, 58:63–70.

Hartman, M., Trnka, O., and Svoboda, K. (1994). Free settling of nonspherical particles. *Ind. Eng. Chem. Res.*, 33:1979–1983.

Hearst, R. J. and Lavoie, P. (2014). Decay of turbulence generated by a square-fractal-element grid. *J. Fluid Mech.*, 741:567–584.

Heisinger, L., Newton, P., and Kanso, E. (2014). Coins falling in water. *J. Fluid Mech.*, 714:243–253.

Hellström, L. H. O., Zlatinov, M. B., Cao, G., and Smits, A. J. (2013). Turbulent pipe flow downstream of a 90 bend. *J. Fluid Mech.*, 735 (R7):1–12.

Heymsfield, A. J. and Westbrook, C. D. (2010). Advances in the estimation of ice particle fall speeds using laboratory and field measurements. *American Met. Soc.*, pages 2469–2482.

Ho, H. W. (1964). Fall velocity of a sphere in an oscillating fluid. *PhD Thesis. University of Iowa.*

Hoef, M. A., Annaland, M., Deen, N. G., and Kuipers, J. A. M. (2008). Numerical simulation of dense gas-solid fluidized beds: A multiscale modeling strategy. *Annu. Rev. Fluid Mech.*, 40:47–70.

Holzer, A. and Sommerfeld, M. (2008). New simple correlation formula for the drag coefficient on non-spherical particles. *Powder Technol.*, 184:361–365.

Huang, M. J. and Leonard, A. (1994). Power-law decay of homogeneous turbulence at low reynolds numbers. *Phys. Fluids*, 6:3765–3775.

Hurst, D. J. and Vassilicos, J. C. (2007). Scalings and decay of fractal-generated turbulence. *Phys. Fluids*, 19:035103.

Hwang, W. and Eaton, J. K. (2004). Creating homogeneous and isotropic turbulence without a mean flow. *Exp. Fluids*, 36:444–454.

Ireland, P. J. and Collins, L. R. (2012). Direct numerical simulation of inertial particle entrainment in a shearless mixing layer. *J. Fluid Mech.*, 704:301–332.

Isomoto, K. and Honami, S. (1989). The effect of inlet turbulence intensity on the reattachment process over a backward-facing step. *J. Fluid Eng*, 111.

Janhall, S. (2015). Review on urban vegetation and particle air pollution - deposition and dispersion. *Atm. Environment*, 105:130–137.

Jayaweera, K. O. L. F. (1972). An equivalent disc for calculating the terminal velocities of plate-like ice crystals. *J. Atmos. Sci.*, 29:596–597.

Jayaweera, K. O. L. F. and Mason, B. J. (1965). The behaviour of freely falling cylinders and cones in a viscous fluid. *J. Fluid Mech.*, 22:709–720.

Kajikawa, M. (1992). Observations of the falling motion of plate-like crystals. part i: The free-fall patterns and velocity variations of unrimed crystals. *J. Meteor. Soc. Japan*, 70:1–9.

Kang, H. S., Chester, S., and Meneveau, C. (2003). Decaying turbulence in an active-grid-generated flow and comparisons with large-eddy simulation. *J. Fluid Mech*, 480:129–160.

Khorsandi, B., Gaskin, S., and Mydlarski, L. (2013). Effect of backgroud turbulence on an axisymmetric turbulent jet. *J. Fluid Mech*, 736:250–286.

Kim, J., Ghajar, A. F., Tang, C., and Foutch, G. L. (2005). Comparison of near-wall treatment methods for high reynolds number backward facing step flow. *J. Comp. Fluid Dynamics*, 19.

Kistler, A. L. and Vrebalovich, T. (1966). Grit turbulence at large reynolds numbers. *J. Fluid Mech*, 26:37–47.

Klein, S., Gibert, M., Berut, A., and Bodenschatz, E. (2013). Simultaneous 3d measurement of the translation and rotation of finite size particles and the flow field in a fully developed turbulent water flow. *Meas. Sci. Technol*, 24.

Klett, J. M. (1995). Orientation model for particles in turbulence. *J. Atmos. Sci.*, 52:2276–2285.

Kolb, C. E. and Worsnop, D. R. (2012). Chemistry and compositions of atmospheric aerosol particles. *Annu. Rev. Phys. Chem*, 63:471–491.

Kolmogorov, A. N. (1941). The local structure of turbulence in incompressible viscous fluid for very large reynolds. *C. R. Acad. Sci. U. R. S. S.*, 30:301.

Krogstad, P. A. and Davidson, P. A. (2011). Freely decaying, homogeneous turbulence generated by multi-scale grids. *J. Fluid Mech.*, 680:417–434.

Kuehn, D. M. (1990). Effects of adverse pressure gradient on the incompressible reattaching flow over a rearward-facing step. *AAIA Journal*, 28.

Larssen, J. V. and Devenport, W. J. (2011). On the generation of large-scale homogeneous turbulence. *Exp. Fluids*, 50:1207–1223.

Lasheras, J. C. and Tio, K. K. (1994). Dynamics of a small spherical particle in steady two-dimensional vortex flows. *Appl. Mech. Rev.*, 6(47):61–69.

Lavertu, T. M., Mydlarski, L., and Gaskin, S. J. (2006). Differential diffusion of high-schmidt-number passive scalars in a turbulent jet. *J. Fluid Mech.*, 612:439–475.

Lavoie, P., Djenidi, L., and Antonia, R. A. (2007). Effects of initial conditions in decaying turbulence generated by passive grids. *J. Fluid Mech*, 585:395–420.

Lee, C., Su, Z., Zhong, H., Chen, S., Zhou, M., and Wu., J. (2013). Experimental investigation of freely falling thin disks. part 2. transition of three-dimensional motion from zigzag to spiral. *J. Fluid Mech.*, 42:77–104.

Leith, D. (1987). Drag on non-spherical objects. *Aerosol. Sci. Tech.*, 6:153–161.

Ling, S. C. and Wang, C. A. (1972). Decay of isotropic turbulence generated by a mechanically agitated grid. *Phys. Fluids*, 15:1363–1369.

List, R. and Schemenauer, R. S. (1971). Free-fall behaviour of planar snow crystals, conical graupel and small hail. *J. Atmos. Sci.*, 28:110–115.

Loth, E. (2008). Drag of non-spherical solid particles of regular and irregular shape. *Powder Technol.*, 182:342–353.

Lu, J., Fugal, J. P., Nordsiek, H., Saw, E. W., Shaw, R. A., and Yang, W. (2008). Lagrangian particle tracking in three dimensions via single-camera in-line digital holography. *New Journal of Physics*, 10:125013.

Mahadevan, L., Ryu, W. S., and Samuel, A. D. T. (1999). Tumbling cards. *Phys. Fluids*, 11:1–3.

Makita, H. (1991). Realization of a large-scale turbulence field in a small wind tunnel. *Fluid Dyn. Res.*, 8:53–64.

Mallier, R. and Maxey, M. (1991). The settling of nonspherical particles in a cellular flow field. *Phys. Fluids A*, 3:1481–1494.

Mando, M. and Rosendahl, L. (2010). On the motion of non-spherical particles at high reynolds number. *Powder Technology*, 202:1–13.

Marcus, G. G., Parsa, S., Kramel, S., Ni, R., and Voth, G. A. (2014). Measurement of the solid-body rotation of anisotropic particles in 3d turbulence. *New Journal of Physics*, 16.

Marie, L. and Daviaud., F. (2004). Experimental measurement of the scale-by-scale momentum transport budget in a turbulent shear flow. *Phys. Fluids*, 16:457–461.

Maxey, M. R. (1987). The gravitational settling of aerosol particle in homogeneous turbulence and random flow fields. *J. Fluid Mech.*, 174:441–465.

Maxey, M. R. and Corrsin, S. (1986). Gravitational settling of aerosol particles in randomly oriented cellular flow fields. *J. Atmos. Sci*, 43:1112–1134.

Maxey, M. R. and Riley, J. J. (1983). Equation of motion for a small rifid sphere in a nonuniform flow. *Phys. Fluids*, 26(4):883–889.

Maxwell, J. C. (1853). On a particular case of the descent of a heavy body in a resisting medium. *Camb. Dublin Math. J.*, 9:115–118.

Mazellier, N. and Vassilicos, J. C. (2010). Turbulence without richardson-kolmogorov cascade. *Phys. Fluids*, 22:075101.

McDougall, T. J. (1979). Measurements of turbulence in a zero-mean shear mixed layer. *J. Fluid Mech.*, 94:409–431.

McKenna, S. P. and McGillis, W. R. (2004). Observations of flow repeatability and secondary circulation in an oscillating grid-stirred tank. *Phys. Fluids*, 16:3499–3502.

Meldi, M. (2016). The signature of initial production mechanisms in isotropic turbulence decay. *Phys. Fluids*, 28:035105.

Meldi, M., Lejemble, H., and Sagaut, P. (2014). On the emergence of non-classical decay regimes in multiscale/fractal generated isotropic turbulence. *J. Fluid Mech.*, 756:816–843.

Meldi, M., P.Sagaut, and Lucor, D. (2011). A stochastic view of isotropic turbulence decay. *J. Fluid Mech.*, 668:351—-362.

Meldi, M. and Sagaut, P. (2014). On non-self-similar regimes in homogeneous isotropic turbulence decay. *J. Fluid Mech.*, 711:364–393.

Meldi, M. and Sagaut, P. (2017). Turbulence in a box: quantification of large-scale resolution effects in isotropic turbulence free decay. *J Fluid Mech*, 818:697–715.

Meyer, C. R., Byron, M. L., and Variano, E. A. (2013). Rotational diffusion of particles in turbulence. *Limnology and Oceanography: Fluids and Environments*, 3:89—102.

Mitchell, D. L. (1996). use of mass- and area-dimensional power laws for determining precipitation particle terminal velocities. *J. Atmos. Sci.*, 53:1710–1723.

Moffat, H. K. (2013). Three coins in a fountain. *J. Fluid Mech.*, 720:1–4.

Moffet, R. C. and Prather, K. A. (2009). In-situ measurements of the mixing state and optical properties of soot with implications for radiative forcing estimates. *PNAS*, 106:11872–77.

Monchaux, R., Bourgoin, M., and Cartellier, A. (2012). Analyzing preferential concentration and clustering of inertial particles in turbulence. *Int. J. Multiphase Flow*, 40.

Muller, R. H., Mader, K., and Gohla, S. (2000). Solid lidip nanoparticles (sln) for controlled drug delivery - a review of the state of the art. *European J. of Pharmaceutics and Biopharmaceutics*, 50:161–177.

Muller, R. H., Radtke, M., and Wissing, S. A. (2002). Solid lidip nanoparticles (sln) and nanostructured lidip carriers (nlc) in cosmetic and dermatological preparations. *Advanced Drug Delivery Reviews.*, 54:131–155.

Murray, S. P. (1970). Settling velocities and vertical diffusion of particles in turbulent water. *J. Geophys. Res.*, 75(9):1647–1654.

Mydlarski, L. and Warhaft, Z. (1996). On the onset of high-reynolds number grid-generated wind tunnel turbulence. *J. Fluid Mech.*, 320:331–368.

Mydlarski, L. and Warhaft, Z. (1998). Passive scalar statistics in high-peclet-number grid turbulence. *J. Fluid Mech.*, 358:135–175.

Navier, C. L. M. H. (1822). Memoire ur les lois du mouvement des fluides. *Mem. Acad. Sci. Inst. France*, 6:389–440.

Ni, R., Ouellette, N. T., and Voth, G. A. (2014). Alignment of vorticity and rods with lagrangian fluid stretching in turbulence. *J. Fluid Mech.*, 743.

Nielsen, P. (1984). On the motion of suspended particles. *Journal of Geophysical Research*, 89:616–626.

Nielsen, P. (1992). Coastal bottom boundary layers and sediment transport. *Singapore, World Scientific.*

Nielsen, P. (1993). Turbulence effects on the settling of suspended particles. *Journal of Sedimentary Research*, 63(5):835—-838.

Noel, V. and Sassen, K. (2005). Study of planar ice crystal orientations in ice clouds from scanning polarization lidar observations. *J. Appl. Meteorol.*, 44:653–64.

Obligado, M., Teitelbaum, T., Cartellier, A., Mininni, P., and Bourgoin, M. (2014). Preferential concentration of heavy particles in turbulence. *J. Turbulence*, 15:293–310.

Oseen, C. W. (1927). Hydrodynamik. *Akademische Verlag, Leipzig*, 2.

Ott, S. and Mann, J. (2000). An experimental investigation of the relative diffusion of particle paris in three-dimensional turbulent flow. *J. FLuid Mech.*, 422:207–223.

Otugen, M. V. (1991). Expansion ratio effects on the separated shear layer and reattachment downstream of a backward-facing step. *Exp. Fluids*, 10.

Parsa, S., Calzavarini, E., Toschi, F., and Voth, G. A. (2012). Rotation rate of rods in turbulent fluid flow. *Physical Review Letters*, 109:1–10.

Perot, J. B. (2011). Determination of the decay exponent in mechanically stirred isotropic turbulence. *AIP Advances*, 1:022104.

Pesavento, U. and Wang, Z. J. (2004). Falling paper: Navier-stokes solutions, model of fluid forces, and center of mass elevation. *Phys. Rev. Lett.*, 93:144501–4.

Pope, S. B. (2000). Turbulent flows. *Cambridge University Press.*

Pothos, S., Troolin, D., Lai., W., and Menon, R. (2009). V3v- volumetric three-component velocitmetry for 3d flow measurements - main principle, theory and applications. *Termotehnica*, 2:25–32.

Qureshi, N. M., Bourgoin, M., Baudet, C., Cartellier, A., and Gagne, Y. (2007). Turbulent transport of material particles: An experimental study of finite size effect. *Pysical Review Letters*, 99.

Reeks, M. W. (1977). On the dispersion of small particles suspended in an isotropic turbulent fluid. *J. Fluid Mech*, 83:529–546.

Rhodes, M. (2008). Introduction to particle technology. *Second Edn Wiley.*

Ross, F. W. and Kegelman, J. T. (1986). Control of coeherent structures in reattaching laminar and turbulent shear layers. *AAIA Journal*, 24.

Ruetsch, G. R. and Meiburg, E. (1993). On the motion of small spherical bubbles in two-dimensional vortical flows. *Phys. Fluids A*, 5:2326–2341.

Saarenrinne, P. and Piirto, M. (2000). Turbulent kinetic energy dissipation rate estimation from piv velocity vector fields. *Exp. in Fluids*, 29:300–307.

Sabban, L. and van Hout, R. (2011). Measurements of pollen grain dispersal in still air and stationary near homogeneous, isotropic turbulence. *J. Aerosol Science.*, 42:867–882.

Scarano, F. and Reithmuller, M. L. (1999). Iterative multigrid approach in piv image processing with discrete window offset. *Exp. Fluids*, 26.

Schmitt, F. G. and Seuront, L. (2008). Intermittent turbulence and copepod dynamics: increase in encounter rates through preferential concentration. *Journal of Marine Systems*, 70:263–272.

Shirolkar, J. S., Coimbra, C. F. M., and McQuay, M. Q. (1996). Fundamental aspect of modelling turbulenc particle dispersion in dilute flows. *Progress in energy and combustion*, 22.

Siewert, C., Kunnen, R. P. J., Meinke, M., and Schroder, W. (2014). Orientation statistics and settling velocity of ellipsoids in decaying turbulence. *Atmos. Res*, 142:45–56.

Sinquin, A., Palermo, T., and Peysson, Y. (2004). Rheological and flow properties of gas hydrate suspensions. *Oil and Gas Science and Technology*, 59(1):41–57.

Skrbek, L. and Stalp, S. R. (2000). On the decay of homogeneous isotropic turbulence. *Phys. Rev. Letters*, 12:1997–2019.

Smith, E. H. (1971). Autorotating wings: an experimental investigation. *J. Fluid Mech*, 50:513–534.

Son, S. Y. and Kihm, K. D. (1998). Effect of coal particle size on coal-water slurry (cws) atomization. *Atomization and Sprays*, 8:503–519.

Squires, K. D. and Eaton, J. K. (1991). Preferential concentration of particles by turbulence. *Phys. Fluids*, 3:1169–1178.

Sreenivasan, K. R. (1984). On the scaling of the energy dissipation rate. *Phys Fluids*, 27:1048.

Sreenivasan, K. R. (1998). An update on the energy dissipation rate in isotropic turbulence. *Physics of Fluids*, 108:528.

Stringham, G. E., Simons, D. B., and Guy, H. P. (1969). The behaviour of large particles falling in quiescent liquids. *U.S. Department of Interior.*

Subramaniam, S. (2013). Lagrangian-eulerian methods for multiphase flows. *Progress in Energy and Combustion Science.*, 39:215–245.

Sullivan, A. P. and Kilpatrick, P. K. (2002). The effects of inorganic solid particles on water and crude oil emulsion stability. *Ind. Eng. Chem. Res.*, 41:3389–3404.

Sun, L., Lin, J. Z., Wu, F. L., and Chen, Y. M. (2004). Effect of non-spherical particles on the fluid turbuelnce in a particulate pipe flow. *Journal of Hydrodynamics*, 16(6).

Swamee, P. K. and Ohja, C. P. (1991). Drag coefficient and fall velocity of nonspherical particles. *J. Hyd. Eng.*, 117:660–667.

Tanaka, T. and Eaton, J. K. (2007). A correction method for measuring turbulence kinetic energy dissipation rate by piv. *Exp. in Fluids*, 42:893–902.

Taylor, G. I. (1935). Statistical theory of turbulence. *Proc. R. Soc. A*, 151:421–444.

Taylor, G. I. (1938). The spectrum of turbulence. *Proc. R. Soc. Lond*, 164:421–444.

Taylor, J. R. (2005). Classical mechanics. *University Science Books, Mill Valley, CA*.

Tchen, C. M. (1947). Mean value and correlation problems connected with the motion of small particles suspended in a turbulent fluid. *PhD thesis, TU Delft, Delft University of Technology.*

Tio, K. K., Ganan, A. M., and Lasheras, J. C. (1993). The dynamics of small, heavy, rigid, spherical particle in a periodic stuart vortex flow. *Phys. Fluids A*, 5:1679–1693.

Toschi, F. and Bodenschatz, E. (2009). Lagrangian properties of particles in turbulence. *Annu. Rev. Fluid Mech.*, 41:375–404.

Touil, H., Bertoglio, J. P., and Shao, L. (2002). The decay of turbulence in a bounded domain. *J. Turbulence*, 3:049.

Tropea, C., Yarin, A., and Foss, J. F. (2007). Handbook of experimental fluid mechanics. *Springer*.

Truesdell, G. C. and Elghobashi, S. (1994). On the two way interaction between homogeneous turbulence and dispersed solid particles. ii. *Phys. Fluids*, 6:1405–1407.

Uberoi, M. S. and Wallis, S. (1967). Effect of grid geometry on turbulence decay. *Phys. Fluids*, 10:1216–1224.

Valente, P. C. and Vassilicos, J. C. (2011). The decay of turbulence generated by a class of multiscale grids. *J. Fluid Mech.*, 687:300–340.

Valente, P. C. and Vassilicos, J. C. (2012). Dependence of decaying homogeneous isotropic turbulence on inflow conditions. *Phys. Letters A*, 376:510–514.

Variano, E. A., Bodenschatz, E., and Cowen, E. A. (2004). A random synthetic jet array driven turbulence tank. *Exp. Fluids*, 37:613–615.

Variano, E. A. and Cowen, E. A. (2008). A random-jet-stirred turbulence tank. *J. Fluid Mech*, 604:1–32.

Vassilicos, J. C. (2015). Dissipation in turbulent flows. *Annu. Rev. Fluid Mech.*, 47:95–114.

Vincent, L., Shambaugh, W. S., and Kanso, E. (2016). Holes stabilize freely falling coins. *J. Fluid Mech.*, 801:250–259.

Volk, R., Odier, P., and Pinton, J. F. (2006). Fluctuation of magnetic induction in von karman swirling flows. *Phys. Fluids*, 18:085105.

Von Karman, T. and Howarth, L. (1938). On the statistical theory of isotropic turbulence. *Proc. R. Soc. Lond. A*, 164:192–215.

Voth, G. A., Porta, A., Crawford, A. M., Alezander, J., and Bodenschatz, E. (2002). Measurement of particle accelerations in fully developed turbulence. *J. FLuid Mech.*, 469:121–160.

Voth, G. A. and Soldati, A. (2017). Anisotropic particles in turbulence. *Annual Reviwe of Fluid Mechanics.*, 49:249–276.

Wadell, H. (1934). Some new sedimentation formulas. *Physics*, 5:281–291.

Wang, L. P. and Maxey, M. R. (1993). Settling velocity and concentration distribution of heavy particles in homogeneous isotropic turbulence. *J. Fluid Mech.*, 256:27–68.

Warnaars, T. A., Hondzo, M., and Carper, M. A. (2006). A desktop apparatus for studying interactions between microorganisms and small-scale fluid motion. *Hydrobiologia*, 563:431–443.

Webster, D. R., Brathwaite, A., and Yen, J. (2004). A novel laboratory apparatus for simulating isotropic oceanic turbulence at low reynolds number. *Limnology and Oceanography: Methods*, 2:1–12.

Willmarth, W. W., Hawk, N. E., and Harvey, R. L. (1964). Steady and unsteady motions and wakes of freely falling disks. *Phys. Fluids*, 7:197–208.

Winant, C. D. and Browand, F. K. (1974). Vortex pairing: the mechanism of turbulent mixing-layer growth at moderate reynolds number. *J. Fluid Mech.*, 63.

Wood, A. M., Hwang, W., and Eaton, J. K. (2005). Preferential concentration of particles in homogeneous and isotropic turbulence. *Int. J. Multiphase Flow*, 31:1220–1230.

Wray, A. (1998). Decaying isotropic turbulence. *Tech. Rep. AGARD Advisory Rep.*

Xu, H. and Bodenschatz, E. (2008). Motion of inertial particles with size larger than kolmogorov scale in turbulent flows. *Physica D Nonlinear Phenomena*.

Yang, C. Y. and Lei, U. (1998). The role of the turbulent scales in the settling velocity of heavy particles in homogeneous isotropic turbulence. *J. Fluid Mech*, 371:179–205.

Yang, T. S. and Shy, S. S. (2003). The settling velocity of heavy particles in an aqueous near-isotropic turbulence. *Physics of Fluids.*, 15(4):868–880.

Yang, T. S. and Shy, S. S. (2005). Two-way interaction between solid particles and homogeneous air turbulence: particle settling rate and turbulence modification measurements. *J. Fluid Mechanics*, 526:171—-216.

Zhong, H., Chen, S., and Lee, C. (2011). Experimental study of freely falling thin disks: transition from planar zigzag to spiral. *Phys Fluids*, 23:011–702.

Zimmermann, R., Gasteuil, Y., Bourgoin, M., Volk, R., Pumir, A., and Pinton, J. F. (2011a). Rotational intermittency and turbulence induced lift experienced by large particles in a turbulent flow. *Physical Review Letters*, 106.

Zimmermann, R., Gasteuil, Y., Bourgoin, M., Volk, R., Pumir, A., and Pinton, J. F. (2011b). Tracking the dynamics of translation and absolute orientation of a sphere in a turbulent flow. *Review of Scientific Intruments*, 82.

Zimmermann, R., Xu, H., Gasteuil, Y., Bourgoin, M., Volk, R., Pinton, J. F., and Bodenschatz, E. (2010). The lagrangian exploration module: an apparatus for the study of statistically homogeneous and isotropic turbulence. *Rev. Sci. Instrum*, 81(055112).